SAHAN DAMITH LIYANAARACHCHI

Waveform Design and Processing for Joint Wireless Communications and Sensing

SAHAN DAMITH LIYANAARACHCHI

Waveform Design and Processing for Joint Wireless Communications and Sensing

ACADEMIC DISSERTATION
To be presented, with the permission of
the Faculty of Information Technology and Communication Sciences
of Tampere University,
for public discussion in the Auditorium TB109
of the Tietotalo building, Korkeakoulunkatu 1, Tampere,
on 12th of June 2023, at 12 o'clock.

The originality of this thesis has been checked using the Turnitin OriginalityCheck service.

Cover design: Roihu Inc.

Carbon dioxide emissions from printing Tampere University dissertations have been compensated.

To my *mother*, who gave me *everything*...
To my *father*, who made *everything* possible for me...

Preface

The thesis work was possible because of many people who contributed in different ways. First and foremost, I would like to thank my supervisor, Associate Professor Taneli Riihonen, for guiding me throughout my Ph.D. journey by helping and advising me regarding technical matters and also helping me grow as a person. Second, I thank my co-supervisor, Professor Mikko Valkama, for supporting and guiding my studies. I acknowledge the pre-examiners, Assistant Research Professor Alex Rajan Chiriyath from the Arizona State University, USA, and Assistant Professor M. R. Bhavani Shankar from the University of Luxembourg, Luxembourg, for reading my thesis and providing valuable feedback that certainly improved it. I thank Associate Professor Besma Smida from the University of Illinois, USA, for agreeing to be the opponent for my defense. I also thank Dr. Himal Suraweera from the University of Peradeniya, Sri Lanka, for guiding me throughout all these years.

Abstract

Since the advent of radar/sensing systems, they have always had fixed frequencies for operation. Due to the exponential growth of communications systems, the need for dedicated spectrum for them also increased, causing spectrum scarcity for both communications and sensing. It was obvious that some form of flexible spectrum sharing was necessary between these two functionalities. Soon enough, this led the researchers to focus on joint communications and sensing (JCAS) systems that share spectral resources efficiently. The hardware convergence due to the similar functioning of the two systems complemented the frequency convergence of JCAS systems. In fact, JCAS is one of the prominent requirements in future sixth-generation (6G) communications systems.

This thesis focuses on integrating the sensing functionality on top of wireless mobile communications systems, such as in fifth-generation (5G). To facilitate effective JCAS, the thesis provides signal processing techniques for designing waveforms that optimally share the spectral resources, for single-input single-output (SISO) as well as multiple-input multiple-output (MIMO) systems. In addition, novel radar processing techniques are investigated for MIMO systems to better detect the targets in the environment.

The standard waveform in 5G, that is, orthogonal frequency-division multiplexing (OFDM), is also considered for joint waveform design. In such a communications system, the resources are usually not fully utilized and there exist unused subcarriers within the OFDM waveform. These subcarriers are filled with optimized

samples to minimize the lower bounds of delay and velocity estimates' error variances of sensing, for SISO JCAS systems. The simulations with standard-compliant 5G waveforms illustrate the improvements possible in sensing, while also helping to maximize the efficiency in the transmit power amplification process, along the same optimization scheme. The simulation results are complemented through practical radio-frequency measurements of an outdoor environment depicting the significant gains that can be obtained in the range–angle map of sensing, due to the waveform optimization.

For MIMO JCAS systems, apart from conventional communications streams, separate transmit (TX) streams are used to improve sensing performance through two separate schemes. One scheme involves optimizing the sensing streams to minimize the lower bounds of delay and angle estimates' error variances of sensing. Simulation results indicate that the errors of sensing can be minimized while striking a good balance with the communications capacity. The other scheme depicts that the target detection can be enhanced using sensing streams on top of a communications stream. Specifically, the number of false targets detected can be significantly reduced in comparison to single-stream communication.

The antenna arrays in MIMO communications systems nowadays are a combination of analog and digital architectures, i.e., hybrid, instead of consisting of a fully-digital architecture, for reduced costs and power consumption. Radar processing in such a hybrid architecture with multiple TX streams is not straightforward in comparison to the conventional fully-digital MIMO radar. Hence, this thesis also provides novel radar processing techniques to obtain the range–angle and range–velocity maps of the sensed environment. The simulation results illustrate that the targets can be reliably detected through the proposed MIMO processing, while also providing super-resolution in the angular domain.

Table of Contents

List of Publications

[**P1**]   S. D. Liyanaarachchi, T. Riihonen, C. Baquero Barneto and M. Valkama. **Optimized Waveforms for 5G–6G Communication With Sensing: Theory, Simulations and Experiments**. *IEEE Transactions on Wireless Communications* 20.12 (Dec. 2021), 8301–8315. DOI: `10.1109/TWC.2021.3091806`.

[**P2**]   S. D. Liyanaarachchi, C. Baquero Barneto, T. Riihonen and M. Valkama. **Joint OFDM Waveform Design for Communications and Sensing Convergence**. *Proc. IEEE International Conference on Communications (ICC)*. June 2020. DOI: `10.1109/ICC40277.2020.9149408`.

[**P3**]   S. D. Liyanaarachchi, C. Baquero Barneto, T. Riihonen and M. Valkama. **Experimenting Joint Vehicular Communications and Sensing with Optimized 5G NR Waveform**. *Proc. IEEE 93rd Vehicular Technology Conference (VTC2021-Spring)*. Apr. 2021. DOI: `10.1109/VTC2021-Spring51267.2021.9448834`.

[**P4**]   S. D. Liyanaarachchi, T. Riihonen, C. Baquero Barneto and M. Valkama. **Joint MIMO Communications and Sensing with Hybrid Beamforming Architecture and OFDM Waveform Optimization**. *IEEE Transactions on Wireless Communications* (2022). under review after minor revision.

[**P5**] S. D. Liyanaarachchi, C. Baquero Barneto, T. Riihonen, M. Heino and M. Valkama. **Joint Multi-User Communication and MIMO Radar Through Full-Duplex Hybrid Beamforming**. *Proc. IEEE International Online Symposium on Joint Communications Sensing (JC&S)*. Feb. 2021. DOI: `10.1109/JCS52304.2021.9376319`.

[**P6**] S. D. Liyanaarachchi, C. Baquero Barneto, T. Riihonen, M. Heino and M. Valkama. **Range–Angle Processing for Target Detection in Joint MIMO-OFDM Communications and Sensing**. *Proc. IEEE 22nd International Workshop on Signal Processing Advances in Wireless Communications (SPAWC)*. Oct. 2021, 486–490. DOI: `10.1109/SPAWC51858.2021.9593229`.

[**P7**] S. D. Liyanaarachchi and T. Riihonen. **MIMO Ambiguity Function Enhancement for Integrated OFDM Communications and Sensing**. *Proc. IEEE Sensor Array and Multichannel Signal Processing Workshop (SAM)*. June 2022. DOI: `10.1109/SAM53842.2022.9827782`.

Abbreviations

2-D	Two-dimensional
4-D	Four-dimensional
4G	Fourth-generation
5G	Fifth-generation
6G	Sixth-generation
A/D	Analog-to-digital
AF	Ambiguity function
BB	Baseband
BD	Block diagonalization
BS	Base station
CP	Cyclic prefix
CRLB	Cramer–Rao lower bound
D/A	Digital-to-analog
DFT	Discrete Fourier transform
DoA	Direction-of-arrival
FFT	Fast Fourier transform

FMCW	Frequency-modulated continuous wave
IDFT	Inverse discrete Fourier transform
IFFT	Inverse fast Fourier transform
ISI	Inter-symbol interference
ISL	Integrated side-lobe level
JCAS	Joint communications and sensing
LFM	Linear frequency-modulated
LoS	Line-of-sight
MF	Matched-filter
MI	Mutual information
MIMO	Multiple-input multiple-output
MLE	Maximum likelihood estimation
MMSE	Minimum mean square error
MS	Mean square
MUSIC	MUltiple SIgnal Classification
NLoS	Non-line-of-sight
NR	New Radio
NSP	Null-space projection
OFDM	Orthogonal frequency-division multiplexing
OOB	Out-of-band
OTFS	Orthogonal time-frequency space
P/S	Parallel-to-serial
PA	Power amplifier
PAPR	Peak-to-average power ratio
PDF	Probability density function
PRB	Physical resource block
PSD	Power spectral density

PSK	Phase-shift keying
PSL	Peak side-lobe level
QAM	Quadrature amplitude modulation
QoS	Quality-of-service
RCS	Radar cross section
RF	Radio-frequency
RMSE	Root mean square error
ROC	Receiver operating characteristics
RX	Receive
S/P	Serial-to-parallel
SINR	Signal-to-interference-plus-noise ratio
SISO	Single-input single-output
SLL	Side-lobe level
SLM	Selective mapping
SNR	Signal-to-noise ratio
SOI	Signal-of-interest
SVD	Singular value decomposition
TRX	Transceiver
TX	Transmit
VST	Vector signal transceiver

Symbols

α Loading of the communications subcarriers in the waveform

β Power ratio between the communications and sensing streams

$\theta_{c,m}$ Vector of dominant line-of-sight directions of the communications users for the mth OFDM symbol

$\theta_{r,m}$ Vector of radar directions for the mth OFDM symbol

ΔPSD Power spectral density difference

Δf Subcarrier spacing

λ Wavelength

$\log \mathscr{P}_{\mathbf{y}}(\mathbf{y}; \theta)$ Log-likelihood function

$\mathscr{I}(\theta)_{i,j}$ $(i,j)^{\text{th}}$ element of the Fisher matrix

$\mathscr{M}$ Set of OFDM symbol indices

$\mathscr{N}$ Set of subcarrier indices

$\mathscr{X}(\Delta\tau, \Delta f_{\text{D}}, \theta_1, \theta_2)$ Four-dimensional MIMO ambiguity function in delay, Doppler-shift, and angle domains

ρ Gain between communications and sensing in the transmit RF beampattern

σ^2 	 Noise variance

τ_k 	 Two-way delay to the kth target

$\mathbf{a}(\theta)$ 	 Steering vector at an angle θ

$\mathbf{H}_{\text{c},n,m}$ 	 Communications channel for the nth subcarrier and m^{th} OFDM symbol

$\mathbf{H}_{\text{r},n,m}$ 	 Radar channel for the nth subcarrier and m^{th} OFDM symbol

$\mathbf{h}_{n,m,s}$ 	 Vector of effective radar channel for the nth subcarrier and m^{th} OFDM symbol of the sth TX stream

$\mathbf{H}_{n,m}$ 	 Effective radar channel for the nth subcarrier and m^{th} OFDM symbol

$\mathbf{I}$ 	 Identity matrix

$\mathbf{W}_{\text{R,c},n,m}$ 	 Total receive beamforming matrix of all users for the nth subcarrier and m^{th} OFDM symbol

$\mathbf{W}_{\text{R,r},m}^{\text{RF}}$ 	 Receive RF beamforming matrix of radar for the mth OFDM symbol

$\mathbf{W}_{\text{T,c},n,m}$ 	 Total transmit beamforming matrix of all users for the nth subcarrier and m^{th} OFDM symbol

$\mathbf{W}_{\text{T,r},n,m}$ 	 Total transmit beamforming matrix of radar for the nth subcarrier and m^{th} OFDM symbol

$\mathbf{W}_{\text{T,c},n,m}^{\text{BB}}$ 	 Transmit baseband beamforming matrix of communications for the nth subcarrier and m^{th} OFDM symbol

$\mathbf{W}_{\text{T,r},n,m}^{\text{BB}}$ 	 Transmit baseband beamforming matrix of radar for the nth subcarrier and m^{th} OFDM symbol

$\mathbf{W}_{\text{T},m}^{\text{RF}}$ 	 Transmit RF beamforming matrix for the mth OFDM symbol

$\mathbf{W}_{\text{T},n,m}^{\text{BB}}$ 	 Total transmit baseband beamforming matrix for the nth subcarrier and m^{th} OFDM symbol

$\mathbf{x}_{\text{c},n,m}$ 	 Vector of communications frequency-domain symbols for the nth subcarrier and m^{th} OFDM symbol

$\mathbf{x}_{\mathrm{r},n,m}$ Vector of radar frequency-domain symbols for the nth subcarrier and m^{th} OFDM symbol

$\mathbf{x}_{n,m}$ Transmit symbols of the streams

$\mathbf{y}_{n,m}$ Receive baseband symbols

$\mathbf{Z}_{n,m}$ Null-space projection matrix for the nth subcarrier and m^{th} OFDM symbol

$\mathrm{CRLB}(\hat{\tau})$ The CRLB of delay estimate

$\mathrm{CRLB}(\hat{\theta})$ The CRLB of direction-of-arrival estimate

$\mathrm{CRLB}(\hat{f}_{\mathrm{D}})$ The CRLB of Doppler-shift estimate

MS_f Mean square bandwidth

MS_t Mean square time

$\mathrm{MS}_{f,t}$ Mean square bandwidth-time

θ_{r} Radar beam direction

$\theta_{\mathrm{t},k}$ Angle-of-departure of the kth target

$\tilde{\mathbf{x}}_{n,m}$ Transmit symbols at the antennas

$\tilde{\mathbf{y}}_{n,m}$ Receive symbols at the antennas

b_k Attenuation constant of the kth scatterer

f_{c} Carrier frequency

$f_{\mathrm{D},k}$ Doppler-shift of the kth target

K_{t} Total number of point scatterers

L_{T} Number of transmit antennas

$L_{\mathrm{T}}^{\mathrm{RF}}$ Number of transmit RF chains

$L_{\mathrm{R},\mathrm{r}}$ Number of antennas in the MIMO receiver

$L_{\mathrm{R},\mathrm{r}}^{\mathrm{RF}}$ Number of RF chains in the MIMO receiver

$L_{\mathrm{R,c,}u}$	Number of receive antennas in the uth communications user
$L_{\mathrm{R,c,}u}^{\mathrm{RF}}$	Number of RF chains in the uth communications user
M	Total number of OFDM symbols
m	OFDM symbol index
N	Total number of subcarriers
n	Subcarrier index
N_{act}	Total number of activated radar subcarriers
N_{c}	Number of communications subcarriers
N_{r}	Number of radar subcarriers
$P(\theta)$	MUSIC pseudo-spectrum at angle θ
P_{Δ}	Residual power allocated to a radar subcarrier
P_{D}	Probability of detection
P_{FA}	Probability of false alarm
P_{MD}	Probability of missed detection
P_{c}	Communications power
P_{max}	Maximum power of a radar subcarrier
P_{r}	Radar power
P_{t}	Total transmit power
$P_{n,m}$	Power of the nth subcarrier in m^{th} OFDM symbol
S	Total number of transmit streams
s	Stream index
S_{c}	Total number of communications streams
S_{r}	Total number of radar streams

$S_{\mathrm{c},u}$ Number of streams of the uth communications user

T_{CP} Time duration of the cyclic prefix

T_{sym} Time duration of an OFDM symbol

T_{u} Useful time duration of an OFDM symbol

U_{c} Number of communications users' directions

U_{r} Number of radar directions

$v_{n,m}$ Noise sample of the nth subcarrier in m^{th} OFDM symbol

$x(t)$ Transmit time-domain signal

$y_{\mathrm{c}}(t)$ Receive time-domain signal at the communications user

$y_{\mathrm{r}}(t)$ Receive time-domain signal at the radar receiver

1

Introduction

1.1 Background and Motivation

Radar/sensing systems in the past operated at fixed frequency ranges [87], geographically independent from those of communications systems. Due to technological development, communications systems grew exponentially in numbers, e.g., fourth-generation (4G) and fifth-generation (5G), resulting in sensing and communications systems operating simultaneously in the same vicinity, with high probability. Since both systems function around the same operating frequencies, each interferes with the other, degrading the performance of both systems [33, 42, 51].

Numerous methods have since then been developed to minimize the interference between the two systems, which can be broadly classified under three areas: co-existence, co-operation, and co-design [79]. In co-existence methods, each system estimates the other's interference and cancels that from the received signal to gain some performance improvement. In co-operation methods, each system intentionally shares some information with the other system allowing for more improved estimation of the interfering signal. For instance, a passive radar receiver can use signals transmitted by a non-radio system, e.g., a television broadcast system, to sense the environment. In such a scenario, if the radar receiver is unaware of the transmission parameters, it might need to use co-existence methods. In contrast, it would most likely use co-operation methods if it is aware of them.

The most novel methods are encompassed in the co-design category, where both systems are designed from the ground up to enable much-improved performance,

and they are called joint communications and sensing (JCAS) systems. They typically use the same frequency spectrum for both functionalities and the same hardware setup, thus being both radio-frequency (RF)-convergent and hardware-convergent. In doing so, the communications system can use information gathered by the sensing system about the environment to better cater to the communications users. For instance, it can differentiate between moving users from static clutter and only transmit information at the required user directions, improving their service quality.

On the other hand, the development of communications systems, e.g., beyond 5G, saw them functioning around mm-wave frequencies due to the availability of unused spectrum [85]. Since antenna size is typically inversely proportional to the frequency at which a system operates, multiple antennas could be included in a small physical area, resulting in large multiple-input multiple-output (MIMO) antenna arrays. For communications, increased beamforming gains are observed with MIMO arrays due to the ability to point the beams at specific directions, which, in turn, help compensate for high attenuation evident in the mm-wave frequencies [26]. Hence, MIMO arrays provide increased user capacities coupled with spatial multiplexing [122]. Similarly, for sensing, MIMO arrays improve the detection performance [40] while increasing the resolution of direction-of-arrival (DoA) estimation [113]. Therefore, due to MIMO arrays' advantages for communications and sensing, MIMO JCAS systems have gained popularity among the research community [56, 70, 107].

1.2 Thesis Objectives and Scope

The thesis incorporates sensing on top of communications, i.e., a single-input single-output (SISO) or MIMO communications transceiver (TRX), e.g., 5G base station, also sensing the environment. Typically, such systems use the same transmit (TX) waveform for communications and sensing. Since orthogonal frequency-division multiplexing (OFDM) is the standard waveform adopted in modern communications systems, it is used for both functionalities in the thesis. Hence, to facilitate effective JCAS, OFDM waveform optimization is pursued for SISO and MIMO systems. The thesis objectives are then as follows.

- *What kinds of performance improvements are possible in optimizing the joint OFDM waveform of SISO JCAS systems?* In JCAS systems, the performance of communications or sensing depends upon the resources allocated to them, e.g., bandwidth, TX power, or TX time duration. Since they are usually limited, allocating more resources for communications would reduce those for sensing, and vice versa. Thus, it is important to design the joint waveform to provide an optimal trade-off between the two functionalities. Toward this objective, the thesis performs JCAS for SISO systems by optimally sharing the spectral resources between communications and sensing. The improvements in sensing and communications are evaluated through typical performance metrics to depict the feasibility of the proposed OFDM waveform optimization, which are also complemented through practical RF measurements.

- *What kind of radar processing is required in MIMO JCAS systems with combinations of analog and digital architectures, i.e., hybrid, having multiple OFDM TX streams?* Radar processing in SISO JCAS systems using OFDM waveforms is straightforward, which uses the TX and receive (RX) frequency-domain symbols to obtain the range and velocity of targets in the environment [11]. However, in using a MIMO communications TRX with hybrid architecture, conventional radar processing adopted in fully-digital MIMO radars cannot be applied. Radar processing is further complicated due to the availability of multiple TX streams. Hence, the thesis proposes novel radar processing to obtain range–angle and range–velocity maps of the environment in such systems.

- *What kinds of benefits are obtained by incorporating separate TX sensing streams on top of communications streams in MIMO systems?* Typically, multiple TX OFDM streams are used in MIMO communications, which are transmitted to user directions. Sensing can also be performed based on the reflections from these streams; however, they limit the sensing directions to be the same as user directions. Instead, separate TX streams can be used in different directions for sensing purposes. In doing so, reflections from both communications and sensing streams can be used for radar purposes, which give more information about the sensed environment. Another advantage of separate sensing streams is that they can be optimized to improve sensing performance without altering the communications streams. Therefore, the thesis evaluates the feasibility of such a system due to the inclusion of separate sensing streams.

1.3 Contributions and Structure of the Thesis

The main contributions of the thesis are as follows.

- Designing OFDM waveforms for SISO JCAS systems that optimally share the spectral resources, allowing both communications and sensing functionalities to complement each other rather than degrading each other's performance. Therefore, the scarce RF spectrum can be more intelligently utilized, reducing costs for network service providers, apart from the performance benefits. For joint waveform design, an optimization problem to find the power allocation between communications and sensing is formulated by minimizing the lower bounds of range and velocity estimates' error variances of sensing, i.e., Cramer–Rao lower bounds (CRLBs). The solution to this optimization problem is analytically derived. The performance improvements for the two functionalities are evaluated for standard-compliant OFDM waveforms, as well as experimentally verifying the effectiveness of waveform optimization through practical RF measurements to signify the importance of optimally sharing the spectral resources between communications and sensing.

- Deriving novel radar processing techniques to gain information about the environment surrounding a MIMO communications TRX. Since modern and future communications systems operate in highly complex environments and mobility, knowing the communications channel helps achieve the quality-of-service requirements in such systems. To achieve this objective, range–angle and range–velocity maps of the surrounding environment are derived for MIMO transceivers with hybrid architecture.

- Designing OFDM waveforms for MIMO JCAS systems with multiple TX streams. There can be instances where the information transmitted for the communications users, i.e., communications-only streams, cannot be modified. In those scenarios, the sensing performance of the MIMO JCAS system would be at its worst. However, by introducing suitable separate TX streams at different sensing directions, environment sensing can also be performed effectively. Apart from that advantage, techniques are derived to improve the sensing performance further. Those techniques, in turn, help the communications system to gain knowledge about the surrounding environment of a

MIMO TRX in a more sophisticated manner, e.g., accurate directions of users without ambiguity. In the thesis, the separate sensing streams are optimized to minimize the CRLBs of range and angle estimates of sensing for MIMO JCAS systems with hybrid architecture. The optimization problem is analytically solved after deriving the related CRLB expressions. In addition, the effectiveness of including separate sensing streams on top of a conventional communications stream in enhancing the MIMO ambiguity function (AF) is also analyzed, which dictates the performance of sensing in range, velocity, and angle domains.

Chapter 2 introduces the basic concepts of JCAS that are foundational for the following technical chapters. It discusses why OFDM is used as the candidate waveform in modern JCAS systems and its advantages and disadvantages. An overview is also given on SISO JCAS systems. In addition, it summarizes MIMO communications and radar fundamentals, which are required for understanding the later technical chapters, followed up with an overview of MIMO JCAS systems. Chapters 3–5 describe the thesis's main technical contributions.

Figure 1.1 depicts the structure of the technical chapters of the thesis, along with the relations between the different publications and chapters. Chapter 3 is based on the publications [**P4**], [**P5**], and [**P6**]. It mainly discusses the system model used throughout the thesis for a MIMO communications TRX with hybrid architecture that also senses the environment. Two different MIMO JCAS systems are discussed in this chapter, along with their differences. Specifically, publications [**P5**] and [**P6**] use only TX streams of communications users in line-of-sight (LoS) w.r.t. the MIMO TRX for sensing purposes. In contrast, [**P4**] involves using separate TX streams for sensing purposes while considering the communications users are in non-LoS (NLoS) conditions. The TX precoding and RX combining are paramount to MIMO systems that minimize the interference arising in these systems. Hence, this chapter also focuses on designing MIMO TRX's and the communications users' beamformers for improved communications and sensing performance for the two MIMO JCAS systems. Finally, Chapter 3 concludes with MIMO TX and RX beampatterns due to the proposed beamforming designs.

Chapter 3 (System Models)

Chapter 4 **Chapter 5**

P1 Optimized Waveforms for 5G–6G Communication With Sensing: Theory, Simulations and Experiments
IEEE Transactions on Wireless Communications, Dec. 2021

P2 Joint OFDM Waveform Design for Communications and Sensing Convergence
IEEE International Conference on Communications, Jun. 2020

P3 Experimenting Joint Vehicular Communications and Sensing with Optimized 5G NR Waveform
IEEE Vehicular Technology Conference, Apr. 2021

P4 Joint MIMO Communications and Sensing with Hybrid Beamforming Architecture and OFDM Waveform Optimization
IEEE Transactions on Wireless Communications, under review after minor revision

P5 Joint Multi-User Communication and MIMO Radar Through Full-Duplex Hybrid Beamforming
IEEE International Symposium on Joint Communications & Sensing, Feb. 2021

P6 Range–Angle Processing for Target Detection in Joint MIMO-OFDM Communications and Sensing
IEEE Workshop on Signal Processing Advances in Wireless Communications, Oct. 2021

P7 MIMO Ambiguity Function Enhancement for Integrated OFDM Communications and Sensing
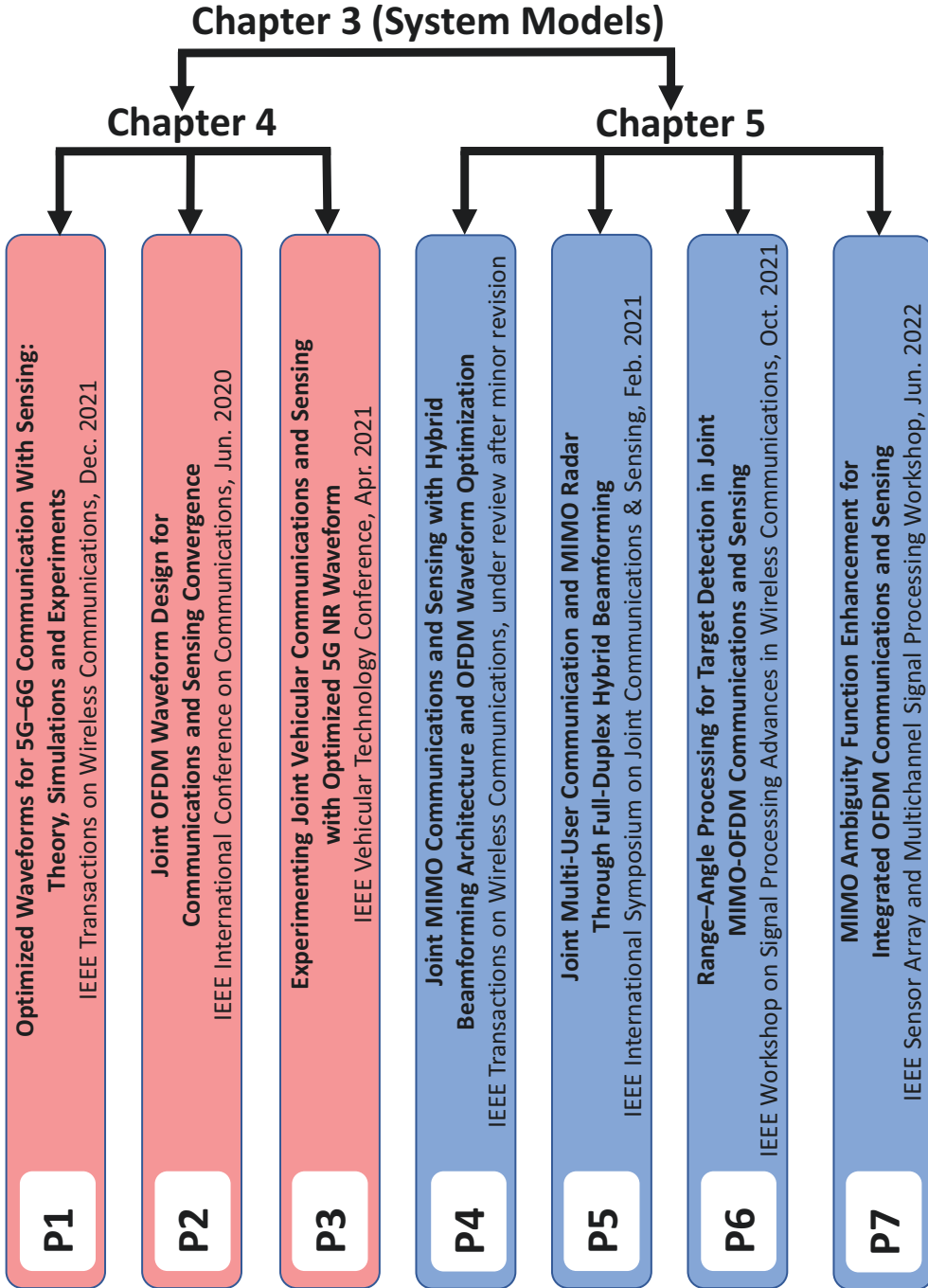IEEE Sensor Array and Multichannel Signal Processing Workshop, Jun. 2022

Figure 1.1 The thesis structure with the relation between the publications and the chapters.

Chapter 4 summarizes the works done in [**P1**], [**P2**], and [**P3**], for SISO JCAS systems. The system model adopted in this chapter is a special case of the MIMO JCAS system model introduced in Chapter 3. It introduces the basic ideas of OFDM radar processing for SISO JCAS systems. The unused subcarriers within the OFDM frames are filled with optimized samples to minimize the CRLBs of delay and velocity estimates. So, the necessary CRLB expressions are derived, followed by the optimization problem and its solution. This chapter contains simulation and experimental results that illustrate the performance improvement due to the waveform optimization, which are based on [**P1**] and [**P3**].

Chapter 5 is the final technical chapter that is based on the publications [**P4**], [**P5**], [**P6**], and [**P7**]. This chapter is based on MIMO JCAS systems using separate TX streams for communications and sensing functionalities. It discusses the radar processing to obtain the range–velocity and range–angle maps for such systems using both sets of TX streams. The thesis consists of two strategies to improve the sensing performance by leveraging the TX sensing streams. One strategy involves optimizing the sensing streams to minimize the CRLBs of delay and DoA estimates jointly, and this chapter discusses this first. The second strategy is elaborated next, which involves enhancing the MIMO AF of sensing. Finally, this chapter concludes with simulation results to illustrate the performance improvement due to the proposed waveform optimization, radar processing, and MIMO AF enhancement.

Chapter 6 presents the conclusions of the thesis. It also includes the thesis summary, with discussions on the main results. This chapter concludes with future work that can be performed by extending the contributions of the thesis. Finally, Appendix A illustrates the methodology through which the CRLBs can be derived for the considered system model of the thesis.

1.4   Author's Contributions

The thesis comprises two journal articles ([**P1**] and [**P4**]) and five conference articles ([**P2**], [**P3**], [**P5**], [**P6**], and [**P7**]). Associate Professor Taneli Riihonen, the supervisor of the author of the thesis (later: the Author), contributed to all of the publications starting from the brainstorming of ideas, discussions on technical contents, and providing feedback on the writing. In addition, Professor Mikko Valkama, co-supervisor of the Author, has contributed to all publications except [**P7**], by sharing

some ideas on the technical contents and writing aspects. Moreover, some publications were done in collaboration with other researchers, whose contributions are discussed as follows.

The measurement setup for observing the performance improvement due to waveform optimization in [**P1**] and [**P3**] was implemented by M.Sc. Matias Turunen. The measurements were performed in collaboration with D.Sc. Carlos Baquero Barneto. In addition, the radar simulator in [**P3**] was collaborated with him. The publication [**P5**] was written in co-operation with D.Sc. Baquero Barneto, where he designed the TX and RX beamforming and focused on self-interference cancellation whereas the Author implemented MIMO radar processing. The beamforming designs were also used in [**P6**]. Moreover, beamforming designs for [**P5**] and [**P6**] were based on antenna array simulations for realistic patch antennas provided by D.Sc. Mikko Heino.

Further, the Author collaborated in the publications [**12**], [**13**], [**14**], [**15**], and [**16**] with D.Sc. Carlos Baquero Barneto, who is the main author of these publications. These works have contributed to the Author's research on JCAS; however, they are not the main publications in the thesis.

1.5 Notations

This section gives an overview of the different notations used throughout the thesis. The superscripts $(\cdot)^{\mathrm{RF}}$ and $(\cdot)^{\mathrm{BB}}$ denote the RF and baseband (BB) parts of either a TX or RX, the subscripts $(\cdot)_{\mathrm{T}}$ and $(\cdot)_{\mathrm{R}}$ denote the TX and RX, and $(\cdot)_{\mathrm{c}}$ and $(\cdot)_{\mathrm{r}}$ denote the components corresponding to communications and radar/sensing. The matrices are denoted by boldface uppercase letters, e.g., $\mathbf{W}_{\mathrm{R,r},m}^{\mathrm{RF}}$, vectors by boldface lowercase letters, e.g., $\mathbf{x}_{n,m}$, and scalars are represented by regular letters, e.g., S_{c}.

In addition, $|\cdot|$ and $\|\cdot\|$ are the absolute and l_2-norm operations, $(\cdot)^*$, $(\cdot)^T$ and $(\cdot)^H$ are the conjugate, transpose and Hermitian operations, and $\mathbb{E}\{\cdot\}$, $(\cdot)^\dagger$, $\det\{\cdot\}$ and $\Re\{\cdot\}$ are the expectation, pseudo-inverse, determinant of a matrix and real operations, respectively.

2

Background and State-of-the-Art

Mobile phones have become a ubiquitous commodity owned by almost every person, young and old. From the essential requirement of contacting another person, they have evolved to provide many functions, such as social networking, listening to music, playing games, and navigation purposes. To facilitate all these different functions effectively, wireless mobile communications systems have also grown exponentially over the last few years. Mainly, the growth was due to the advances in electronics and signal processing techniques, and also due to standardization by the respective governing bodies, e.g., third generation partnership project (3GPP), thereby increasing the need for spectrum for such systems. Since each wireless communications system needs some frequency bandwidth for operation, the frequency resources must be utilized optimally to prevent interference due to frequency overlap with some other system. The major problem with this requirement is the existence of other radio systems which have fixed frequencies for operation, with radar/sensing systems causing much trouble. Although radar systems have some defined frequency ranges for certain types of operations, e.g., L-band (1—2 GHz) - long-range air-surveillance radar and X-band (8—12 GHz) - military airborne radar, lack of standardization between different radar systems is another reason for this issue of frequency overlap. Due to the existence of such systems, the availability of interference-free spectrum for communications systems decreased, causing spectrum scarcity [124].

It was soon evident that the communications and sensing systems needed to be combined to address this challenge, giving rise to joint communications and sensing (JCAS) systems [67, 79, 108, 120, 121]. In such systems, the available radio-frequency (RF) spectrum is intelligently shared between the two functionalities with a uni-

fied/joint waveform [23, 30, 100]. In addition, the same hardware resources are used in JCAS systems, giving also cost benefits. Nowadays, JCAS systems are evident in many fields, e.g., automotive industry [38, 50, 57], sensing through the cellular-network [11], health monitoring [4], and high-precision motion tracking [43].

The JCAS systems can be designed based on two perspectives, i.e., radar-centric [46, 47] or communications-centric [72, 76]. The former means that the communications function is embedded on top of a radar system, while the latter considers incorporating sensing on top of a communications system. This thesis approaches the JCAS system design with the second approach. As such, the communications transmitter (TX) and receiver (RX) are also used for sensing purposes with the same TX communications waveform. Since orthogonal frequency-division multiplexing (OFDM) is used in modern mobile cellular networks, e.g., fourth-generation (4G) and fifth-generation (5G) [1], it is also used for sensing purposes in the thesis.

When the communications waveform is used for sensing purposes, the resources, e.g., time and frequency, should be shared between the two functionalities. The resource allocation is performed to have an optimal trade-off between the performance metrics for both sensing and communications. For sensing, some of them are: the probability of detection and false alarm, RX signal-to-noise-plus-interference ratio (SINR) of the reflected signal [87], side-lobe level (SLL) and integrated side-lobe level (ISL) of different profiles [44], mutual information (MI) of the RX reflected signal [21], different properties of the ambiguity function (AF) [66, 91], and the Cramer–Rao lower bounds (CRLBs) of the estimates [55, 60]. For communications, some of them are the MI [117], signal-to-noise ratio (SNR) of the RX signal, and peak-to-average power ratio (PAPR) [96]. The most usual metric is the capacity of the communications user [30, 52, 77]. More details on these metrics are also discussed in this chapter.

Until recently, most wireless communications systems operated around the sub-6 gigahertz frequencies. Due to the availability of untapped spectrum in mm-wave frequencies, most wireless communications systems soon began to operate also around these high carrier frequencies [49, 84, 110]. Apart from the increased bandwidth opportunities by order of a few hundred megahertz, an important characteristic of antenna arrays used in these frequencies is that many antennas could be packed in quite a small area, resulting in massive multiple-input multiple-output (MIMO) arrays [9]. A direct result of such arrays is that their spatial beampattern can be made

more focused at specific directions due to beamforming (or *precoding*, when there are multiple TX streams) [9, 101]. Such narrow beams help communications systems to send information to specific users' directions, directly improving their quality-of-service (QoS) [101, 122]. On the other hand, a slight variation in the angle can be detected, improving the performance of sensing systems operating at mm-wave frequencies [25, 40, 65]. In addition, range estimation of the targets is also improved due to increased bandwidth [11]. Hence, MIMO arrays are advantageous for both communications and sensing, thereby leading to the development of MIMO JCAS systems.

Considering all the aspects above, this chapter gives an overview of both single-input single-output (SISO) and MIMO JCAS systems. The different options available in the design of joint waveforms for SISO systems are discussed first. Secondly, the advantages and disadvantages of OFDM for communications and sensing are investigated. Next, state-of-the-art SISO JCAS systems are discussed. Then, an overview is given regarding MIMO systems, followed by MIMO communications and MIMO radar functionalities. Finally, this chapter concludes with a discussion on MIMO JCAS systems.

2.1 Waveform Design for SISO JCAS Systems

The joint waveform for a SISO JCAS system is designed based on an explicit optimization problem. The cost function of that problem can be some performance metric for communications, while the sensing performance metric is used as a constraint, or vice versa [23]. In addition, several other constraints can also be used that control how the resources, e.g., time and frequency, are allocated between the two functionalities. Depending on a particular application, the JCAS system designer can choose various performance metrics for the optimization problem, and these are discussed next.

2.1.1 Sensing Performance Metrics

Depending on the two main tasks a sensing system performs, i.e., detection and estimation, various performance metrics are used for waveform optimization. A brief description of each one of these is discussed next.

Probability of detection and false alarm   The task of a sensing system is to *detect* the targets in the vicinity, which alternatively means to know if there is a possible target in some area. A time-domain signal $x(t)$ is transmitted to the surrounding environment for this. Considering a single point target with no velocity, for simplicity, the TX signal is reflected from it and received as $y(t)$, which can be given as

$$y(t) = hx(t-\tau) + n(t). \tag{2.1}$$

Here, h is the complex channel coefficient, τ is the two-way delay to the target, and $n(t)$ is the noise signal at the RX. Sampling the RX signal at a frequency of F_s results

$$y[k] = hx[k-l] + n[k], \tag{2.2}$$

where k is the sample index corresponding to the kth sampling instant $t_k = \frac{k}{F_s}$ and l is the sample index corresponding to the delay as $\tau = \frac{l}{F_s}$. Here, it is assumed that the delay is an integer multiple of the sampling time $t = \frac{1}{F_s}$. The RX samples in (2.2) are next correlated with the TX samples as

$$R[a] = \sum_{k=-K}^{K} x[k]y^*[k-a] = h^* \sum_{k=-K}^{K} x[k]x^*[k-(a+l)] + h^* \sum_{k=-K}^{K} x[k]n^*[k-a],$$
$$\tag{2.3}$$

where $2K+1$ is the length of the time-domain sequence and a is the cross-correlation lag. The power of the cross-correlation for different lags, i.e., $|R[a]|^2$, are then plotted as in Fig. 2.1. For any RX sample, only two outcomes are possible, i.e., either a target is present or not. Therefore, the detection problem can be represented as [55]

$$H_0 : \text{A target is absent,}$$
$$H_1 : \text{A target is present,}$$
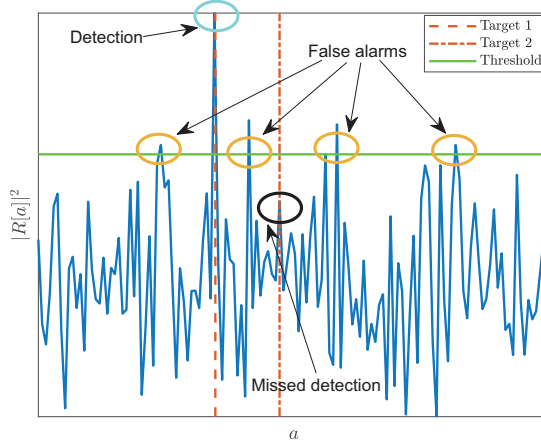
Figure 2.1 The output of the cross-correlation between TX and RX signals.

where H_0 and H_1 are the null and alternate hypotheses.

Next, a target *detection* is made for $|R[a]|^2 > \Gamma$, while it is not detected for $|R[a]|^2 \leq \Gamma$, where Γ represents the threshold. Due to noise and other imperfections evident in the TX and RX systems, it is sometimes possible for an actual target to be undetected, termed as a *missed detection*. In addition, it is also possible for a false target to be detected if it exceeds the threshold, which is termed a *false alarm*. These different incidents are also depicted in Fig. 2.1.

In detecting for multiple instances, the probability density functions (PDFs) for the null and alternate hypotheses can be plotted as in Fig. 2.2. Based on these, the probability of false alarm and missed detection can be given separately as

$$P_{\text{FA}} = \int_{\Gamma}^{\Gamma_{\text{max}}} p_{H_0}(|R[a]|^2) \, d|R[a]|^2, \tag{2.4}$$

$$P_{\text{MD}} = \int_{\Gamma_{\text{min}}}^{\Gamma} p_{H_1}(|R[a]|^2) \, d|R[a]|^2, \tag{2.5}$$

where $p_{H_0}(|R[a]|^2)$ and $p_{H_1}(|R[a]|^2)$ are the PDFs of null and alternate hypotheses, and Γ_{min} and Γ_{max} are the limits of integration. In addition, the probability of detection is given as $P_{\text{D}} = 1 - P_{\text{MD}}$. The choice of Γ is thus important for sensing since it defines these probabilities. From Fig. 2.2, increasing Γ would help in reducing P_{FA}, but at the cost of increased P_{MD}. Decreasing Γ would also have a similar effect. In radar literature, receiver operating characteristic (ROC) is an important concept.
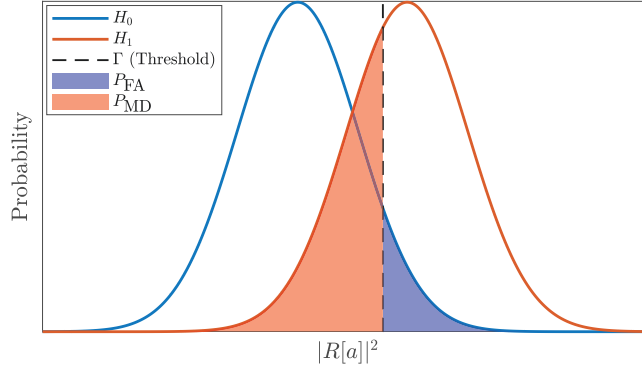
Figure 2.2 The PDFs of the null and alternate hypotheses and the areas corresponding to the missed detection and false alarm probabilities. The area corresponding to the probability of detection is the complement of the area corresponding to the probability of missed detection.

This is defined as the probability of detection as a function of the probability of false alarm, for all considered threshold values Γ. Hence, a specific operating point in ROC illustrates the trade-off between detection and false targets.

Signal-to-noise ratio Targets of the environment can be better detected if the RX power of the reflected signal is high. The average RX power can be estimated through the *radar range equation* [87]. Then, since the TX power of the signal is also known, the RX SNR is generally used instead of the RX power of the signal, defined as

$$\text{SNR} = \frac{\sigma\,G_\text{T}G_\text{R}\lambda^2}{P_\text{N}(4\pi)^3 R^4},\tag{2.6}$$

where σ, G_T, G_R, and λ are the radar cross-section, gains of the TX and RX antennas, and the wavelength, while P_N and R are the noise power and the range to the target, respectively.

Side-lobe and integrated side-lobe levels As shown in Fig. 2.3, SLL is defined as the ratio between the energy of the second highest peak to that of the main-lobe. Here, it is shown for the angular beampattern, but it can be defined for any other
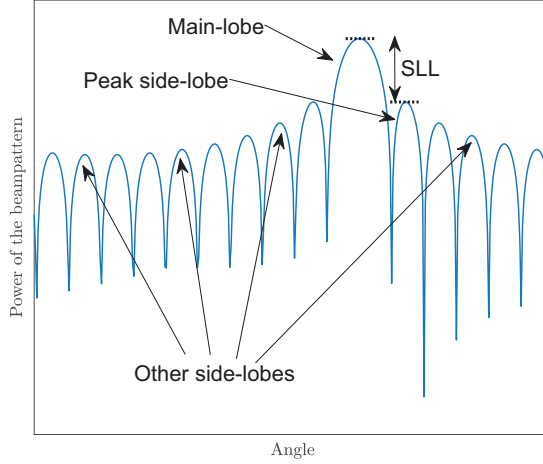
Figure 2.3 Illustration of a beampattern's main-lobe, side-lobes, and SLL.

estimate, e.g., range or velocity. It is given as

$$\text{SLL} = \frac{\int_{\theta_{\text{SLL},1}}^{\theta_{\text{SLL},2}} \mathbf{h}(\theta) d\theta}{\int_{\theta_{\text{main},1}}^{\theta_{\text{main},2}} \mathbf{h}(\theta) d\theta}, \tag{2.7}$$

where $\theta_{\text{SLL},1} + \theta_{\text{SLL},2}$ and $\theta_{\text{main},1} + \theta_{\text{main},2}$ are the widths of the second highest peak and main-lobe of the beampattern, and $\mathbf{h}(\theta)$ is a non-negative vector corresponding to the gains in the angular domain.

Similar to the SLL definition, another metric used is the ISL. Here, ISL is quantified as the energy of all the side-lobes to that of the main-lobe. It is given similar to (2.7) as

$$\text{ISL} = \frac{\int_{-\theta_{\text{min}}}^{\theta_{\text{main},1}} \mathbf{h}(\theta) d\theta + \int_{\theta_{\text{main},2}}^{\theta_{\text{max}}} \mathbf{h}(\theta) d\theta}{\int_{\theta_{\text{main},1}}^{\theta_{\text{main},2}} \mathbf{h}(\theta) d\theta}, \tag{2.8}$$

where $-\theta_{\text{min}}$ and θ_{max} are minimum and maximum values for the parameter.

Mutual information   Although MI is generally used for communications, it is also used in sensing [18]. It is shown in [115] that maximizing the MI for sensing minimizes its minimum mean square error (MMSE). Generally, a TX signal $x(t)$ is transmitted towards a target, and based on the RX signal $y(t)$, the target response $h(t)$

15

needs to be estimated. Here, $I(h(t); y(t)|x(t))$ is defined as the MI between $h(t)$ and $y(t)$ when $x(t)$ is known, and it denotes the extent to which radar processing can be used to gain information about $h(t)$ [52, 90]. Hence, this metric is usually sought to be maximized.

Ambiguity function   The AF is another crucial metric for sensing purposes. The two-dimensional AF is defined as [102]

$$\mathscr{X}(\Delta\tau, \Delta f_{\mathrm{D}}) = \int x(t)x^*(t - \Delta\tau)e^{j2\pi\Delta f_{\mathrm{D}}t}\,dt, \tag{2.9}$$

where $\Delta\tau$ and Δf_{D} are the time delay and Doppler-shift differences between two point targets. The AF is important because it defines the resolutions of the sensing parameters [2]. The resolution means the minimum separation between two targets so they can be detected as separate targets, for example, in range or velocity. When the resolutions are very high, very closely situated targets can be detected, whereas if they are low, both targets are observed as a single target. Therefore, in radar literature, the ideal shape of the AF is a thumbtack shape, having only a peak at the origin, whereas everywhere else, it is near zero, i.e., low side-lobes [5].

Cramer–Rao lower bounds   Once the targets are detected, further radar processing can be applied to estimate their parameters, e.g., range and velocity. The estimation process becomes more accurate as the error variance between the actual and the estimated target parameters is minimized. The error variance can be given as

$$\mathrm{var}(\theta) = \mathbb{E}\{(\theta - \hat{\theta})^2\}, \tag{2.10}$$

where θ and $\hat{\theta}$ are the actual and estimated target parameter values, $\mathrm{var}(\cdot)$ is the variance operation, and $\mathbb{E}\{\cdot\}$ is the expectation operation. In reality, it is difficult to analytically derive the error variance of a target parameter's estimation process. Therefore, this cannot be applied straightforwardly in an optimization problem. However, the lower bound of the error variance of unbiased estimation of a target parameter can be explicitly formulated, and it is defined as the CRLB, given as

$$\mathrm{var}(\theta) \geq \mathrm{CRLB}(\theta). \tag{2.11}$$

Therefore, when the CRLB metric is used in the joint waveform design, it is generally minimized, ensuring the lower bound of the error variance is minimized.

2.1.2 Communications Performance Metrics

Unlike sensing, a handful of parameters are used for communications, such as MI, SNR, and PAPR. A communications system's main objective is to maximize the capacity of the communications user, i.e., how much information can be transmitted per unit time interval reliably. For this reason, the communications performance in JCAS waveform design is mainly evaluated through the capacity instead of the other separate parameters.

For communications, a TX signal $x(t)$ is transmitted and received as $y(t)$, under a communications channel $h(t)$. Generally, $h(t)$ is assumed to be known/estimated using pilot symbols. In that case, the MI is defined as $I(x(t);y(t)|h(t))$, and the channel capacity is defined as the maximum value of this metric and given as [34]

$$\text{Channel capacity} = \max_{p_X(x(t))} \big(I(x(t);y(t)|h(t))\big), \tag{2.12}$$

where $p_X(x(t))$ is the probability distribution of $x(t)$.

2.1.3 Other Constraints

Apart from the communications-specific and sensing-specific performance metrics, other constraints in the optimization problem are generally used to share the resources between the communications and sensing functionalities. The resources are mainly allocated between the time [111], frequency, i.e., bandwidth [22], space [46, 72], and code domains [53], as illustrated in Fig. 2.4. In doing so, the total TX power is indirectly shared between the two. Thus, the performance trade-off between either functionality depends upon this power allocation.

2.2 OFDM as a Joint Waveform

Although many waveforms can be used for JCAS, i.e., linear frequency-modulated (LFM), frequency-modulated continuous wave (FMCW) [108], single-carrier wave-
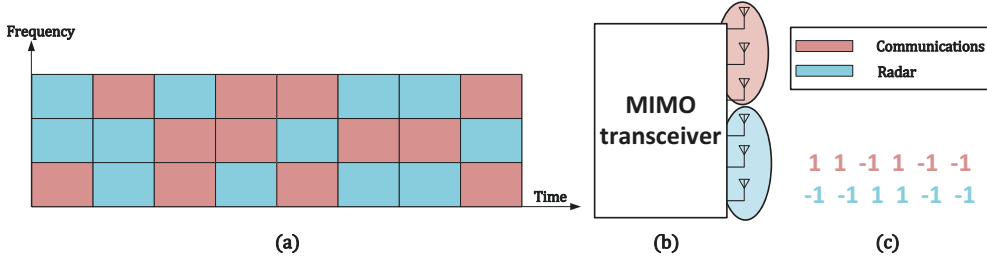
Figure 2.4 Resource allocation in (a) time and frequency, (b) space, and (c) code domains.

form [118], and single-carrier frequency-domain equalization [39], OFDM is the waveform of choice in most JCAS systems since it is used in modern communications systems such as in 4G and 5G. The main reason is that it gives good communications capacity compared to the other waveforms. Hence, this section first discusses how OFDM is used for communications transmission and reception. Then, the advantages and disadvantages of OFDM as a JCAS waveform are discussed.

2.2.1 OFDM Communications

The OFDM waveform is defined in both time and frequency domains. It can be considered as a two-dimensional matrix: the rows contain the frequency resources, called subcarriers, while the columns contain the time resources, the OFDM symbols, similar to as depicted in Fig. 4.2 in Chapter 4. For communications, the transmission and reception of OFDM waveforms are illustrated in Fig. 2.5.

First, the TX bits are modulated according to the required constellation map, e.g., quadrature amplitude modulation (QAM) or phase-shift keying (PSK), to generate the TX frequency-domain symbols $x_{n,m}$. Here, n denotes the subcarrier index and m denotes the OFDM symbol index, with $n \in [\frac{-N}{2}, \frac{N}{2} - 1]$ and $m \in [\frac{-M}{2}, \frac{M}{2} - 1]$, where N and M are the total number of subcarriers and OFDM symbols in the waveform. In addition, the separation between each subcarrier in the frequency domain is represented by Δf.

The frequency-domain symbols are then fed into a serial-to-parallel (S/P) converter. An inverse fast Fourier transform (IFFT) is next applied to the parallel frequency-domain symbols to obtain the time-domain samples for transmission. The discrete time-domain samples are then obtained by parallel-to-serial (P/S) conversion
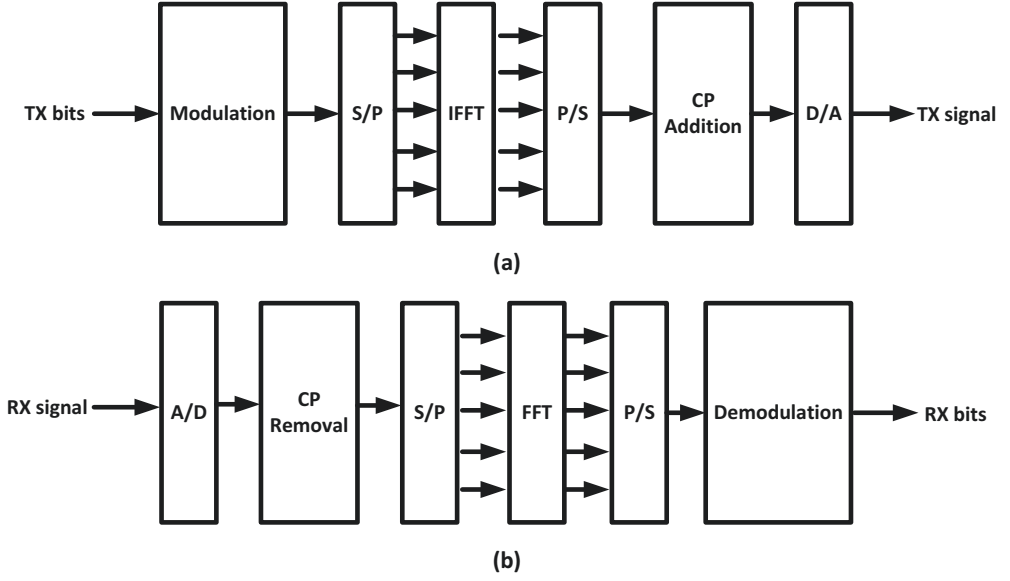
Figure 2.5 The different blocks in the (a) transmission and (b) reception of OFDM waveforms.

and can be represented as

$$x[k] = \sum_{m=\frac{-M}{2}}^{\frac{M}{2}-1} \sum_{n=\frac{-N}{2}}^{\frac{N}{2}-1} x_{n,m} e^{j2\pi n\Delta f(k-mL)} p[k-mL], \tag{2.13}$$

where k is the time-domain sample index, $p[k]$ is the time-domain sequence corresponding to the pulse-shaping function, and L is the number of samples within a particular OFDM symbol.

An important characteristic of OFDM transmission is cyclic prefix (CP) addition, which prevents inter-symbol interference (ISI). For this, a set of time-domain samples at the end of a particular OFDM symbol is copied and added to the start of that OFDM symbol, and it is called the CP. Finally, the CP-added discrete signal is converted to the analog domain by using a digital-to-analog (D/A) converter and transmitted as

$$x(t) = \sum_{m=\frac{-M}{2}}^{\frac{M}{2}-1} \sum_{n=\frac{-N}{2}}^{\frac{N}{2}-1} x_{n,m} e^{j2\pi n\Delta f(t-mT_{\text{sym}})} p\left(t - mT_{\text{sym}}\right), \tag{2.14}$$

where $T_{\text{sym}} = T_{\text{u}} + T_{\text{CP}}$. Here, T_{u} is the useful time duration of the signal and given

by $T_{\mathrm{u}} = \frac{1}{\Delta f}$ in OFDM processing. In addition, T_{CP} is the duration of the CP. Similar steps are performed on the RX side to obtain the RX frequency-domain symbols.

2.2.2 Advantages and Disadvantages of OFDM for JCAS

Due to OFDM resources being already defined in the time and frequency domains, it naturally supports MIMO transmission since they can be spatially multiplexed easily. Efficient channel equalization is another advantage of OFDM. This is because the data modulated in a single subcarrier is assumed to undergo frequency-flat fading, requiring only a multiplication by a single complex number for channel equalization.

Adding CP is necessary for communications, and the communications user discards the CP to obtain the RX frequency-domain symbols. However, for sensing, since the time-domain OFDM signal consists of the useful signal and the CP, conventional cross-correlation of the time-domain TX and RX signals would result in ambiguities. These arise because the CP contains repeated time-domain samples of some of the samples in the useful signal. However, for the delay corresponding to the CP, it would mean that the corresponding target is situated at a far-away distance. Hence, although the CP would cause ambiguities, the RX power from the target reflection would be low without affecting the radar processing drastically. In fact, [109] discusses a method to remove the ambiguities corresponding to the CP.

Instead of time-domain radar processing for OFDM waveforms, nowadays, frequency-domain processing is the preferred option [11]. The RX time-domain signal is used to obtain the corresponding frequency-domain symbols using a similar approach as in Fig. 2.5. These RX frequency-domain symbols are then correlated with the corresponding TX frequency-domain symbols to obtain the radar channel. Further processing is next applied to extract the different parameters of the targets in the environment, e.g., range and velocity.

The OFDM waveform generally has noise-like properties due to many subcarriers containing data symbols. Due to this reason, the OFDM waveform has an ideal thumbtack shape in the two-dimensional ambiguity function consisting of the delay and Doppler variables [63]. Therefore, the peak corresponding to a specific delay and Doppler has a narrow main-lobe width with minimized side-lobes, for a sufficient number of subcarriers and OFDM symbols. In fact, [79] depicts that the OFDM waveform with arbitrary data symbols has almost two times lower main-lobe width
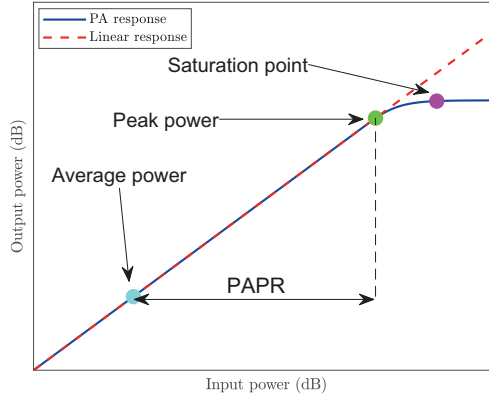
Figure 2.6 The response of the PA with important parameters.

than the LFM chirp, indicating the superiority of range estimation of the OFDM waveform. The OFDM waveform does not exhibit range-Doppler coupling compared to LFM or FMCW. Hence, range and Doppler processing could be processed independently from each other [108]. In contrast, due to range-Doppler coupling in LFM or FMCW waveforms, the existence of a Doppler mismatch translates into an error in the estimated range [88].

A major drawback of OFDM is having a high PAPR [83]. It is defined as

$$\text{PAPR} = 10\log_{10} \frac{\max\{|x[1]|^2, \cdots, |x[A]|^2\}}{\frac{1}{A}\sum_{a=1}^{A}|x[a]|^2}, \tag{2.15}$$

where $x[a]$ is the ath time-domain sample and A is the total number of time-domain samples. High PAPR values affect the power amplification process in the transmission. The conceptual amplitude response of a power amplifier (PA) is given in Fig. 2.6. Here, the highest efficiency values are closer to the saturation point, beyond which the PA response becomes non-linear. However, operating the PA in the non-linear region distorts the signal. Hence, the PA generally functions in the linear region, and there is an inherent trade-off between linearity and efficiency. For a high PAPR signal, the PA should operate with a large back-off value that determines how far from the saturation point the PA functions, reducing its efficiency. Therefore, the PAPR of the TX OFDM waveform should be reasonable to perform efficient transmissions. Although there are many methods to reduce the PAPR of an OFDM waveform [54], they are not in the scope of the thesis. However, one method used

in Chapter 4 of the thesis is selective mapping (SLM) [62], where the TX OFDM waveform is multiplied with sets of different random phases. For transmission, the waveform with the minimum PAPR out of all possible waveforms is selected.

2.2.3 Single-Input Single-Output JCAS Systems

In SISO JCAS systems, the main idea of waveform optimization is to design the joint waveform suitably for both functionalities. For instance, in [20], the OFDM waveform is designed to maximize the probability of detection of sensing while constraining the probability of false alarm. Hence, this essentially controls the ROC of sensing. For communications, the capacity is constrained to be above some threshold. In addition, the total TX power of the system is also controlled. In the end, this optimization allocates different powers to the individual subcarriers. To improve the detection of sensing, the SINR of the RX signal can also be maximized, as used in [7] and [8] by *Aubry et al*. There, the same frequency allocation is used for both communications and sensing. The radar waveform is found through maximizing radar SINR, subject to a few constraints. Apart from the usual TX power constraint, interference to communications from radar waveform is also constrained. Moreover, the radar waveform designed is made similar to a reference radar waveform known already to have good radar performance, e.g., low SLL.

Another method used in optimizing the waveform is to maximize the MI of sensing, as discussed in [19, 21, 22, 52, 123], which results in a trade-off between the communications capacity and MMSE of sensing. Interestingly, in [22], the OFDM subcarriers are divided between communications and radar sets, similar to the spectral resource allocation in Chapter 4 of the thesis. Here, the two sets of subcarriers are chosen based on the MI metric maximization. However, in practical communications systems, communications subcarriers are fixed, as decided by the scheduler of the base station. In that case, the subcarriers that can be optimized for radar purposes are what remain after communications subcarriers are decided, which is the main idea behind the work in Chapter 4.

Researchers have also sought to improve the AF of sensing for OFDM waveforms that provides better detection in both range and velocity domains. The work in [93] designs the AF for OFDM waveforms that have a thumbtack shape through the use of the AF synthesis method proposed by *Sussman* in [102]. Here, it is designed to

minimize the error between the generated and desired thumbtack-shaped AFs, and the solution results in the weights for the subcarriers of the OFDM waveform. A similar approach is used in [94]. However, the authors only focus on a sub-region around the origin of delay–Doppler domains in designing the AF that closely resembles the desired AF. The reason for such an approach is that the delay and Doppler-shift of targets far away from the origin are received with high attenuation. Thus, their side-lobes are low, and the optimization does not need to consider those delays and Doppler-shifts. The work in [44] focuses on improving the AF's delay domain, i.e., TX signal auto-correlation. First, the OFDM subcarriers are divided into two groups: in-band, i.e., useful, and out-of-band (OOB), i.e., unwanted. For example, in-band frequencies could be the spectrum dedicated for one user, while the OOB frequencies are for another. It is vital for the first user not to transmit information on the OOB frequencies as it might interfere with the other user. Hence, this article maximizes the ratio between the power of in-band and OOB frequencies. In addition, the auto-correlation of the TX OFDM signal is made better by constraining it to have a narrow main-lobe with reduced side-lobes. The PAPR of the waveform is another metric that can be used for waveform design. For instance, [96] discusses the trade-off between PAPR minimization and side-lobe increase of the AF of the waveform.

Minimizing the CRLBs of sensing estimates for joint waveform design is investigated in [23]. Here, the CRLB of the delay estimate is minimized for an OFDM waveform, subject to a power constraint and communications capacity constraint. The waveform optimization discussed in Chapter 4 is also based on CRLB minimization. However, unlike in [23], CRLBs of delay and Doppler-shift estimates are jointly minimized here in the thesis while also considering standard-compliant 5G OFDM waveforms. Similar to the communications rate, *Chiriyath et al.* have defined an *estimation rate* for target tracking scenarios [31]. For those scenarios, the radar usually predicts the target's parameters, e.g., range, velocity, and angle, based on prior information. Hence, the estimation rate indicates the amount of information about the target once this predicted amount is subtracted from the RX signal, similar to the MI metric. The joint waveform is designed here by considering both the estimation rate and communications rate [32].

2.3 Multiple-Input Multiple-Output Systems

This section overviews the concept of MIMO arrays and discusses different MIMO architectures. Then, the advantages of using MIMO arrays for communications and sensing are investigated, leading to MIMO JCAS systems.

Wireless communications systems operate in the mm-wave frequencies due to the untapped spectrum opportunities [85]. Further research considers extending these frequencies even beyond, e.g., terahertz frequencies [86]. This resulted in the usage of MIMO arrays, and even massive-MIMO arrays, with a very high number of antennas [61]. Since each antenna element's beampattern can be controlled separately, MIMO arrays provide flexibility to control the beampattern of many antennas. Therefore, the beams in MIMO arrays' antenna pattern can be narrow, focusing energy only on the intended directions. This is especially useful in these carrier frequencies due to their high attenuation.

2.3.1 MIMO Communications

For communications, the ability of MIMO arrays to beamform users' signals in their directions improves the QoS since most of the TX energy can be received by the users' RX antennas, which would otherwise be transmitted in unwanted directions. This is quite helpful in increasing the spatial diversity of line-of-sight communications channels. In addition, if there is rich scattering in the communications channel, multiple TX streams can be transmitted in parallel, i.e., spatial multiplexing. Therefore, using MIMO arrays, in the end, provides high capacities to the users.

An important concept in MIMO communications is intra-user and inter-user interference. The former is visible when multiple TX streams are used for each user, which is usually true in MIMO systems. Here, a user's TX stream interferes with its other TX streams. In contrast, in the latter, streams of one user interfere with other users' streams. Hence, TX precoding and RX combining must be performed optimally to cancel the interference [9]. They are designed either by minimizing the TX power for a fixed QoS or vice versa [99].

Three different architectures are used for the MIMO arrays in communications systems, as illustrated in Fig. 2.7. First, fully-analog architecture, contains only analog beamforming [49]. All the antennas are connected to a single RF chain, and only

a single TX stream can be used with this architecture, thereby being unable to provide multi-stream communications with different users. The analog beamforming is achieved by modifying the weights of the phase shifters, which generally consist of only phases, whereas the amplitudes are considered fixed. Hence, it is difficult to fine-tune the beams as required since the phases are also usually quantized [49]. As a result, the beampattern generally has a wide main-beam and is not entirely focused on a particular direction. However, the fully-analog beamforming is less costly. Second, fully-digital architecture, in contrast, has only digital beamforming that can modify both amplitudes and phases digitally. Hence, in this beamforming architecture, the beampattern can be narrower than in the fully-analog architecture. This architecture also supports multi-stream communications. However, since each antenna is connected to an RF chain, the implementation cost increases, which is the main drawback of this architecture. As a compromise between the fully-digital and fully-analog architectures, hybrid analog–digital architectures came into being [6, 9]. Here, both analog and digital beamforming are present, and this architecture is mainly used in the thesis. Hybrid arrays are primarily used due to their flexibility in choosing between cost and performance.

Conventionally, in the hybrid architecture, the analog beamforming only consisted of phase shifters. Although they reduce the hardware complexity, the related optimization problem to find the phases that result in the desired beampattern is quite complicated and cannot be implemented in a real-time scenario [98]. Due to this reason, both amplitudes and phases of the elements of the RF beamforming are controlled [78]. Moreover, it has been shown that such a system can be implemented even at mm-wave frequencies, having a good accuracy, low cost, and complexity [28, 81]. Hence, in the thesis, both amplitudes and phases of analog beamforming are controlled. As shown in [14], this also allows for the improvement of the beampattern compared to the RF beamforming, where only the phases are controlled.

2.3.2 MIMO Radar

Radar processing using MIMO arrays is done through the MIMO radar, which is generally a fully-digital architecture, for both TX and RX sides. The most basic definition of a MIMO radar is having multiple TX and RX antennas, where different waveforms can be transmitted from the different TX antennas [65]. There are two
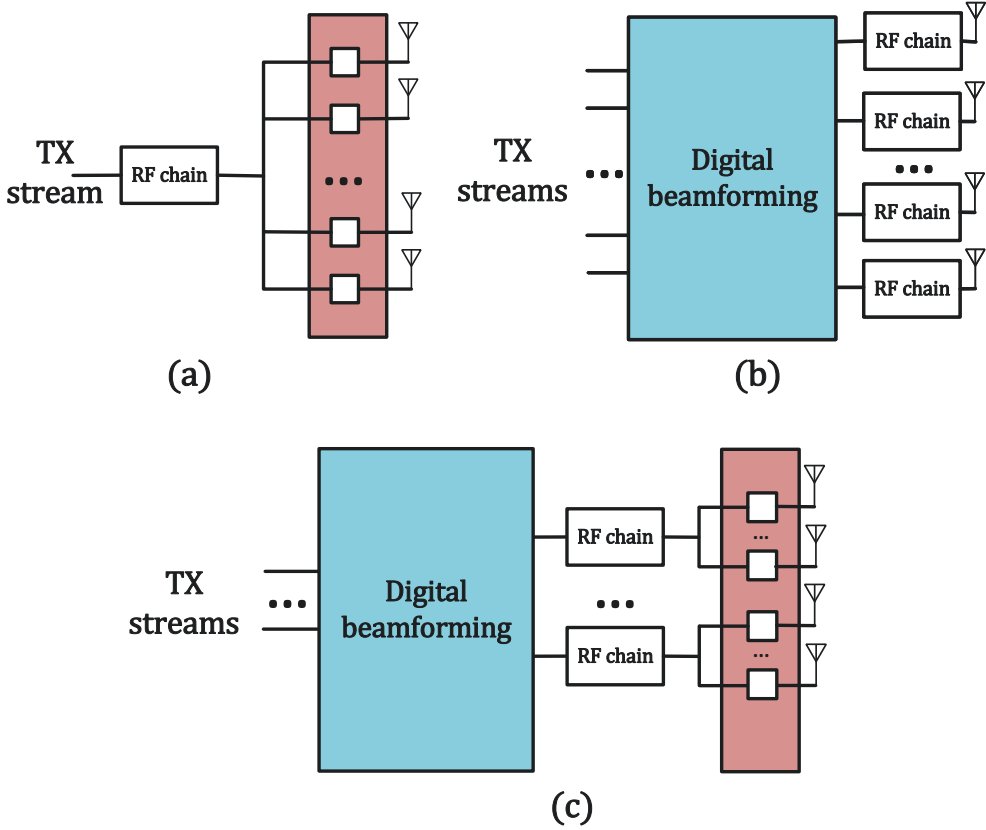
Figure 2.7 Three different architectures for MIMO arrays with (a) fully-analog, (b) fully-digital, and (c) hybrid analog–digital architectures.

main types of MIMO radar, coherent MIMO radar and statistical MIMO radar [24], as depicted in Fig. 2.8. In the former, the antenna elements in the TX and RX are placed closer to each other, with the conventional half-wavelength, i.e., $\frac{\lambda}{2}$, distance. As a result, the radar channel between each TX and RX antenna is essentially the same, but with a phase-shift relative to their position in the antenna array [17, 25, 89]. Typically, orthogonal waveforms are transmitted from the antenna elements, helping to formulate an RX virtual array where its number of elements corresponds to the product of the number of elements in the real TX and RX arrays, facilitating MIMO radar processing [35].

In contrast, in the latter MIMO radar, the antenna elements are placed far away in the TX, and the radar channel between each antenna pair is considered independent [40, 41]. The element spacing between the TX antenna elements is much higher
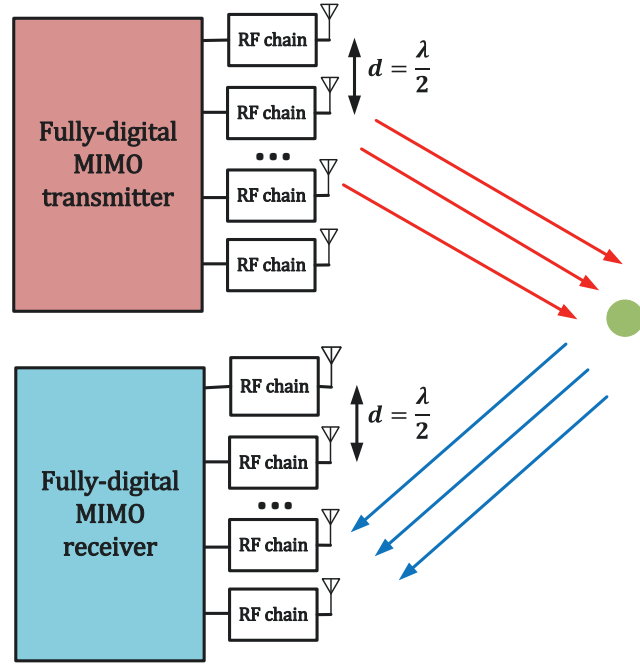
(a) The coherent MIMO radar
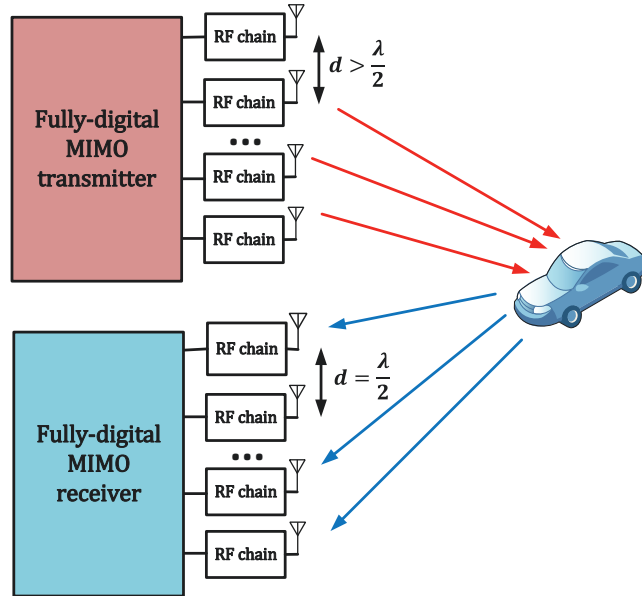
(b) The statistical MIMO radar

Figure 2.8 The two types of MIMO radar.

than the $\frac{\lambda}{2}$ distance, while the separation in the RX side remains to be $\frac{\lambda}{2}$ [97], as depicted in Fig. 2.8(b). A statistical MIMO radar can capture the spatial properties of a target, e.g., an extended target, when compared to that of a coherent MIMO radar, where the target is considered a point target [40]. In addition, the performance of the MIMO radar is improved by ensuring the signals from different TX antenna elements are independent to each other [29].

A MIMO radar can provide many benefits for sensing. Since a slight variation in angle can be detected due to multiple antennas, the resolution of angle estimation is increased [17, 89, 97, 113]. By transmitting independent waveforms from the MIMO radar's TX antennas, each waveform traverses different paths to the different targets in the environment. As such, the received signals from the different targets are also independent to each other, improving the parameter identifiability [112], i.e., the total number of targets that can be detected uniquely [65]. In addition, [48] discusses a scenario where the MIMO radar is utilized to detect slowly moving targets through processing reflections received from multiple directions. Moreover, for an extended target comprising of a complex shape, being able to illuminate it from multiple directions allows improvement in the sensing performance since a different set of information can be gathered for each direction, i.e., spatial diversity [40], increasing probability of detection.

In the thesis, radar tasks are performed from the perspective of a MIMO communications transceiver. It is therefore assumed that the antenna element spacing in the MIMO TX and RX is the same half-wavelength distance. As such, the coherent MIMO radar model is used in the thesis.

An important parameter estimated using MIMO radars is the angle of a target w.r.t. either the TX or RX array, where MUltiple SIgnal Classification (MUSIC) is one algorithm used for the task [92]. It is briefly discussed here since it is used in the later chapters. The RX signal model for a general MIMO array is given by

$$\mathbf{y}(t) = \mathbf{F}\mathbf{x}(t) + \mathbf{n}(t), \tag{2.16}$$

where $\mathbf{y}(t)$, $\mathbf{x}(t)$, and $\mathbf{n}(t)$ are the vector of time-domain samples at the L RX antennas, vector of K TX time-domain samples, and the vector of noise samples, respectively. In addition, the size of $\mathbf{x}(t)$ corresponds to the number of targets in the environment. The size of $\mathbf{F}$ is given by $L \times K$, and it contains the K steering vectors corresponding to each target as columns. The covariance matrix of $\mathbf{y}(t)$ is then

calculated as

$$\mathbf{R}_y = \mathbb{E}\{\mathbf{y}(t)\mathbf{y}^H(t)\} = \mathbf{F}\mathbb{E}\{\mathbf{x}(t)\mathbf{x}^H(t)\}\mathbf{F}^H + \sigma^2\mathbf{I} = \mathbf{FR}_x\mathbf{F}^H + \sigma^2\mathbf{I}, \qquad (2.17)$$

where it is assumed that $\mathbf{x}(t)$ and $\mathbf{n}(t)$ are uncorrelated. Here, σ^2 is the noise variance, $\mathbf{I}$ denotes an identity matrix, and $\mathbf{R}_x$ is the covariance matrix of the TX samples.

The rank of the first term in the right side of (2.17), i.e., $\mathbf{FR}_x\mathbf{F}^H$, is given by K. Hence, it contains K eigenvectors corresponding to non-zero eigenvalues while $L-K$ eigenvectors of zero eigenvalues. Further, the null sub-space can be denoted as $\mathbf{\Gamma} = [\gamma_1, \cdots, \gamma_{L-K}]$, where each column of $\mathbf{\Gamma}$ represents an eigenvector of zero eigenvalue. Similarly, eigenvectors corresponding to the non-zero eigenvalues can be stacked column-wise to obtain the signal sub-space as $\mathbf{\Upsilon} = [\upsilon_1, \cdots, \upsilon_K]$. Denoting the eigenvector of the lth zero eigenvalue as γ_l, it can be written that

$$\mathbf{FR}_x\mathbf{F}^H\gamma_l = \mathbf{0}, \qquad (2.18)$$

due to γ_l being in the null sub-space. Here, $\mathbf{0}$ is the zero vector. The equation in (2.18) can be rearranged as

$$(\mathbf{F}^H\gamma_l)^H\mathbf{R}_x(\mathbf{F}^H\gamma_l) = \mathbf{0}, \qquad (2.19)$$

denoting a quadratic form. Hence, $\mathbf{F}^H\gamma_l = \mathbf{0}$, and the steering vectors are orthogonal to the null sub-space. However, in practice, what can be calculated is not the product $\mathbf{FR}_x\mathbf{F}^H$ in (2.17), but once the noise is added to it. Next, multiplying $\mathbf{R}_y$ by γ_l results in

$$\mathbf{R}_y\gamma_l = \mathbf{FR}_x\mathbf{F}^H\gamma_l + \sigma^2\mathbf{I}\gamma_l = \sigma^2\gamma_l, \qquad (2.20)$$

where $\mathbf{FR}_x\mathbf{F}^H\gamma_l = \mathbf{0}$ because of (2.18). Similarly, multiplying $\mathbf{R}_y$ by υ_l results in

$$\mathbf{R}_y\upsilon_l = \mathbf{FR}_x\mathbf{F}^H\upsilon_l + \sigma^2\mathbf{I}\upsilon_l = (\sigma_l^2 + \sigma^2)\upsilon_l, \qquad (2.21)$$

where υ_l is the eigenvector of the lth non-zero eigenvalue of $\mathbf{\Upsilon}$.

Comparing between (2.20) and (2.21) shows that the eigenvectors of $\mathbf{R}_y$ corresponding to the $L-K$ lowest eigenvalues are the same as the eigenvectors corresponding to the zero eigenvalues in $\mathbf{FR}_x\mathbf{F}^H$ in (2.17). Therefore, the angles of the

targets can be found by first taking the eigendecomposition of $\mathbf{R}_y$ to find the eigenvectors corresponding to the $L-K$ lowest eigenvalues, i.e., $\boldsymbol{\Gamma}$. Secondly, the MUSIC pseudo-spectrum is constructed as

$$P(\theta) = \frac{1}{\mathbf{a}^H(\theta)\boldsymbol{\Gamma}\boldsymbol{\Gamma}^H\mathbf{a}(\theta)}, \tag{2.22}$$

where $\mathbf{a}(\theta)$ is the steering vector at angle θ. For any angle θ that corresponds to the actual angle of the target, $P(\theta)$ will ideally be infinite since the steering vector at that angle is orthogonal to the null sub-space. However, due to noise and other imperfections, the peaks will be finite, and the K highest peaks correspond to the angles of the targets.

2.3.3 Multiple-Input Multiple-Output JCAS Systems

The MIMO arrays are helpful for both communications and sensing functionalities. Hence, the natural step is to combine them, resulting in MIMO JCAS systems [27, 56, 82, 107]. Unlike in SISO JCAS systems, the system must be optimized in the spatial domain. Hence, apart from the transmitted information-bearing signal, e.g., OFDM, the beamforming/precoding should also be optimally designed to construct the beams used for JCAS operations. Typically, the term 'waveform' in MIMO systems denotes the combination between the precoding and the data stream. In MIMO JCAS systems, precoding for communications is performed to focus the beams in the users' directions to minimize the energy transmitted in other directions. In contrast, for sensing, the beams would ideally be needed to be omnidirectional to 'view' the whole environment. For instance, [58, 59] discuss designing the TX precoding and RX combining to address this issue. The authors propose to transmit a portion of the TX power towards the communications users, i.e., main-lobe, while the remaining power is transmitted uniformly across the angular domain, i.e., side-lobes, apart from the users' directions. Hence, the field of view of sensing is widened, improving the detection of targets at the cost of a reduced communications rate.

Although sensing can still be performed using the beams used for communications, the sensing directions are then restricted to be the same as those used for communications. In this regard, an important concept is the design of multiple spatial beams (multi-beams) for the two operations [**14**, 73, 74, 119]. Hence, there are ded-

icated beams for communications, while sensing beams periodically scan the environment, thereby scanning the whole angular domain. For example, *Luo et al.* in [74] design the two beams separately for communications and sensing. For this, the beampatterns are designed by minimizing the error between the required beampattern and some desired beampattern. Once the different beams are designed for the two functionalities, the total beampattern is obtained through their weighted summation. Power scaling is also performed depending on the required trade-off between the two functionalities [75]. Separate beams could be designed based on the spatial matched-filter, as done in [80]. The multi-beams can also be designed through an explicit optimization problem. For instance, in [119], the joint TX beampattern is designed by minimizing the error between the required and desired beampatterns.

The works in [68, 69, 105] design the joint MIMO waveform by minimizing the CRLBs of the estimation parameters while constraining the users' SINR to be above some threshold, while in [114], the communications capacity is constrained. In [3, 64], the precoding design for communications and sensing is performed by maximizing the SINR of the RX radar signal while having power and communications rate constraints. Some have also designed the MIMO waveform by maximizing the MI for communications and sensing [36, 95, 116, 117]. Moreover, *Liu et al.* in [71] obtain the waveform by minimizing the weighted summation between the ISL of the range side-lobes, multi-user interference, and the error between the generated waveform and some desired waveform. The authors in [10] design the precoding jointly with the scheduling of user resources. This is useful in MIMO systems since the interference between different users is a function of which resources are allocated to the different users, i.e., scheduling, as well as precoding. In radar literature, 'clutter' is the set of unwanted targets in the environment [87]. For example, trees and buildings in an urban environment can be the clutter for a vehicular sensing application. The MIMO waveform can also be designed by minimizing the reflections from the clutter, as done in [37], while improving the SNR for communications.

3

System Models for
Joint Communications and Sensing

This chapter presents the general system model used for joint communications and sensing (JCAS) throughout the thesis.[1] It first discusses the leveraging of a multiple-input multiple-output (MIMO) communications transceiver (TRX), e.g., a 5G base station (BS), to perform also sensing. Next, the receive (RX) signal models for communications and sensing are derived. The transmit (TX) precoding and RX combining required to facilitate effective JCAS are then discussed for two different scenarios: when the communications users are in line-of-sight (LoS) and non-LoS (NLoS) conditions w.r.t. the MIMO TRX, respectively. Moreover, only communications streams illuminate the radar targets in the first scenario. In contrast, both communications and separate radar streams are used for target illumination in the second scenario. Finally, this chapter concludes with some TX and RX beampatterns for the considered scenarios.

3.1 Signal Model

Figure 3.1 depicts the general system model of the MIMO JCAS system, where the communications BS also acts as a radar TRX. It has a hybrid beamforming architecture, with L_T antennas and L_T^RF radio-frequency (RF) chains on the TX side, while the MIMO RX has $L_\mathrm{R,r}$ RX antennas and $L_\mathrm{R,r}^\mathrm{RF}$ RF chains. The TX streams $\mathbf{x}_{n,m}$

---

[1]This chapter consists mainly of the works presented in [**P4**], [**P5**], and [**P6**].
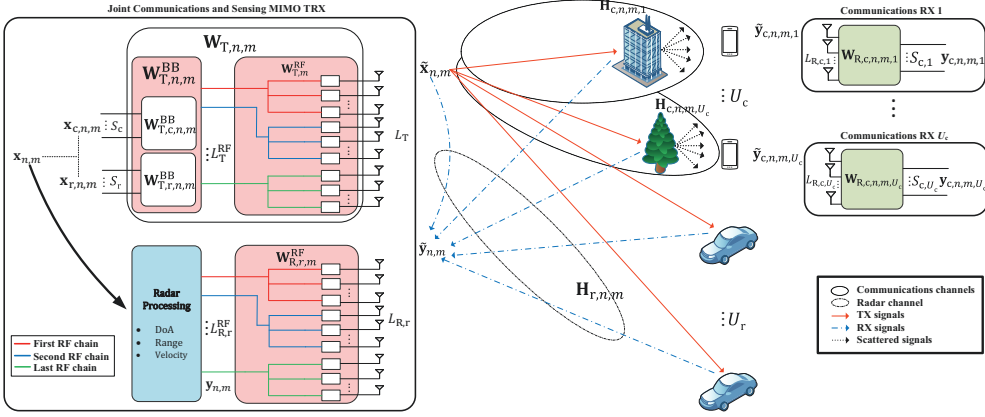
Figure 3.1 The MIMO JCAS system, where the communications TRX is leveraged for sensing purposes. A joint TX waveform is used for both purposes. Each set of colored lines within $\mathbf{W}_{\text{T},m}^{\text{RF}}$ and $\mathbf{W}_{\text{R},\text{r},m}^{\text{RF}}$ denotes the antenna elements connected to a particular RF chain. Lines outside the joint communications and sensing MIMO TRX represent the TX, RX, and scattered signals.

consist of separate communications and radar streams, denoted as $\mathbf{x}_{\text{c},n,m}$ and $\mathbf{x}_{\text{r},n,m}$, respectively. The communications streams are transmitted at U_{c} communications user directions while sensing streams are transmitted at U_{r} radar directions at the radar targets. The communications users' channels can either be LoS or NLoS.

Each TX stream is an OFDM waveform with N active subcarriers and M OFDM symbols, having a subcarrier spacing of Δf. Assuming the uth communications user has $S_{\text{c},u}$ TX streams, frequency-domain symbols of all users for the nth subcarrier and the mth OFDM symbol are given by $\mathbf{x}_{\text{c},n,m} = [\mathbf{x}_{\text{c},n,m,1}^T, \ldots, \mathbf{x}_{\text{c},n,m,U_{\text{c}}}^T]^T$, with $n \in [1, N]$ and $m \in [1, M]$, and $u \in [1, U_{\text{c}}]$, where $\mathbf{x}_{\text{c},n,m}$ is of size $S_{\text{c}} \times 1$ and $S_{\text{c}} = \sum_{u=1}^{U_{\text{c}}} S_{\text{c},u}$. Similarly, the radar streams are given by $\mathbf{x}_{\text{r},n,m} = [\mathbf{x}_{\text{r},n,m,1}^T, \ldots, \mathbf{x}_{\text{r},n,m,U_{\text{r}}}^T]^T$, which is of size $S_{\text{r}} \times 1$. Then, the combination of both types of streams is given by $\mathbf{x}_{n,m} = [\mathbf{x}_{\text{c},n,m}^T, \mathbf{x}_{\text{r},n,m}^T]^T$, which is of size $S \times 1$, where $S = S_{\text{c}} + S_{\text{r}}$. The instantaneous TX powers for communications and sensing streams are given by

$$P_{\text{c}} = \sum_{m=1}^{M} \sum_{n=1}^{N} \sum_{s=1}^{S_{\text{c}}} |x_{n,m,s}|^2 \text{ and } P_{\text{r}} = \sum_{m=1}^{M} \sum_{n=1}^{N} \sum_{s=S_{\text{c}}+1}^{S} |x_{n,m,s}|^2, \qquad (3.1)$$

where $(\mathbf{x}_{n,m})_s = x_{n,m,s}$ represents the sth element of $\mathbf{x}_{n,m}$, while $P_{\text{t}} = P_{\text{c}} + P_{\text{r}}$ denotes the total instantaneous TX power of the streams.

The communications streams have their baseband (BB) beamformer $\mathbf{W}_{\mathrm{T,c},n,m}^{\mathrm{BB}}$, while radar streams have their own, $\mathbf{W}_{\mathrm{T,r},n,m}^{\mathrm{BB}}$, which are of sizes $L_{\mathrm{T}}^{\mathrm{RF}} \times S_{\mathrm{c}}$ and $L_{\mathrm{T}}^{\mathrm{RF}} \times S_{\mathrm{r}}$, respectively. They can be combined to formulate a single BB beamformer as

$$\mathbf{W}_{\mathrm{T},n,m}^{\mathrm{BB}} = [\mathbf{W}_{\mathrm{T,c},n,m}^{\mathrm{BB}}, \mathbf{W}_{\mathrm{T,r},n,m}^{\mathrm{BB}}], \tag{3.2}$$

which is a matrix of size $L_{\mathrm{T}}^{\mathrm{RF}} \times S$. Both of these beamformers are frequency-dependent, or they are separately designed for each OFDM subcarrier. Further, $\mathbf{W}_{\mathrm{T,c},n,m}^{\mathrm{BB}}$ consists of the BB precoders of all users as

$$\mathbf{W}_{\mathrm{T,c},n,m}^{\mathrm{BB}} = [\mathbf{W}_{\mathrm{T,c},n,1}^{\mathrm{BB}}, \ldots, \mathbf{W}_{\mathrm{T,c},n,U_{\mathrm{c}}}^{\mathrm{BB}}]. \tag{3.3}$$

Both the RF beamformers, i.e., MIMO TX and RX, are frequency-independent and common to all subcarriers. They are denoted by $\mathbf{W}_{\mathrm{T},m}^{\mathrm{RF}}$ and $\mathbf{W}_{\mathrm{R,r},m}^{\mathrm{RF}}$, which have sizes $L_{\mathrm{T}} \times L_{\mathrm{T}}^{\mathrm{RF}}$ and $L_{\mathrm{R,r}} \times L_{\mathrm{R,r}}^{\mathrm{RF}}$, respectively. Therefore, the TX frequency-domain symbols at the antenna elements $\tilde{\mathbf{x}}_{n,m}$ are given by

$$\tilde{\mathbf{x}}_{n,m} = \underbrace{\mathbf{W}_{\mathrm{T},m}^{\mathrm{RF}} \mathbf{W}_{\mathrm{T},n,m}^{\mathrm{BB}}}_{\mathbf{W}_{\mathrm{T},n,m}} \mathbf{x}_{n,m}, \tag{3.4}$$

where it is of size $L_{\mathrm{T}} \times 1$, and $\mathbf{W}_{\mathrm{T},n,m}$ can also alternatively be written as

$$\mathbf{W}_{\mathrm{T},n,m} = [\mathbf{W}_{\mathrm{T},m}^{\mathrm{RF}} \mathbf{W}_{\mathrm{T,c},n,m}^{\mathrm{BB}}, \mathbf{W}_{\mathrm{T},m}^{\mathrm{RF}} \mathbf{W}_{\mathrm{T,r},n,m}^{\mathrm{BB}}], \tag{3.5}$$

where it is a combination of communications and radar precoding.

3.1.1 RX Signal for Sensing

Denoting $\tilde{\mathbf{x}}(t)$ as the equivalent continuous-time TX signal of $\tilde{\mathbf{x}}_{n,m}$, once transmitted, it is reflected from the targets in the environment and received at the MIMO RX as $\tilde{\mathbf{y}}(t)$. This can be written as

$$\tilde{\mathbf{y}}(t) = \sum_{k=1}^{K_{\mathrm{t}}} b_k \mathbf{a}_{\mathrm{R}}(\theta_k) \mathbf{a}_{\mathrm{T}}^H(\theta_k) \tilde{\mathbf{x}}(t - \tau_k) e^{j2\pi f_{\mathrm{D},k} t} + \tilde{\mathbf{v}}(t), \tag{3.6}$$

where K_t is the number of point targets, b_k, τ_k, and $f_{D,k}$ are the complex attenuation constant, two-way delay and Doppler-shift of the kth target, respectively. The angles of departure and arrival of the kth target are given by θ_k, assuming that the MIMO TX and RX are situated close to each other and targets are in the far field. In addition, the RX and TX steering vectors are given by $\mathbf{a}_R(\theta_k)$ and $\mathbf{a}_T(\theta_k)$, respectively. The time-domain noise vector is denoted by $\tilde{\mathbf{v}}(t)$. For a uniform linear array with half-wavelength spacing, the steering vector for an angle θ is given by

$$
\begin{aligned}
\mathbf{a}_n(\theta) &= \left[1, e^{J\pi\frac{\lambda}{\lambda_n}\sin(\theta)}, \ldots, e^{J\pi(L-1)\frac{\lambda}{\lambda_n}\sin(\theta)} \right]^T \\
&= \left[1, e^{J\pi\frac{f_c+n\Delta f}{f_c}\sin(\theta)}, \ldots, e^{J\pi(L-1)\frac{f_c+n\Delta f}{f_c}\sin(\theta)} \right]^T \\
\mathbf{a}(\theta) &\approx \left[1, e^{J\pi\sin(\theta)}, \ldots, e^{J\pi(L-1)\sin(\theta)} \right]^T,
\end{aligned}
\tag{3.7}
$$

where f_c is the carrier frequency, and λ and λ_n are the wavelengths of f_c and n^{th} subcarrier frequency. In the thesis, it is assumed that $\frac{f_c+n\Delta f}{f_c} \approx 1$, i.e., bandwidth w.r.t. the carrier frequency is not high. Under this assumption, (3.7) shows that the steering vectors become frequency independent.

As denoted in (2.6), reflected power from a target depends on its radar cross-section (RCS), which is generally defined according to the Swerling model [88]. Depending on how complex the target is, it can be represented as a collection of different scatterers. The Swerling model accounts for the fluctuations of the target reflections from these scatterers. Throughout the thesis, a Swerling 0 model is adopted, which means that point targets are considered with non-fluctuating RCSs.

Next, sampling the time-domain signals in (3.6), and applying the discrete Fourier transform (DFT) results in the frequency-domain representation as

$$
\tilde{\mathbf{y}}_{n,m} = \sum_{k=1}^{K_t} b_k e^{-J2\pi n\Delta f \tau_k} e^{J2\pi m\frac{f_{D,k}}{\Delta f}} \mathbf{a}_R(\theta_k)\mathbf{a}_T^H(\theta_k)\tilde{\mathbf{x}}_{n,m} + \tilde{\mathbf{v}}_{n,m},
\tag{3.8}
$$

where the RX symbols' vector $\tilde{\mathbf{y}}_{n,m}$ and the noise vector $\tilde{\mathbf{v}}_{n,m}$ are of size $L_{R,r} \times 1$. Converting (3.8) to matrix form by applying combining at the MIMO RX gives

$$
\mathbf{y}_{n,m} = \underbrace{(\mathbf{W}_{R,r,m}^{\text{RF}})^H \mathbf{A}_R(\theta)\mathbf{H}_{r,n,m}\mathbf{A}_T^H(\theta)\mathbf{W}_{T,m}^{\text{RF}}\mathbf{W}_{T,n,m}^{\text{BB}}}_{\mathbf{H}_{n,m}} \mathbf{x}_{n,m} + \mathbf{v}_{n,m},
\tag{3.9}
$$

where $\theta = [\theta_1, \ldots, \theta_{K_t}]^T$ contains all targets' directions, and the steering vectors for the K_t targets are stacked for the RX and TX as $\mathbf{A}_R(\theta) = [\mathbf{a}_R(\theta_1), \ldots, \mathbf{a}_R(\theta_{K_t})]$ and $\mathbf{A}_T(\theta) = [\mathbf{a}_T(\theta_1), \ldots, \mathbf{a}_T(\theta_{K_t})]$, where they are of sizes $L_{R,r} \times K_t$ and $L_T \times K_t$, respectively. The radar channel is represented by $\mathbf{H}_{r,n,m}$ and it is a $K_t \times K_t$ diagonal matrix, with the kth diagonal element given by $(\mathbf{H}_{r,n,m})_{k,k} = b_k e^{-j2\pi n \Delta f \tau_k} e^{j2\pi m \frac{f_{D,k}}{\Delta f}}$. The RX BB symbols and noise samples are given by $\mathbf{y}_{n,m}$ and $\mathbf{v}_{n,m}$, of size $L_{R,r}^{RF} \times 1$. In addition, $\mathbf{v}_{n,m} = (\mathbf{W}_{R,r,m}^{RF})^H \tilde{\mathbf{v}}_{n,m}$. The variable $\mathbf{H}_{n,m}$ represents the effective radar channel between the TX streams and RX BB symbols and is of size $L_{R,r}^{RF} \times S$.

The RX BB frequency-domain symbols in (3.9) can be written alternatively by considering the different TX streams and their radar channels as

$$\mathbf{y}_{n,m} = \underbrace{[x_{n,m,1}\mathbf{I}, \ldots, x_{n,m,S}\mathbf{I}]}_{\mathbf{X}_{n,m}} \underbrace{[\mathbf{h}_{n,m,1}^T, \ldots, \mathbf{h}_{n,m,S}^T]^T}_{\mathbf{h}_{n,m}} + \mathbf{v}_{n,m}, \tag{3.10}$$

where $\mathbf{I}$ is the $L_{R,r}^{RF} \times L_{R,r}^{RF}$ identity matrix, $\mathbf{X}_{n,m}$ contains the TX symbols for the different streams of size $L_{R,r}^{RF} \times (L_{R,r}^{RF} \cdot S)$, and $\mathbf{h}_{n,m}$ contains channels for different TX streams and is a vector of size $(L_{R,r}^{RF} \cdot S) \times 1$. In addition, $\mathbf{h}_{n,m,s} = (\mathbf{H}_{n,m})_s$ contains s^{th} streams's radar channel given by the sth column of $\mathbf{H}_{n,m}$, and is represented as

$$\mathbf{h}_{n,m,s} = (\mathbf{W}_{R,r,m}^{RF})^H \mathbf{A}_R(\theta) \mathbf{H}_{r,n,m} \mathbf{A}_T^H(\theta) \mathbf{W}_{T,m}^{RF} (\mathbf{W}_{T,n,m}^{BB})_s. \tag{3.11}$$

By considering multiple OFDM symbols, (3.10) can be rewritten as

$$\underbrace{\begin{bmatrix} \mathbf{y}_{n,1} \\ \mathbf{y}_{n,2} \\ \vdots \\ \mathbf{y}_{n,M} \end{bmatrix}}_{\mathbf{y}_n} = \underbrace{\begin{bmatrix} \mathbf{X}_{n,1} & 0 & \ldots & 0 \\ 0 & \mathbf{X}_{n,2} & \ldots & 0 \\ \vdots & \vdots & \vdots & \vdots \\ 0 & 0 & \ldots & \mathbf{X}_{n,M} \end{bmatrix}}_{\mathbf{X}_n} \underbrace{\begin{bmatrix} \mathbf{h}_{n,1} \\ \mathbf{h}_{n,2} \\ \vdots \\ \mathbf{h}_{n,M} \end{bmatrix}}_{\mathbf{h}_n} + \mathbf{v}_n. \tag{3.12}$$

This expression is later used in Chapter 5 for MIMO radar processing.

3.1.2 RX Signal for Communications

The RX frequency-domain symbols at the uth communications user with $L_{\text{R,c},u}$ antennas can be given using (3.4) and (3.5) as

$$
\begin{aligned}
\tilde{\mathbf{y}}_{\text{c},n,m,u} &= \mathbf{H}_{\text{c},n,m,u} \mathbf{W}_{\text{T},m}^{\text{RF}} \mathbf{W}_{\text{T,c},n,m,u}^{\text{BB}} \mathbf{x}_{\text{c},n,m,u} \\
&+ \mathbf{H}_{\text{c},n,m,u} \mathbf{W}_{\text{T},m}^{\text{RF}} \sum_{u'=1,u'\neq u}^{U_{\text{c}}} \mathbf{W}_{\text{T,c},n,m,u'}^{\text{BB}} \mathbf{x}_{\text{c},n,m,u'} \\
&+ \mathbf{H}_{\text{c},n,m,u} \mathbf{W}_{\text{T},m}^{\text{RF}} \mathbf{W}_{\text{T,r},n,m}^{\text{BB}} \mathbf{x}_{\text{r},n,m} + \tilde{\mathbf{v}}_{\text{c},n,m,u}.
\end{aligned} \tag{3.13}
$$

The first term represents the RX signal due to u^{th} user's TX streams, whereas the second and third terms are the inter-user and radar–communications interference, respectively. The RX symbols' vector $\tilde{\mathbf{y}}_{\text{c},n,m,u}$ and $\tilde{\mathbf{v}}_{\text{c},n,m,u}$ are of size $L_{\text{R,c},u} \times 1$, $\mathbf{H}_{\text{c},n,m,u}$ represents the communications channel between MIMO TX antennas and u^{th} user's RX antennas for the nth subcarrier and m^{th} OFDM symbol, and is of size $L_{\text{R,c},u} \times L_{\text{T}}$. Further, $\mathbf{H}_{\text{c},n,m,u}$ can be written similar to (3.8) as

$$
\mathbf{H}_{\text{c},n,m,u} = \sum_{k=1}^{K_{\text{c},u}} b_{\text{c},u,k} e^{-j2\pi n \Delta f \tau_{\text{c},u,k}} e^{j2\pi m \frac{f_{\text{c,D},u,k}}{\Delta f}} \mathbf{a}_{\text{R},u}(\theta'_{\text{c},u,k}) \mathbf{a}_{\text{T}}^{H}(\theta_{\text{c},u,k}), \tag{3.14}
$$

where the total number of scatterers considered for the uth user is given by $K_{\text{c},u}$. The variables $b_{\text{c},u,k}$, $\tau_{\text{c},u,k}$, and $f_{\text{c,D},u,k}$ denote the attenuation constant, one-way delay and Doppler-shift of the kth scatterer, respectively. The angle of the kth scatterer w.r.t. the MIMO TX and RX are given by $\theta_{\text{c},u,k}$ and $\theta'_{\text{c},u,k}$. Applying combining, RX BB symbols can be represented as

$$
\begin{aligned}
\mathbf{y}_{\text{c},n,m,u} &= (\mathbf{W}_{\text{R,c},n,m,u})^{H} \mathbf{H}_{\text{c},n,m,u} \mathbf{W}_{\text{T},m}^{\text{RF}} \mathbf{W}_{\text{T,c},n,m,u}^{\text{BB}} \mathbf{x}_{\text{c},n,m,u} \\
&+ (\mathbf{W}_{\text{R,c},n,m,u})^{H} \mathbf{H}_{\text{c},n,m,u} \mathbf{W}_{\text{T},m}^{\text{RF}} \sum_{u'=1,u'\neq u}^{U_{\text{c}}} \mathbf{W}_{\text{T,c},n,m,u'}^{\text{BB}} \mathbf{x}_{\text{c},n,m,u'} \\
&+ (\mathbf{W}_{\text{R,c},n,m,u})^{H} \mathbf{H}_{\text{c},n,m,u} \mathbf{W}_{\text{T},m}^{\text{RF}} \mathbf{W}_{\text{T,r},n,m}^{\text{BB}} \mathbf{x}_{\text{r},n,m} + \mathbf{v}_{\text{c},n,m,u} \tag{3.15} \\
&= \mathbf{G}_{\text{c},n,m,u} \mathbf{W}_{\text{T,c},n,m,u}^{\text{BB}} \mathbf{x}_{\text{c},n,m,u} + \mathbf{G}_{\text{c},n,m,u} \sum_{u'=1,u'\neq u}^{U_{\text{c}}} \mathbf{W}_{\text{T,c},n,m,u'}^{\text{BB}} \mathbf{x}_{\text{c},n,m,u'} \\
&+ \mathbf{G}_{\text{c},n,m,u} \mathbf{W}_{\text{T,r},n,m}^{\text{BB}} \mathbf{x}_{\text{r},n,m} + \mathbf{v}_{\text{c},n,m,u}, \tag{3.16}
\end{aligned}
$$

where $\mathbf{G}_{c,n,m,u} = (\mathbf{W}_{R,c,n,m,u})^H \mathbf{H}_{c,n,m,u} \mathbf{W}_{T,m}^{RF}$, $\mathbf{W}_{R,c,n,m,u}$ is the uth user's combiner of size $L_{R,c,u} \times S_{c,u}$, and $\mathbf{y}_{c,n,m,u}$ and $\mathbf{v}_{c,n,m,u}$ are vectors of size $S_{c,u} \times 1$, representing the RX BB symbols and noise samples, respectively. In addition, $\mathbf{v}_{c,n,m,u} = (\mathbf{W}_{R,c,n,m,u})^H \tilde{\mathbf{v}}_{c,n,m,u}$. Radar–communications interference, and inter-user and intra-user interference are canceled by optimizing the TX precoders and RX combiners, as thoroughly discussed in Section 3.3.

The multi-user model containing RX BB symbols of all users can be written using (3.15) as

$$
\begin{aligned}
\mathbf{y}_{c,n,m} = {} & (\mathbf{W}_{R,c,n,m})^H \mathbf{H}_{c,n,m} \mathbf{W}_{T,m}^{RF} \mathbf{W}_{T,c,n,m}^{BB} \mathbf{x}_{c,n,m} \\
& + (\mathbf{W}_{R,c,n,m})^H \mathbf{H}_{c,n,m} \mathbf{W}_{T,m}^{RF} \mathbf{W}_{T,r,n,m}^{BB} \mathbf{x}_{r,n,m} + \mathbf{v}_{c,n,m},
\end{aligned} \tag{3.17}
$$

where the first term of (3.17) includes the first two terms of (3.15). The RX combiner for all users is given as

$$
\mathbf{W}_{R,c,n,m} = \begin{bmatrix} \mathbf{W}_{R,c,n,1} & \cdots & \mathbf{0} \\ \vdots & \vdots & \vdots \\ \mathbf{0} & \cdots & \mathbf{W}_{R,c,n,U_c} \end{bmatrix}, \tag{3.18}
$$

which is a matrix of size $L_{R,c} \times S_c$, with $L_{R,c} = \sum_{u=1}^{U_c} L_{R,c,u}$. In addition, $\mathbf{H}_{c,n,m} = [\mathbf{H}_{c,n,1}^T, \ldots, \mathbf{H}_{c,n,U_c}^T]^T$ contains the communications channels of all users, which is of size $L_{R,c} \times L_T$.

To evaluate the channel capacity of the uth user, covariance matrices of the different terms in (3.16) need to be calculated. They are given respectively for the signal-of-interest (SOI), inter-user interference, and radar–communications interference as

$$
\mathbf{R}_{\text{SOI},n,m,u} = \mathbf{G}_{c,n,m,u} \mathbf{W}_{T,c,n,m,u}^{BB} \mathbb{E}\{\mathbf{x}_{c,n,m,u} \mathbf{x}_{c,n,m,u}^H\} (\mathbf{W}_{T,c,n,m,u}^{BB})^H \mathbf{G}_{c,n,m,u}^H, \tag{3.19}
$$

$$
\mathbf{R}_{\text{int},c,n,m,u} = \mathbf{G}_{c,n,m,u} \mathbb{E}\left\{ \left(\sum_{u'=1,u'\neq u}^{U_c} \mathbf{W}_{TX,c,n,m,u'}^{BB} \mathbf{x}_{c,n,m,u'} \right) \right.
$$
$$
\left. \cdot \left(\sum_{u'=1,u'\neq u}^{U_c} \mathbf{W}_{TX,c,n,m,u'}^{BB} \mathbf{x}_{c,n,m,u'} \right)^H \right\} \mathbf{G}_{c,n,m,u}^H, \tag{3.20}
$$

$$
\mathbf{R}_{\text{int},r,n,m,u} = \mathbf{G}_{c,n,m,u} \mathbf{W}_{T,r,n,m}^{BB} \mathbb{E}\{\mathbf{x}_{r,n,m} \mathbf{x}_{r,n,m}^H\} (\mathbf{W}_{T,r,n,m}^{BB})^H \mathbf{G}_{c,n,m,u}^H. \tag{3.21}
$$

Next, channel capacity for all communications users for a given channel realization can be represented as

$$\zeta_{\text{int,c}} = \sum_{u=1}^{U_{\text{c}}} \sum_{m=1}^{M} \sum_{n=1}^{N} \log_2 \det\left\{ \mathbf{I} + \left(\mathbf{R}_{\text{int,c},n,m,u} + \mathbf{R}_{\text{int,r},n,m,u} + \sigma_u^2 \mathbf{I} \right)^{-1} \mathbf{R}_{\text{SOI},n,m,u} \right\},$$

$$(3.22)$$

where σ_u^2 is the noise variance at the uth user. When JCAS is not performed, but only communications, channel capacity for all users can be written as

$$\bar{\zeta}_{\text{c}} = \sum_{u=1}^{U_{\text{c}}} \sum_{m=1}^{M} \sum_{n=1}^{N} \log_2 \det\left\{ \mathbf{I} + \left(\bar{\mathbf{R}}_{\text{int,c},n,m,u} + \sigma_u^2 \mathbf{I} \right)^{-1} \bar{\mathbf{R}}_{\text{SOI},n,m,u} \right\}, \qquad (3.23)$$

where $\bar{\mathbf{R}}_{\text{int,c},n,m,u}$ and $\bar{\mathbf{R}}_{\text{SOI},n,m,u}$ are similar covariance matrices for inter-user interference and SOI when only communications is performed, respectively.

Finally, Table 3.1 lists the main parameters of the system model, while Table 3.2 lists the important vectors and matrices used throughout the thesis.

3.2 Considered MIMO JCAS Systems

This section discusses two different scenarios considered for JCAS in the thesis. The main differences between them are illustrated in Fig. 3.3, whereas other parts are the same in both cases, as in Fig. 3.1. Moreover, these differences are also summarized in Table 3.3 for clarity.

In the first scenario *LoS with no radar streams*, communications users are in LoS w.r.t. the MIMO TRX. There are no separate radar streams, but the communications streams are also transmitted in the radar directions. Hence, there is no radar–communications interference, and since there is only a single stream per user, only inter-user interference needs to be canceled. Due to the existence of a single TX stream per user, only a single RX antenna is considered for each user, and hence no RX combiner is needed. Moreover, the beamforming matrices are the same for all subcarriers and OFDM symbols, i.e., frequency/time-independent.

In the second scenario *NLoS with radar streams*, communications users are in NLoS conditions with a dominant LoS path. In this scenario, as illustrated in Fig. 3.2, scatterers can be surrounding a particular user, directly behind the user, or an-

Table 3.1 General parameters

Parameter	Definition
U_c	Number of communications users
U_r	Number of sensing beams
L_T	Number of antenna elements of MIMO TX
L_T^{RF}	Number of RF chains of MIMO TX
$L_{R,r}$	Number of antenna elements of MIMO RX
$L_{R,r}^{RF}$	Number of RF chains of MIMO RX
M	Number of OFDM symbols in one TX stream
N	Number of active subcarriers in one TX stream
Δf	Subcarrier spacing
$S_{c,u}$	Number of TX streams of uth user
S_c	Total number of communications streams
S_r	Total number of radar streams
S	Total number of streams
K_t	Number of point targets

gled to the user when the direct LoS direction is blocked, e.g., due to a building or trees. In all of these cases, the user is in NLoS conditions. However, in practice, the TRX has some directional information about the user to perform precoding, as it wastes energy to transmit the communications streams randomly in all directions. Therefore, it can be assumed that the TRX knows each user's dominant/best direction. This direction could be the actual angle between the user and the TRX, for example, in Figs. 3.2(a) and 3.2(b), but it does not necessarily mean that the user is in LoS condition.

In *NLoS with radar streams* scenario, separate radar streams are transmitted in radar directions, apart from the communications streams transmitted in the users' directions. All three types of interference exist, i.e., inter-user, intra-user, and radar–communications, and must be canceled. Each communications user is assumed to have more than one antenna, also having a hybrid RX combiner. Further, all beamforming matrices are considered to be time-dependent, while the BB beamforming matrices and communications users' RX combiners are frequency-dependent.

Table 3.2 System model variables

Variable	Definition	Size
$\mathbf{x}_{c,n,m}$	TX communications streams' symbols	$S_c \times 1$
$\mathbf{x}_{r,n,m}$	TX sensing streams' symbols	$S_r \times 1$
$\mathbf{x}_{n,m}$	All TX streams' symbols	$S \times 1$
$\tilde{\mathbf{x}}_{n,m}$	Samples at MIMO TX antennas	$L_T \times 1$
$\mathbf{y}_{n,m}$	Baseband streams' symbols at MIMO RX	$L_{R,r}^{RF} \times 1$
$\tilde{\mathbf{y}}_{n,m}$	Samples at MIMO RX antennas	$L_{R,r} \times 1$
$\mathbf{y}_{c,n,m}$	RX streams' symbols of all users	$S_c \times 1$
$\mathbf{W}_{T,c,n,m}^{BB}$	TX baseband weights for communications	$L_T^{RF} \times S_c$
$\mathbf{W}_{T,r,n,m}^{BB}$	TX baseband weights for radar	$L_T^{RF} \times S_r$
$\mathbf{W}_{T,n,m}^{BB}$	Total TX baseband weights	$L_T^{RF} \times S$
$\mathbf{W}_{T,m}^{RF}$	RF weights of MIMO TX	$L_T \times L_T^{RF}$
$\mathbf{W}_{T,n,m}$	Total TX precoder weights	$L_T \times S$
$\mathbf{W}_{R,r,m}^{RF}$	RF weights of MIMO RX	$L_{R,r} \times L_{R,r}^{RF}$
$\mathbf{W}_{R,c,n,m,u}$	RX combiner of uth user	$L_{R,c,u} \times S_{c,u}$
$\mathbf{W}_{R,c,n,m}$	RX combiner of all users	$L_{R,c} \times S_c$
$\mathbf{A}_{TX}(\theta)$	TX steering vectors for all targets	$L_T \times K_t$
$\mathbf{A}_R(\theta)$	RX steering vectors for all targets	$L_{R,r} \times K_t$
$\mathbf{H}_{r,n,m}$	Radar channel	$K_t \times K_t$
$\mathbf{H}_{n,m}$	Effective radar channel	$L_{R,r}^{RF} \times S$
$\mathbf{H}_{c,n,m,u}$	Communications channel for u^{th} user	$L_{R,c,u} \times L_T$
$\mathbf{H}_{c,n,m}$	Communications channel for all users	$L_{R,c} \times L_T$

3.3 Beamforming Design

A hybrid analog–digital MIMO TRX is considered, where the TX and RX RF beam-formers are partially connected, where a subset of antennas is connected to an RF chain, as in Fig. 3.3.
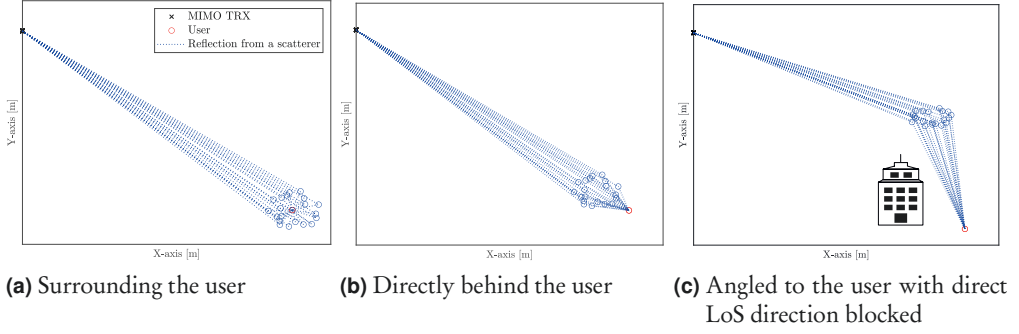
(a) Surrounding the user   **(b)** Directly behind the user   **(c)** Angled to the user with direct LoS direction blocked

Figure 3.2   Scatterer locations w.r.t. a particular communications user.

(a) LoS with no radar streams
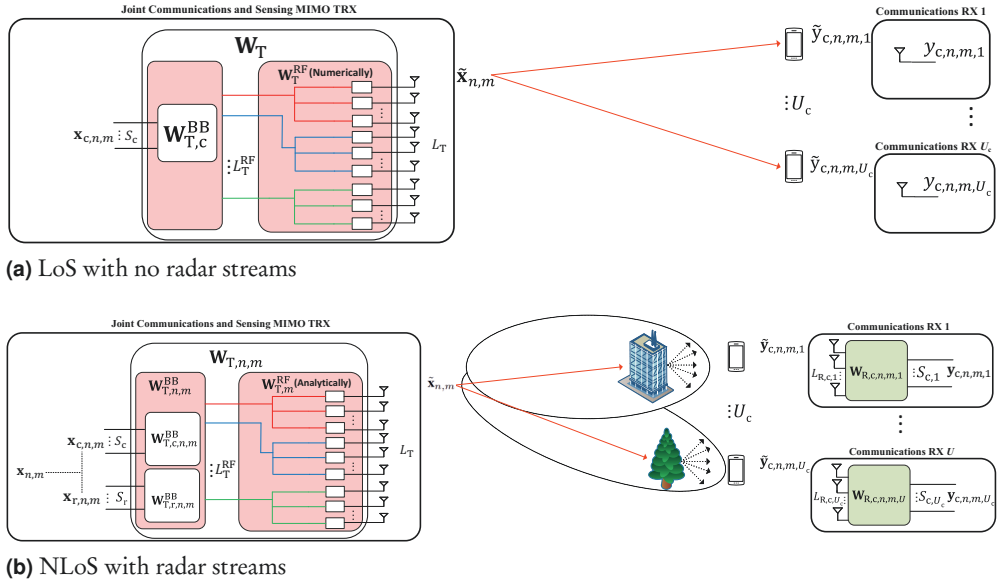

(b) NLoS with radar streams

Figure 3.3   The main differences between the two considered MIMO JCAS systems, with LoS and NLoS conditions.

3.3.1   Receive Radio-Frequency Beamforming

The MIMO RX's RF weights are designed to receive the reflections from the radar directions. Considering the NLoS scenario, dominant LoS directions of the users for the mth OFDM symbol can be denoted by $\theta_{\text{c},m} = [\theta_{\text{c},m,1}, \ldots, \theta_{\text{c},m,U_\text{c}}]^T$ while radar directions as $\theta_{\text{r},m} = [\theta_{\text{r},m,1}, \ldots, \theta_{\text{r},m,U_\text{r}}]$. All these angles can be combined as

$$\theta_{\text{T},m} = [\theta_{\text{c},m}^T, \theta_{\text{r},m}^T]^T. \tag{3.24}$$

43

Table 3.3 Differences between the two beamforming scenarios

Difference	LoS scenario	NLoS scenario
Communications channels	LoS	NLoS
TX RF beamformer design	Numerical optimization	Analytical
Time-varying beamforming matrices	No	Yes
Frequency-dependent BB weights	No	Yes
Separate radar streams	No	Yes
$S_{c,u}$	1	> 1
$L_{R,c,u}$	1	> 1
Communication users' combiners	No	Yes

Then, weights corresponding to the l_R^{th} RF chain, m^{th} OFDM symbol, and radar direction u' are given by

$$
\mathbf{w}_{R,r,l_R,m,u'}^{RF} = \frac{\mathbf{a}_{R,l_R}^{*}(\theta_{r,m,u'})}{||\mathbf{a}_{R,l_R}(\theta_{r,m,u'})||}, \tag{3.25}
$$

where $l_R \in [1, L_{R,r}^{RF}]$, while $\mathbf{a}_{R,l_R}(\theta_{r,m,u'})$ is the RX steering vector for the l_R^{th} RF chain, and $||\cdot||$ is the l_2-norm operation. To receive reflections from all radar directions, weights corresponding to each direction are summed as

$$
\mathbf{w}_{R,r,l_R,m}^{RF} = \sum_{u'=1}^{U_r} \mathbf{w}_{R,r,l_R,m,u'}^{RF}. \tag{3.26}
$$

Then, the radar RX RF beamformer $\mathbf{W}_{R,r,m}^{RF}$ can be formulated by stacking the normalized weights for each RF chain as

$$
\mathbf{W}_{R,r,m}^{RF} = \left[\frac{\mathbf{w}_{R,r,1,m}}{||\mathbf{w}_{R,r,1,m}||}, \dots, \frac{\mathbf{w}_{R,r,L_{R,r}^{RF},m}}{||\mathbf{w}_{R,r,L_{R,r}^{RF},m}||} \right]. \tag{3.27}
$$

For the LoS scenario, (3.25) can be simplified by dropping the subscript m, and the weights corresponding to the l_R^{th} RF chain can be obtained accordingly by substituting to (3.26).

3.3.2 Transmit Beamforming–LoS without Radar Streams

Here, communications TX frequency-domain symbols at the antenna elements are given based on (3.4) and (3.5) as

$$\tilde{\mathbf{x}}_{n,m} = \underbrace{\mathbf{W}_{\mathrm{T}}^{\mathrm{RF}}\mathbf{W}_{\mathrm{T,c}}^{\mathrm{BB}}}_{\mathbf{W}_{\mathrm{T}}}\mathbf{x}_{\mathrm{c},n,m}, \tag{3.28}$$

where $\mathbf{W}_{\mathrm{T,c}}^{\mathrm{BB}}$ is frequency-independent, as depicted in Fig. 3.3(a). Further, the RX frequency-domain symbols of all users can be represented based on (3.17), without $\mathbf{W}_{\mathrm{R,c},n,m}$ and radar–communications interference, as

$$\mathbf{y}_{\mathrm{c},n,m} = \mathbf{H}_{\mathrm{c}}\mathbf{W}_{\mathrm{T}}^{\mathrm{RF}}\mathbf{W}_{\mathrm{T,c}}^{\mathrm{BB}}\mathbf{x}_{\mathrm{c},n,m} + \mathbf{v}_{\mathrm{c},n,m}, \tag{3.29}$$

where due to the LoS condition, $\mathbf{H}_{\mathrm{c}} = \left[\sqrt{g_1}\mathbf{a}_{\mathrm{T}}(\theta_{\mathrm{c},1}),\cdots,\sqrt{g_{U_{\mathrm{c}}}}\mathbf{a}_{\mathrm{T}}(\theta_{\mathrm{c},U_{\mathrm{c}}})\right]^{T}$, with $\sqrt{g_{\mathrm{u}}}$ representing the free-space attenuation for the uth user. The matrix $\mathbf{W}_{\mathrm{T}}^{\mathrm{RF}}$ and $\mathbf{W}_{\mathrm{T,c}}^{\mathrm{BB}}$ are then chosen to cancel the inter-user interference. The uth user's beamforming can be selected so that it does not interfere with the other users as

$$\mathbf{a}_{\mathrm{T}}^{H}(\theta_{\mathrm{c},\tilde{u}})\mathbf{W}_{\mathrm{T}}^{\mathrm{RF}}\mathbf{w}_{\mathrm{T,c},u}^{\mathrm{BB}} = 0, \forall \tilde{u}, \tilde{u} \neq u, \tag{3.30}$$

where $\mathbf{w}_{\mathrm{T,c},u}^{\mathrm{BB}}$ is the TX BB beamforming vector of the uth user, and $\tilde{u} \in [1, U_{\mathrm{c}}]$. This can also be written by considering all users as

$$\underbrace{\left[\left(\mathbf{a}_{\mathrm{T}}^{H}(\theta_{\mathrm{c},1})\mathbf{W}_{\mathrm{T}}^{\mathrm{RF}}\right)^{T},\ldots,\left(\mathbf{a}_{\mathrm{T}}^{H}(\theta_{\mathrm{c},U_{\mathrm{c}}})\mathbf{W}_{\mathrm{T}}^{\mathrm{RF}}\right)^{T}\right]^{T}}_{\mathbf{Z}_{u}}\mathbf{w}_{\mathrm{T,c},u}^{\mathrm{BB}} = 0, \tag{3.31}$$

where $\mathbf{Z}_{u}$ contains the information about all the other users for the uth user. Using the null-space projection (NSP) method [P5], $\mathbf{w}_{\mathrm{T,c},u}^{\mathrm{BB}}$ can be found as

$$\mathbf{w}_{\mathrm{T,c},u}^{\mathrm{BB}} = (\mathbf{I} - \mathbf{Z}_{u}^{\dagger}\mathbf{Z}_{u})\hat{\mathbf{w}}_{\mathrm{T,c},u}^{\mathrm{BB}}, \tag{3.32}$$

where $\hat{\mathbf{w}}_{T,c,u}^{BB}$ is any vector of the same size as $\mathbf{w}_{T,c,u}^{BB}$. Hence, considering all users, the TX BB matrix can be given as

$$\mathbf{W}_{T,c}^{BB} = \left[(\mathbf{I} - \mathbf{Z}_1^\dagger \mathbf{Z}_1)\hat{\mathbf{w}}_{T,c,1}^{BB}, \dots, (\mathbf{I} - \mathbf{Z}_{U_c}^\dagger \mathbf{Z}_{U_c})\hat{\mathbf{w}}_{T,c,U_c}^{BB} \right]. \tag{3.33}$$

The matrix $\hat{\mathbf{W}}_{T,c}^{BB} = \left[\hat{\mathbf{w}}_{T,c,1}^{BB}, \dots, \hat{\mathbf{w}}_{T,c,U_c}^{BB} \right]$ which contains the arbitrary vectors for all users, as well as $\mathbf{W}_T^{RF}$ are then found through an optimization problem as

$$\max_{\hat{\mathbf{W}}_{T,c}^{BB}, \mathbf{W}_T^{RF}} \sum_{u'=1}^{U_r} |\mathbf{a}_T^H(\theta_{r,u'})\mathbf{W}_T^{RF}\mathbf{w}_{T,c,u}^{BB}|^2 \tag{3.34a}$$

subject to

$$|\mathbf{a}_T^H(\theta_{c,u})\mathbf{W}_T^{RF}\mathbf{w}_{T,c,u}^{BB}|^2 \geq G_u, \forall u, \tag{3.34b}$$

$$\mathbf{W}_{T,c}^{BB} = \left[(\mathbf{I} - \mathbf{Z}_1^\dagger \mathbf{Z}_1)\hat{\mathbf{w}}_{T,c,1}^{BB}, \dots, (\mathbf{I} - \mathbf{Z}_{U_c}^\dagger \mathbf{Z}_{U_c})\hat{\mathbf{w}}_{T,c,U_c}^{BB} \right], \tag{3.34c}$$

$$||\mathbf{W}_T^{RF}(\mathbf{W}_{T,c}^{BB})_s|| = 1, \forall s, \tag{3.34d}$$

where $s \in [1, S_c]$ denotes the sth column of $\mathbf{W}_{T,c}^{BB}$. Hence, this optimization maximizes the summation of gains at the U_r radar directions for all the communications streams' beampatterns since they are transmitted at the radar directions. Moreover, the gain of the TX beampatterns at u^{th} communications direction is also set at a definite level G_u. Hence, this optimization ascertains that the communications streams are transmitted at the communications directions with some specific gains, but also canceling the inter-user interference due to the adopted NSP method. The norm of each column of total communications TX precoder $\mathbf{W}_T^{RF}\mathbf{W}_{T,c}^{BB}$ is constrained to limit the beamforming vectors having unnecessarily high magnitudes. This optimization problem is solved numerically, and the results are discussed in Section 3.4.

3.3.3 Precoding/Combining–NLoS with Radar Streams

The NLoS scenario where the communications users are in NLoS conditions w.r.t. the MIMO TRX represents a more general MIMO JCAS system. Communications streams are transmitted in communications directions, while radar streams are transmitted in radar directions. The interference, i.e., inter-user, intra-user, and radar–

communications, must be canceled for improved performance. The TX RF beamforming, which is frequency-independent, is designed first. The interference cancellation happens mainly by the design of the TX BB beamforming (both $\mathbf{W}_{T,c,n,m}^{BB}$ and $\mathbf{W}_{T,r,n,m}^{BB}$) and RX combiners of the users, which are frequency-dependent.

TX RF Beamforming The TX RF and BB beamforming matrices cannot be designed as done in (3.34a)–(3.34d) since $\mathbf{W}_{T,m}^{RF}$ is frequency-independent due to the considered steering vectors in (3.7), while the BB matrices are frequency-dependent. This is because $\mathbf{W}_{T,m}^{RF}$ matrix obtained using the earlier single optimization problem could be optimal for a specific frequency but not for any other frequency. Hence, $\mathbf{W}_{T,m}^{RF}$ is designed first, which is common to all frequencies.

Since multiple beams need to be catered corresponding to U_c communications users and U_r radar directions, TX RF weights are obtained to facilitate this requirement. Adopting a similar method as in (3.25), TX RF weights for the l_T^{th} RF chain for a particular direction are given by

$$
\mathbf{w}_{T,l_T,m,i}^{RF} = \begin{cases} \rho \dfrac{\mathbf{a}_{T,l_T}^*(\theta_{T,m,i})}{\|\mathbf{a}_{T,l_T}(\theta_{T,m,i})\|}, & \theta_{T,m,i} \in \theta_{c,m}, \\ (1-\rho) \dfrac{\mathbf{a}_{T,l_T}^*(\theta_{T,m,i})}{\|\mathbf{a}_{T,l_T}(\theta_{T,m,i})\|}, & \theta_{T,m,i} \in \theta_{r,m}, \end{cases} \tag{3.35}
$$

where i corresponds to the angle index of $\theta_{T,m}$ in (3.24) with $i \in [1,(U_c + U_r)]$, l_T denotes the index of the RF chain with $l_T \in [1, L_T^{RF}]$, and $\mathbf{a}_{T,l_T}(\theta_{T,m,i})$ corresponds to the TX steering vector of the l_T^{th} RF chain. Here, by changing $\rho \in [0,1]$, the gain trade-off between communications and radar directions can be controlled, where increasing ρ increases the gains for communications.

For each angle of $\theta_{T,m}$, (3.35) designs a main-beam at that particular angle. Since $U_c + U_r$ such angles are needed, weights corresponding to all of them for a specific RF chain are obtained by summing the weights for different angles as

$$
\mathbf{w}_{T,l_T,m}^{RF} = \sum_{i=1}^{U_c+U_r} \mathbf{w}_{T,l_T,m,i}^{RF}. \tag{3.36}
$$

Finally, $\mathbf{W}_{T,m}^{RF}$ is given by stacking the weights for the different RF chains as $\mathbf{W}_{T,m}^{RF} = \left[\dfrac{\mathbf{w}_{T,1,m}^{RF}}{\|\mathbf{w}_{T,1,m}^{RF}\|}, \cdots, \dfrac{\mathbf{w}_{T,L_T^{RF},m}^{RF}}{\|\mathbf{w}_{T,L_T^{RF},m}^{RF}\|} \right]$, where each column is normalized to have unit norm.

TX BB Beamforming and Users' RX Combiners Design   Firstly, the communications beamformers, i.e., $\mathbf{W}_{\text{T},c,n,m}^{\text{BB}}$ and $\mathbf{W}_{\text{R},c,n,m}$, are designed to cancel the inter-user and intra-user interference. This cancellation can be attained by selecting the matrix product $(\mathbf{W}_{\text{R},c,n,m})^H \mathbf{H}_{c,n,m} \mathbf{W}_{\text{T},m}^{\text{RF}} \mathbf{W}_{\text{T},c,n,m}^{\text{BB}}$ in the first term of (3.17) such that it is a diagonal matrix. It is achieved using the block diagonalization (BD) method, where inter-user and intra-user interferences are canceled using two consecutive singular value decompositions (SVDs). For this, other users' RF-equivalent channels, i.e., also including $\mathbf{W}_{\text{T},m}^{\text{RF}}$, without the uth user's RF-equivalent channel are represented as

$$\bar{\mathbf{H}}_{c,n,m,u} = \left[\mathbf{H}_{c,n,m,1}^T \mathbf{W}_{\text{T},m}^{\text{RF}}, \mathbf{H}_{c,n,m,u-1}^T \mathbf{W}_{\text{T},m}^{\text{RF}}, \mathbf{H}_{c,n,m,u+1}^T \mathbf{W}_{\text{T},m}^{\text{RF}} \cdots, \mathbf{H}_{c,n,m,U_{\text{c}}}^T \mathbf{W}_{\text{T},m}^{\text{RF}} \right]^T .$$

$$(3.37)$$

Next, to ascertain the uth user does not interfere with other users, its BB beamforming matrix, $\mathbf{W}_{\text{T},c,n,m,u}^{\text{BB}}$, should be in the null-space of $\bar{\mathbf{H}}_{c,n,m,u}$. Calculating the SVD of $\bar{\mathbf{H}}_{c,n,m,u}$ as

$$\bar{\mathbf{H}}_{c,n,m,u} = \bar{\mathbf{V}}_{\text{left},u} \bar{\boldsymbol{\Sigma}}_u \left(\bar{\mathbf{V}}_{\text{right},u}^{(1)}, \bar{\mathbf{V}}_{\text{right},u}^{(0)} \right)^H , \qquad (3.38)$$

where the subscripts 'left' and 'right' are the left and right singular vectors, while the matrices with the superscripts 0 and 1 contain the eigenvectors corresponding to the zero and non-zero eigenvalues. Notice that the subscripts n and m are removed, on the right side of (3.38), for simplicity. Since $\bar{\mathbf{V}}_{\text{right},u}^{(0)}$ contains the eigenvectors of the zero eigenvalues, vectors of $\bar{\mathbf{V}}_{\text{right},u}^{(0)}$ are candidate vectors for $\mathbf{W}_{\text{T},c,n,m,u}^{\text{BB}}$.

Hence, $\mathbf{H}_{c,n,m,u} \mathbf{W}_{\text{T},m}^{\text{RF}} \bar{\mathbf{V}}_{\text{right},u}^{(0)}$ represents the effective channel after inter-user interference is canceled, with this product's SVD given by

$$\mathbf{H}_{c,n,m,u} \mathbf{W}_{\text{T},m}^{\text{RF}} \bar{\mathbf{V}}_{\text{right},u}^{(0)} = \mathbf{V}_{\text{left},u} \boldsymbol{\Sigma}_u \left(\mathbf{V}_{\text{right},u}^{(1)}, \mathbf{V}_{\text{right},u}^{(0)} \right)^H . \qquad (3.39)$$

The intra-user interference is next canceled by choosing the matrices as [99]

$$\mathbf{W}_{\text{T},c,n,m,u}^{\text{BB}} = \bar{\mathbf{V}}_{\text{right},u}^{(0)} \mathbf{V}_{\text{right},u}^{(1)}, \quad \mathbf{W}_{\text{R},c,n,m,u} = \mathbf{V}_{\text{left},u}^H . \qquad (3.40)$$

Doing this for all the communications users ensures $(\mathbf{W}_{\text{R},c,n,m})^H \mathbf{H}_{c,n,m} \mathbf{W}_{\text{T},m}^{\text{RF}} \mathbf{W}_{\text{T},c,n,m}^{\text{BB}}$ in the first term of (3.17) is diagonal.

Next, $\mathbf{W}_{\mathrm{T,r},n,m}^{\mathrm{BB}}$ is designed to cancel the radar–communications interference, since not canceling it results in degradation of the communications performance. For this, $\mathbf{Z}_{n,m} = (\mathbf{W}_{\mathrm{R,c},n,m})^H \mathbf{H}_{\mathrm{c},n,m} \mathbf{W}_{\mathrm{T},m}^{\mathrm{RF}} \mathbf{W}_{\mathrm{T,r},n,m}^{\mathrm{BB}}$ in the second term of (3.17) needs to be a matrix of zeros. This requirement is due to NLoS conditions, whereas in an LoS scenario, canceling radar–communications interference results in imposing a null for the radar streams at the communications directions in the TX beampattern. Thus, BB weights of each radar direction are obtained by maximizing gains at that direction while also ensuring they cancel the radar–communications interference. Hence, the BB weights are given by also utilizing the NSP criterion as

$$\mathbf{w}_{\mathrm{T,r},n,m,u'}^{\mathrm{BB}} = \frac{\left(\mathbf{I} - \mathbf{Z}_{n,m}^{\dagger} \mathbf{Z}_{n,m}\right)(\mathbf{W}_{\mathrm{T},m}^{\mathrm{RF}})^H \mathbf{a}_{\mathrm{T}}(\theta_{\mathrm{r},m,u'})}{\|(\mathbf{W}_{\mathrm{T},m}^{\mathrm{RF}})^H \mathbf{a}_{\mathrm{T}}(\theta_{\mathrm{r},m,u'})\|}. \tag{3.41}$$

Finally, TX BB beamformer for radar streams is given by stacking the normalized weights as $\mathbf{W}_{\mathrm{T,r},n,m}^{\mathrm{BB}} = \left[\frac{\mathbf{w}_{\mathrm{T,r},n,m,1}^{\mathrm{BB}}}{\|\mathbf{w}_{\mathrm{T,r},n,m,1}^{\mathrm{BB}}\|}, \ldots, \frac{\mathbf{w}_{\mathrm{T,r},n,m,U_{\mathrm{r}}}^{\mathrm{BB}}}{\|\mathbf{w}_{\mathrm{T,r},n,m,U_{\mathrm{r}}}^{\mathrm{BB}}\|}\right]$. It should be noted that to implement $\mathbf{W}_{\mathrm{T,r},n,m}^{\mathrm{BB}}$, it is assumed that the MIMO TX knows the RX combiners and communications channels of all users, i.e., $\mathbf{W}_{\mathrm{R,c},n,m}$ and $\mathbf{H}_{\mathrm{c},n,m}$ in $\mathbf{Z}_{n,m}$.

3.4 MIMO TX and RX Beampatterns

This section illustrates both scenarios' MIMO TX and RX beampatterns for $L_{\mathrm{T}} = L_{\mathrm{R,r}} = 32$ antennas. The communications and radar directions are selected as $\theta_{\mathrm{c}} = [-40°, 30°]^T$ and $\theta_{\mathrm{r}} = [-10°, 5°]^T$. Uniform linear arrays are assumed for TX and RX antennas, where the steering vector for a general angle θ for either of them is given by (3.7).

LoS Scenario

Firstly, Fig. 3.4 shows the effective TX beampattern, i.e., the combination of RF and BB beamforming, for the LoS scenario, for different numbers of RF chains. Two communications users are considered, with each having only a single stream. Hence, there are two TX streams in total, and the figures depict the beampatterns for the two streams or the two users. Each stream has a main-beam corresponding to that user's direction. Then, each stream also has a null corresponding to the other user's
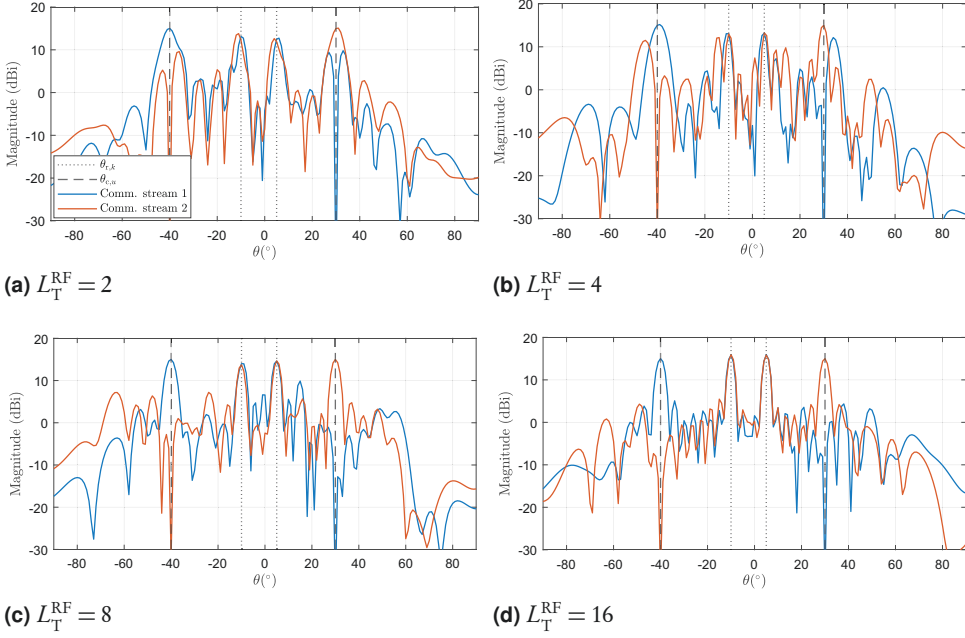
(a) $L_T^{RF} = 2$

(b) $L_T^{RF} = 4$

(c) $L_T^{RF} = 8$

(d) $L_T^{RF} = 16$

Figure 3.4 The effective (BB+RF) MIMO TX beampatterns for two users in the LoS scenario.

direction, ensuring that the inter-user interference is canceled, as enforced by the optimization problem in (3.34a)–(3.34d). Another observation is that as L_T^{RF} increases, the beampatterns improve, further canceling the inter-user interference. This happens because the flexibility in optimization increases due to the increased number of variables that can be optimized, i.e., $\mathbf{W}_{T,c}^{BB}$ matrix.

NLoS Scenario

Next, the beampatterns for the NLoS scenario are discussed. Here, $S_{c,u} = 2$, while a separate radar stream is used for each radar direction, totaling six streams. Figure 3.5 depicts the TX RF beampattern for different numbers of RF chains. When $L_T^{RF} = 2$, the four narrow main-beams correspond to communications and radar directions. When $L_T^{RF} = 4$, beams have become wider than in the first case, but still, they are distinctly observed. However, when $L_T^{RF} = 8$ and $L_T^{RF} = 16$, main-beams disappear, and all four directions have almost the same gain. When L_T^{RF} increases, the number of antenna elements connected to a particular RF chain decreases, decreasing the ability to perform beamforming.
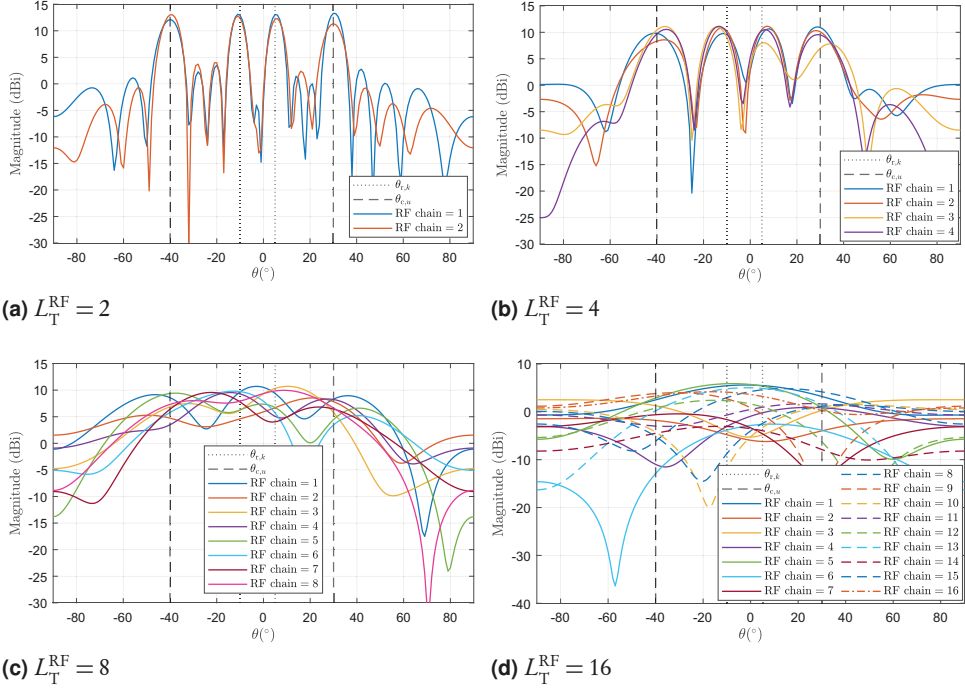
(a) $L_T^{RF} = 2$

(b) $L_T^{RF} = 4$

(c) $L_T^{RF} = 8$

(d) $L_T^{RF} = 16$

Figure 3.5 The MIMO TX RF beampatterns for different RF chains, with $L_T = 32$.

Then, Fig. 3.6 illustrates the effective average TX beampatterns for different ρ values by considering all streams, i.e., communications only - four, radar only - two, and JCAS - six, respectively. As shown in (3.35), ρ controls the gains between the communications and radar directions in the TX RF beampattern, thus also in the effective beampattern.

When $\rho = 0$, only sensing is performed, and the TX beampattern has two main-beams in the radar directions. The gains at communications directions are attenuated by around 20 dB. When $\rho = 1$, only communications to the users are performed without sensing. The beampattern is not directional since it is designed to cancel the inter-user and intra-user interference in NLoS conditions. In addition, gains in the radar directions are attenuated more than 20dB, when compared to the sensing-only case. However, $\rho = 0.5$ denotes a MIMO JCAS system performing both function-alities. In this case, all four directions have almost the same gain, meaning that both types of streams are transmitted in communications and radar directions. As a result, radar–communications interference exists but is canceled at the communications RX when used in conjunction with its combiner.
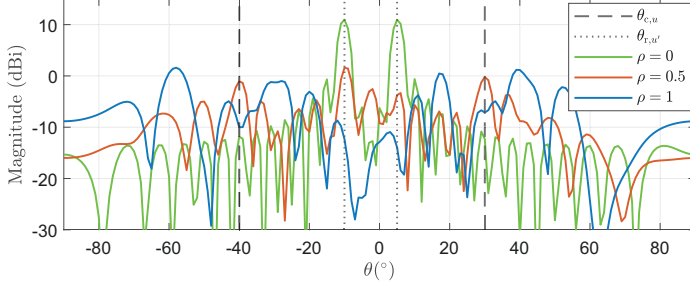
51

Figure 3.6 The effective MIMO TX beampatterns for different ρ values in the NLoS scenario. Since the TX beampatterns depend on the frequency of the OFDM subcarrier, these curves correspond to only a single subcarrier. Depending on the frequency-selective channel, TX beampatterns can vary between subcarriers. Three different beampatterns correspond to: $\rho = 0$ (Sensing-only case), $\rho = 0.5$ (MIMO JCAS case), and $\rho = 1$ (Communications-only case).

Finally, Fig. 3.7 illustrates the RX RF beampattern when $L_{R,r}^{RF} = 8$ and $L_{R,r} = 32$. The RX RF beamforming is designed to receive reflections from the radar directions. A single wide main-beam is observed for each RF chain, since the two radar directions are closer to each other, and four antenna elements connected to a specific RF chain cannot produce very narrow beams. In addition, some RF chains have the same response.
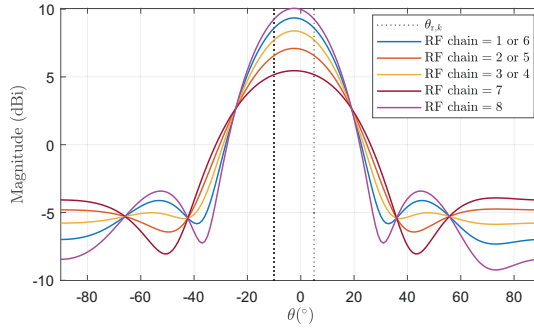

Figure 3.7 The MIMO RX RF beampattern with $L_{R,r} = 32$ RX antennas and $L_{R,r}^{RF} = 8$ RX RF chains.

4

Waveform Optimization for
Single Antenna Systems

This chapter discusses the design of a joint transmit (TX) orthogonal frequency-division multiplexing (OFDM) waveform for single antenna JCAS systems. [1] The waveform design is through an optimization problem where the Cramer–Rao lower bounds (CRLBs) of the range and velocity estimates of the sensing system are minimized while ensuring the communications system's performance is reasonable.

Hence, an overview of radar processing to estimate the range and velocity parameters is discussed. Based on these parameters, the CRLBs are next derived. The waveform optimization methodology is discussed next, which is primarily based on filling the unused subcarriers within the time–frequency grid of the OFDM waveform with optimized samples, which are called *radar subcarriers* after filling. The total TX power is shared between the communications and these radar subcarriers, directly controlling the trade-off between the two functionalities. The analytical solution to the optimization problem is also derived, which shows that only the subcarriers' amplitudes affect the CRLB minimization, not their phases.

Simulation results are next presented using a standard-compliant 5G New Radio (NR) waveform to evaluate the performance improvement due to waveform optimization. They depict that in addition to minimizing the CRLBs, main-lobe widths and peak side-lobe levels (PSLs) of the radar image corresponding to the range and velocity profiles can also be improved. Further, they also illustrate that the OFDM waveform's peak-to-average power ratio (PAPR) can be minimized by separately op-

---

[1]The work presented in this chapter is based on the publications of [**P1**], [**P2**], and [**P3**].
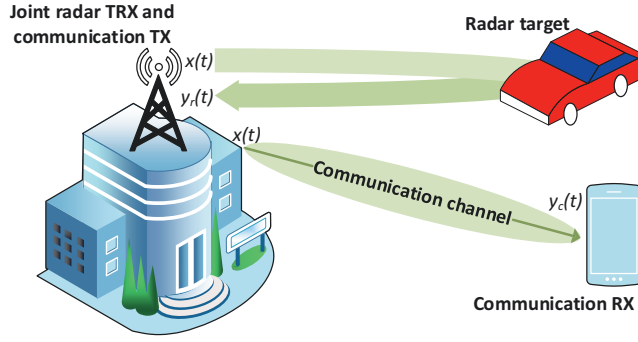
Figure 4.1 The considered single-antenna JCAS system utilizing the same waveform $x(t)$ for communications and sensing.

timizing the phases of the radar subcarriers. Moreover, an optimal trade-off between the two functionalities can be achieved by controlling the power allocation between communications and radar subcarriers. Finally, the optimized waveform is used to experimentally map an outdoor environment, with a JCAS system operating at a mm-wave frequency. The measurement results illustrate that significant performance improvement in the radar map can be obtained in terms of the PSL of the range profile, signifying the validity of the proposed waveform optimization also in a practical scenario.

4.1 OFDM Radar Processing

A monostatic JCAS system is considered as in Fig. 4.1, where both the BS and the communications RX has a single antenna. The transmit OFDM signal $x(t)$ consists of N_c communications subcarriers and N_r radar subcarriers, with $N_c + N_r = NM$. Both data and control subcarriers of the waveform are considered to be communications subcarriers. The frequency-domain samples of communications subcarriers are considered fixed and not modified by waveform optimization. It is assumed that the communications system is not fully loaded, meaning that some subcarriers are empty, and not used as communications subcarriers. Hence, these empty subcarriers can be filled with optimized frequency-domain samples, i.e., *radar subcarriers*, which is the basic premise behind waveform optimization. An important note is that the term *radar subcarriers* is a concept of notation. However, both communications and radar subcarriers are used for radar processing, i.e., all subcarriers of the waveform.

4.1.1 Relation Between TX and RX Symbols

Once the OFDM waveform is transmitted, it is reflected from the targets in the environment and received back at the RX of the BS. The frequency-domain representation of the RX signal can be written using a simplified version of (3.8) for a single-antenna system as

$$y_{n,m} = \sum_{k=1}^{K_t} b_k e^{-j2\pi n \Delta f \tau_k} e^{j2\pi m \frac{f_{D,k}}{\Delta f}} x_{n,m} + v_{n,m}, \tag{4.1}$$

where the TX and RX frequency-domain symbol on the nth subcarrier and m^{th} OFDM symbol are given by $x_{n,m}$ and $y_{n,m}$, respectively. In addition, the TX symbol can either be a communications or radar subcarrier. Moreover, the instantaneous communications and radar power are given by

$$P_r = \sum_{m=1}^{M} \sum_{n \in \mathcal{R}_m} |x_{n,m}|^2 \text{ and } P_c = \sum_{m=1}^{M} \sum_{n \in \mathcal{C}_m} |x_{n,m}|^2, \tag{4.2}$$

respectively, and $P_t = P_c + P_r$ denotes the total instantaneous power. The variables $\mathcal{R}_m$ and $\mathcal{C}_m$ are the subcarrier indices corresponding to radar and communications in the mth OFDM symbol, with $\mathcal{R}_m \cup \mathcal{C}_m = \{n | n \in [1, \ldots, N]\}$.

Re-writing (4.1) for a single radar target can be denoted as

$$y_{n,m} = \underbrace{x_{n,m} e^{-j2\pi n \Delta f \tau} e^{j2\pi m \frac{f_D}{\Delta f}}}_{s_{n,m}} + v_{n,m}, \tag{4.3}$$

where the index k is dropped since one target is considered. Here, the attenuation constant is normalized to unity, and the noise sample is also scaled appropriately. However, separate terms are not introduced for simplicity. Hence, due to the delay and Doppler-shift, the RX frequency-domain symbol's phase changes from that of the TX frequency-domain symbol. Moreover, the delay causes a linear phase-shift between the OFDM subcarriers, while the Doppler-shift introduces a linear phase-shift between OFDM symbols. The expression in (4.3) can then be represented in matrix notation by considering all subcarriers and OFDM symbols as

$$\mathbf{Y} = \mathbf{D}\mathbf{X}\mathbf{B} + \mathbf{V}, \tag{4.4}$$

where $\mathbf{X}$, $\mathbf{Y}$, and $\mathbf{V}$ consist of TX symbols, RX symbols, and noise samples for all the subcarriers and OFDM symbols, respectively, which are of the same size $N \times M$. In addition, $(\mathbf{Y})_{n,m} = y_{n,m}$, $(\mathbf{X})_{n,m} = x_{n,m}$, and $(\mathbf{V})_{n,m} = v_{n,m}$. The matrices $\mathbf{D}$ and $\mathbf{B}$ are diagonal, of sizes $N \times N$ and $M \times M$, respectively. Each diagonal element of these matrices is given by $(\mathbf{D})_{n,n} = D_{n,n} = e^{-j2\pi n \Delta f \tau}$ and $(\mathbf{B})_{m,m} = B_{m,m} = e^{j2\pi m \frac{f_D}{\Delta f}}$.

4.1.2 Maximum Likelihood Estimation

The idea behind radar processing is to estimate the delay and Doppler-shift of a target, which can be denoted as

$$\theta = [\tau, f_D]^T. \tag{4.5}$$

All RX frequency-domain symbols, i.e., communications and radar subcarriers, are used to estimate these parameters based on maximum likelihood estimation (MLE). To perform this, (4.4) is vectorized as

$$\mathbf{y} = \mathbf{s} + \mathbf{v}, \tag{4.6}$$

where $\mathbf{y} = \text{vec}(\mathbf{Y})$, $\mathbf{s} = \text{vec}(\mathbf{DXB})$, and $\mathbf{v} = \text{vec}(\mathbf{V})$ are all vectors of size $NM \times 1$, and $\text{vec}(\cdot)$ denotes the vectorization operation. In addition, the noise vector $\mathbf{v}$ is assumed to have a zero-mean Gaussian distribution, and hence, the likelihood function of the RX symbols' vector can be written as

$$\mathscr{P}_{\mathbf{y}}(\mathbf{y};\theta) = \frac{1}{\det\{\Sigma\}\pi^{NM}} \exp\left(-(\mathbf{y}-\mathbf{s})^H \Sigma^{-1}(\mathbf{y}-\mathbf{s})\right), \tag{4.7}$$

where $\det\{\cdot\}$ denotes the determinant of a matrix. Here, $\Sigma = \sigma_r^2 \mathbf{I}$ represents the covariance matrix of the noise samples, with σ_r^2 denoting the noise variance and $\mathbf{I}$ being the identity matrix. Then, the log-likelihood function can be written as

$$\log \mathscr{P}_{\mathbf{y}}(\mathbf{y};\theta) = -\log\left(\sigma_r^2 \pi^{NM}\right) - \frac{(\mathbf{y}-\mathbf{s})^H(\mathbf{y}-\mathbf{s})}{\sigma_r^2}. \tag{4.8}$$

This log-likelihood function can be further simplified by removing terms that do not depend on the parameter vector θ as

$$\log \mathscr{P}_{\mathbf{y}}'(\mathbf{y};\theta) = \Re\{\mathbf{y}^H \mathbf{s}\}, \tag{4.9}$$

where $\log \mathscr{P}_{\mathbf{y}}'(\mathbf{y}; \theta)$ is the simplified log-likelihood function and $\Re\{\cdot\}$ denotes the real operation. Based on (4.3), this can be written as

$$\log \mathscr{P}_{\mathbf{y}}'(\mathbf{y}; \theta) = \sum_{m=1}^{M} \sum_{n=1}^{N} y_{n,m}^* x_{n,m} e^{-j2\pi n \Delta f \tau} e^{j2\pi m \frac{f_D}{\Delta f}}. \tag{4.10}$$

The variables τ and f_D need to be then quantized as

$$\tau_{n'} = \frac{n'}{N\Delta f}, \; n' \in [1, N], \tag{4.11}$$

$$f_{D\,m'} = \frac{m'\Delta f}{M}, \; m' \in [1, M]. \tag{4.12}$$

The simplified log-likelihood function then becomes

$$\log \mathscr{P}_{\mathbf{y}}'(n', m') = \Re \left\{ \sum_{m=1}^{M} \overbrace{\left(\underbrace{\sum_{n=1}^{N} y_{n,m}^* x_{n,m} e^{\frac{-j2\pi nn'}{N}}}_{\text{element } n' \text{ in } N\text{-length DFT}} \right) e^{\frac{j2\pi mm'}{M}}}^{\text{element } m' \text{ in } M\text{-length IDFT}} \right\}. \tag{4.13}$$

Hence, the simplified log-likelihood function can be obtained through discrete Fourier transform (DFT) and inverse DFT (IDFT) operations. Then, the MLE process can be represented as the maximization of $\log \mathscr{P}_{\mathbf{y}}'(n', m')$ as

$$[n'_{\max}, m'_{\max}]^T = \max_{n', m'} \log \mathscr{P}_{\mathbf{y}}'(n', m'), \tag{4.14}$$

where $n'_{\max}$ and $m'_{\max}$ are the indices that maximize the log-likelihood. Finally, the estimated variables are given by substituting the found indices to (4.11) and (4.12) as

$$\hat{\theta} = [\hat{\tau}, \hat{f}_D]^T = \left[\frac{n'_{\max}}{N\Delta f}, \frac{m'_{\max}\Delta f}{M} \right]^T, \tag{4.15}$$

where $\hat{\theta}$ contains estimated delay and Doppler-shift parameters $\hat{\tau}$ and $\hat{f}_D$, respectively.

4.2 Joint Waveform Design

The goal of a sensing system is to accurately estimate the sensing parameters, i.e., reduced error variances. Based on (4.5) and (4.15), these can be represented as $\text{var}\{\hat{\tau}\} = \mathbb{E}\{(\tau - \hat{\tau})^2\}$ and $\text{var}\{\hat{f}_\text{D}\} = \mathbb{E}\{(f_\text{D} - \hat{f}_\text{D})^2\}$, respectively, where $\text{var}\{\cdot\}$ and $\mathbb{E}\{\cdot\}$ are the variance and expectation operations. Ideally, these variances need to be minimized, but obtaining explicit expressions for them is difficult. However, the lower bounds of these error variances can be calculated explicitly and are given by the Cramer–Rao lower bounds as

$$\text{var}\{\hat{\tau}\} \geq \text{CRLB}(\hat{\tau}), \ \text{var}\{\hat{f}_\text{D}\} \geq \text{CRLB}(\hat{f}_\text{D}), \tag{4.16}$$

where $\text{CRLB}(\hat{\tau})$ and $\text{CRLB}(\hat{f}_\text{D})$ denote the CRLB of the delay and Doppler-shift estimates, respectively. Hence, the waveform is optimized to minimize these theoretical CRLBs, assuming they improve the performance of the sensing system. As shown later in Section 4.3, such improvements are possible.

Therefore, the joint waveform is designed by filling the empty subcarriers within the OFDM time–frequency grid with optimized frequency-domain samples such that they minimize the CRLBs of delay and Doppler-shift estimates. The CRLB expressions are derived in this section, followed by the optimization problem and its solution.

4.2.1 The CRLBs of Sensing Estimates

To calculate the CRLBs, the Fisher information matrix first needs to be calculated [55]. The Appendix A derives the relation between the CRLBs and this Fisher matrix $\mathscr{I}(\theta)$, which is of size 2×2 since only two parameters are estimated. To find the CRLBs of delay and Doppler-shift parameters, the log-likelihood function in (4.8) needs to be substituted to (A.10) to obtain

$$\mathscr{I}(\theta)_{i,j} = \left(\frac{2}{\sigma_\text{r}^2}\right)\Re\left\{\frac{\partial \mathbf{s}^H}{\partial \theta_i}\frac{\partial \mathbf{s}}{\partial \theta_j}\right\} = \frac{2}{\sigma_\text{r}^2}\Re\left\{\mathbf{s}^H\mathbf{D}_{\theta_i}^H\mathbf{D}_{\theta_j}\mathbf{s}\right\}, \tag{4.17}$$

where $i, j \in [1,2]$, and $\mathbf{D}_{\theta_1} = (-j2\pi)\mathrm{diag}(\mathbf{d}_1)$ and $\mathbf{D}_{\theta_2} = (j2\pi)\mathrm{diag}(\mathbf{d}_2)$, respectively. The variables $\mathbf{d}_1$ and $\mathbf{d}_2$ are vectors of size $NM \times 1$. In addition, $\mathbf{d}_1 = [\underbrace{\bar{\mathbf{f}}, \ldots, \bar{\mathbf{f}}}_{M \text{ times}}]^T$ where $\bar{\mathbf{f}} = [-\frac{N}{2}\Delta f, \ldots, (\frac{N}{2}-1)\Delta f]$ contains the frequencies of the subcarriers. Similarly, $\mathbf{d}_2 = [\bar{\mathbf{t}}_{-\frac{M}{2}}, \ldots, \bar{\mathbf{t}}_{\frac{M}{2}-1}]^T$ where $\bar{\mathbf{t}}_m = [\underbrace{\frac{m}{\Delta f}, \ldots, \frac{m}{\Delta f}}_{N \text{ times}}]$. Each element of $\mathscr{I}(\theta)$ is then given by

$$\mathscr{I}(\theta)_{1,1} = 8\pi^2(\mathrm{SNR}_\mathrm{r})(\Delta f)^2 \sum_{m=1}^{M}\sum_{n=1}^{N}\left(n-1-\frac{N}{2}\right)^2 P_{n,m} = 8\pi^2(\mathrm{SNR}_\mathrm{r})(\mathrm{MS}_f),$$
(4.18a)

$$\mathscr{I}(\theta)_{1,2} = \mathscr{I}(\theta)_{2,1} = -8\pi^2(\mathrm{SNR}_\mathrm{r})\sum_{m=1}^{M}\sum_{n=1}^{N}\left(n-1-\frac{N}{2}\right)\left(m-1-\frac{M}{2}\right)P_{n,m}$$
(4.18b)

$$= -8\pi^2(\mathrm{SNR}_\mathrm{r})(\mathrm{MS}_{f,t}),$$

$$\mathscr{I}(\theta)_{2,2} = 8\pi^2(\mathrm{SNR}_\mathrm{r})\frac{1}{(\Delta f)^2}\sum_{m=1}^{M}\sum_{n=1}^{N}\left(m-1-\frac{M}{2}\right)^2 P_{n,m} = 8\pi^2(\mathrm{SNR}_\mathrm{r})(\mathrm{MS}_t),$$
(4.18c)

where $P_{n,m} = \frac{|x_{n,m}|^2}{P_\mathrm{t}}$, $\mathrm{SNR}_\mathrm{r} = \frac{P_\mathrm{t}}{\sigma_\mathrm{r}^2}$, and the variables MS_f, MS_t and $\mathrm{MS}_{f,t}$ are the mean square bandwidth, time, and bandwidth–time parameters of the waveform, respectively.

As mentioned in Appendix A, the CRLBs are given by the diagonal elements of $\mathscr{I}^{-1}(\theta)$, and since $\mathscr{I}(\theta)$ is a 2×2 matrix, $\mathscr{I}^{-1}(\theta)$ can be easily calculated to find the two CRLBs as

$$\mathrm{CRLB}(\hat{\tau}) = \frac{\mathscr{I}(\theta)_{2,2}}{\mathscr{I}(\theta)_{1,1}\mathscr{I}(\theta)_{2,2} - \mathscr{I}(\theta)_{1,2}^2}, \quad \mathrm{CRLB}(\hat{f}_\mathrm{D}) = \frac{\mathscr{I}(\theta)_{1,1}}{\mathscr{I}(\theta)_{1,1}\mathscr{I}(\theta)_{2,2} - \mathscr{I}(\theta)_{1,2}^2},$$
(4.19)

and hence can be represented as

$$\mathrm{CRLB}(\hat{\tau}) = \frac{1}{8\pi^2(\mathrm{SNR}_\mathrm{r})f(\mathbf{P})}, \mathrm{CRLB}(\hat{f}_\mathrm{D}) = \frac{1}{8\pi^2(\mathrm{SNR}_\mathrm{r})g(\mathbf{P})}, \qquad (4.20)$$

where

$$f(\mathbf{P}) = (\mathrm{MS}_f) - \frac{(\mathrm{MS}_{f,t})^2}{(\mathrm{MS}_t)} \tag{4.21a}$$

$$= (\Delta f)^2 \sum_{m=1}^{M} \sum_{n=1}^{N} \left(n - 1 - \frac{N}{2} \right)^2 P_{n,m}$$

$$- \frac{\left(\sum_{m=1}^{M} \sum_{n=1}^{N} \left(n - 1 - \frac{N}{2} \right) \left(m - 1 - \frac{M}{2} \right) P_{n,m} \right)^2}{\frac{1}{(\Delta f)^2} \sum_{m=1}^{M} \sum_{n=1}^{N} \left(m - 1 - \frac{M}{2} \right)^2 P_{n,m}},$$

$$g(\mathbf{P}) = (\mathrm{MS}_t) - \frac{(\mathrm{MS}_{f,t})^2}{(\mathrm{MS}_f)}. \tag{4.21b}$$

Interestingly, it can be noted that the two CRLBs are independent of the corresponding parameters being estimated.

4.2.2 Optimization Problem and Solution

As observed from (4.20)–(4.21b), the CRLBs depend on $P_{n,m}$, i.e., the powers of the subcarriers, or their amplitudes, and not their phases. Hence, the amplitudes of the radar subcarriers can be optimized to minimize the CRLBs. In addition, radar subcarriers' phases can be separately optimized to improve some other metric, where here, it is chosen as the PAPR of the waveform. Hence, amplitude optimization is first discussed, followed by the phase optimization of radar subcarriers.

Amplitude Optimization   The optimization problem is given as

$$\min_{P_{n,m}, \mathcal{R}_m} \mathrm{CRLB}(\hat{\tau}) \tag{4.22a}$$

subject to

$$\mathrm{CRLB}(\hat{f}_\mathrm{D}) \le \phi, \tag{4.22b}$$

$$P_\mathrm{r} \le P_\mathrm{t} - P_\mathrm{c}, \tag{4.22c}$$

$$0 \le P_{n,m} \le P_\mathrm{max}, \; n \in \mathcal{R}_m, \forall m. \tag{4.22d}$$

Hence, the goal of the optimization problem is to minimize $\mathrm{CRLB}(\hat{\tau})$ while constraining $\mathrm{CRLB}(\hat{f}_{\mathrm{D}})$ to be lower than some value ϕ, which can vary depending on the application. The total power allocated to all radar subcarriers is constrained by P_{r}, while also limiting the maximum power allocated to a single radar subcarrier by P_{max}. It should be noted that amplitude optimization modifies only the powers of the radar subcarriers, whereas those of the communications subcarriers are unaltered and considered to be given.

Depending on the chosen P_{max}, there are $N_{\mathrm{act}} = \lceil \frac{P_{\mathrm{r}}}{P_{\mathrm{max}}} \rceil$ activated radar subcarriers, where $\lceil \cdot \rceil$ denotes the ceiling operation. Here it is assumed that $N_{\mathrm{act}} \ll N_{\mathrm{r}}$. Hence, $N_{\mathrm{act}} - 1$ radar subcarriers are activated with power P_{max} while a single radar subcarrier receives a power of $P_{\Delta} = P_{\mathrm{r}} - P_{\mathrm{max}}(N_{\mathrm{act}} - 1)$ due to the ceiling operation. Once this power allocation for the activated radar subcarriers is known, it is then necessary to identify their indices in each OFDM symbol $\mathscr{R}_{m,\mathrm{act}}$ out of all possible radar subcarrier indices $\mathscr{R}_m$.

The solution to the joint optimization problem is derived in [**P1**], where first using the power allocation to any set of activated radar subcarrier indices, results in the $\mathrm{CRLB}(\hat{\tau})$ value as given by

$$\mathrm{CRLB}(\hat{\tau}) = \frac{\phi}{(\Delta f)^4} \frac{\mathrm{NUM_c} + P_{\mathrm{max}} \sum_{m=1}^{M} \sum_{n \in \mathscr{R}_{m,\mathrm{act}}} \left(m - 1 - \frac{M}{2}\right)^2 + \left(L - 1 - \frac{M}{2}\right)^2 P_{\Delta}}{\mathrm{DEN_c} + P_{\mathrm{max}} \sum_{m=1}^{M} \sum_{n \in \mathscr{R}_{m,\mathrm{act}}} \left(n - 1 - \frac{N}{2}\right)^2 + \left(K - 1 - \frac{N}{2}\right)^2 P_{\Delta}},$$

(4.23)

where the contribution from the communications subcarriers is represented by

$$\mathrm{NUM_c} = \sum_{m=1}^{M} \sum_{n \in \mathscr{C}_m} \left(m - 1 - \frac{M}{2}\right)^2 P_{n,m},$$

(4.24)

$$\mathrm{DEN_c} = \sum_{m=1}^{M} \sum_{n \in \mathscr{C}_m} \left(n - 1 - \frac{N}{2}\right)^2 P_{n,m},$$

(4.25)

while $\{K, L\}$ are the subcarrier and OFDM symbol indices of the single radar subcarrier receiving power P_{Δ}.

The next task is to find the indices of the optimal radar subcarriers that are activated. Since there are N_{r} possible indices for only N_{act} activated radar subcarriers, there are $\binom{N_{\mathrm{r}}}{N_{\mathrm{act}}}$ possibilities which result in a massive search space. Hence, to reduce

the complexity, the activated radar subcarrier indices of the separate minimization of the CRLBs of delay and Doppler-shift estimates are used. These separate minimization problems are given as

(a) $\min\limits_{\mathscr{R}_m} \text{CRLB}(\hat{\tau})$, $\forall m$,   (b) $\min\limits_{\mathscr{R}_m} \text{CRLB}(\hat{f}_\text{D})$, $\forall m$.

Since the power allocation is already found and only the optimal indices are needed, $\mathscr{R}_m$ is the only optimization variable in the separate minimization problems. Therefore, for these two separate optimization problems when only a single parameter needs to be estimated, the Fisher matrix reduces into a scalar, i.e., (4.18a) and (4.18c), and the corresponding CRLBs can be given as

$$\text{CRLB}_\text{sep}(\hat{\tau}) = \frac{1}{\mathscr{I}(\theta)_{1,1}} = \frac{1}{8\pi^2(\text{SNR}_\text{r})(\text{MS}_f)}, \qquad (4.26)$$

$$\text{CRLB}_\text{sep}(\hat{f}_\text{D}) = \frac{1}{\mathscr{I}(\theta)_{2,2}} = \frac{1}{8\pi^2(\text{SNR}_\text{r})(\text{MS}_t)}, \qquad (4.27)$$

where $\text{CRLB}_\text{sep}(\hat{\tau})$ and $\text{CRLB}_\text{sep}(\hat{f}_\text{D})$ are the corresponding CRLB values when separate minimizations of the two estimates are performed. Then, either MS_f or MS_t needs to be maximized for $\text{CRLB}_\text{sep}(\hat{\tau})$ or $\text{CRLB}_\text{sep}(\hat{f}_\text{D})$ minimization, respectively. This means that for minimum $\text{CRLB}_\text{sep}(\hat{\tau})$, the edge-most N_act radar subcarriers in the frequency spectrum need to be activated (4.18a). In contrast, for minimum $\text{CRLB}_\text{sep}(\hat{f}_\text{D})$, radar subcarriers at the edges of the time-domain signal are activated (4.18c).

To find the activated radar subcarriers for the joint optimization in (4.22a)–(4.22d), the radar subcarriers are divided into two groups; one for minimizing $\text{CRLB}(\hat{\tau})$ or maximizing MS_f, while the other group minimizes $\text{CRLB}(\hat{f}_\text{D})$ or maximizes MS_t. Denoting $N_\text{act,1}$ and $N_\text{act,2}$ as the number of radar subcarriers for either minimization with $N_\text{act,1} + N_\text{act,2} = N_\text{act}$, $N_\text{act,1}$ radar subcarriers having highest frequencies are activated while simultaneously activating $N_\text{act,2}$ radar subcarriers at the edge-most OFDM symbols. Moreover, $N_\text{act,1}$ and $N_\text{act,2}$ can be decided based on the required CRLB trade-off between either estimate, as depicted later in Section 4.3.

Due to the complexity of the amplitude optimization problem in (4.22a)–(4.22d), a two-fold approach is used to derive the solution. Firstly, the power allocation for the activated radar subcarriers is found. Once the powers are known, indices of the activated radar subcarriers are found. For this, the minimum $\text{CRLB}_\text{sep}(\hat{\tau})$ in (4.26) is used as the starting point. Hence, N_act radar subcarriers at the edges of the fre-

quency spectrum are first activated. Next, depending on the portion of activated radar subcarriers dedicated for $\text{CRLB}(\hat{f}_D)$ minimization, $N_{\text{act},2}$ activated radar subcarriers from the edges of the frequency spectrum are moved iteratively to the edges of the time-domain signal, i.e., OFDM symbols. If all the N_{act} radar subcarriers are moved from the edges of the frequency spectrum to the edges of the time-domain signal, it results in the waveform with minimum $\text{CRLB}_{\text{sep}}(\hat{f}_D)$ in (4.27).

However, the solution obtained through this two-fold approach could be suboptimal w.r.t. the global optimum. Nevertheless, the approach adopted here is of low complexity in comparison to the brute-force approach to finding the global optimum. In addition, the simulation and experimental results discussed in Section 4.3 illustrate that the solution obtained through the two-fold approach results in comprehensive gains for sensing, indicating the sufficiency of the adopted low-complex approach.

Phase Optimization Since the phases of the activated radar subcarriers do not contribute to the minimization of the CRLBs, they can be separately optimized to improve any performance metric of either communications or sensing. Since the PAPR of OFDM waveforms is considered a drawback in communications, phase optimization is considered for PAPR minimization. Defining the PAPR of the mth OFDM symbol as

$$\text{PAPR}_m = 10 \log_{10} \frac{\max\{|x_{m,1}|^2, \cdots, |x_{m,A}|^2\}}{\frac{1}{A} \sum_{a=1}^{A} |x_{m,a}|^2}, \tag{4.28}$$

where $x_{m,a}$ denotes the ath time-domain sample for the mth OFDM symbol, A is the total number of time-domain samples for the mth OFDM symbol, and $\max\{\cdot\}$ is the maximum operation. Then, the unconstrained optimization problem is given as

$$\min_{\zeta_m} \text{PAPR}_m, \tag{4.29}$$

where ζ_m is the set of phases of the activated radar subcarriers in the mth OFDM symbol. Here, the selective mapping (SLM) algorithm is used, where random phases are allocated for the activated radar subcarriers, and the PAPR is calculated. This is performed for many random realizations, and the phases resulting in the minimum PAPR are chosen to be the optimum.
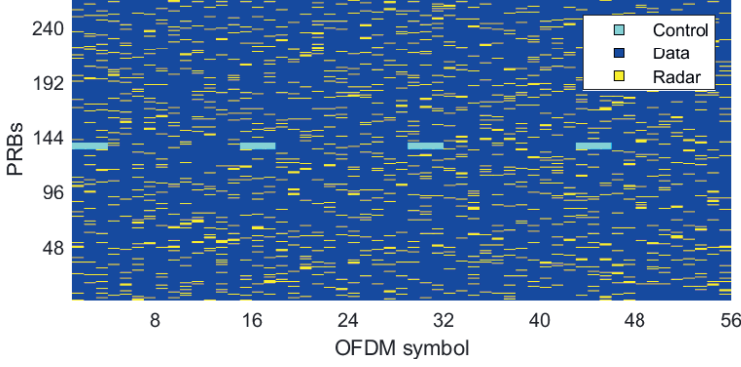
Figure 4.2 The considered 5G NR waveform with $\alpha = 90\%$.

4.3 Performance of the Joint Waveform

This section evaluates the JCAS performance of the optimized waveform. Simulation results are separately presented for sensing and communications performance, and then RF measurement results show the validity of waveform optimization on sensing performance improvement.

4.3.1 Simulation Results

A 5G NR waveform is considered with $M = 560$, $\Delta f = 120$ kHz, 264 physical resource blocks (PRBs) that result in $N = 3168$ with a bandwidth of 400 MHz, $f_c = 28$ GHz, $P_t = 30$ dBm, and a total time-duration of 5 ms. Here, the separation between communications and radar subcarriers is quantified through $\alpha = \frac{N_c}{NM}\%$, which is the loading percentage of the communications subcarriers in the waveform. An example of such a waveform is given in Fig. 4.2 for $\alpha = 90\%$. The control PRBs are at fixed locations, while data and radar PRBs are uniformly distributed throughout the OFDM waveform. It should be noted that communications PRBs encompass both data and control PRBs. In addition, a set of 12 radar subcarriers (one radar PRB) is contiguous in the frequency domain, but two sets of radar PRBs can be contiguous or non-contiguous, depending on the locations of the data PRBs.

Sensing Performance First, the effect of amplitude optimization on root CRLB minimization of delay and velocity estimates is depicted in Fig. 4.3. In addition, Figs.

4.3(a) and 4.3(b) correspond to two ΔPSD values, 3 dB and 1 dB, respectively, where ΔPSD indicates power spectral density (PSD) difference between a communications and radar subcarrier. It can be observed that a decrease of α decreases both CRLBs since it increases the number of available radar subcarriers, thereby improving the sensing performance. In addition, as the percentage of activated radar subcarriers for MS_f maximization decreases, the CRLB of range increases while decreasing the CRLB of velocity. This is because maximizing MS_f improves the CRLB of range while maximizing MS_t improves the CRLB of velocity. In essence, Fig. 4.3 depicts the inherent trade-off between the two estimates, where the CRLB of one can be improved at the cost of the other.

Moreover, it can be observed that optimizing the waveform allows for minimizing the CRLBs from that of the unoptimized waveform. In the unoptimized waveform, there are empty subcarriers, but they are not filled with any samples, and the total TX power is used only for the communications subcarriers. The variable α for the unoptimized waveform means how much of the waveform is filled with communications subcarriers. Considering the highlighted area in Fig. 4.3(a), it is clear that increasing ΔPSD allows a decrease in the CRLBs. An increase of ΔPSD implies an increase of $P_{\max}$ and thus a decrease of N_{act} since $N_{\text{act}} = \lceil \frac{P_{\text{r}}}{P_{\max}} \rceil$, which allows to maximize MS_f or MS_t as necessary, and therefore decreasing the CRLBs.

Simulations are then performed to evaluate the sensing performance. A point target is placed at a specific range with some velocity, and radar processing is performed at the radar RX to estimate the sensing parameters. Once they are estimated, the main-lobe width and PSL of the target in both range and velocity profiles are calculated. This process is performed for many iterations, and the average values are plotted in Fig. 4.4 where Fig. 4.4(a) corresponds to the main-lobe width while Fig. 4.4(b) illustrates the PSL. The main-lobe width is calculated as the null-to-null length of the main-lobe corresponding to the target. The PSL is defined as the difference between the target peak and the next peak within 40 samples. Hence, a low value for the main-lobe width and a high value for the PSL are important for improved sensing performance. Note that the definition of PSL differs from classical radar literature, where it is defined as the level of the second-highest peak. Thus, a low value for PSL implies low side-lobes, different from the definition adopted in the thesis.

The main-lobe width of the range profile decreases when α decreases or the percentage of radar subcarriers for MS_f increases, which maximizes MS_f, thereby nar-
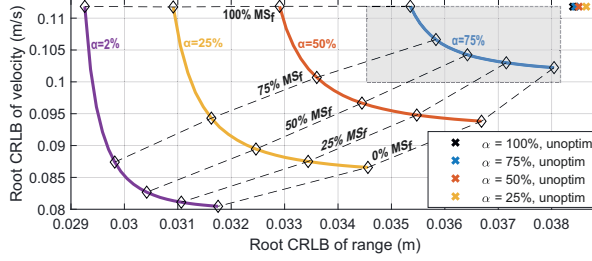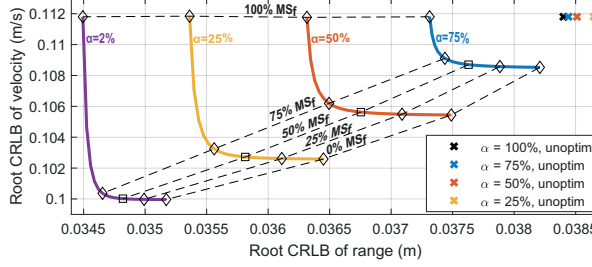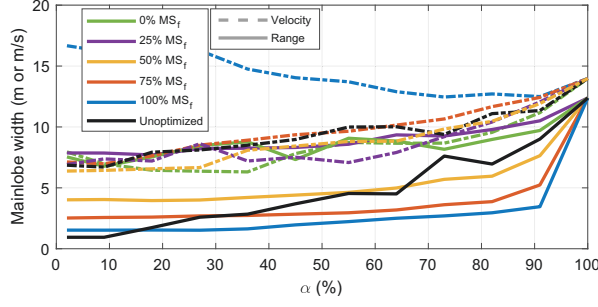
(a) ΔPSD $= 3$ dB


(b) ΔPSD $= 1$ dB

Figure 4.3 The root CRLBs of range and velocity estimates for different α values and percentages of activated radar subcarriers for MS$_f$ maximization. Figure (a) corresponds to ΔPSD $= 3$ dB and (b) for ΔPSD $= 1$ dB. The highlighted area in (a) represents the area occupied by (b).

rowing the target in the range profile. Similarly, a decrease in the percentage of radar subcarriers for MS$_f$ (or increasing that for MS$_t$) decreases the main-lobe width in the velocity profile. This observation is due to the increase of MS$_t$, which narrows the target in the velocity profile. Therefore, waveform optimization narrows the target in both domains, reducing errors in estimation. Moreover, the range or velocity profile's main-lobe width can be lowered than that of the unoptimized waveform for certain combinations of α and percentage of radar subcarriers for MS$_f$.

However, regarding the PSL of the two profiles, an opposite behavior to the main-lobe width is observed. Hence, when α decreases or radar subcarriers for MS$_f$ increase, the PSL in the range profile decreases. When either happens, more radar power is allocated to the edges of the frequency spectrum (an increase of MS$_f$), increasing the ambiguity in range estimation. Similarly, when radar subcarriers for MS$_t$ increase, the PSL in the velocity profile decreases., which is due to the ambiguity in velocity estimation because of the MS$_t$ maximization. Regardless of these variations, the PSL can be higher than the unoptimized waveform in both profiles by appropriately choosing the parameters.

66
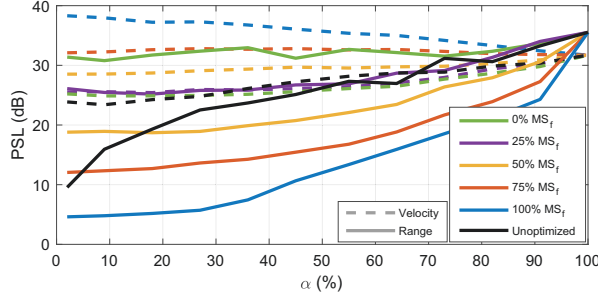
(a) Main-lobe width

(b) Peak side-lobe level

Figure 4.4 The main-lobe width and PSL of the target in range and velocity profiles for $\Delta\mathrm{PSD} = 3$ dB.

Hence, allocating more power to the edges of the frequency spectrum decreases the main-lobe width of the range profile but at the cost of increased PSL. Similarly, allocating more power to the edge OFDM symbols in the time domain decreases the main-lobe width of the velocity profile while increasing its PSL. However, by choosing the optimization parameters, main-lobe width or PSL of either profile can be improved when compared with the default unoptimized 5G waveform.

For the same target ranges and velocities where the main-lobe width and PSL are calculated, the root mean square errors (RMSEs) are also calculated for the range and velocity estimates, and these are shown in Fig. 4.5. It can be observed that optimizing the waveform also allows for minimizing these errors compared with the unoptimized waveform's errors. This improvement is visible in the range estimate than the velocity estimate.

Therefore, these results illustrate that although the waveform is optimized based on a theoretical bound, i.e., CRLB, it also improves the sensing performance for a practical scenario in terms of the main-lobe width, PSL, and the RMSE, indicating the feasibility of the waveform optimization.
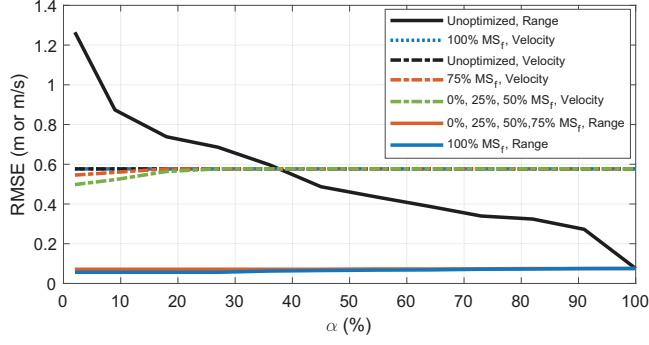
Figure 4.5 The RMSEs of range and velocity estimates when $\Delta\text{PSD} = 3$ dB.

Communication Performance Figure 4.6 shows how optimizing the activated radar subcarriers' phases minimizes the waveform's PAPR, where Figs. 4.6(a) and 4.6(b) are when $\Delta\text{PSD} = 3$ dB and $\Delta\text{PSD} = 1$ dB, respectively. In both figures, *unoptimized phases* correspond to the waveforms where the amplitudes and indices of the activated radar subcarriers are optimized to minimize the CRLBs. However, the phases are uniformly distributed in $[0, 2\pi]$, and not optimized. In contrast, in the *optimized phases* curves, the phases of the activated radar subcarriers are further optimized for PAPR minimization. Here, a set of random phases for the SLM algorithm is further optimized numerically using *fmincon* function in the optimization toolbox of MATLAB. This optimization is done for multiple realizations of random phases, and the set with the minimum PAPR is chosen as the optimum.

In general, for both *unoptimized* and *optimized* phases curves, decreasing the percentage of radar subcarriers for MS_f and increasing ΔPSD tend to increase the PAPR. When either of these happens, the number of activated radar subcarriers in the edge OFDM symbols increases and they are allocated more power. Hence, more radar power is pushed to the edge time-domain OFDM symbols compared to the center OFDM symbols. Therefore, the peak power of edge OFDM symbols increases, although the time-domain signal's mean power remains constant. Using (4.28), it becomes intuitive that the PAPR increases in these OFDM symbols, increasing the PAPR of the whole waveform. However, optimizing the phases of the activated radar subcarriers allows for a decrease in the PAPR. Moreover, the PAPR can be even minimized than that of the *unoptimized* waveform when $50\% < \alpha < 100\%$ for the $\Delta\text{PSD} = 3$ dB scenario whereas, for $\Delta\text{PSD} = 1$ dB, the PAPR can always be made lower than the unoptimized waveform.
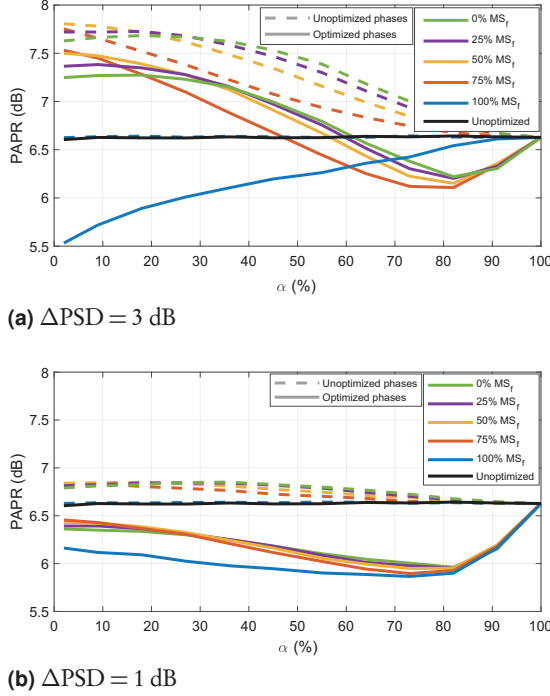
(a) $\Delta\text{PSD} = 3$ dB

(b) $\Delta\text{PSD} = 1$ dB

Figure 4.6 The PAPR of the optimized waveform for different α and percentages of activated radar sub-carriers for MS_f maximization. The figure (a) corresponds to when $\Delta\text{PSD} = 3$ dB and (b) when $\Delta\text{PSD} = 1$ dB.
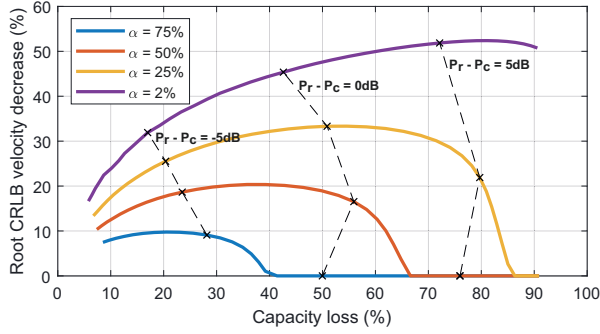
To evaluate the communications performance, a user's capacity is calculated for a multipath channel with a free-space path loss of 121.4 dB and RX noise power of -87.1 dBm. For the single-antenna system considered here, instantaneous capacity can be given based on a simplified version of (3.23) as

$$\bar{\zeta}_\text{c} = \sum_{m=1}^{M}\sum_{n=1}^{N}\log_2\left\{1 + \frac{P_\text{c}}{MN\sigma_\text{c}^2}|\mathbf{h}_{\text{c},n,m}|^2\right\}. \tag{4.30}$$

Since activated radar subcarriers are allocated a proportion of total TX power that would otherwise be fully utilized by communications subcarriers, there is an inherent trade-off between the two functionalities dependent on this power allocation. To visualize this relation, $P_\text{r} - P_\text{c}$ is varied between -10 dB and 10 dB and Fig. 4.7 illustrates these results. Here, Figs. 4.7(a) and 4.7(b) are when the waveform is separately optimized for $\text{CRLB}(\hat{\tau})$ and $\text{CRLB}(\hat{f}_\text{D})$, i.e., $\text{CRLB}_\text{sep}(\hat{\tau})$ in (4.26) and $\text{CRLB}_\text{sep}(\hat{f}_\text{D})$ in (4.27), respectively. The capacity loss/decrease of CRLBs indicates the reduction
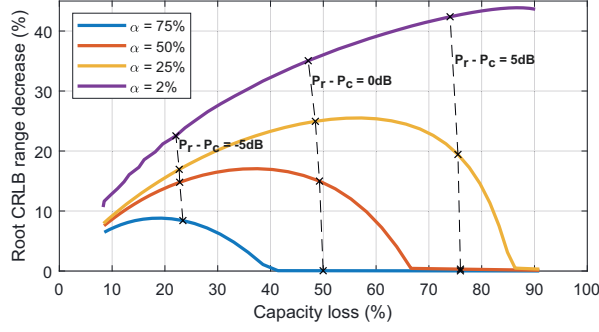
(a) Trade-off between communications capacity and root CRLB($\hat{\tau}$), when $MS_f = 100\%$

(b) Trade-off between communications capacity and root CRLB($\hat{f}_D$), when $MS_t = 100\%$

Figure 4.7 The relation between the communications and sensing performance for different α and $P_r - P_c$ values, for $\Delta PSD = 3$ dB.

in capacity/improvement in the CRLBs, compared to the unoptimized case, where the total TX power is used for communications subcarriers.

Capacity decreases as $P_r - P_c$ increases due to the decrease of P_c, reducing the power allocated to the communications subcarriers. Further, as α decreases, sensing performance can be improved, but the communications performance decreases, understandably due to the power allocation. Moreover, as $P_r - P_c$ increases, CRLBs become better at the cost of reduced capacity, but once they reach a maximum, improvements decrease. Depending on α, a specific number of empty subcarriers can be filled as radar subcarriers. For a certain P_r, if $N_{act} > N_r$, a residual power of $P_r - P_{max}(N_r - 1) - P_\Delta$ is given back to communications subcarriers. Hence, this reduces the improvement of the CRLBs. However, power allocation $P_r - P_c$ can be varied to obtain the required trade-off between the two functionalities.

Figure 4.8 Outdoor environment with static reference targets.

4.3.2 Experimental Outdoor Mapping

To validate the feasibility of waveform optimization in a practical scenario, an outdoor environment is mapped using optimized and unoptimized 5G NR waveforms. The environment is first modeled through simulations to observe the effects of waveform optimization, which are later compared with actual measurements. The waveform parameters are similar to those discussed in Section 4.3.1. Since the chosen environment has static targets, only $M = 20$ OFDM symbols are used with $\Delta\text{PSD} = 3$ dB, and 100% of activated radar subcarriers for MS_f maximization.

   Figure 4.8 shows the outdoor environment with four reference areas highlighted, with A representing a tall building, B representing a wall and a grassy surface, C indicating a set of buildings, and D showing bicycles with metallic structures nearby, respectively. These four areas are also highlighted in the obtained mapping results for comparison. Figure 4.9 shows the used measurement setup. A vector signal transceiver (VST) at 3.2 GHz performs TX and RX processing. The TX signal at 3.2 GHz is up-converted to a mm-wave frequency using a mixer functioning at 24.5 GHz, making $f_c = 27.7$ GHz. A similar mixer is used for down-conversion. Two horn antennas are used for the TX and RX. They both have a 3-dB beamwidth of 17° and a gain of 20 dBi. The horn antennas are mechanically rotated between 5° and 85°. For each angle, the waveform is transmitted (either unoptimized or optimized). The received reflections are used to obtain a single range profile by coherently combining the range profiles of multiple OFDM symbols. Combining range profiles for all angles results in the range–angle map of the environment.
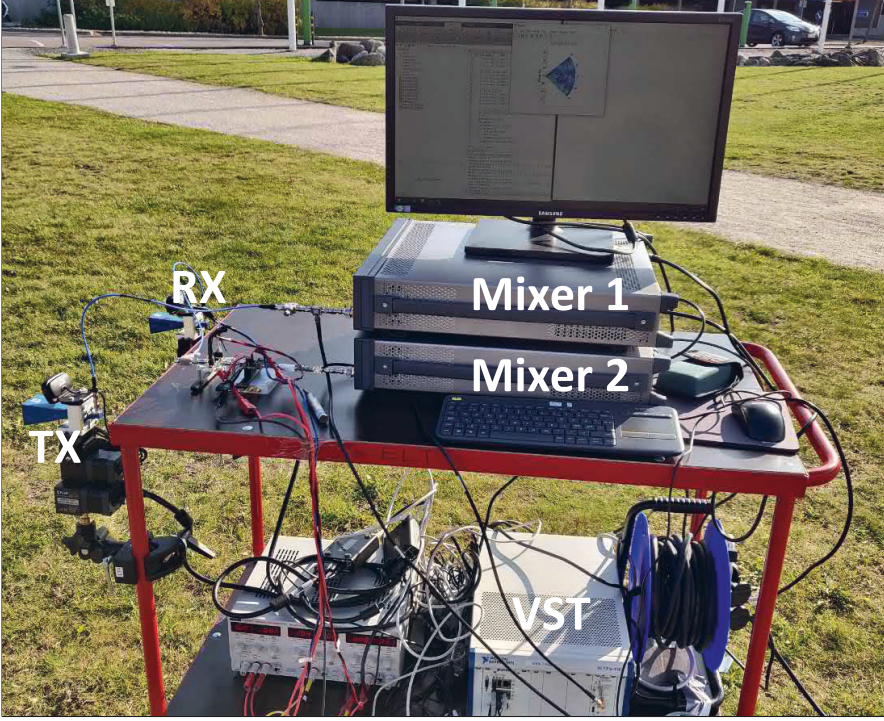
Figure 4.9 The measurement setup.

Figure 4.10 first illustrates the single range profile obtained at an angle of 20° with $\alpha = 25\%$ with both the unoptimized and optimized waveforms. That angle is selected since only target D is in that direction, while the contributions from other targets are also minor. The range profiles from simulations in Fig. 4.10(a) illustrate that both unoptimized and optimized waveforms have some peaks corresponding to target D. However, for the other ranges, optimized waveform results in lesser side-lobes than the unoptimized waveform. A similar phenomenon is also noticed through the range profile obtained experimentally, as depicted in Fig. 4.10(b).

The mapping results are next shown in Fig. 4.11 for both the simulation and experimental results. The figures in each column correspond to a different α value. In addition, the first two rows are with the unoptimized waveform for simulation and experimental results, respectively. Similarly, the bottom two rows are with the optimized waveform for simulation and experimental results, respectively. The targets A, B, C, and D in Fig. 4.8 are indicated in Fig. 4.11(l) for comparison.
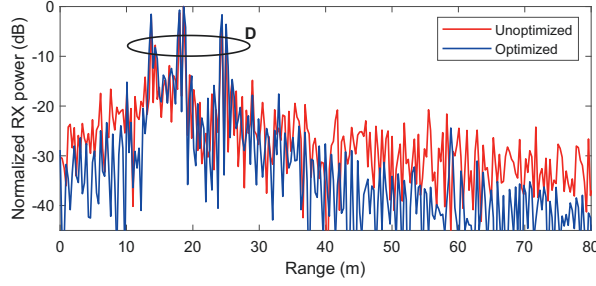
(a) Range profile, simulation
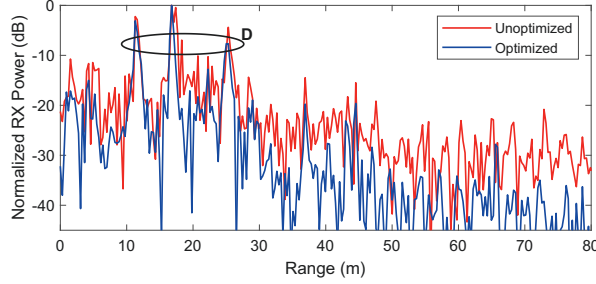
(b) Range profile, experimental

Figure 4.10 Range profile along $20°$ for both simulation and experimental results with the unoptimized and optimized waveforms ($\alpha = 25\%$).

When the unoptimized waveform is used, side-lobes increase as α decreases. This effect is observed between Figs. 4.11(a) and 4.11(c) for the simulation results while between Figs. 4.11(d) and 4.11(f) for the experimental results. This is because as α decreases, the number of empty subcarriers in the waveform increases, although the TX power is the same. Then, when the waveform is optimized, the range–angle map has lesser side-lobes when compared with the one from the unoptimized waveform for the same α. This is distinctively observed between Figs. 4.11(a) and 4.11(g) for the simulations, while between Figs. 4.11(d) and 4.11(j) for the experimental results. Therefore, optimizing the waveform reduces the side-lobes of the obtained range–angle map.
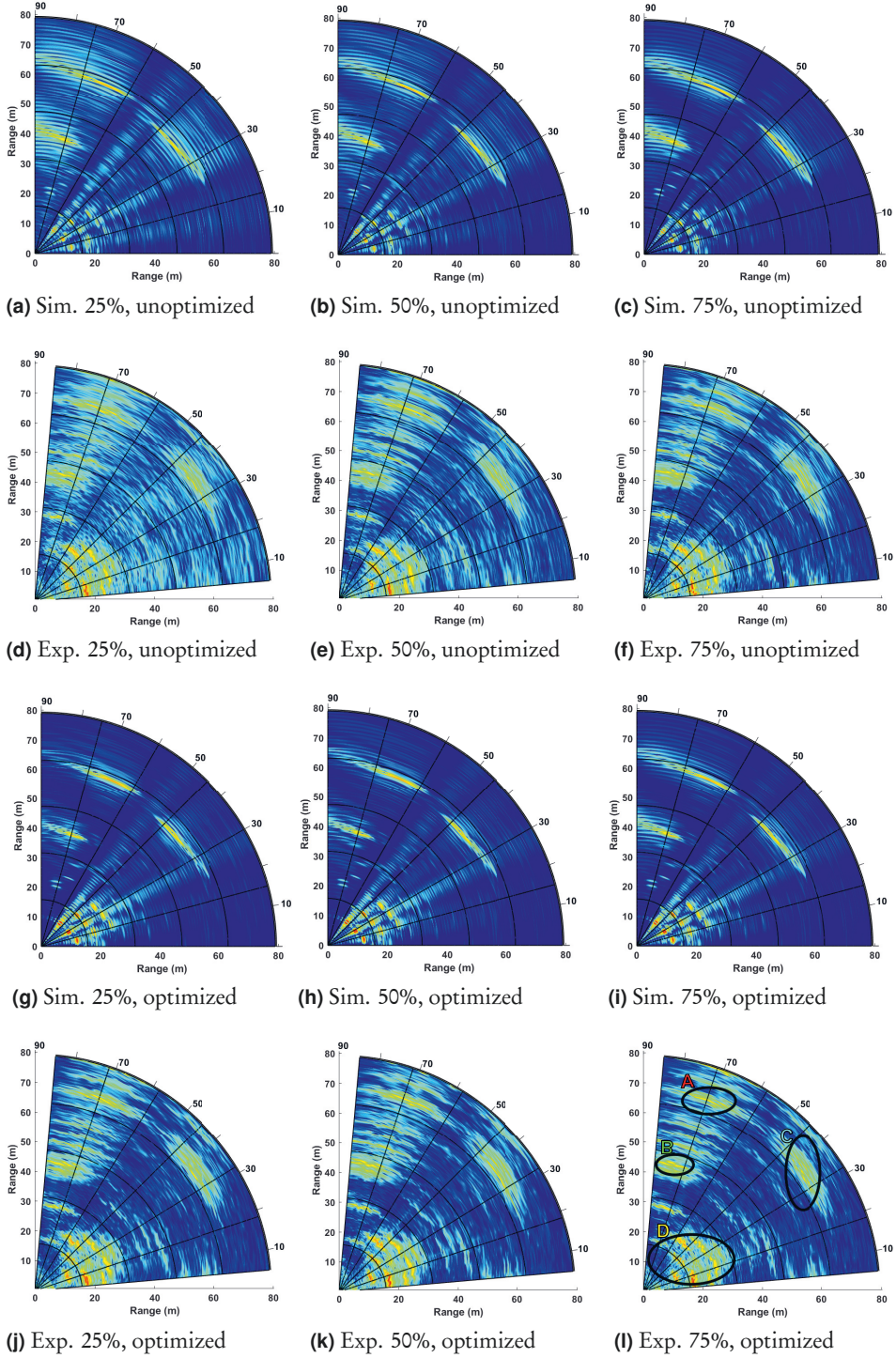
(a) Sim. 25%, unoptimized **(b)** Sim. 50%, unoptimized **(c)** Sim. 75%, unoptimized

(d) Exp. 25%, unoptimized **(e)** Exp. 50%, unoptimized **(f)** Exp. 75%, unoptimized

(g) Sim. 25%, optimized **(h)** Sim. 50%, optimized **(i)** Sim. 75%, optimized

(j) Exp. 25%, optimized **(k)** Exp. 50%, optimized **(l)** Exp. 75%, optimized

Figure 4.11 Outdoor mapping results for different α values for the simulation and experimental results.

5

Waveform Optimization for Multiple Antenna Systems

This chapter focuses on performing JCAS for MIMO systems.[1] Here, communications and sensing functionalities use their own TX streams. Therefore, total TX power is shared between the communications and sensing streams, due to which the trade-off between the two functionalities is observed. To improve the sensing performance, samples of the sensing streams are optimized to improve some metric of performance. Hence, in the thesis, two different strategies for this are discussed.[2]

The system model used for the first strategy is discussed extensively in Section 3.2 under *NLoS scenario*, where a hybrid analog–digital MIMO communications TRX is used for sensing. Hence, the conventional properties of the MIMO radar cannot anymore be used for super-resolution in direction-of-arrival (DoA) estimation. As discussed in Section 2.3.2, these are the fully-digital architecture and orthogonal TX signals. In addition, radar processing becomes complicated due to multiple TX streams. Taking these limitations into consideration, a novel methodology is discussed in this chapter to obtain range–angle and range–velocity maps of the sensed environment. Moreover, performance is improved by optimizing the samples of the sensing streams to minimize the CRLBs of range and DoA estimates.

The second strategy for improving sensing performance involves enhancing the ambiguity function (AF) of a MIMO system with fully-digital architecture. Typically, a thumbtack shape is sought in the conventional delay-Doppler AF, which is

---

[1]This chapter consists mainly of the works presented in [**P4**], [**P5**], [**P6**], and [**P7**].
[2]Most of the variables and equations of this chapter are used directly from Chapter 3.

two-dimensional (2-D). However, the MIMO AF, which is four-dimensional (4-D), ideally needs to have a thumbtack shape also in all of these dimensions, and it is discussed next.

This chapter concludes with simulation results of the proposed methodologies. They contain the radar processing to obtain the range–angle and range–velocity maps of the environment for the two scenarios discussed in Section 3.2 with different beamforming designs. Further results illustrate the performance improvement due to sensing streams' optimization using CRLB minimization, which enhances the receiver operating characteristics (ROC) of sensing and decreases root mean square errors (RMSEs) of range and DoA estimates. In addition, communications capacity can also be controlled, illustrating the importance of varying the optimization variables to obtain an optimal trade-off between communications and sensing. Finally, it is illustrated that although noise-like OFDM waveforms have an ideal thumbtack shape in 2-D AF, using such a waveform to also sense the environment can cause high ambiguities in the angle profile of the MIMO AF in performing conventional single-stream communication. As a solution, including separate radar streams, decreases the ambiguities, considerably enhancing the MIMO AF.

5.1 Radar Processing

To perform radar processing in MIMO systems, the TX and RX frequency-domain symbols are used as in (3.12). For this, the vector $\mathbf{h}_n$ in (3.12) needs to be estimated since it contains all the necessary information about the radar targets, i.e., delay, Doppler-shift, and DoA. Once it is estimated, the range profiles of the different OFDM symbols are calculated. Then, these calculated profiles are separately used for obtaining the range–velocity and range–angle maps of the environment.

5.1.1 Range-Profile Calculation

The radar channel vector $\mathbf{h}_n$ is estimated first based on the least-squares method using the TX and RX frequency-domain symbol matrices, $\mathbf{X}_n$ and $\mathbf{y}_n$, based on (3.12) as

$$\hat{\mathbf{h}}_n = \mathbf{X}_n^\dagger \mathbf{y}_n = \mathbf{h}_n + \Delta \mathbf{h}_n, \tag{5.1}$$

where $\hat{\mathbf{h}}_n$ is the estimated channel vector while $\Delta\mathbf{h}_n$ is the error vector. Here, $\hat{\mathbf{h}}_n = [(\hat{\mathbf{h}}_{n,1})^T,\ldots,(\hat{\mathbf{h}}_{n,M})^T]^T$ contains the estimated channel for each OFDM symbol and $(\cdot)^\dagger$ represents the pseudo-inverse operation. Similarly, the radar channel for each TX stream can be expressed after the estimation of $\hat{\mathbf{h}}_n$ as

$$\hat{\mathbf{h}}_{n,m,s} = \mathbf{h}_{n,m,s} + \Delta\mathbf{h}_{n,m,s}, \tag{5.2}$$

where $\hat{\mathbf{h}}_{n,m,s}$ is of size $L_{\mathrm{R,r}}^{\mathrm{RF}} \times 1$, and it is the estimate of (3.11). Next, an inverse discrete Fourier transform (IDFT) is applied to $\hat{\mathbf{h}}_{n,m,s}$ to obtain the ith range bin value as

$$\mathbf{d}_{i,m,s} = \sum_{n=1}^{N} q_{i,n}\hat{\mathbf{h}}_{n,m,s} = \left[\hat{\mathbf{h}}_{1,m,s},\ldots,\hat{\mathbf{h}}_{N,m,s}\right]\mathbf{q}_i. \tag{5.3}$$

Here, $i \in [1,N]$, $\mathbf{d}_{i,m,s}$ is of size $L_{\mathrm{R,r}}^{\mathrm{RF}} \times 1$, $\mathbf{q}_i$ is the IDFT vector with each element given by $q_{i,n} = e^{\frac{j2\pi ni}{N}}$. The delay to each target is quantized as $\tau_i = \frac{i}{N\Delta f}$.

The $L_{\mathrm{R,r}}^{\mathrm{RF}}$ values in (5.3) can be combined for the different TX streams also using BB weights at the MIMO RX as

$$\mathbf{d}_{i,m} = [(\mathbf{w}_{\mathrm{R},m}^{\mathrm{BB}}(\theta))^H\mathbf{d}_{i,m,1},\ldots,(\mathbf{w}_{\mathrm{R},m}^{\mathrm{BB}}(\theta))^H\mathbf{d}_{i,m,S}]^T, \tag{5.4}$$

where $\mathbf{w}_{\mathrm{R},m}^{\mathrm{BB}}(\theta)$ is the vector of BB weights. In addition, the angle-dependent complex coefficient of the effective RX beampattern is given by

$$g_{\mathrm{R},m}(\theta) = (\mathbf{w}_{\mathrm{R},m}^{\mathrm{BB}}(\theta))^H(\mathbf{W}_{\mathrm{R,r},m}^{\mathrm{RF}})^H\mathbf{a}_{\mathrm{R}}(\theta). \tag{5.5}$$

Based on this expression, $\mathbf{w}_{\mathrm{R},m}^{\mathrm{BB}}(\theta)$ can be found such that it maximizes $g_{\mathrm{R},m}(\theta)$ as

$$\mathbf{w}_{\mathrm{R},m}^{\mathrm{BB}}(\theta) = \frac{(\mathbf{W}_{\mathrm{R,r},m}^{\mathrm{RF}})^H\mathbf{a}_{\mathrm{R}}(\theta)}{\|(\mathbf{W}_{\mathrm{R,r},m}^{\mathrm{RF}})^H\mathbf{a}_{\mathrm{R}}(\theta)\|}. \tag{5.6}$$

5.1.2 Range–Velocity Maps

The calculated range profiles in (5.3) are then used to calculate the velocity profiles, thereby obtaining the range–velocity maps. For this, a discrete Fourier transform

(DFT) is applied to $\mathbf{d}_{i,m,s}$ as

$$\mathbf{f}_{i,j,s} = \sum_{m=1}^{M} q'_{j,m}\mathbf{d}_{i,m,s} = \left[\mathbf{d}_{i,1,s},\ldots,\mathbf{d}_{i,M,s}\right]\mathbf{q}'_j. \tag{5.7}$$

Here, $j \in [1, M]$, $\mathbf{q}'_j$ is the DFT vector with each element given by $q'_{j,m} = e^{\frac{-j2\pi m j}{M}}$, and $\mathbf{f}_{i,j,s}$ is a vector of size $L_{\text{R,r}}^{\text{RF}} \times 1$, and it contains the $(i,j)^{\text{th}}$ element of the range–velocity map for the different RF chains.

5.1.3 Range–Angle Maps

The MUSIC algorithm is used for angle-profile calculation. For this, the covariance matrix of range bin values across the RF chains is calculated from (5.3) as

$$\mathbf{R}_{i,m,s} = \mathbb{E}\{\mathbf{d}_{i,m,s}\mathbf{d}_{i,m,s}^H\} = \mathbb{E}\left\{ \left(\sum_{n_1=1}^{N} q_{i,n_1}\hat{\mathbf{h}}_{n_1,m,s}\right) \left(\sum_{n_2=1}^{N} q_{i,n_2}^* \hat{\mathbf{h}}_{n_2,m,s}^H\right) \right\}$$

$$= \sum_{n_1=1}^{N}\sum_{n_2=1}^{N} q_{i,n_1}q_{i,n_2}^* \mathbb{E}\{\hat{\mathbf{h}}_{n_1,m,s}\hat{\mathbf{h}}_{n_2,m,s}^H\}$$

$$= \sum_{n_1=1}^{N}\sum_{n_2=1}^{N} q_{i,n_1}q_{i,n_2}^* \mathbf{h}_{n_1,m,s}\mathbf{h}_{n_2,m,s}^H + \sigma^2\mathbf{I}, \tag{5.8}$$

where $\sigma^2\mathbf{I} = \sum_{n_1=1}^{N}\sum_{n_2=1}^{N} q_{i,n_1}q_{i,n_2}^* \mathbb{E}\{\Delta\mathbf{h}_{n_1,m,s}\Delta\mathbf{h}_{n_2,m,s}^H\}$ is the covariance matrix of the error vector in (5.2). With the use of (3.11), (5.8) can be rewritten in the form

$$\mathbf{R}_{i,m,s} = \mathbf{A}_{\text{RF}}(\theta)\bar{\mathbf{R}}_{i,m,s}\mathbf{A}_{\text{RF}}^H(\theta) + \sigma^2\mathbf{I}, \tag{5.9}$$

where $\mathbf{A}_{\text{RF}}(\theta) = (\mathbf{W}_{\text{R,r},m}^{\text{RF}})^H\mathbf{A}_{\text{R}}(\theta)$ and $\bar{\mathbf{R}}_{i,m,s}$ is the covariance matrix of the other terms in (3.11) without $(\mathbf{W}_{\text{R,r},m}^{\text{RF}})^H\mathbf{A}_{\text{R}}(\theta)$, and can be given as

$$\bar{\mathbf{R}}_{i,m,s} = \mathbf{H}_{\text{r},n,m}\mathbf{A}_{\text{T}}^H(\theta)\mathbf{W}_{\text{T},m}^{\text{RF}}(\mathbf{W}_{\text{T},n,m}^{\text{BB}})_s \left(\mathbf{H}_{\text{r},n,m}\mathbf{A}_{\text{T}}^H(\theta)\mathbf{W}_{\text{T},m}^{\text{RF}}(\mathbf{W}_{\text{T},n,m}^{\text{BB}})_s\right)^H. \tag{5.10}$$

For the MUSIC algorithm, the number of targets must be known to estimate the angle profile, i.e., K_{t}. For U_{c} communications users, one angle w.r.t. the MIMO TX is considered the best direction for the user to receive the TX signal, e.g., line-of-sight

direction. Hence, the communications streams of a particular user are beamformed in that direction, which would mean that there are U_c communications beams. In addition, U_r sensing beams are used. Therefore, the TX beampattern consists of $U_c + U_r$ different main beams.

Since the MIMO TX knows about the communications users, some targets are in U_c directions. However, depending on the chosen U_r directions, it is possible/not possible for some targets to be in those directions. If targets are in those directions, these will be detected, whereas if they are not there, the radar processing will not show any target. In this case, it is assumed that the total number of targets is the summation of the number of communications and sensing beams, i.e., $K_t = U_c + U_r$. Once this assumption is made, the MUSIC pseudo-spectrum is given by

$$P(\theta)_{i,m,s} = \frac{1}{\tilde{\mathbf{a}}^H(\theta)\mathbf{\Gamma}_{i,m,s}\mathbf{\Gamma}_{i,m,s}^H\tilde{\mathbf{a}}(\theta)}, \tag{5.11}$$

where $\tilde{\mathbf{a}}(\theta) = (\mathbf{W}_{\mathrm{R,r},m}^{\mathrm{RF}})^H\mathbf{a}_{\mathrm{R}}(\theta)$ is the effective RX steering vector for a general angle θ and $\mathbf{\Gamma}_{i,m,s} = [\gamma_{i,m,s,1},\ldots,\gamma_{i,m,s,L_{\mathrm{R,r}}^{\mathrm{RF}}-K_t}]$ is the matrix containing eigenvectors of the lowest $(L_{\mathrm{R,r}}^{\mathrm{RF}} - K_t)$ eigenvalues of $\mathbf{R}_{i,m,s}$ in (5.9). It should be mentioned that in classical MUSIC processing, e.g., in MIMO systems with fully-digital arrays, DoAs are detected based on the Vandermonde structure of the RX steering matrix $\mathbf{A}_{\mathrm{R}}(\theta)$ [106]. However, when hybrid analog-digital beamforming is considered, the RX steering matrix is affected by $\mathbf{W}_{\mathrm{R,r},m}^{\mathrm{RF}}$, and the effective RX steering matrix $\mathbf{A}_{\mathrm{RF}}(\theta)$ should be used for the detection of DoAs.

In evaluating (5.11) for all N range bin values, the range–angle map of each OFDM symbol and TX stream can be obtained. In the sensing perspective, a single map of the environment is required instead of many maps. The combined range–angle map for the mth OFDM symbol can be obtained through maximum-ratio combining as

$$P(\theta)_{i,m} = \sum_{s=1}^{S}|g_{\mathrm{T},n,m,s}(\theta)|^2 P(\theta)_{i,m,s} = \sum_{s=1}^{S}\frac{|g_{\mathrm{T},n,m,s}(\theta)|^2}{\tilde{\mathbf{a}}^H(\theta)\mathbf{\Gamma}_{i,m,s}\mathbf{\Gamma}_{i,m,s}^H\tilde{\mathbf{a}}(\theta)}, \tag{5.12}$$

where $g_{\mathrm{T},n,m,s}(\theta) = \mathbf{a}_T^H(\theta)\mathbf{W}_{\mathrm{T},m}^{\mathrm{RF}}(\mathbf{W}_{\mathrm{T},n,m}^{\mathrm{BB}})_s$ is the gain of the TX beampattern at a general θ direction. One important point to note is that $\mathbf{R}_{i,m,s}$ in practice is difficult to be calculated based on the expectation operation as $\mathbf{R}_{i,m,s} = \mathbb{E}\{\mathbf{d}_{i,m,s}\mathbf{d}_{i,m,s}^H\}$. Instead, it is calculated as the sample covariance matrix $\mathbf{R}_{i,m,s} \approx \mathbf{d}_{i,m,s}\mathbf{d}_{i,m,s}^H$.

5.2 Optimized Sensing Streams for CRLB Minimization

This section discusses the method through which the sensing streams are optimized.[3] Specifically, they are optimized to jointly minimize the CRLBs of delay and DoA estimates. The CRLB expressions are first derived[4], followed by the optimization problem and its solution.

5.2.1 CRLB Expressions

The log-likelihood function of the RX frequency-domain symbols is needed to obtain the entries in the 2×2 Fisher information matrix. For this, RX symbols in (3.12) are stacked for all subcarriers as

$$\mathbf{y} = [\mathbf{y}_1^T, \ldots, \mathbf{y}_N^T]^T, \tag{5.13}$$

where $\mathbf{y}$ is the vector containing all RX frequency-domain symbols. The log-likelihood function of it is then given similar to (4.8) as

$$\log \mathcal{P}_{\mathbf{y}}(\mathbf{y}; \boldsymbol{\alpha}) = -\log\left(\sigma_r^2 \pi^{NML_{R,r}^{RF}}\right) - \frac{1}{\sigma_r^2}\left(\sum_{n=1}^{N} \mathbf{y}_n^H \mathbf{y}_n \right.$$
$$\left. + \mathbf{h}_n^H \mathbf{X}_n^H \mathbf{X}_n \mathbf{h}_n - 2\Re\{\mathbf{y}_n^H \mathbf{X}_n \mathbf{h}_n\}\right), \tag{5.14}$$

where $\boldsymbol{\alpha} = [\theta, \tau]^T$. Then, using (A.10), each element of the Fisher matrix can be obtained as [P4]

$$\mathscr{I}(\boldsymbol{\alpha})_{i,j} = \frac{2}{\sigma_r^2} \Re\left\{\sum_{n=1}^{N} \frac{\partial \mathbf{h}_n^H}{\partial \alpha_j} \mathbf{P}_n \frac{\partial \mathbf{h}_n}{\partial \alpha_i}\right\}, \tag{5.15}$$

where $\mathbf{P}_n = \mathrm{diag}\{|x_{n,1,1}|^2\mathbf{I}, \cdots, |x_{n,m,s}|^2\mathbf{I}, \cdots, |x_{n,M,S}|^2\mathbf{I}\}$ contains the powers of the subcarriers for different OFDM symbols and streams.

---

[3]It is solved through a similar approach as used in Section 4.2.2.
[4]The derived CRLBs for SISO JCAS systems in Section 4.2.1 are a special case of the CRLB expressions derived in this section, although the derivation steps are similar.

Next, using (3.11),

$$\frac{\partial \mathbf{h}_{n,m,s}}{\partial \tau} = (-\jmath 2\pi n \Delta f) b e^{-\jmath 2\pi n \Delta f \tau} e^{\jmath 2\pi m \frac{f_D}{\Delta f}} \underbrace{(\mathbf{W}_{\mathrm{R,r},m}^{\mathrm{RF}})^H \mathbf{a}_{\mathrm{R}}(\theta) \mathbf{a}_{\mathrm{T}}^H(\theta) \mathbf{W}_{\mathrm{T},m}^{\mathrm{RF}} (\mathbf{W}_{\mathrm{T},n,m}^{\mathrm{BB}})_s}_{\mathbf{g}_{n,m,s}},$$
(5.16)

$$\frac{\partial \mathbf{h}_{n,m}}{\partial \tau} = (-\jmath 2\pi n \Delta f) b e^{-\jmath 2\pi n \Delta f \tau} e^{\jmath 2\pi m \frac{f_D}{\Delta f}} \mathbf{g}_{n,m},$$
(5.17)

with $\mathbf{g}_{n,m} = [\mathbf{g}_{n,m,1}^T, \cdots, \mathbf{g}_{n,m,S}^T]^T$. Similarly, the following expression can be derived using (3.7).

$$\frac{\partial \mathbf{a}(\theta)}{\partial \theta} = \left[0, \ldots, e^{\jmath \pi (L-1)\sin(\theta)} \jmath \pi (L-1)\cos(\theta)\right]^T = \jmath \pi \cos(\theta) \mathbf{D} \mathbf{a}(\theta),$$
(5.18)

where $\mathbf{D} = \mathrm{diag}\{[0, \ldots, L-1]\}$. Thus, using (3.11) again,

$$\frac{\partial \mathbf{h}_{n,m,s}}{\partial \theta} = \jmath \pi b e^{-\jmath 2\pi n \Delta f \tau} e^{\jmath 2\pi m \frac{f_D}{\Delta f}} \cos(\theta)$$
$$\cdot \underbrace{(\mathbf{W}_{\mathrm{R,r},m}^{\mathrm{RF}})^H \left(\mathbf{D}_{\mathrm{R}} \mathbf{a}_{\mathrm{R}}(\theta) \mathbf{a}_{\mathrm{T}}^H(\theta) - \mathbf{a}_{\mathrm{R}}(\theta) \mathbf{a}_{\mathrm{T}}^H(\theta) \mathbf{D}_{\mathrm{T}}\right) \mathbf{W}_{\mathrm{T},m}^{\mathrm{RF}} (\mathbf{W}_{\mathrm{T},n,m}^{\mathrm{BB}})_s}_{\mathbf{g}_{n,m,s}'},$$
(5.19)

$$\frac{\partial \mathbf{h}_{n,m}}{\partial \theta} = \jmath \pi b e^{-\jmath 2\pi n \Delta f \tau_k} e^{\jmath 2\pi m \frac{f_D}{\Delta f}} \cos(\theta) \mathbf{g}_{n,m}',$$
(5.20)

where $\mathbf{g}_{n,m}' = [(\mathbf{g}_{n,m,1}')^T, \cdots, (\mathbf{g}_{n,m,S}')^T]^T$.

Then, (5.15) is used to obtain the individual element of the Fisher matrix as

$$\mathscr{I}(\boldsymbol{\alpha})_{1,1} = 2\pi^2 \cos^2(\theta)(\mathrm{SNR}) \sum_{m=1}^M \sum_{n=1}^N \sum_{s=1}^S P_{n,m,s} (\mathbf{g}_{n,m,s}')^H \mathbf{g}_{n,m,s}',$$
(5.21)

$$\mathscr{I}(\boldsymbol{\alpha})_{2,2} = 8\pi^2 (\Delta f)^2 (\mathrm{SNR}) \sum_{m=1}^M \sum_{n=1}^N \sum_{s=1}^S \bar{n}^2 P_{n,m,s} (\mathbf{g}_{n,m,s})^H \mathbf{g}_{n,m,s},$$
(5.22)

$$\mathscr{I}(\boldsymbol{\alpha})_{1,2} = -4\pi^2 (\Delta f) \cos(\theta)(\mathrm{SNR}) \Re \left\{ \sum_{m=1}^M \sum_{n=1}^N \sum_{s=1}^S \bar{n} P_{n,m,s} (\mathbf{g}_{n,m,s})^H \mathbf{g}_{n,m,s}' \right\},$$
(5.23)

where $P_{n,m,s} = \frac{|x_{n,m,s}|^2}{P_{\mathrm{t}}}$, $\bar{n} = n - \frac{N+1}{2}$, and $\mathscr{I}(\boldsymbol{\alpha})_{2,1} = \mathscr{I}(\boldsymbol{\alpha})_{1,2}$. The CRLBs of delay

81

and DoA estimates are finally given by the diagonal elements of $\mathscr{I}^{-1}(\boldsymbol{\alpha})$ as

$$\text{CRLB}(\hat{\theta}) = \frac{1}{2\pi^2 \cos^2(\theta)(\text{SNR})f_\theta(\mathbf{P})}, \tag{5.24}$$

$$\text{CRLB}(\hat{\tau}) = \frac{1}{8\pi^2(\Delta f)^2(\text{SNR})f_\tau(\mathbf{P})}, \tag{5.25}$$

where

$$
\begin{aligned}
f_\theta(\mathbf{P}) = &\sum_{m=1}^{M}\sum_{n=1}^{N}\sum_{s=1}^{S} P_{n,m,s}(\mathbf{g}'_{n,m,s})^H \mathbf{g}'_{n,m,s} \\
&- \frac{\left(\Re\left\{\sum_{m=1}^{M}\sum_{n=1}^{N}\sum_{s=1}^{S} \bar{n}P_{n,m,s}(\mathbf{g}_{n,m,s})^H \mathbf{g}'_{n,m,s}\right\}\right)^2}{\sum_{m=1}^{M}\sum_{n=1}^{N}\sum_{s=1}^{S} \bar{n}^2 P_{n,m,s}(\mathbf{g}_{n,m,s})^H \mathbf{g}_{n,m,s}},
\end{aligned}
\tag{5.26a}
$$

$$
\begin{aligned}
f_\tau(\mathbf{P}) = &\sum_{m=1}^{M}\sum_{n=1}^{N}\sum_{s=1}^{S} \bar{n}^2 P_{n,m,s}(\mathbf{g}_{n,m,s})^H \mathbf{g}_{n,m,s} \\
&- \frac{\left(\Re\left\{\sum_{m=1}^{M}\sum_{n=1}^{N}\sum_{s=1}^{S} \bar{n}P_{n,m,s}(\mathbf{g}_{n,m,s})^H \mathbf{g}'_{n,m,s}\right\}\right)^2}{\sum_{m=1}^{M}\sum_{n=1}^{N}\sum_{s=1}^{S} P_{n,m,s}(\mathbf{g}'_{n,m,s})^H \mathbf{g}'_{n,m,s}}.
\end{aligned}
\tag{5.26b}
$$

5.2.2 Joint CRLB Delay and DoA Minimization

The joint optimization problem that minimizes the CRLBs of delay and DoA estimates is given similar to the SISO optimization problem in (4.22a)–(4.22d) as

$$\min_{\mathbf{x}_{\text{r},n,m}, \mathscr{R}_{n,m,\tilde{s}}} \text{CRLB}(\hat{\theta}) \tag{5.27a}$$

subject to

$$\text{CRLB}(\hat{\tau}) \le \tau_{\max}^2, \tag{5.27b}$$

$$\frac{\bar{\zeta}_{\text{int,c}}}{\bar{\zeta}_{\text{c}}} = \eta, \tag{5.27c}$$

$$P_{\text{r}} \le P_{\text{t}} - P_{\text{c}}, \tag{5.27d}$$

$$0 \le P_{n,m,\tilde{s}} \le P_{\max}, \tilde{s} \in [1, S_{\text{r}}]. \tag{5.27e}$$

Hence, the goal of the optimization problem is to find the frequency-domain symbols of the sensing streams $\mathbf{x}_{\text{r},n,m}$ along with their optimal indices $\mathscr{R}_{n,m,\tilde{s}}$ such that

they minimize $\text{CRLB}(\hat{\theta})$ while constraining $\text{CRLB}(\hat{\tau})$ to be less than τ_{max}^2, which can be chosen depending on the required application. The power allocated to the radar streams P_{r} depends on the total TX streams power P_{t} and the power allocated to the communications streams P_{c}. The power allocated to the communications streams is controlled through (5.27c), since it ensures a certain sum communications capacity of the MIMO JCAS system (3.22), compared to when only communications are performed without JCAS (3.23). Varying $\eta = [0, 1]$ results in varying P_{c}, and therefore, $\eta = f(P_{\text{c}})$ (or $P_{\text{c}} = f^{-1}(\eta)$), where $f(\cdot)$ is some function. Moreover, a certain maximum power P_{max} can be allocated to a subcarrier in a sensing stream.

Similar to the SISO optimization problem in (4.22a)–(4.22d), N_{act} subcarriers are activated in the sensing streams, with $N_{\text{act}} - 1$ subcarriers having power P_{max} and a single subcarrier with power P_{Δ}. The $\text{CRLB}(\hat{\theta})$ value due to this power allocation for indices of the activated subcarriers $\mathcal{R}_{n,m,\tilde{s}}$ of the sensing streams can then be written, as given in Section IV-B of [P4] as

$$
\text{CRLB}(\hat{\theta}) = \tau_{\text{max}}^2 \frac{4(\Delta f)^2}{\cos^2(\theta)}
$$
$$
\cdot \frac{\text{NUM}_{\text{c}} + P_{\text{max}} \sum_{m=1}^{M} \sum_{\tilde{s}=1}^{S_{\text{r}}} \sum_{n \in \mathcal{R}_{n,m,\tilde{s}}} \bar{n}^2 (\mathbf{g}_{n,m,\tilde{s}})^H \mathbf{g}_{n,m,\tilde{s}} + P_{\Delta} \bar{n}_0^2 (\mathbf{g}_{n_0,m_0,\tilde{s}_0})^H \mathbf{g}_{n_0,m_0,\tilde{s}_0}}{\text{DEN}_{\text{c}} + P_{\text{max}} \sum_{m=1}^{M} \sum_{\tilde{s}=1}^{S_{\text{r}}} \sum_{n \in \mathcal{R}_{n,m,\tilde{s}}} (\mathbf{g}'_{n,m,\tilde{s}})^H \mathbf{g}'_{n,m,\tilde{s}} + P_{\Delta} (\mathbf{g}'_{n_0,m_0,\tilde{s}_0})^H \mathbf{g}'_{n_0,m_0,\tilde{s}_0}},
$$
$$(5.28)$$

where

$$
\text{DEN}_{\text{c}} = \sum_{m=1}^{M} \sum_{n=1}^{N} \sum_{s=1}^{S_{\text{c}}} P_{n,m,s} (\mathbf{g}'_{n,m,s})^H \mathbf{g}'_{n,m,s}, \tag{5.29}
$$

$$
\text{NUM}_{\text{c}} = \sum_{m=1}^{M} \sum_{n=1}^{N} \sum_{s=1}^{S_{\text{c}}} \bar{n}^2 P_{n,m,s} (\mathbf{g}_{n,m,s})^H \mathbf{g}_{n,m,s}. \tag{5.30}
$$

The next step is to identify the indices of the N_{act} subcarriers that are activated. Since out of NMS_{r} subcarriers in sensing streams, only N_{act} subcarriers are activated, it is a vast search space. To reduce the complexity, the separate optimization problems of the two CRLBs are used, given by

(a) $\min_{\mathcal{R}_{n,m,\tilde{s}}} \text{CRLB}(\hat{\theta})$, $\tilde{s} \in [1, S_{\text{r}}]$ (b) $\min_{\mathcal{R}_{n,m,\tilde{s}}} \text{CRLB}(\hat{\tau})$, $\tilde{s} \in [1, S_{\text{r}}]$.

The activated indices to these two optimization problems can be readily found. As discussed in [P4], for (a), they are given by the N_{act} subcarriers having the highest

---

Algorithm 1 Calculation of sensing streams' optimal subcarrier indices for joint minimization of $\mathrm{CRLB}(\hat{\tau})$ and $\mathrm{CRLB}(\hat{\theta})$

1: Set $z = 0$
2: Set $\mathscr{R}$ as the set of subcarrier indices for sensing streams
3: Set $\mathscr{R}_{n,m,\tilde{s}}$ as sensing streams' activated subcarriers having the highest $(\mathbf{g}'_{n,m,\tilde{s}})^H \mathbf{g}'_{n,m,\tilde{s}}$, in descending order
4: **while** $z \leq N_{\mathrm{act}}$ **do**
5:      Calculate $\mathrm{CRLB}(\hat{\theta})_z$ and $\mathrm{CRLB}(\hat{\tau})_z$
6:      Set $\mathscr{R}'_{n,m,\tilde{s}} = (\mathscr{R} \cap \mathscr{R}_{n,m,\tilde{s}})'$
7:      Move the symbol of activated subcarrier in $\mathscr{R}_{n,m,\tilde{s}}$ with least $(\mathbf{g}'_{n,m,\tilde{s}})^H \mathbf{g}'_{n,m,\tilde{s}}$
        to the unactivated subcarrier in $\mathscr{R}'_{n,m,\tilde{s}}$ with highest $\bar{n}^2 (\mathbf{g}_{n,m,\tilde{s}})^H \mathbf{g}_{n,m,\tilde{s}}$
8:      Update the set $\mathscr{R}_{n,m,\tilde{s}}$
9:      $z \leftarrow z + 1$

$(\mathbf{g}'_{n,m,\tilde{s}})^H \mathbf{g}'_{n,m,\tilde{s}}$ values. For (b), they are the subcarriers having the highest $\bar{n}^2 (\mathbf{g}_{n,m,\tilde{s}})^H \mathbf{g}_{n,m,\tilde{s}}$ values.

Finally, the activated subcarrier indices for the joint optimization are found using the solution to the separate optimization problem (a) as a starting point. Hence, N_{act} subcarriers having the highest $(\mathbf{g}'_{n,m,\tilde{s}})^H \mathbf{g}'_{n,m,\tilde{s}}$ values are activated. Then, the frequency-domain symbol of the activated subcarrier having the least $(\mathbf{g}'_{n,m,\tilde{s}})^H \mathbf{g}'_{n,m,\tilde{s}}$ value is moved to the unactivated subcarrier having the highest $\bar{n}^2 (\mathbf{g}_{n,m,\tilde{s}})^H \mathbf{g}_{n,m,\tilde{s}}$ value. This process is repeated until all N_{act} subcarriers are moved, resulting in the waveform having the minimum $\mathrm{CRLB}(\hat{\tau})$, i.e., the solution arrived at by the separate optimization problem (b). This process ensures that for each subcarrier moved, $\mathrm{CRLB}(\hat{\theta})$ is degraded the least while $\mathrm{CRLB}(\hat{\tau})$ is minimized. The algorithm for calculating these optimal subcarrier indices is given in Algorithm 1.

5.3 MIMO AF Enhancement

This section discusses an alternative approach to using the sensing streams. Firstly, the MIMO AF for two targets is derived. Secondly, the ambiguity problem in the angular domain is discussed when conventional communications are performed. Next, the methodology to minimize such ambiguities through separate independent random radar streams is discussed.

5.3.1 MIMO AF Definition

A fully-digital architecture is considered for the MIMO TRX in deriving the MIMO AF. When a single TX stream is used to communicate with a user at θ_c direction, the TX time-domain signal can be written as the IDFT of a simpler version of (3.4) as

$$\tilde{\mathbf{x}}(t) = \mathbf{w}_{\mathrm{T,c}}^{\mathrm{BB}} x_{\mathrm{c}}(t), \tag{5.31}$$

where $\mathbf{w}_{\mathrm{T,c}}^{\mathrm{BB}}$ is the beamforming vector, $x_{\mathrm{c}}(t)$ and $\tilde{\mathbf{x}}(t)$ are the time-domain sample of the TX stream and samples at the TX antenna elements, respectively. Assuming the TX signals from the L_{T} different elements reflect off a point target, the signal received at the $l_{\mathrm{R}}^{\mathrm{th}}$ antenna element of the MIMO RX can be written as

$$y_{l_{\mathrm{R}}}(t, \boldsymbol{\Phi}_1) = \sum_{l_{\mathrm{T}}=1}^{L_{\mathrm{T}}} b_{l_{\mathrm{T}}, l_{\mathrm{R}}} \tilde{x}_{l_{\mathrm{T}}}\left(t - \tau_{l_{\mathrm{T}}, l_{\mathrm{R}}}(\mathbf{p}_1)\right) e^{-\jmath 2\pi \tau_{l_{\mathrm{T}}, l_{\mathrm{R}}}(\mathbf{p}_1) f_{\mathrm{c}}} e^{\jmath 2\pi f_{l_{\mathrm{T}}, l_{\mathrm{R}}}(\mathbf{p}_1) t} + n_{l_{\mathrm{R}}}(t). \tag{5.32}$$

Here, the 2-D co-ordinates vector of the target is given by $\mathbf{p}_1$, with the two-way delay and Doppler-shift between the $l_{\mathrm{T}}^{\mathrm{th}}$ TX antenna and $l_{\mathrm{R}}^{\mathrm{th}}$ RX antenna are given by $\tau_{l_{\mathrm{T}}, l_{\mathrm{R}}}(\mathbf{p}_1)$ and $f_{l_{\mathrm{T}}, l_{\mathrm{R}}}(\mathbf{p}_1)$, respectively, which are functions of $\mathbf{p}_1$. In addition, $\boldsymbol{\Phi}_1 = [\tau_{l_{\mathrm{T}}, l_{\mathrm{R}}}(\mathbf{p}_1), f_{l_{\mathrm{T}}, l_{\mathrm{R}}}(\mathbf{p}_1)]$ contains the parameters of the target. The attenuation constant for the target reflection between a TX-RX antenna pair is denoted by $b_{l_{\mathrm{T}}, l_{\mathrm{R}}}$, $\tilde{x}_{l_{\mathrm{T}}}(t)$ is the signal at the $l_{\mathrm{T}}^{\mathrm{th}}$ TX antenna, and f_{c} is the carrier frequency. The RX signal and noise samples at the $l_{\mathrm{R}}^{\mathrm{th}}$ RX antenna are given by $y_{l_{\mathrm{R}}}(t, \boldsymbol{\Phi}_1)$ and $n_{l_{\mathrm{R}}}(t)$, respectively.

The received signal $y_{l_{\mathrm{R}}}(t, \boldsymbol{\Phi}_1)$ is then matched to different TX signals assuming they reflect off from a second point target. The 2-D co-ordinates of that target are given by $\mathbf{p}_2$, with its delay and Doppler-shift represented by $\boldsymbol{\Phi}_2 = [\tau_{i, l_{\mathrm{R}}}(\mathbf{p}_2), f_{i, l_{\mathrm{R}}}(\mathbf{p}_2)]$. The matched-filtering can be given as

$$\bar{y}_{l_{\mathrm{R}}}(\boldsymbol{\Phi}_1, \boldsymbol{\Phi}_2) = \sum_{l_{\mathrm{T}}=1}^{L_{\mathrm{T}}} b_{l_{\mathrm{T}}, l_{\mathrm{R}}} \left(\int \tilde{x}_{l_{\mathrm{T}}}\left(t - \tau_{l_{\mathrm{T}}, l_{\mathrm{R}}}(\mathbf{p}_1)\right) \tilde{x}_i^*\left(t - \tau_{i, l_{\mathrm{R}}}(\mathbf{p}_2)\right) \right.$$
$$\left. \cdot e^{\jmath 2\pi \left(f_{l_{\mathrm{T}}, l_{\mathrm{R}}}(\mathbf{p}_1) - f_{i, l_{\mathrm{R}}}(\mathbf{p}_2) \right) t} dt \right)$$
$$\cdot e^{-\jmath 2\pi \tau_{l_{\mathrm{T}}, l_{\mathrm{R}}}(\mathbf{p}_1) f_{\mathrm{c}}} e^{\jmath 2\pi \tau_{i, l_{\mathrm{R}}}(\mathbf{p}_2) f_{\mathrm{c}}} + \bar{n}_{l_{\mathrm{R}}}, \tag{5.33}$$

where $\tilde{x}_i^*(t)$ is one of the signals from the TX antenna elements with $i \in [1, L_T]$, $\bar{y}_{l_R}(\Phi_1, \Phi_2)$ represents the output of the matched-filter, and $\bar{n}_{l_R}$ is the corresponding noise sample. The expression in (5.33) can alternatively be written using

$$\mathbf{R}_{l_T,i}(\Phi_1, \Phi_2, l_R) = \int b_{l_T, l_R} \tilde{x}_{l_T}\left(t - \tau_{l_T, l_R}(\mathbf{p}_1)\right) \tilde{x}_i^*\left(t - \tau_{i, l_R}(\mathbf{p}_2)\right) e^{j2\pi\left(f_{l_T, l_R}(\mathbf{p}_1) - f_{i, l_R}(\mathbf{p}_2)\right)t} dt \tag{5.34}$$

to represent the covariance matrix of the TX signals as

$$\bar{y}_{l_R}(\Phi_1, \Phi_2) = \sum_{l_T=1}^{L_T} \mathbf{R}_{l_T,i}(\Phi_1, \Phi_2, l_R) e^{-j2\pi\tau_{l_T, l_R}(\mathbf{p}_1)f_c} e^{j2\pi\tau_{i, l_R}(\mathbf{p}_2)f_c} + \bar{n}_{l_R}. \tag{5.35}$$

The general MIMO AF is defined based on the first term of (5.35) as [91]

$$\mathcal{X}(\Phi_1, \Phi_2) = \left| \sum_{l_T=1}^{L_T} \mathbf{R}_{l_T,i}(\Phi_1, \Phi_2, l_R) e^{-j2\pi\tau_{l_T, l_R}(\mathbf{p}_1)f_c} e^{j2\pi\tau_{i, l_R}(\mathbf{p}_2)f_c} \right|^2. \tag{5.36}$$

The general AF derived in (5.36) can be simplified by certain assumptions, that are: MIMO TX and RX arrays are situated close to each other, as usually is the case with a monostatic MIMO TRX, the considered targets are in the far-field of the MIMO TRX, and the waveforms used are narrowband. For the narrowband assumption, it is important for the relation $2NM\frac{v_r}{v_{\text{light}}} \ll 1$ to hold for an OFDM waveform, where v_r and v_{light} are the velocities of the target and light, respectively. Using these assumptions, the simplified MIMO AF is given by [66]

$$\mathcal{X}(\Delta\tau, \Delta f_D, \theta_1, \theta_2) = \left| \mathbf{a}_T^H(\theta_1) \mathbf{R}(\Delta\tau, \Delta f_D) \mathbf{a}_T(\theta_2) \right|^2 \left| \mathbf{a}_R^H(\theta_1) \mathbf{a}_R(\theta_2) \right|^2, \tag{5.37}$$

where since $b_{l_T, l_R} = b$, $\forall l_T, l_R$, the effect of b can be neglected. The variables $\Delta\tau$ and Δf_D represent the difference in delays and Doppler-shifts between the two point targets. The angles θ_1 and θ_2 are the directions of the targets w.r.t. the MIMO TRX. Further, under these assumptions, the $L_T \times L_T$ covariance matrix in (5.34) can be simplified as $\mathbf{R}(\Delta\tau, \Delta f_D)$, where each element of it is given by

$$R_{l_T,i}(\Delta\tau, \Delta f_D) = \int \tilde{x}_{l_T}(t) \tilde{x}_i^*(t - \Delta\tau) e^{j2\pi\Delta f_D t} dt. \tag{5.38}$$

It can also be observed from (5.37) that the MIMO AF is a 4-D function.

5.3.2 MIMO Communications Signal

Based on the TX communications signal in (5.31), the RX signal at the communications RX with a single antenna can be represented as

$$\tilde{y}_{\mathrm{c}}(t) = \mathbf{h}_{\mathrm{c}}^{H}(t)\mathbf{w}_{\mathrm{T,c}}^{\mathrm{BB}}x_{\mathrm{c}}(t) + \tilde{n}_{\mathrm{c}}(t), \tag{5.39}$$

where $\mathbf{h}_{\mathrm{c}}(t) = \sqrt{g}\mathbf{a}_{\mathrm{T}}(\theta_{\mathrm{c}})$ is the $L_{\mathrm{T}} \times 1$ LoS channel vector for the communications user with $\sqrt{g}$ representing the free-space path loss and $\mathbf{a}_{\mathrm{T}}(\theta_{\mathrm{c}})$ is the TX steering vector. Due to LoS conditions, the beamforming vector can be found based on the matched-filter (MF) response that gives a main-beam at θ_{c} as

$$\mathbf{w}_{\mathrm{T,c}}^{\mathrm{BB}} = \frac{\mathbf{a}_{\mathrm{T}}^{*}(\theta_{\mathrm{c}})}{\sqrt{L_{\mathrm{T}}}}. \tag{5.40}$$

This is referred to as the *single-beam case* later in Section 5.4.2.

5.3.3 Ambiguities in Range and Angle Domains

The 2-D AF of an OFDM waveform generally has a near-ideal thumbtack shape because it is similar to a Gaussian noise signal [63]. Hence, the AF has fewer side-lobes in the range and velocity domains. However, the OFDM waveform can result in high side-lobes (or ambiguities) in the angular profiles θ_1 or θ_2 in the MIMO AF (5.37), based on what kinds of OFDM signals are at the different TX antenna elements, as depicted later in Fig. 5.10. To compare and quantify these ambiguities, two different cuts of the MIMO AF are defined as

$$\mathbf{h}_{\theta_2} = \mathscr{X}(0, 0, \theta, \theta_2), \tag{5.41}$$

$$\mathbf{h}_{\Delta\tau} = \mathscr{X}(\Delta\tau, 0, \theta, \theta). \tag{5.42}$$

Here, θ is the angle of a particular target while θ_2 is the angle of a second target nearby. Hence, $\mathbf{h}_{\theta_2}$ is the cut along the θ_2 dimension while $\mathbf{h}_{\Delta\tau}$ corresponds to the cut along $\Delta\tau$.

Next, to quantify the side-lobes of these two cuts, the integrated side-lobe levels (ISLs) for them are defined separately as the ratio between the energy of the side-lobes

to that of the main-lobe, and can be given using (2.8) as

$$\text{ISL}_{\text{angle}} = \frac{\int_{-\frac{\pi}{2}}^{\theta_{\text{main},1}} \mathbf{h}_{\theta_2}(\theta')d\theta' + \int_{\theta_{\text{main},2}}^{\frac{\pi}{2}} \mathbf{h}_{\theta_2}(\theta')d\theta'}{\int_{\theta_{\text{main},1}}^{\theta_{\text{main},1}} \mathbf{h}_{\theta_2}(\theta')d\theta'}, \tag{5.43}$$

$$\text{ISL}_{\text{delay}} = \frac{\int_{-\tau_{\text{min}}}^{\tau_{\text{main},1}} \mathbf{h}_{\Delta\tau}(\tau)d\tau + \int_{\tau_{\text{main},2}}^{\tau_{\text{max}}} \mathbf{h}_{\Delta\tau}(\tau)d\tau}{\int_{\tau_{\text{main},1}}^{\tau_{\text{main},2}} \mathbf{h}_{\Delta\tau}(\tau)d\tau}. \tag{5.44}$$

The variables $\theta_{\text{main},1} + \theta_{\text{main},2}$ and $\tau_{\text{main},1} + \tau_{\text{main},2}$ correspond to the null-to-null lengths of the main-lobes in angle and delay profiles, respectively, and τ_{min} and τ_{max} are the minimum and maximum delays of the delay profile. According to these two definitions, a low value of ISL indicates fewer side-lobes/ambiguities.

As discussed later in Section 5.4.2, single-stream communication at θ_c results in high ambiguities in the angle profile of the MIMO AF. These ambiguities can somewhat be minimized by splitting the communication stream also in another direction θ_r, apart from θ_c. It is also helpful in sensing since the MIMO RX receives reflections from those two directions. In this case, the beamforming vector is given by

$$\mathbf{w}_{\text{T,c}}^{\text{BB}} = \frac{\mathbf{a}_{\text{T}}^*(\theta_c) + \mathbf{a}_{\text{T}}^*(\theta_r)}{||\mathbf{a}_{\text{T}}(\theta_c) + \mathbf{a}_{\text{T}}(\theta_r)||}, \tag{5.45}$$

and is referred to as the *two-beams case*.

5.3.4 Inclusion of Independent Radar Streams

Although using two beamforming directions in *two-beams case* minimizes the ambiguities, as shown in Fig. 5.11(a), they persist, and a solution for lowering them is discussed next. For this, instead of the TX signal consisting of just a communication stream, separate independent radar streams are now concatenated as

$$\mathbf{x}(t) = [x_c(t), \overbrace{x_{\text{r},1}(t), \dots, x_{\text{r},S_r}(t)}^{\mathbf{x}_r^T(t)}]^T, \tag{5.46}$$

where $x_{\text{r},s}, s \in [1, S_r]$ represents the sample of the sth radar stream, with S_r denoting the total number of such radar streams. The total instantaneous TX power is also

shared between the communication and radar streams, similar to (3.1) as

$$P_c = |x_c(t)|^2, \; P_r = \sum_{s=1}^{S_r} |x_{r,s}(t)|^2. \qquad (5.47)$$

However, including separate radar streams causes interference for the communications users and must be mitigated for effective communications. The TX time-domain signal is then given similar to (5.31) as

$$\tilde{\mathbf{x}}(t) = \mathbf{W}_T^{BB} \mathbf{x}(t) = \left[\mathbf{w}_{T,c}^{BB}, \mathbf{W}_{T,r}^{BB} \right] \left[x_c(t), \mathbf{x}_r^T(t) \right]^T. \qquad (5.48)$$

The RX signal at the communications RX can be given similar to (5.39) as

$$\tilde{y}_c(t) = \sqrt{g} \mathbf{a}_T^H(\theta_c) \mathbf{w}_{T,c}^{BB} x_c(t) + \sqrt{g} \mathbf{a}_T^H(\theta_c) \mathbf{W}_{T,r}^{BB} \mathbf{x}_r(t) + \tilde{n}_c(t), \qquad (5.49)$$

where the first term is the useful time-domain communications RX signal while the second term is the radar–communications interference. The interference can be canceled by designing $\mathbf{W}_{T,r}^{BB}$ based on the NSP method as used in Section 3.3 given by

$$\mathbf{W}_{T,r}^{BB} = \left(\mathbf{I} - \left(\mathbf{a}_T^H(\theta_c) \right)^\dagger \mathbf{a}_T^H(\theta_c) \right) \hat{\mathbf{W}}_{T,r}^{BB} = \left(\mathbf{I} - \frac{1}{L_T} \mathbf{a}_T(\theta_c) \mathbf{a}_T^H(\theta_c) \right) \hat{\mathbf{W}}_{T,r}^{BB}, \qquad (5.50)$$

where $\hat{\mathbf{W}}_{T,r}^{BB}$ is chosen as a random orthonormal matrix, so that the different radar streams illuminate different directions of the environment. Moreover, the design of $\mathbf{W}_{T,r}^{BB}$ ensures that beampatterns corresponding to all radar streams have a null at θ_c to cancel the radar–communications interference.

5.4 Performance of the MIMO JCAS System

This section discusses the simulation results for the MIMO JCAS system. Firstly, the results when the sensing streams are optimized to minimize the CRLBs of range and DoA estimates are discussed, followed up with the results for the MIMO AF enhancement. An analog–digital hybrid architecture and fully-digital architecture are considered for the former and latter, respectively.
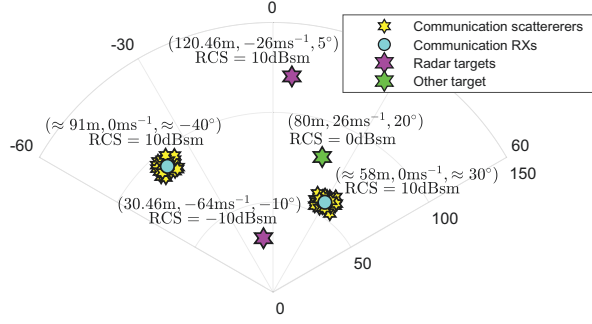
Figure 5.1 The simulation scenario with targets' ranges, velocities, DoAs, and RCSs.

5.4.1 Joint CRLB Minimization

First, the improvements obtained through waveform optimization are discussed. Second, the performance improvements in radar processing due to optimized sensing streams are presented. Results for both *LoS scenario* and *NLoS scenario* are presented, as discussed in Section 3.2. Since there are no separate sensing streams in the former, waveform optimization cannot be performed. Hence, only the results for radar processing are discussed for the former, while radar processing and waveform optimization results are presented for the latter.

For the simulations, the MIMO system is assumed to work around $f_c = 28$ GHz, having $L_T = L_{R,r} = 32$ antennas in the TX and RX sides, with $L_T^{RF} = L_{R,r}^{RF} = 8$ RF chains. In addition, for communications, $U_c = 2$, with $S_{c,u} = 2$, while for sensing $U_r = 2$ with a single radar stream at each sensing direction, i.e., $S_r = U_r$. The waveform parameters are $M = 50$ OFDM symbols and $N = 3168$ subcarriers with a spacing of $\Delta f = 120$ kHz. The total power of the streams is fixed at $P_t = 40$ dBm. The communications power is given by $P_c = \beta P_t$ where $\beta \in [0, 1]$ proportionately divides the power between the communications and sensing streams.

NLoS Scenario

Figure 5.1 shows the targets considered for the simulations. There are two communications users and two radar targets, and another target is also placed at a different direction to them. Specifically for the communications RXs, 20 point targets are considered to be situated around them to simulate NLoS multipath communications channels, as illustrated similarly in Fig. 3.2(a).
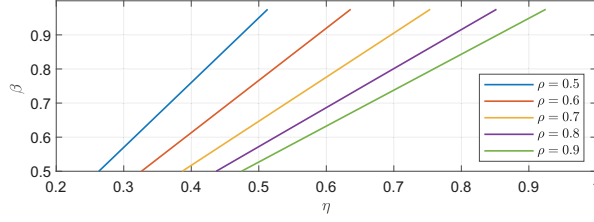
Figure 5.2 Variation of β for different η values.
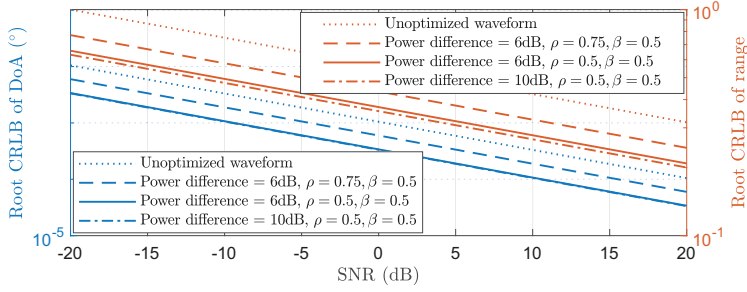
(a) Variation of root CRLBs with SNR
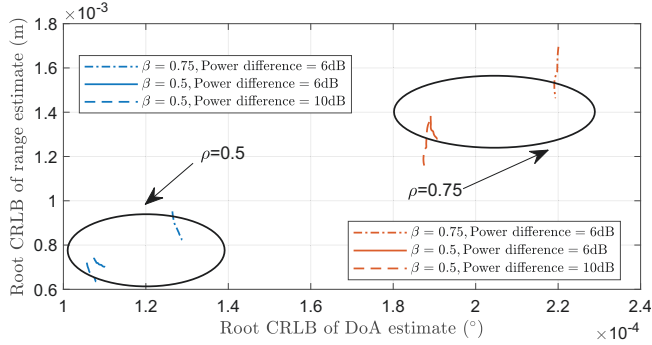
(b) Trade-off between the two root CRLBs due to the joint optimization. For the unoptimized waveform with $\rho = \beta = 1$, root CRLBs are given by $(0.000332°, 0.0032m)$

Figure 5.3 Variation of the root CRLBs due to the joint optimization.

Figure 5.2 depicts the dependence of β on η in (5.27c), for different ρ values. As in (3.35), ρ controls the gains between communications and sensing in the TX RF beampattern, while β controls the power between the two sets of streams since $P_c = \beta P_t$ or $P_r = (1-\beta)P_t$. For a particular ρ, an increase of η increases β, since the TX power needs to be increased to improve the communications capacity. Moreover, the same capacity can be achieved for a low β if ρ can be increased.
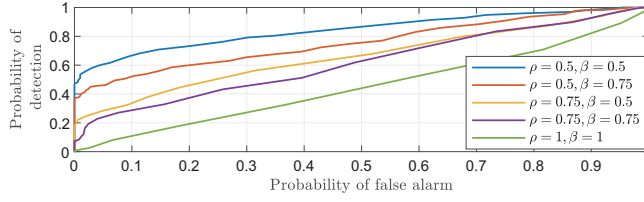
Figure 5.4 The ROC for the radar target at $5°$.

The improvement of the CRLBs is then depicted in Fig. 5.3. First, Fig. 5.3(a) depicts the root CRLBs of the separate delay and DoA estimations (as discussed in Section 5.2.2) as a function of SNR. Here, 'Power difference' indicates the difference in powers between $P_{\max}$ and a communications subcarrier in decibels. Optimizing the waveform improves both CRLBs when compared with the communications-only (unoptimized) waveform. As ρ decreases, CRLBs also decrease due to increased power in terms of TX beamforming for sensing purposes. Increasing the power difference also decreases the CRLBs since that increases $P_{\max}$, thereby decreasing the number of activated subcarriers, which allows maximizing the functions in (5.26a) and (5.26b).

Figure 5.3(b) then illustrates the effect of the joint CRLB minimization when the SNR is fixed at 10 dB. It is observed that decreasing β minimizes the CRLBs since it increases the power of the sensing streams. Moreover, each curve in this figure illustrates the trade-off between the two CRLBs. Additionally, the joint optimization minimizes the CRLBs compared to the communications-only scenario. Although the absolute values of the two CRLBs are very low, it is next illustrated that they improve the sensing performance. Therefore, minimizing the theoretical metric of CRLB enables improvement in the performance also in a practical scenario.

The sensing performance due to waveform optimization is first evaluated through the ROC curve, which is calculated empirically. For this, the radar target in $5°$ is placed at different, uniformly distributed ranges over many iterations. Next, using the corresponding range–angle map, the average power value is calculated for a set of range and angle bins surrounding the target's actual DoA and range values to obtain the detection probabilities. Similarly, false alarm probabilities are calculated when the target is not placed there. Figure 5.4 shows the results for the ROC for different ρ and β values. It shows that decreasing ρ or β improves the ROC since more power is allocated for the sensing beams and streams, respectively.
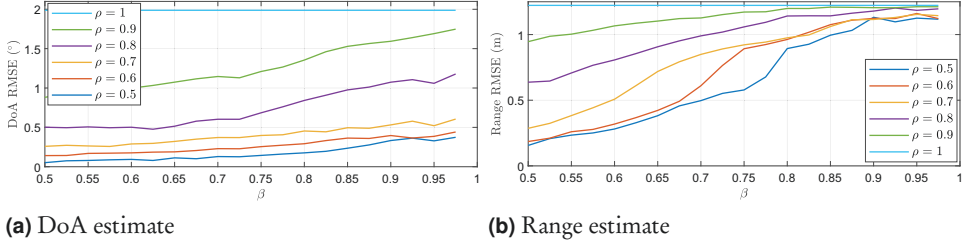
(a) DoA estimate

(b) Range estimate

Figure 5.5 The RMSEs of DoA and range estimates for the radar target at $5°$.

(a) Trade-off between DoA RMSE and η

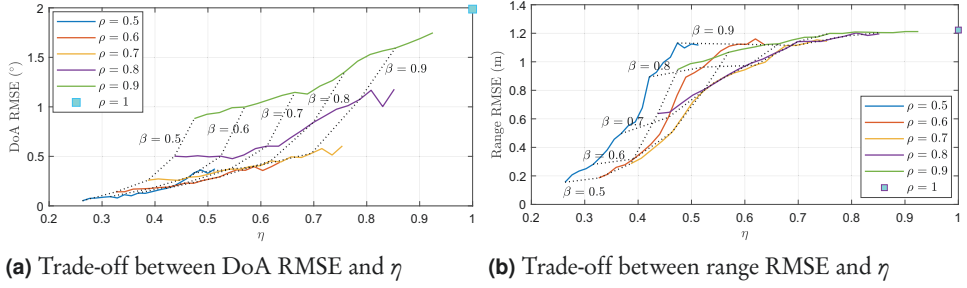**(b)** Trade-off between range RMSE and η

Figure 5.6 The communications and sensing performance trade-off.

Secondly, the sensing performance is evaluated through the RMSEs of DoA and range estimates. For this, the radar target's range is also considered to be uniformly distributed over many iterations, and the RMSEs are calculated based on the range–angle map. These results are shown in Figs. 5.5(a) and 5.5(b) separately for the two estimates. The general trend from both figures is that increasing either ρ or β increases the RMSEs since more power is allocated for communications. Moreover, the worst RMSE values are obtained for the communications-only case.

Figure 5.6 depicts the trade-off between the sensing performance illustrated in Fig. 5.5 and the communications performance in Fig. 5.2, for different ρ and β values. For the trade-off between the DoA RMSE and η in Fig. 5.6(a), when ρ is low, i.e., $\rho \leq 0.7$, η can be increased while keeping the DoA RMSE almost under $0.5°$. Hence, for those ρ values, allocating more power for communications does not necessarily reduce the sensing performance too much. However, when $\rho = 0.8$ or 0.9, increasing η is observed to increase the DoA RMSE much fast. In addition, the figure also shows the dependence of β on communications and sensing performance. For $\rho \leq 0.7$, an increase of β affects both systems' performance rather mildly, but when $\rho = 0.8$ or 0.9, its increase can be observed to affect either performance considerably.

Figure 5.6(b) depicts a similar trade-off for the range RMSE. However, when $\rho \leq$ 0.6, an increase of η increases the RMSE of range much faster, compared to when $\rho \geq$ 0.7. A similar trend is observed w.r.t. the β values. Therefore, these figures depict that generally β and ρ should be high (closer to 1) for improved communications, while for sensing, they should be low (closer to 0.5). Hence, it is important to choose these optimization parameters to obtain a good trade-off between communications and sensing.

Finally, Fig. 5.7 illustrates the range–angle and range–velocity maps obtained for sensing-only, communications-only, and JCAS cases. For the sensing-only case, i.e., Figs. 5.7(a) and (d), radar targets' parameters are clearly detected. Although the other targets are not observed in the range–angle map, a glimpse of them can be observed in the range–velocity map. For the case when only communications are performed, i.e., Figs. 5.7(b) and (e), the information that can be gained is not enough or not consistent with the actual targets' parameters. However, for the JCAS case, i.e., Figs. 5.7(c) and (f), all targets' parameters are detected. Therefore, this shows the importance of allocating more power for the radar beams and streams to sense the environment.

LoS Scenario

The range–angle maps in Figs. 5.7(a)–(c) correspond to the *NLoS scenario*, discussed in Section 3.2. Similarly, Fig. 5.8 depicts the range–angle maps corresponding to the *LoS scenario*. Here, Figs. 5.8(a), (b), and (c) show the range–angle maps obtained with the MF response as a reference, while Figs. 5.8(d), (e), and (f) are with the proposed MUSIC processing. The two main differences w.r.t. the targets in the *LoS scenario* when compared to the *NLoS scenario* as depicted in Fig. 5.1 are that no point scatterers are surrounding the communications RXs (due to LoS), while all targets have zero velocity. Hence, the radar channel is time-invariant and there are LoS conditions to all targets w.r.t. the MIMO TRX.

In the MF approach, the range bin values are combined using (5.3)–(5.6) for a specific θ. The range–angle map for a specific TX stream is obtained by performing this for $\theta \in [-90°, 90°]$. In the MUSIC-based approach, range–profiles are combined also using (5.3)–(5.6), but only for the two radar directions. However, for both cases, the different range–angle maps for the two sets of streams are combined using (5.12).
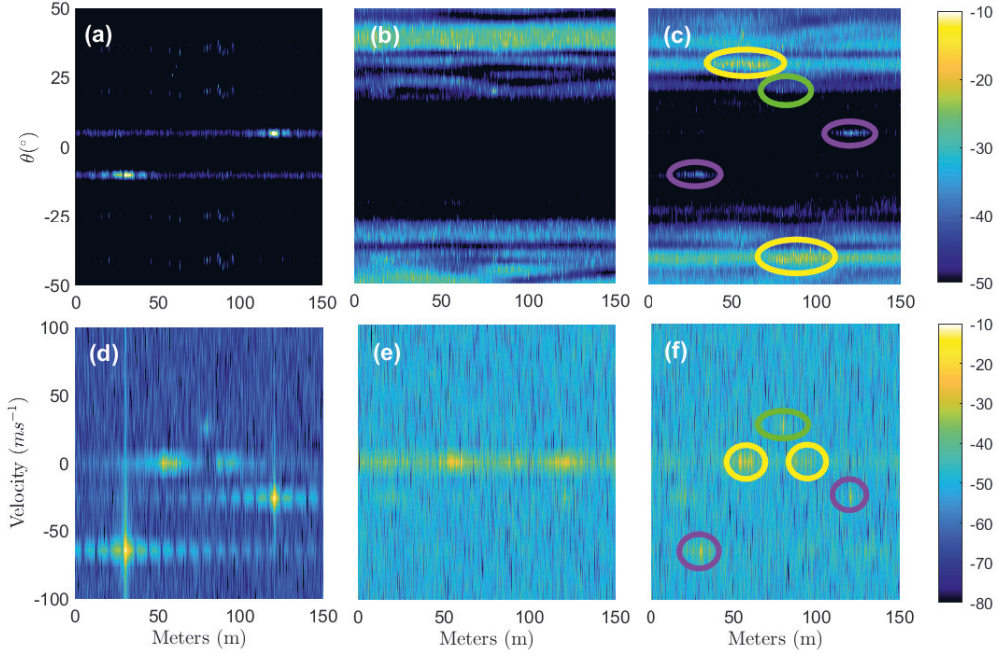
Figure 5.7 Range–angle maps in (a),(b), and (c), while range–velocity maps in (d), (e), and (f). Each column shows the maps for sensing-only ($\rho, \beta = 0$), communications-only ($\rho, \beta = 1$), and JCAS ($\rho, \beta = 0.5$), respectively. The targets in Fig. 5.1 are also circled for ease of comparison.

Figures 5.8(a) and (b) show that the communications and radar targets' ranges in the MF approach are clearly illustrated, but there are ambiguities in the angular domain. These are due to the appearance of grating lobes in the effective beampattern (combination of RF and BB) of the MIMO RX in hybrid architectures. This approach's combined range–angle map in Fig. 5.8(c) more clearly shows the directional ambiguities. Hence, it is difficult to pinpoint the actual targets' angles.

In contrast, MUSIC-based approach detects the communications and radar targets' ranges and angles with fewer ambiguities. Although there are ambiguities in the maps of the first and second TX streams as in Figs. 5.8(d) and (e), combined map in Fig. 5.8(f) has almost no ambiguities, showing the superiority of the proposed radar processing over the MF-based approach. The first communications RX is not detected in the range–angle map of the second TX stream and vice versa. This is because each communications user has a null at the other user's direction in the TX beampattern, as in Fig. 3.4(c). However, since both streams are transmitted in radar directions, the radar targets are observed in each TX stream's range–angle map.

95
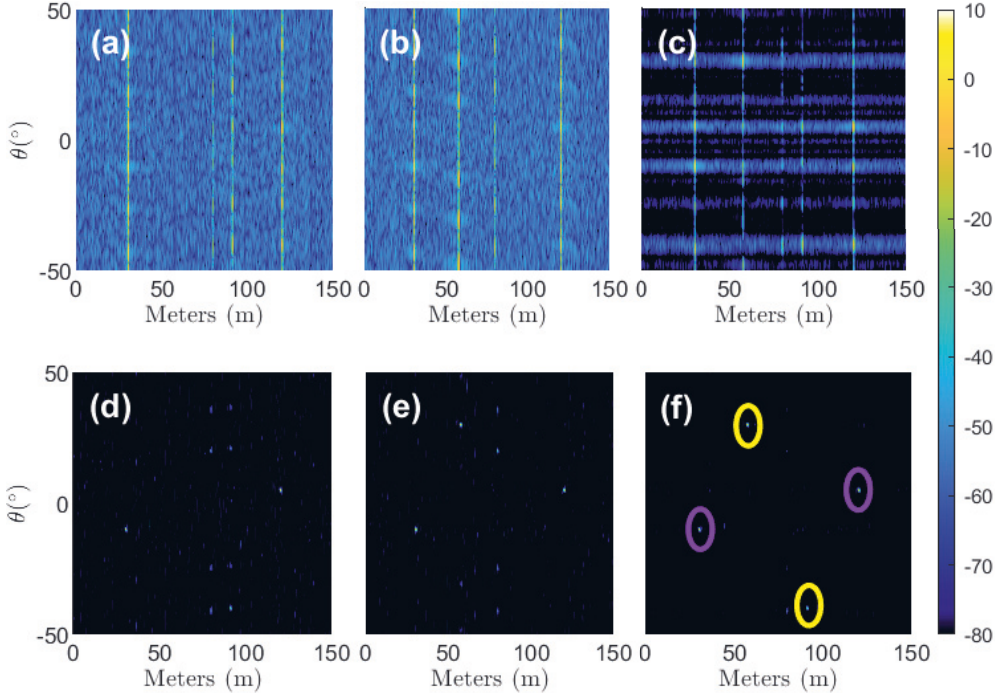
Figure 5.8 Range–angle maps in (a),(b), and (c), correspond to the ones obtained from the first TX stream, second TX stream, and the combination of two streams, respectively, obtained using the MF response. Range–angle maps in (d),(e), and (f), correspond to the ones obtained using MUSIC processing for the same TX streams.

In both MF-based and MUSIC-based processing in *LoS scenario*, the 'other' target is not detected quite well when compared to that in the *NLoS scenario* maps in Fig. 5.7. The reason for this lies in the TX beampattern of the two scenarios. Figure 3.4(c) depicts the TX beampattern in the *LoS scenario*, where the gain at $20°$ is almost 0dBi, i.e., attenuated by around $10-15$ dB for the two streams compared to the peaks. It is the same for all frequencies since BB beamforming is the same. In contrast, the TX beampattern of the *NLoS scenario* illustrated in Fig. 3.6 shows that depending on the ρ value, the gain at $20°$ can vary. Moreover, since the BB beamforming differs for different frequencies, some frequencies can have a gain comparable with the main-lobe gain. As such, the 'other' target can also be detected, as shown in Fig. 5.7.

(a) The TX beampattern for different S_r values

(b) The magnitude of the TX beampattern at θ_c and θ_r directions
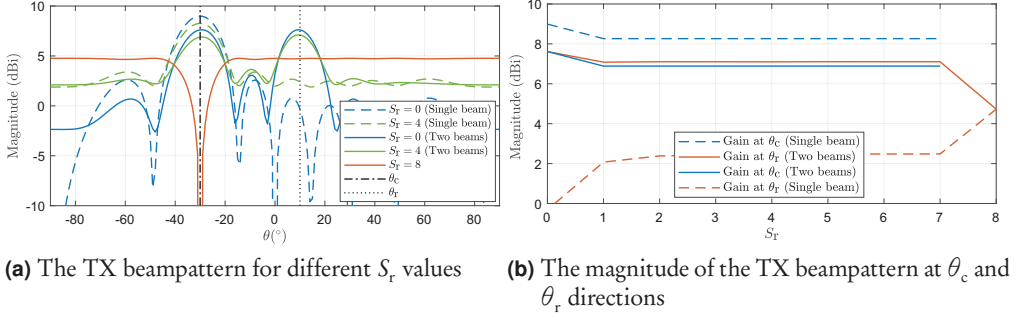
Figure 5.9 The TX beampattern and its gains at θ_c and θ_r for different number of independent radar streams S_r.

5.4.2 Improvement of MIMO AF

The parameters considered for the simulations are: each TX stream being an OFDM waveform with $M = 10$ OFDM symbols and $N = 256$ active subcarriers, a fully-digital architecture with $L_T = L_{R,r} = 8$ antennas, TX streams power of $P_t = 30$ dBm, and $\theta_c = -30°$ and $\theta_r = 10°$. In addition, the frequency-domain samples of the radar streams are considered to be Gaussian distributed.

First, Fig. 5.9(a) shows the TX beampatterns for different numbers of independent radar streams S_r in (5.46). The gain in each direction is obtained through

$$P(\theta) = \mathbb{E}\{|\mathbf{a}_T^H(\theta)\mathbf{W}_T^{BB}\mathbf{x}(t)|^2\}. \tag{5.51}$$

When there are not any radar streams (only communications stream), i.e., $S_r = 0$, the beampattern corresponds to the MF response in *single-beam* and *two-beams* cases, as in (5.40) and (5.45), respectively. For the former, there is a single beam at θ_c, while for the latter, there are two beams at θ_c and θ_r, as expected. When $S_r \neq 0$, radar beampatterns corresponding to the radar streams have random beampatterns obtained through (5.50). The beampatterns shown in Fig. 5.9(a) are the average for such different random radar beampatterns over many iterations, also including the communications beampattern obtained through the MF.

When $S_r = 4$, the gains at θ_c/θ_r are reduced by a little compared to $S_r = 0$. This happens due to the inclusion of random radar beampatterns. For a single iteration, the radar beampattern of a radar stream would be random, having a null at θ_c. How-

ever, averaging over multiple iterations would result in an average radar beampattern with uniform gain over all directions except at θ_c. Then, when this average radar beampattern is concatenated with the communications-only beampattern, the gain at θ_c is decreased a little due to the null of the average radar beampattern. The gain at θ_r in *two-beams* case also decreases since the gain at θ_r for $S_r = 0$ is higher than the gain at that direction of the average radar beampattern. These observations result in the TX beampattern observed in Fig. 5.9(a) for $S_r = 4$. Finally, when $S_r = 8$, only radar streams exist without the communications stream. As a result, a null is observed at θ_c while the gain is uniform across all other directions.

Secondly, Fig. 5.9(b) illustrates the gains at θ_c and θ_r. The gain at θ_c is the highest for both cases when $S_r = 0$. The gain decreases after introducing a single radar stream and remaining constant after that. When $S_r = 8$, since there is a null at that direction, a gain cannot be defined which is why it does not contain any point in the curve. For θ_r, the lowest gain is when $S_r = 0$ in the *single-beam* case since only a main-beam at θ_c exists. Next, increasing S_r increases the gain in that direction. An opposite behavior is observed for θ_r for the *two-beams* case.

Next, Fig. 5.10 depicts the angle profile of the MIMO AF along θ_2 when $\theta = \theta_1 = -5°$, based on (5.41). It shows that when $S_r = 0$ and for either of the beamforming cases, the peak of the angle profile does not coincide for $\theta_2 = -5°$, while there are significant side-lobes in other directions as well. For radar processing, this means that whenever there is a target at an actual angle of $-5°$, it is observed a little bit shifted in the angular domain, while there will also be peaks in other directions that act as false targets. This, in turn, represents the ambiguity observed in the angle profile of the MIMO AF whenever single-stream communication is performed. However, having $S_r = 8$ allows the main peak to coincide exactly on $5°$ while significantly decreasing the ambiguities observed in other directions.
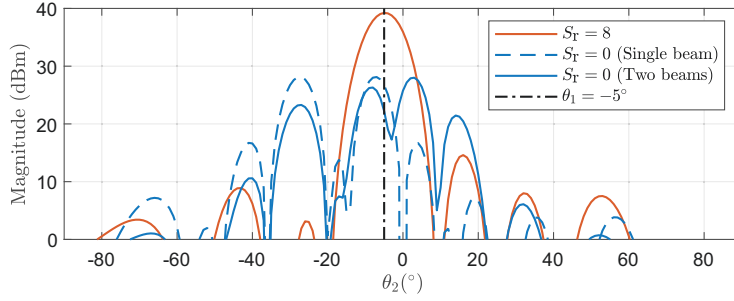
**Figure 5.10**   Angle profile of MIMO AF corresponding to $\theta_1 = -5°$.

Figure 5.11 illustrates the performance improvement of ISL values due to independent radar streams. Figure 5.11(a) first depicts the ISL values observed in the MIMO AF's angle profile for all possible target directions when $P_c - P_r = 4$ dB, as in (5.47). It shows that the worse ISL values are observed for both beamforming cases when $S_r = 0$. The best ISL values for single-stream communication are observed around θ_c/θ_c and θ_r respectively for the *single-beam* and *two-beams* cases since most of the energy is used at those directions due to the main beams of the TX beampattern. However, the increase of S_r is observed to decrease the ISL values, thereby decreasing the ambiguities in the angle profile. Moreover, when $S_r = 8$, there is a peak at $\theta_1 = \theta_c$, due to the deep null of the TX beampattern in Fig. 5.9(a) at the same direction, i.e., since there is not any TX power at that direction, even if there is an actual target at that direction, it will not be observed.

Figure 5.11(b) then depicts the variation of the ISL values for $\theta_1 = -15°$ when the power allocation between the communications and radar streams is changed. By allocating more power for the radar streams but at the cost of decreasing the power of the communications stream, the ISL values can be decreased, thereby also decreasing the ambiguities.

Finally, Fig. 5.11(c) shows the ISL values observed in the MIMO AF's delay profile. The best ISL value is when $S_r = 0$, while the increase of S_r increases the ISL values, with the highest ISL value observed when $S_r = 8$. However, the delay profile's ISL values are quite low when compared to those of the angle profile, showing that OFDM waveforms already have low side-lobes in the delay profile. Hence, it can be noted that including independent radar streams reduces the angle ambiguity while almost keeping the delay ambiguity the same. The ISL values can be slightly modified by changing S_r, as denoted within the embedded plot.
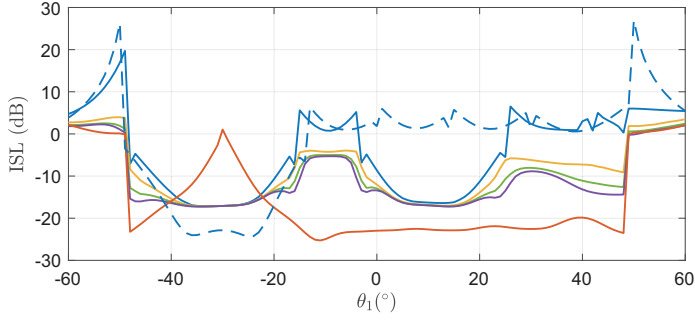
(a) The ISL values of the MIMO AF's angle profile for $P_c - P_r = 4$ dB
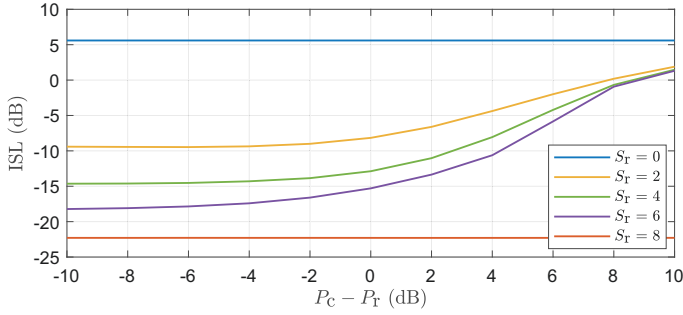
(b) The variation of ISL values of MIMO AF's angle profile of $\theta_1 = -15°$ for different $P_c - P_r$ values
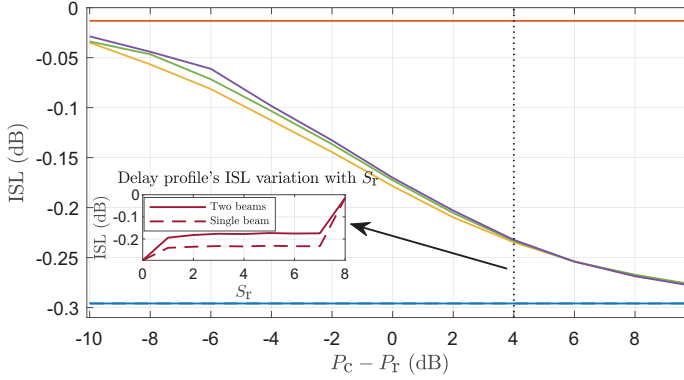
(c) The ISL values of the MIMO AF's delay profile at $\theta_1 = \theta_2 = -15°$ for different $P_c - P_r$ values

Figure 5.11 The ISL variation of angle and delay profiles of the MIMO AF, where the blue-dashed curve in (a) corresponds to $S_r = 0$ with a single beam, while all others are with two beams.

6

Conclusions

This thesis discussed including sensing on top of a modern communications system such as in 5G. The main focus is OFDM waveform optimization, which achieves an optimal trade-off between communications and sensing. In addition, this thesis also investigated radar processing needed in MIMO JCAS systems in obtaining the ranges, velocities, and directions-of-arrival (DoAs) of different targets in the environment. Towards this end, first, the following section points out the main conclusions of the thesis. Second, the overall summary of the thesis is discussed, followed by prospects that could be pursued using the work in this thesis as a baseline.

6.1 Conclusions and Summary

The main conclusions of the thesis, in line with objectives in Chapter 1 are as follows.

- For SISO JCAS systems, the Pareto trade-off between the two functionalities can be obtained by optimally sharing the frequency resources. Hence, co-designing such systems allows intelligent utilization of the available scarce spectrum so as not to inhibit the performance of either system. Once the required performance trade-off is derived, the operating point, e.g., the portion of bandwidth allocated to each system, can be selected based on a certain application. For instance, if many communications users need to be catered, e.g., in a public gathering, all the bandwidth can be allocated for that purpose, while if there are not that many users, e.g., in a rural area, more bandwidth can be used for radar purposes. Hence, the proposed resource allocation is flexible.

- Future mobile communications systems will feature massive MIMO antenna arrays with a hybrid architecture comprising many antenna elements for the TX and RX. Multiple TX streams will inevitably be used to provide service to many users. Hence, radar processing in such systems is crucial in gaining knowledge about the surrounding environment. Especially one of the key objectives in 6G systems is to provide a bridge between the physical and the digital worlds [104], and the proposed radar processing in the thesis helps to bridge the gap. The information gained from sensing can be used to enhance the performance of the communications users further. For example, knowing the directions of static clutter can help the MIMO TX decide the best precoding and combining necessary to maximize energy transmission in the required directions, not in unwanted directions.

- In including separate OFDM sensing streams on top of the communications streams for MIMO JCAS systems, special attention needs to be given to deciding the powers allocated to the two sets of streams to obtain an optimal trade-off. However, the advantage of having separate streams for sensing is that they can be optimized fully for sensing purposes, improving either detection or estimation metrics of sensing without modifying communications streams. They can also be transmitted in arbitrary directions, which provide more information in terms of sensing due to receiving reflections from these directions. An important remark to note here is that the sensing streams will cause radar–communications interference for the communications users. Thus, precoding and combining must be designed to cancel this interference.

The main results of the thesis and their summary are discussed next. The first set of results concerns waveform optimization in SISO JCAS systems. Precisely, the unused subcarriers within the OFDM waveform are filled with optimized samples to jointly minimize the CRLBs of range and velocity estimates. Hence, some TX power of the communications-only subcarriers, i.e., data and control, is reallocated in filling the empty subcarriers, which, once filled, are called *radar subcarriers*. In addition, only the amplitudes of the subcarriers' samples affect the joint optimization, not their phases. Therefore, phases of the radar subcarriers are further optimized to minimize the PAPR of the TX signal.

Although joint optimization minimizes the theoretical metric of CRLB, the thesis demonstrates that it also improves practical performance metrics. By appropri-

ately choosing the optimization parameters, the main-lobe widths and side-lobes of either range or velocity profile can be minimized when compared with using a communications-only waveform without radar subcarriers. In addition, the practical counterpart of CRLB, i.e., RMSE, of either estimate can also be minimized through this optimization. Apart from these improvements observed in sensing, the PAPR of the communications TX waveform can also be reduced through phase optimization of the radar subcarriers, thereby improving the efficiency of the power amplification process in transmission. In addition, appropriately choosing the power allocation and the optimization parameters are essential to obtain an optimal trade-off between CRLB minimization and communications capacity.

The side-lobe suppression due to optimizing the waveform through CRLB minimization is investigated further through experimental RF measurements. For this, a standard-compliant 5G NR waveform is used to sense an outdoor environment with the system operating at a mm-wave frequency of 28 GHz. The results illustrate that optimizing the waveform gives considerable performance gain by minimizing the side-lobes of the radar image, which also helps reduce the overall clutter level.

The next set of results of the thesis is regarding radar processing from the perspective of a MIMO communications system with hybrid architecture. In such an architecture, RX samples that can be used for radar processing convey less information about the targets of the environment due to dimensionality reduction compared to a fully-digital architecture. Moreover, the TX signals at the different antenna elements are not necessarily orthogonal in a MIMO communications system. In addition, the existence of multiple data streams can also complicate radar processing. Therefore, radar processing for such a system must consider all these issues.

In MIMO JCAS systems, multiple TX streams of the communications users can be used for sensing the environment. For the first set of results, static radar targets are considered while also assuming frequency-independent communications channels with LoS conditions to the communications users w.r.t. the MIMO TRX. Apart from transmitting the streams of the respective users in their directions, all communications streams are transmitted in a separate sensing direction. The received reflections from the streams are then used to obtain the range–angle map of the environment through novel radar processing techniques. The results show that super-resolution can be achieved in DoA estimation, allowing differentiation between two nearby targets with minute separation in the angular domain. Moreover, the pro-

posed radar processing is shown to work considerably better than the conventional matched-filtering approach, depicting the effectiveness of the radar processing.

In contrast, separate TX streams for sensing can also be used while also considering the users' channels to be frequency-selective with NLoS conditions and moving radar targets; thus, a more advanced system for the second set of results. The MIMO TRX's, and the communications users' beamformers, are also designed appropriately to cancel the inter-user and intra-user interference, as well as the radar–communications interference due to the separate sensing streams. The radar processing is also extended to perform velocity estimation, thus obtaining the range–velocity map in addition to the range–angle map.

The final set of results discusses utilizing the sensing TX streams to improve the sensing performance, i.e., joint waveform design for MIMO JCAS systems. One strategy for the waveform design involves optimizing the sensing streams to jointly minimize the CRLBs of range and DoA estimates. The results here illustrate that the joint optimization improves the receiver operating characteristics (ROC) of sensing while minimizing the RMSEs of range and DoA estimates. Therefore, similar to the waveform optimization of SISO systems, optimizing the MIMO waveform also improves performance in a practical scenario.

The second strategy in using separate sensing streams is to enhance the MIMO AF. Here, a fully-digital MIMO system's AF is derived, which is a function of the range, velocity, and DoA of a radar target. Conventional 2-D AF of range and velocity variables of OFDM waveforms has the required thumbtack shape because OFDM is noise-like. However, in considering the AF of MIMO systems, the DoA variable also becomes important. Performing only single-stream communication can result in high ambiguities in MIMO AF's angle profile, reducing the sensing performance due to the emergence of many false targets. To alleviate this issue of ambiguities, separate sensing streams can be used in conjunction with the communication stream to reduce the ambiguities. The sequential increase in the number of separate sensing streams results in further decreasing the ambiguities.

Therefore, the thesis has contributed to the domain of JCAS by providing effective waveform optimization strategies that allow obtaining an optimal performance trade-off between the communications and sensing functionalities. In addition, efficient radar processing techniques are proposed for MIMO systems to visualize the surrounding environment better.

6.2 Future Work

This section outlines the future work that can be performed by using the work in the thesis as a baseline.

Recently, research on wireless communications systems has evolved quickly, with one of the major contributors being the development of future 6G systems. The 6G systems will work around much higher carrier frequencies, e.g., terahertz, enabling much more frequency bandwidth. Further, they will cater to high-mobility scenarios. Hence, in these systems, frequency dispersion increases due to the Doppler-shift and phase noise, which are, in fact, significant challenges in using OFDM waveforms [103]. Therefore, although OFDM has been used as the standard waveform in 4G and 5G, the development of 6G systems may result in utilizing a different candidate waveform, e.g., orthogonal time-frequency space (OTFS) [45]. Such a waveform would encompass some properties of OFDM, if not all. Therefore, the work in this thesis needs to be extended to use such a novel waveform to incorporate with future JCAS systems.

The PAPR minimization scheme applied in the thesis for SISO JCAS systems involved an exhaustive search. The idea was to illustrate the performance improvements that can be realized by also optimizing the phases of the radar subcarriers, in addition to optimizing the amplitudes for CRLB minimization. As a result, the PAPR minimization cannot be applied directly to a real-time system. Hence, once the waveform is optimized to minimize the CRLBs, a new approach needs to be used to further optimize the phases of the radar subcarriers with less complexity. In addition, the effect of optimizing the phases was only evaluated through the improvement of the PAPR. Observing how phase optimization affects the side-lobes in either range or velocity profile would also be interesting.

The MIMO AF enhancement procedure involved separate random sensing TX streams on top of the communication stream. There, the beamforming matrix of the sensing streams is designed based on the null-space projection to cancel the radar–communications interference while also ascertaining that each beamforming vector of a sensing stream is random and orthonormal. Hence, the method adopted in the thesis is of low complexity while improving performance significantly. However, the TX sensing streams and their beamforming matrix could be designed based on an explicit optimization problem to minimize ambiguities further. Although

it may increase the complexity, it would be beneficial to observe the possible improvements, thereby allowing to decide whether to use a high or low-complexity method for a given application. Since the radar beamforming matrix controls radar–communications interference, observing the trade-off between fully optimizing the matrix to minimize ambiguities and using null-space projection to cancel radar–communications interference would be interesting.

Similarly, OFDM waveform optimization discussed for the MIMO JCAS system involved choosing the sensing streams' beamforming matrix to cancel radar–communications interference and optimizing the OFDM waveform to minimize the CRLBs. Instead, the OFDM waveform and the beamforming matrix could be optimized together to minimize the CRLBs, and then observe the trade-off between the CRLB minimization and the radar–communications interference cancellation.

Moreover, TX beamforming for MIMO JCAS systems with LoS conditions is performed using numerical optimization where the gains at the needed directions are maximized. However, TX beampattern's side-lobes are not considered, where their existence would mask weak targets. Hence, an additional constraint can be added for side-lobe minimization. Although the new constraint can incur high complexity, it would be beneficial to observe if such a constraint can indeed further improve the JCAS performance.

Waveform optimization for single-antenna and multi-antenna systems involved in single-target CRLB minimization. However, optimizing the waveform by considering multi-target CRLB minimization would be beneficial for a scenario where multiple targets need to be detected. Therefore, the difference between single-target and multi-target CRLB minimization problems would be an interesting topic. In addition, how the latter minimization affects the different parameters, e.g., side-lobes, main-lobe widths, and RMSEs, would also be interesting.

An important concept related to the works of the thesis is standardization aspects. For instance, waveform design for SISO JCAS systems focuses on filling up the unused subcarriers in the OFDM waveform with optimized samples such that a part of the TX power is reallocated to them. However, in practical communications systems, filling up any unused subcarrier with some power might not be possible due to different constraints, e.g., interference to some other wireless system or insufficient TX power for reallocation due to link budget. In such a scenario, the industry must standardize the different aspects of waveform optimization, e.g., a dedicated set of

subcarriers out of the unused subcarriers that can be filled with optimized samples or total maximum power that can be reallocated to filling the empty subcarriers.

Another instance where standardization becomes essential is related to multi-stream waveform design for MIMO JCAS systems. There, separate sensing streams are reallocated a portion of the total TX power, which needs to be standardized. Further, the sensing TX streams require suitable precoding and combining design to prevent radar–communications interference. Hence, if a codebook-based approach is used to design them, they must also be standardized. Especially since there are already discussions on JCAS being one of the key features in future 6G systems, e.g., the European 6G flagship project (Hexa-X) [104], the industry needs to consider the standardization aspects related to joint waveform design, as proposed by the thesis.

References

[1]   3GPP TS 38.104 v15.10.0, "NR; Base Station (BS) radio transmission and reception", Tech. Spec. Group Radio Access Network, Rel. 15. (July 2020).

[2]   T. Aittomäki and V. Koivunen. Radar Waveform Sidelobe Level Optimality and Sampling. *IEEE Signal Processing Letters* 23.3 (Mar. 2016), 371–375. DOI: 10.1109/LSP.2016.2515361.

[3]   M. Alaee-Kerahroodi, K. V. Mishra, M. R. Bhavani Shankar and B. Ottersten. Discrete-Phase Sequence Design for Coexistence of MIMO Radar and MIMO Communications. *Proc. IEEE International Workshop on Signal Processing Advances in Wireless Communications*. July 2019. DOI: 10.1109/SPAWC.2019.8815508.

[4]   M. Alloulah and H. Huang. Future Millimeter-Wave Indoor Systems: A Blueprint for Joint Communication and Sensing. *Computer* 52.7 (July 2019), 16–24. DOI: 10.1109/MC.2019.2914018.

[5]   F. Arlery, R. Kassab, U. Tan and F. Lehmann. Efficient gradient method for locally optimizing the periodic/aperiodic ambiguity function. *Proc. IEEE Radar Conference*. May 2016. DOI: 10.1109/RADAR.2016.7485309.

[6]   A. Arora, C. G. Tsinos, B. S. M. R. Rao, S. Chatzinotas and B. Ottersten. Hybrid Transceivers Design for Large-Scale Antenna Arrays Using Majorization-Minimization Algorithms. *IEEE Transactions on Signal Processing* 68 (Dec. 2019), 701–714. DOI: 10.1109/TSP.2019.2957611.

[7] A. Aubry, A. D. Maio, Y. Huang, M. Piezzo and A. Farina. A new radar waveform design algorithm with improved feasibility for spectral coexistence. *IEEE Transactions on Aerospace and Electronic Systems* 51.2 (Apr. 2015), 1029–1038. DOI: 10.1109/TAES.2014.140093.

[8] A. Aubry, V. Carotenuto, A. De Maio, A. Farina and L. Pallotta. Optimization theory-based radar waveform design for spectrally dense environments. *IEEE Aerospace and Electronic Systems Magazine* 31.12 (Dec. 2016), 14–25. DOI: 10.1109/MAES.2016.150216.

[9] O. E. Ayach, S. Rajagopal, S. Abu-Surra, Z. Pi and R. W. Heath. Spatially Sparse Precoding in Millimeter Wave MIMO Systems. *IEEE Transactions on Wireless Communications* 13.3 (Mar. 2014), 1499–1513. DOI: 10.1109/TWC.2014.011714.130846.

[10] A. Bandi, B. Shankar M. R, S. Chatzinotas and B. Ottersten. A Joint Solution for Scheduling and Precoding in Multiuser MISO Downlink Channels. *IEEE Transactions on Wireless Communications* 19.1 (Jan. 2020), 475–490. DOI: 10.1109/TWC.2019.2946161.

[11] C. Baquero Barneto, T. Riihonen, M. Turunen, L. Anttila, M. Fleischer, K. Stadius, J. Ryynänen and M. Valkama. Full-Duplex OFDM Radar With LTE and 5G NR Waveforms: Challenges, Solutions, and Measurements. *IEEE Transactions on Microwave Theory and Techniques* 67.10 (Oct. 2019), 4042–4054. DOI: 10.1109/TMTT.2019.2930510.

[12] C. Baquero Barneto, M. Turunen, S. D. Liyanaarachchi, L. Anttila, A. Brihuega, T. Riihonen and M. Valkama. High-Accuracy Radio Sensing in 5G New Radio Networks: Prospects and Self-Interference Challenge. *Proc. Asilomar Conference on Signals, Systems, and Computers*. Nov. 2019, 1159–1163. DOI: 10.1109/IEEECONF44664.2019.9048786.

[13] C. Baquero Barneto, S. D. Liyanaarachchi, M. Heino, T. Riihonen and M. Valkama. Full Duplex Radio/Radar Technology: The Enabler for Advanced Joint Communication and Sensing. *IEEE Wireless Communications* 28.1 (Feb. 2021), 82–88. DOI: 10.1109/MWC.001.2000220.

[14] C. Baquero Barneto, S. D. Liyanaarachchi, T. Riihonen, L. Anttila and M. Valkama. Multibeam Design for Joint Communication and Sensing in 5G

New Radio Networks. *Proc. IEEE International Conference on Communications (ICC)*. June 2020. DOI: 10.1109/ICC40277.2020.9148935.

[15]   C. Baquero Barneto, S. D. Liyanaarachchi, T. Riihonen, M. Heino, L. Anttila and M. Valkama. Beamforming and Waveform Optimization for OFDM-based Joint Communications and Sensing at mm-Waves. *Proc. 54th Asilomar Conference on Signals, Systems, and Computers*. Nov. 2020, 895–899. DOI: 10.1109/IEEECONF51394.2020.9443340.

[16]   C. Baquero Barneto, T. Riihonen, S. D. Liyanaarachchi, M. Heino, N. González-Prelcic and M. Valkama. Beamformer Design and Optimization for Joint Communication and Full-Duplex Sensing at mm-Waves. *IEEE Transactions on Communications* 70.12 (Dec. 2022), 8298–8312. DOI: 10.1109/TCOMM.2022.3218623.

[17]   I. Bekkerman and J. Tabrikian. Target Detection and Localization Using MIMO Radars and Sonars. *IEEE Transactions on Signal Processing* 54.10 (Oct. 2006), 3873–3883. DOI: 10.1109/TSP.2006.879267.

[18]   M. Bell. Information theory and radar waveform design. *IEEE Transactions on Information Theory* 39.5 (Sept. 1993), 1578–1597. DOI: 10.1109/18.259642.

[19]   M. Bică, K.-W. Huang, V. Koivunen and U. Mitra. Mutual information based radar waveform design for joint radar and cellular communication systems. *Proc. IEEE International Conference on Acoustics, Speech and Signal Processing*. Mar. 2016, 3671–3675. DOI: 10.1109/ICASSP.2016.7472362.

[20]   M. Bică, K.-W. Huang, U. Mitra and V. Koivunen. Opportunistic Radar Waveform Design in Joint Radar and Cellular Communication Systems. *Proc. IEEE Global Communications Conference*. Dec. 2015. DOI: 10.1109/GLOCOM.2015.7417624.

[21]   M. Bică and V. Koivunen. Generalized Multicarrier Radar: Models and Performance. *IEEE Transactions on Signal Processing* 64.17 (Sept. 2016), 4389–4402. DOI: 10.1109/TSP.2016.2566610.

[22]   M. Bică and V. Koivunen. Multicarrier Radar-communications Waveform Design for RF Convergence and Coexistence. *Proc. IEEE International Conference on Acoustics, Speech and Signal Processing*. May 2019, 7780–7784. DOI: 10.1109/ICASSP.2019.8683655.

[23]   M. Bică and V. Koivunen. Radar Waveform Optimization for Target Parameter Estimation in Cooperative Radar-Communications Systems. *IEEE Transactions on Aerospace and Electronic Systems* 55.5 (Oct. 2019), 2314–2326. DOI: 10.1109/TAES.2018.2884806.

[24]   D. W. Bliss, K. W. Forsythe, S. K. Davis, G. S. Fawcett, D. J. Rabideau, L. L. Horowitz and S. Kraut. GMTI MIMO radar. *Proc. IEEE International Waveform Diversity and Design Conference*. Feb. 2009, 118–122. DOI: 10.1109/WDDC.2009.4800327.

[25]   D. Bliss and K. Forsythe. Multiple-input multiple-output (MIMO) radar and imaging: degrees of freedom and resolution. *Proc. IEEE Asilomar Conference on Signals, Systems, and Computers*. Vol. 1. Nov. 2003, 54–59. DOI: 10.1109/ACSSC.2003.1291865.

[26]   S. A. Busari, K. M. S. Huq, S. Mumtaz, L. Dai and J. Rodriguez. Millimeter-Wave Massive MIMO Communication for Future Wireless Systems: A Survey. *IEEE Communications Surveys and Tutorials* 20.2 (Dec. 2017), 836–869. DOI: 10.1109/COMST.2017.2787460.

[27]   S. Buzzi, C. D'Andrea and M. Lops. Using Massive MIMO Arrays for Joint Communication and Sensing. *Proc. Asilomar Conference on Signals, Systems, and Computers*. Nov. 2019. DOI: 10.1109/IEEECONF44664.2019.9048857.

[28]   M. R. Castellanos, V. Raghavan, J. H. Ryu, O. H. Koymen, J. Li, D. J. Love and B. Peleato. Hybrid Multi-User Precoding with Amplitude and Phase Control. *Proc. IEEE International Conference on Communications*. May 2018. DOI: 10.1109/ICC.2018.8422136.

[29]   C.-Y. Chen and P. P. Vaidyanathan. Properties of the MIMO radar ambiguity function. *Proc. IEEE International Conference on Acoustics, Speech and Signal Processing*. Apr. 2008, 2309–2312. DOI: 10.1109/ICASSP.2008.4518108.

[30]   A. R. Chiriyath, B. Paul, G. M. Jacyna and D. W. Bliss. Inner Bounds on Performance of Radar and Communications Co-Existence. *IEEE Transactions on Signal Processing* 64.2 (Jan. 2016), 464–474. DOI: 10.1109/TSP.2015.2483485.

[31]   A. R. Chiriyath, B. Paul and D. W. Bliss. Joint radar-communications in-
         formation bounds with clutter: The phase noise menace. *Proc. IEEE Radar
         Conference*. May 2016. DOI: 10.1109/RADAR.2016.7485311.

[32]   A. R. Chiriyath, S. Ragi, H. D. Mittelmann and D. W. Bliss. Novel Radar
         Waveform Optimization for a Cooperative Radar-Communications System.
         IEEE Transactions on Aerospace and Electronic Systems 55.3 (June 2019), 1160–
         1173. DOI: 10.1109/TAES.2019.2908739.

[33]   B. D. Cordill, S. A. Seguin and L. Cohen. Electromagnetic interference to
         radar receivers due to in-band OFDM communications systems. *Proc. IEEE
         International Symposium on Electromagnetic Compatibility*. Aug. 2013, 72–
         75. DOI: 10.1109/ISEMC.2013.6670384.

[34]   T. Cover and J. Thomas. *Elements of Information Theory*. Wiley, 2012. ISBN:
         9781118585771.

[35]   M. S. Davis, G. A. Showman and A. D. Lanterman. Coherent MIMO radar:
         The phased array and orthogonal waveforms. *IEEE Aerospace and Electronic
         Systems Magazine* 29.8 (Aug. 2014), 76–91. DOI: 10.1109/MAES.2014.
         130148.

[36]   S. H. Dokhanchi, M. R. Bhavani Shankar, K. V. Mishra and B. Ottersten.
         Multi-constraint Spectral Co-design for Colocated MIMO Radar and MIMO
         Communications. *Proc. IEEE International Conference on Acoustics, Speech
         and Signal Processing*. May 2020, 4567–4571. DOI: 10.1109/ICASSP40776.
         2020.9054680.

[37]   S. H. Dokhanchi, M. R. B. Shankar, M. Alaee-Kerahroodi and B. Ottersten.
         Adaptive Waveform Design for Automotive Joint Radar-Communication
         Systems. *IEEE Transactions on Vehicular Technology* 70.5 (May 2021), 4273–
         4290. DOI: 10.1109/TVT.2021.3072157.

[38]   S. H. Dokhanchi, M. R. B. Shankar, T. Stifter and B. Ottersten. OFDM-
         based automotive joint radar-communication system. *Proc. IEEE Radar Con-
         ference*. Apr. 2018, 0902–0907. DOI: 10.1109/RADAR.2018.8378680.

[39]   D. Falconer, S. Ariyavisitakul, A. Benyamin-Seeyar and B. Eidson. Frequency
         domain equalization for single-carrier broadband wireless systems. *IEEE Com-
         munications Magazine* 40.4 (Apr. 2002), 58–66. DOI: 10.1109/35.995852.

[40]   E. Fishler, A. Haimovich, R. Blum, L. Cimini, D. Chizhik and R. Valen-
         zuela. Spatial Diversity in Radars—Models and Detection Performance. *IEEE
         Transactions on Signal Processing* 54.3 (Mar. 2006), 823–838. DOI: `10.1109/
         TSP.2005.862813`.

[41]   K. W. Forsythe and D. W. Bliss. MIMO Radar Waveform Constraints for
         GMTI. *IEEE Journal of Selected Topics in Signal Processing* 4.1 (Feb. 2010),
         21–32. DOI: `10.1109/JSTSP.2009.2038969`.

[42]   M. Ghorbanzadeh, E. Visotsky, P. Moorut, W. Yang and C. Clancy. Radar
         inband and out-of-band interference into LTE macro and small cell uplinks
         in the 3.5 GHz band. *Proc. IEEE Wireless Communications and Networking
         Conference*. Mar. 2015, 1829–1834. DOI: `10.1109/WCNC.2015.7127746`.

[43]   C. Gu, Z. Peng and C. Li. High-Precision Motion Detection Using Low-
         Complexity Doppler Radar With Digital Post-Distortion Technique. *IEEE
         Transactions on Microwave Theory and Techniques* 64.3 (Mar. 2016), 961–971.
         DOI: `10.1109/TMTT.2016.2519881`.

[44]   T. Guo and R. Qiu. OFDM waveform design compromising spectral nulling,
         side-lobe suppression and range resolution. *Proc. IEEE Radar Conference*.
         May 2014, 1424–1429. DOI: `10.1109/RADAR.2014.6875823`.

[45]   R. Hadani, S. Rakib, A. F. Molisch, C. Ibars, A. Monk, M. Tsatsanis, J.
         Delfeld, A. Goldsmith and R. Calderbank. Orthogonal Time Frequency
         Space (OTFS) modulation for millimeter-wave communications systems.
         Proc. IEEE International Microwave Symposium. June 2017, 681–683. DOI:
         `10.1109/MWSYM.2017.8058662`.

[46]   A. Hassanien, M. G. Amin, E. Aboutanios and B. Himed. Dual-Function
         Radar Communication Systems: A Solution to the Spectrum Congestion
         Problem. *IEEE Signal Processing Magazine* 36.5 (Sept. 2019), 115–126. DOI:
         `10.1109/MSP.2019.2900571`.

[47]   A. Hassanien, M. G. Amin, Y. D. Zhang and F. Ahmad. Signaling strategies
         for dual-function radar communications: an overview. *IEEE Aerospace and
         Electronic Systems Magazine* 31.10 (Oct. 2016), 36–45. DOI: `10.1109/MAES.
         2016.150225`.

[48] Q. He, N. H. Lehmann, R. S. Blum and A. M. Haimovich. MIMO Radar Moving Target Detection in Homogeneous Clutter. *IEEE Transactions on Aerospace and Electronic Systems* 46.3 (July 2010), 1290–1301. DOI: `10.1109/TAES.2010.5545189`.

[49] R. W. Heath, N. González-Prelcic, S. Rangan, W. Roh and A. M. Sayeed. An Overview of Signal Processing Techniques for Millimeter Wave MIMO Systems. *IEEE Journal of Selected Topics in Signal Processing* 10.3 (Apr. 2016), 436–453. DOI: `10.1109/JSTSP.2016.2523924`.

[50] A. Herschfelt, A. R. Chiriyath, S. Srinivas and D. W. Bliss. An Introduction to Spectral Convergence: Challenges and Paths to Solutions. *Proc. IEEE International Online Symposium on Joint Communications & Sensing*. Feb. 2021. DOI: `10.1109/JCS52304.2021.9376388`.

[51] F. Hessar and S. Roy. Spectrum sharing between a surveillance radar and secondary Wi-Fi networks. *IEEE Transactions on Aerospace and Electronic Systems* 52.3 (June 2016), 1434–1448. DOI: `10.1109/TAES.2016.150114`.

[52] K.-W. Huang, M. Bică, U. Mitra and V. Koivunen. Radar waveform design in spectrum sharing environment: Coexistence and cognition. *Proc. IEEE Radar Conference*. May 2015, 1698–1703. DOI: `10.1109/RADAR.2015.7131272`.

[53] M. Jamil, H.-J. Zepernick and M. I. Pettersson. On integrated radar and communication systems using Oppermann sequences. *Proc. IEEE Military Communications Conference*. Nov. 2008. DOI: `10.1109/MILCOM.2008.4753277`.

[54] T. Jiang and Y. Wu. An Overview: Peak-to-Average Power Ratio Reduction Techniques for OFDM Signals. *IEEE Transactions on Broadcasting* 54.2 (June 2008), 257–268. DOI: `10.1109/TBC.2008.915770`.

[55] S. M. Kay. *Fundamentals of Statistical Signal Processing: Estimation Theory*. Prentice Hall, 1997.

[56] M. F. Keskin, H. Wymeersch and V. Koivunen. MIMO-OFDM Joint Radar-Communications: Is ICI Friend or Foe?: *IEEE Journal of Selected Topics in Signal Processing* 15.6 (Nov. 2021), 1393–1408. DOI: `10.1109/JSTSP.2021.3109431`.

[57] P. Kumari, J. Choi, N. González-Prelcic and R. W. Heath. IEEE 802.11ad-Based Radar: An Approach to Joint Vehicular Communication-Radar System. *IEEE Transactions on Vehicular Technology* 67.4 (Apr. 2018), 3012–3027. DOI: `10.1109/TVT.2017.2774762`.

[58] P. Kumari, N. J. Myers and R. W. Heath. Adaptive and Fast Combined Waveform-Beamforming Design for mmWave Automotive Joint Communication-Radar. *IEEE Journal of Selected Topics in Signal Processing* 15.4 (June 2021), 996–1012. DOI: `10.1109/JSTSP.2021.3071592`.

[59] P. Kumari, N. J. Myers, S. A. Vorobyov and R. W. Heath. A Combined Waveform-Beamforming Design for Millimeter-Wave Joint Communication-Radar. *Proc. Asilomar Conference on Signals, Systems, and Computers*. Nov. 2019, 1422–1426. DOI: `10.1109/IEEECONF44664.2019.9049020`.

[60] P. Kumari, S. A. Vorobyov and R. W. Heath. Adaptive Virtual Waveform Design for Millimeter-Wave Joint Communication–Radar. *IEEE Transactions on Signal Processing* 68 (Nov. 2019), 715–730. DOI: `10.1109/TSP.2019.2956689`.

[61] E. G. Larsson, O. Edfors, F. Tufvesson and T. L. Marzetta. Massive MIMO for next generation wireless systems. *IEEE Communications Magazine* 52.2 (Feb. 2014), 186–195. DOI: `10.1109/MCOM.2014.6736761`.

[62] S. Y. Le Goff, S. S. Al-Samahi, B. K. Khoo, C. C. Tsimenidis and B. S. Sharif. Selected mapping without side information for PAPR reduction in OFDM. *IEEE Transactions on Wireless Communications* 8.7 (July 2009), 3320–3325. DOI: `10.1109/TWC.2009.070463`.

[63] N. Levanon. Multifrequency radar signals. *Proc. IEEE International Radar Conference*. May 2000, 683–688. DOI: `10.1109/RADAR.2000.851916`.

[64] B. Li and A. Petropulu. MIMO radar and communication spectrum sharing with clutter mitigation. *Proc. IEEE Radar Conference*. May 2016. DOI: `10.1109/RADAR.2016.7485158`.

[65] J. Li and P. Stoica. MIMO Radar with Colocated Antennas. *IEEE Signal Processing Magazine* 24.5 (Sept. 2007), 106–114. DOI: `10.1109/MSP.2007.904812`.

[66]   Y. Li, S. A. Vorobyov and V. Koivunen. Generalized ambiguity function for the MIMO radar with correlated waveforms. *Proc. IEEE International Conference on Acoustics, Speech and Signal Processing (ICASSP).* May 2014, 5302–5306. DOI: `10.1109/ICASSP.2014.6854615`.

[67]   F. Liu, C. Masouros, A. P. Petropulu, H. Griffiths and L. Hanzo. Joint Radar and Communication Design: Applications, State-of-the-Art, and the Road Ahead. *IEEE Transactions on Communications* 68.6 (June 2020), 3834–3862. DOI: `10.1109/TCOMM.2020.2973976`.

[68]   F. Liu, Y.-F. Liu, A. Li, C. Masouros and Y. C. Eldar. Cramér-Rao Bound Optimization for Joint Radar-Communication Beamforming. *IEEE Transactions on Signal Processing* 70 (Dec. 2021), 240–253. DOI: `10.1109/TSP.2021.3135692`.

[69]   F. Liu, Y.-F. Liu, C. Masouros, A. Li and Y. C. Eldar. A Joint Radar-Communication Precoding Design Based on Cramér-Rao Bound Optimization. *Proc. IEEE Radar Conference.* Mar. 2022. DOI: `10.1109/RadarConf2248738.2022.9764187`.

[70]   F. Liu, C. Masouros, A. Li, H. Sun and L. Hanzo. MU-MIMO Communications With MIMO Radar: From Co-Existence to Joint Transmission. *IEEE Transactions on Wireless Communications* 17.4 (Apr. 2018), 2755–2770. DOI: `10.1109/TWC.2018.2803045`.

[71]   F. Liu, C. Masouros, T. Ratnarajah and A. Petropulu. On Range Sidelobe Reduction for Dual-Functional Radar-Communication Waveforms. *IEEE Wireless Communications Letters* 9.9 (Sept. 2020), 1572–1576. DOI: `10.1109/LWC.2020.2997959`.

[72]   F. Liu, L. Zhou, C. Masouros, A. Li, W. Luo and A. Petropulu. Toward Dual-functional Radar-Communication Systems: Optimal Waveform Design. *IEEE Transactions on Signal Processing* 66.16 (Aug. 2018), 4264–4279. DOI: `10.1109/TSP.2018.2847648`.

[73]   X. Liu, T. Huang, N. Shlezinger, Y. Liu, J. Zhou and Y. C. Eldar. Joint Transmit Beamforming for Multiuser MIMO Communications and MIMO Radar. *IEEE Transactions on Signal Processing* 68 (June 2020), 3929–3944. DOI: `10.1109/TSP.2020.3004739`.

[74]   Y. Luo, J. A. Zhang, X. Huang, W. Ni and J. Pan. Optimization and Quantization of Multibeam Beamforming Vector for Joint Communication and Radio Sensing. *IEEE Transactions on Communications* 67.9 (Sept. 2019), 6468–6482. DOI: 10.1109/TCOMM.2019.2923627.

[75]   Y. Luo, J. A. Zhang, X. Huang, W. Ni and J. Pan. Multibeam Optimization for Joint Communication and Radio Sensing Using Analog Antenna Arrays. *IEEE Transactions on Vehicular Technology* 69.10 (Oct. 2020), 11000–11013. DOI: 10.1109/TVT.2020.3006481.

[76]   D. Ma, N. Shlezinger, T. Huang, Y. Liu and Y. C. Eldar. Joint Radar-Communication Strategies for Autonomous Vehicles: Combining Two Key Automotive Technologies. *IEEE Signal Processing Magazine* 37.4 (July 2020), 85–97. DOI: 10.1109/MSP.2020.2983832.

[77]   K. V. Mishra, M. R. Bhavani Shankar, V. Koivunen, B. Ottersten and S. A. Vorobyov. Toward Millimeter-Wave Joint Radar Communications: A Signal Processing Perspective. *IEEE Signal Processing Magazine* 36.5 (Sept. 2019), 100–114. DOI: 10.1109/MSP.2019.2913173.

[78]   A. F. Molisch, V. V. Ratnam, S. Han, Z. Li, S. L. H. Nguyen, L. Li and K. Haneda. Hybrid Beamforming for Massive MIMO: A Survey. *IEEE Communications Magazine* 55.9 (Sept. 2017), 134–141. DOI: 10.1109/MCOM.2017.1600400.

[79]   B. Paul, A. R. Chiriyath and D. W. Bliss. Survey of RF Communications and Sensing Convergence Research. *IEEE Access* 5 (2017), 252–270. DOI: 10.1109/ACCESS.2016.2639038.

[80]   L. Pucci, E. Matricardi, E. Paolini, W. Xu and A. Giorgetti. Performance Analysis of Joint Sensing and Communication based on 5G New Radio. *Proc. IEEE Globecom Workshops*. Dec. 2021. DOI: 10.1109/GCWkshps52748.2021.9682124.

[81]   V. Raghavan, A. Partyka, A. Sampath, S. Subramanian, O. H. Koymen, K. Ravid, J. Cezanne, K. Mukkavilli and J. Li. Millimeter-Wave MIMO Prototype: Measurements and Experimental Results. *IEEE Communications Magazine* 56.1 (Jan. 2018), 202–209. DOI: 10.1109/MCOM.2017.1601184.

[82]   M. L. Rahman, J. A. Zhang, X. Huang, Y. J. Guo and R. W. Heath. Frame-work for a Perceptive Mobile Network Using Joint Communication and Radar Sensing. *IEEE Transactions on Aerospace and Electronic Systems* 56.3 (June 2020), 1926–1941. DOI: 10.1109/TAES.2019.2939611.

[83]   Y. Rahmatallah and S. Mohan. Peak-To-Average Power Ratio Reduction in OFDM Systems: A Survey And Taxonomy. *IEEE Communications Surveys & Tutorials* 15.4 (Mar. 2013), 1567–1592. DOI: 10.1109/SURV.2013.021313.00164.

[84]   T. S. Rappaport, G. R. MacCartney, M. K. Samimi and S. Sun. Wideband Millimeter-Wave Propagation Measurements and Channel Models for Future Wireless Communication System Design. *IEEE Transactions on Communications* 63.9 (Sept. 2015), 3029–3056. DOI: 10.1109/TCOMM.2015.2434384.

[85]   T. S. Rappaport, S. Sun, R. Mayzus, H. Zhao, Y. Azar, K. Wang, G. N. Wong, J. K. Schulz, M. Samimi and F. Gutierrez. Millimeter Wave Mobile Communications for 5G Cellular: It Will Work!: *IEEE Access* 1 (May 2013), 335–349. DOI: 10.1109/ACCESS.2013.2260813.

[86]   T. S. Rappaport, Y. Xing, O. Kanhere, S. Ju, A. Madanayake, S. Mandal, A. Alkhateeb and G. C. Trichopoulos. Wireless Communications and Applications Above 100 GHz: Opportunities and Challenges for 6G and Beyond. *IEEE Access* 7 (June 2019), 78729–78757. DOI: 10.1109/ACCESS.2019.2921522.

[87]   M. A. Richards, J. A. Scheer, J. Scheer and W. A. Holm. *Principles of Modern Radar: Basic Principles, Volume 1.* Institution of Engineering and Technology, 2010.

[88]   M. Richards. *Fundamentals Of Radar Signal Processing.* McGraw-Hill Education Pvt. Limited, 2005. ISBN: 9780070607378.

[89]   F. Robey, S. Coutts, D. Weikle, J. McHarg and K. Cuomo. MIMO radar theory and experimental results. *Proc. Asilomar Conference on Signals, Systems and Computers.* Vol. 1. Nov. 2004, 300–304. DOI: 10.1109/ACSSC.2004.1399141.

[90] Y. Rong, A. R. Chiriyath and D. W. Bliss. Multiple-antenna multiple-access joint radar and communications systems performance bounds. *Proc. Asilomar Conference on Signals, Systems, and Computers*. Oct. 2017, 1296–1300. DOI: `10.1109/ACSSC.2017.8335562`.

[91] G. San Antonio, D. R. Fuhrmann and F. C. Robey. MIMO Radar Ambiguity Functions. *IEEE Journal of Selected Topics in Signal Processing* 1.1 (June 2007), 167–177. DOI: `10.1109/JSTSP.2007.897058`.

[92] R. Schmidt. Multiple emitter location and signal parameter estimation. *IEEE Transactions on Antennas and Propagation* 34.3 (Mar. 1986), 276–280. DOI: `10.1109/TAP.1986.1143830`.

[93] M. A. Sebt, Y. Norouzi, A. Sheikhi and M. M. Nayebi. OFDM radar signal design with optimized Ambiguity Function. *Proc. IEEE Radar Conference*. May 2008. DOI: `10.1109/RADAR.2008.4720801`.

[94] S. Sen and A. Nehorai. Adaptive Design of OFDM Radar Signal With Improved Wideband Ambiguity Function. *IEEE Transactions on Signal Processing* 58.2 (Feb. 2010), 928–933. DOI: `10.1109/TSP.2009.2032456`.

[95] S. Sen and A. Nehorai. OFDM MIMO Radar With Mutual-Information Waveform Design for Low-Grazing Angle Tracking. *IEEE Transactions on Signal Processing* 58.6 (June 2010), 3152–3162. DOI: `10.1109/TSP.2010.2044834`.

[96] S. Sharma, M. Bică and V. Koivunen. Reduced PMEPR Multicarrier Radar Waveform Design. *Proc. IEEE Asilomar Conference on Signals, Systems, and Computers*. Nov. 2019, 2048–2052. DOI: `10.1109/IEEECONF44664.2019.9048815`.

[97] Y. L. Sit, C. Sturm, J. Baier and T. Zwick. Direction of arrival estimation using the MUSIC algorithm for a MIMO OFDM radar. *Proc. IEEE Radar Conference*. May 2012, 226–229. DOI: `10.1109/RADAR.2012.6212141`.

[98] X. Song, T. Kühne and G. Caire. Fully-/Partially-Connected Hybrid Beamforming Architectures for mmWave MU-MIMO. *IEEE Transactions on Wireless Communications* 19.3 (Mar. 2020), 1754–1769. DOI: `10.1109/TWC.2019.2957227`.

[99]   Q. Spencer, A. Swindlehurst and M. Haardt. Zero-forcing methods for down-link spatial multiplexing in multiuser MIMO channels. *IEEE Transactions on Signal Processing* 52.2 (Feb. 2004), 461–471. DOI: 10.1109/TSP.2003.821107.

[100]   C. Sturm and W. Wiesbeck. Waveform Design and Signal Processing Aspects for Fusion of Wireless Communications and Radar Sensing. *Proceedings of the IEEE* 99.7 (July 2011), 1236–1259. DOI: 10.1109/JPROC.2011.2131110.

[101]   S. Sun, T. S. Rappaport, R. W. Heath, A. Nix and S. Rangan. MIMO for millimeter-wave wireless communications: beamforming, spatial multiplexing, or both?: *IEEE Communications Magazine* 52.12 (Dec. 2014), 110–121. DOI: 10.1109/MCOM.2014.6979962.

[102]   S. Sussman. Least-square synthesis of radar ambiguity functions. *IRE Transactions on Information Theory* 8.3 (Apr. 1962), 246–254. DOI: 10.1109/TIT.1962.1057703.

[103]   H. Tataria, M. Shafi, A. F. Molisch, M. Dohler, H. Sjöland and F. Tufvesson. 6G Wireless Systems: Vision, Requirements, Challenges, Insights, and Opportunities. *Proceedings of the IEEE* 109.7 (July 2021), 1166–1199. DOI: 10.1109/JPROC.2021.3061701.

[104]   M. A. Uusitalo, P. Rugeland, M. R. Boldi, E. C. Strinati, P. Demestichas, M. Ericson, G. P. Fettweis, M. C. Filippou, A. Gati, M.-H. Hamon, M. Hoffmann, M. Latva-Aho, A. Pärssinen, B. Richerzhagen, H. Schotten, T. Svensson, G. Wikström, H. Wymeersch, V. Ziegler and Y. Zou. 6G Vision, Value, Use Cases and Technologies From European 6G Flagship Project Hexa-X. *IEEE Access* 9 (Nov. 2021), 160004–160020. DOI: 10.1109/ACCESS.2021.3130030.

[105]   I. Valiulahi, C. Masouros, A. Salem and F. Liu. Antenna Selection for Energy-Efficient Dual-Functional Radar-Communication Systems. *IEEE Wireless Communications Letters* 11.4 (Apr. 2022), 741–745. DOI: 10.1109/LWC.2022.3142043.

[106]   M. Wagner, Y. Park and P. Gerstoft. Gridless DoA Estimation and Root-MUSIC for Non-Uniform Linear Arrays. *IEEE Transactions on Signal Processing* 69 (Mar. 2021), 2144–2157. DOI: 10.1109/TSP.2021.3068353.

[107]   F. Wang and H. Li. Power Allocation for Coexisting Multicarrier Radar and Communication Systems in Cluttered Environments. *IEEE Transactions on Signal Processing* 69 (Feb. 2021), 1603–1613. DOI: `10.1109/TSP.2021.3060003`.

[108]   T. Wild, V. Braun and H. Viswanathan. Joint Design of Communication and Sensing for Beyond 5G and 6G Systems. *IEEE Access* 9 (Feb. 2021), 30845–30857. DOI: `10.1109/ACCESS.2021.3059488`.

[109]   K. Wu, J. A. Zhang, X. Huang and Y. J. Guo. Removing False Targets For Cyclic Prefixed OFDM Sensing With Extended Ranging. *Proc. IEEE Vehicular Technology Conference*. June 2022. DOI: `10.1109/VTC2022-Spring54318.2022.9860914`.

[110]   M. Xiao, S. Mumtaz, Y. Huang, L. Dai, Y. Li, M. Matthaiou, G. K. Karagiannidis, E. Björnson, K. Yang, C.-L. I and A. Ghosh. Millimeter Wave Communications for Future Mobile Networks. *IEEE Journal on Selected Areas in Communications* 35.9 (Sept. 2017), 1909–1935. DOI: `10.1109/JSAC.2017.2719924`.

[111]   Z. Xiao and Y. Zeng. Full-Duplex Integrated Sensing and Communication: Waveform Design and Performance Analysis. *Proc. IEEE International Conference on Wireless Communications and Signal Processing*. Oct. 2021. DOI: `10.1109/WCSP52459.2021.9613663`.

[112]   L. Xu, J. Li and P. Stoica. Adaptive Techniques for MIMO Radar. *Fourth IEEE Workshop on Sensor Array and Multichannel Processing, 2006.* July 2006, 258–262. DOI: `10.1109/SAM.2006.1706133`.

[113]   S. Xu, J. Wang and A. Yarovoy. Super Resolution DOA for FMCW Automotive Radar Imaging. *Proc. IEEE Conference on Antenna Measurements Applications*. Sept. 2018. DOI: `10.1109/CAMA.2018.8530609`.

[114]   Z. Xu, F. Liu and A. Petropulu. Cramér-Rao Bound and Antenna Selection Optimization for Dual Radar-Communication Design. *Proc. IEEE International Conference on Acoustics, Speech and Signal Processing*. May 2022, 5168–5172. DOI: `10.1109/ICASSP43922.2022.9747651`.

[115] Y. Yang and R. S. Blum. MIMO radar waveform design based on mutual information and minimum mean-square error estimation. *IEEE Transactions on Aerospace and Electronic Systems* 43.1 (Jan. 2007), 330–343. DOI: `10.1109/TAES.2007.357137`.

[116] X. Yuan, Z. Feng, W. Ni, Z. Wei and R. P. Liu. Waveform Optimization for MIMO Joint Communication and Radio Sensing Systems with Imperfect Channel Feedbacks. *Proc. IEEE International Conference on Communications Workshops*. June 2020. DOI: `10.1109/ICCWorkshops49005.2020.9145467`.

[117] X. Yuan, Z. Feng, J. A. Zhang, W. Ni, R. P. Liu, Z. Wei and C. Xu. Spatio-Temporal Power Optimization for MIMO Joint Communication and Radio Sensing Systems With Training Overhead. *IEEE Transactions on Vehicular Technology* 70.1 (Jan. 2021), 514–528. DOI: `10.1109/TVT.2020.3046438`.

[118] Y. Zeng, Y. Ma and S. Sun. Joint Radar-Communication With Cyclic Prefixed Single Carrier Waveforms. *IEEE Transactions on Vehicular Technology* 69.4 (Apr. 2020), 4069–4079. DOI: `10.1109/TVT.2020.2975243`.

[119] J. A. Zhang, X. Huang, Y. J. Guo, J. Yuan and R. W. Heath. Multibeam for Joint Communication and Radar Sensing Using Steerable Analog Antenna Arrays. *IEEE Transactions on Vehicular Technology* 68.1 (Jan. 2019), 671–685. DOI: `10.1109/TVT.2018.2883796`.

[120] J. A. Zhang, F. Liu, C. Masouros, R. W. Heath, Z. Feng, L. Zheng and A. Petropulu. An Overview of Signal Processing Techniques for Joint Communication and Radar Sensing. *IEEE Journal of Selected Topics in Signal Processing* 15.6 (Nov. 2021), 1295–1315. DOI: `10.1109/JSTSP.2021.3113120`.

[121] J. A. Zhang, M. L. Rahman, K. Wu, X. Huang, Y. J. Guo, S. Chen and J. Yuan. Enabling Joint Communication and Radar Sensing in Mobile Networks - A Survey. *IEEE Communications Surveys and Tutorials* (Oct. 2021). DOI: `10.1109/COMST.2021.3122519`.

[122] J. Zhang, E. Björnson, M. Matthaiou, D. W. K. Ng, H. Yang and D. J. Love. Prospective Multiple Antenna Technologies for Beyond 5G. *IEEE Journal on Selected Areas in Communications* 38.8 (Aug. 2020), 1637–1660. DOI: `10.1109/JSAC.2020.3000826`.

[123]   Z. Zhang, Z. Du and W. Yu. Mutual-Information-Based OFDM Waveform Design for Integrated Radar-Communication System in Gaussian Mixture Clutter. *IEEE Sensors Letters* 4.1 (Jan. 2020). DOI: 10.1109/LSENS.2019.2946735.

[124]   Q. Zhao and A. Swami. A Survey of Dynamic Spectrum Access: Signal Processing and Networking Perspectives. *Proc. IEEE International Conference on Acoustics, Speech and Signal Processing*. Vol. 4. Apr. 2007, 1349–1352. DOI: 10.1109/ICASSP.2007.367328.

A

Relation Between CRLBs and Fisher Matrix

When the estimation process is unbiased

$$\int (\hat{\theta} - \theta)\mathscr{P}_{\mathbf{y}}(\mathbf{y}; \theta) dy = \mathbf{0}, \tag{A.1}$$

in which the likelihood function $\mathscr{P}_{\mathbf{y}}(\mathbf{y}; \theta)$ has a mean around the zero vector and θ is the k-element vector consisting of the parameters to be estimated. Differentiating this expression w.r.t. the parameter vector θ results in

$$\int (\hat{\theta} - \theta)\frac{\partial \mathscr{P}_{\mathbf{y}}(\mathbf{y}; \theta)^T}{\partial \theta} dy - \int \mathscr{P}_{\mathbf{y}}(\mathbf{y}; \theta) dy = \mathbf{0}, \tag{A.2}$$

which can then be modified as

$$\int (\hat{\theta} - \theta)\frac{\partial \log \mathscr{P}_{\mathbf{y}}(\mathbf{y}; \theta)^T}{\partial \theta} \mathscr{P}_{\mathbf{y}}(\mathbf{y}; \theta) dy = \mathbf{I}. \tag{A.3}$$

This can be rewritten in terms of the expectation operation as

$$\mathbb{E}\left\{(\hat{\theta} - \theta)\frac{\partial \log \mathscr{P}_{\mathbf{y}}(\mathbf{y}; \theta)^T}{\partial \theta}\right\} = \mathbf{I}. \tag{A.4}$$

Left-multiplying (A.4) by $\mathbf{w}^T$ and right-multiplying by $\mathscr{I}^{-1}(\theta)\mathbf{w}$ results in

$$\mathbb{E}\left\{\mathbf{w}^T(\hat{\theta} - \theta)\frac{\partial \log \mathscr{P}_{\mathbf{y}}(\mathbf{y}; \theta)^T}{\partial \theta} \mathscr{I}^{-1}(\theta)\mathbf{w}\right\} = \mathbf{w}^T \mathscr{I}^{-1}(\theta)\mathbf{w}, \tag{A.5}$$

where $\mathbf{w}$ is an arbitrary vector used for the derivation and Fisher information matrix is denoted by $\mathscr{I}(\theta)$. Next, using the Cauchy–Schwarz inequality for (A.5) results in

$$(\mathbf{w}^T \mathscr{I}^{-1}(\theta)\mathbf{w})^2 \leq \mathbb{E}\left\{ \mathbf{w}^T (\hat{\theta} - \theta)(\hat{\theta} - \theta)\mathbf{w} \right\}$$

$$\cdot \mathbb{E}\left\{ \mathbf{w}^T \mathscr{I}^{-1}(\theta) \frac{\partial \log \mathscr{P}_{\mathbf{y}}(\mathbf{y};\theta)}{\partial \theta} \frac{\partial \log \mathscr{P}_{\mathbf{y}}(\mathbf{y};\theta)}{\partial \theta}^T \mathscr{I}^{-1}(\theta)\mathbf{w} \right\}$$

$$(\mathbf{w}^T \mathscr{I}^{-1}(\theta)\mathbf{w})^2 \leq \mathbf{w}^T \mathbb{E}\left\{ (\hat{\theta} - \theta)\left(\hat{\theta} - \theta\right)^T \right\} \mathbf{w}$$

$$\cdot \mathbf{w}^T \mathscr{I}^{-1}(\theta)\mathbb{E}\left\{ \frac{\partial \log \mathscr{P}_{\mathbf{y}}(\mathbf{y};\theta)}{\partial \theta} \frac{\partial \log \mathscr{P}_{\mathbf{y}}(\mathbf{y};\theta)}{\partial \theta}^T \right\} \mathscr{I}^{-1}(\theta)\mathbf{w}. \quad \text{(A.6)}$$

Defining $\text{cov}(\hat{\theta}) = \mathbb{E}\{(\hat{\theta} - \theta)(\hat{\theta} - \theta)^T\}$ as the covariance matrix of the set of parameters and

$$\mathscr{I}(\theta)_{i,j} = \mathbb{E}\left\{ \frac{\partial \log \mathscr{P}_{\mathbf{y}}(\mathbf{y};\theta)}{\partial \theta_i} \frac{\partial \log \mathscr{P}_{\mathbf{y}}(\mathbf{y};\theta)}{\partial \theta_j} \right\}, \quad \text{(A.7)}$$

where i and j are the row and column indices, the inequality in (A.6) can be simplified to conclude that the matrix $\text{cov}(\hat{\theta}) - \mathscr{I}^{-1}(\theta)$ is positive semi-definite. Hence, the CRLBs of the kth parameter are given by the corresponding k^{th} diagonal element.

A different expression is derived for (A.7) that is used throughout the thesis. For this, (A.7) can be rewritten by utilizing the definition of the second derivative as

$$\mathscr{I}(\theta)_{i,j} = \mathbb{E}\left\{ \frac{\frac{\partial \mathscr{P}_{\mathbf{y}}(\mathbf{y};\theta)}{\partial \theta_i} \frac{\partial \mathscr{P}_{\mathbf{y}}(\mathbf{y};\theta)}{\partial \theta_j}}{(\mathscr{P}_{\mathbf{y}}(\mathbf{y};\theta))^2} \right\} = \mathbb{E}\left\{ \frac{\frac{\partial^2 \mathscr{P}_{\mathbf{y}}(\mathbf{y};\theta)}{\partial \theta_i \partial \theta_j}}{\mathscr{P}_{\mathbf{y}}(\mathbf{y};\theta)} - \frac{\partial^2 \log \mathscr{P}_{\mathbf{y}}(\mathbf{y};\theta)}{\partial \theta_i \partial \theta_j} \right\}. \quad \text{(A.8)}$$

Since $\frac{\partial^2}{\partial \theta_i \partial \theta_j} \int \mathscr{P}_{\mathbf{y}}(\mathbf{y};\theta) dy = 0$, the expectation of first term can be written as

$$\mathbb{E}\left\{ \frac{\frac{\partial^2 \mathscr{P}_{\mathbf{y}}(\mathbf{y};\theta)}{\partial \theta_i \partial \theta_j}}{\mathscr{P}_{\mathbf{y}}(\mathbf{y};\theta)} \right\} = \frac{\partial^2}{\partial \theta_i \partial \theta_j} \int \mathscr{P}_{\mathbf{y}}(\mathbf{y};\theta) dy = 0. \quad \text{(A.9)}$$

Hence, the expression for each element of the Fisher information matrix is given by

$$\mathscr{I}(\theta)_{i,j} = -\mathbb{E}\left\{ \frac{\partial^2 \log \mathscr{P}_{\mathbf{y}}(\mathbf{y};\theta)}{\partial \theta_i \partial \theta_j} \right\}. \quad \text{(A.10)}$$

Publications

Publication 1

Optimized Waveforms for 5G–6G Communication With Sensing: Theory, Simulations and Experiments

S. D. Liyanaarachchi, T. Riihonen, C. Baquero Barneto and M. Valkama

Optimized Waveforms for 5G–6G Communication With Sensing: Theory, Simulations and Experiments

Sahan Damith Liyanaarachchi, *Graduate Student Member, IEEE*, Taneli Riihonen, *Member, IEEE*,
Carlos Baquero Barneto, *Graduate Student Member, IEEE*,
and Mikko Valkama, *Senior Member, IEEE*

Abstract—Joint communication and sensing (JCAS) is an emerging technology for managing efficiently the scarce radio frequency (RF) spectrum, and is expected to be a key ingredient in beyond fifth-generation (5G) networks. We consider a JCAS system, where the full-duplex radar transceiver and the communication transmitter are the same device, and pursue orthogonal frequency-division multiplexing (OFDM) waveform optimization by jointly minimizing the lower bounds of delay and Doppler estimation. This is attained by filling the empty subcarriers within the OFDM frame with optimized samples while reallocating a proportion of the communication subcarriers' power, which essentially controls the fairness between the two functionalities. Both communication and filled *radar subcarriers* are used for radar processing. The optimized sample values are found analytically, and a computationally feasible algorithm is presented for this task. We also address how the peak-to-average power ratio of the waveform can be controlled and minimized along the optimization process. The results are then numerically evaluated in 5G New Radio (NR) network context, which indicate a trade-off between the minimization of the lower bounds. The main-lobe width and the peak side-lobe level (PSL) of the range and velocity profiles of the radar image are also analyzed. An inverse relation between the lower bounds and the PSLs is observed, while the main-lobe width can be minimized simultaneously. The trade-off between communication and sensing is investigated, which indicates that the lower bounds can be improved at the cost of the communication capacity. Moreover, over-the-air RF measurements are carried out with unoptimized and optimized 5G NR waveforms at the 28 GHz mm-wave band, to validate the range profile's PSL improvement in an outdoor mapping scenario, depicting considerable performance gain.

Index Terms—5G NR, 6G, JCAS, joint communication and sensing, joint radar-communication, LTE, multi-functional RF systems, OFDM, radar, RF convergence.

I. Introduction

COMMUNICATION and radar/sensing systems have functioned separately and independently from each other in the past. The former have since then developed considerably, e.g., in the form of fifth-generation (5G) mobile communication networks [1] while there are already emerging research efforts towards the sixth-generation (6G) systems. With further advances in, e.g., electronics and signal processing techniques, the communication and sensing systems can be potentially co-located [2]. Due to similar operating frequencies in both systems, their spectra will coincide [3], resulting in mutual interference and potential performance degradation [4]–[6]. The major reason for this is that the radar systems operate at fixed frequencies, which cause the available dedicated spectrum for communication systems to become a scarce resource [7]. Radio frequency (RF) convergence is the umbrella of solutions under which the most novel methodologies exist to combat this challenge [8], where the scarce spectrum is utilized to jointly improve the sensing and communication functionalities. The use of similar hardware solutions in the two systems, such as phased-arrays, has also complemented RF convergence. Thus, a joint communication and sensing (JCAS) system can be pursued [2], [9], with shared waveform and hardware, and minimal performance degradation for both functionalities. For further information, prominent surveys on the topic can be found in [2], [8]–[15] to name but a few.

There are various application contexts for JCAS research, such as cellular networks [16], [17], joint vehicular-communication systems [18]–[20] and indoor mapping [21]. In such applications, the transmit (TX) antennas for the two subsystems are considered to be the same, allowing a single joint waveform to be used for both subsystems' tasks. Since the resources are shared, this will create an inherent trade-off between the two [22]. In designing and optimizing the joint waveform, performance metrics of both subsystems are thus to be taken into consideration. To this end, constrained optimization can be pursued to maximize or minimize the chosen metric of one subsystem, while the other subsystem's metric is properly constrained [23]. For communications, the primary metric is the achievable capacity [24]. For sensing, in turn, various

metrics are available, including the signal-to-interference-plus-noise ratio at the radar receiver (RX) [25], detection and false alarm probabilities [26], mutual information of the RX signal [27], different characteristics of the time-domain autocorrelation function, e.g., main-lobe width, peak side-lobe level (PSL) and the integrated side-lobe level [28], the PSL of the spatial waveform [29], [30], and the Cramer–Rao lower bounds (CRLBs) of the estimates [31].

Designing a JCAS waveform by minimizing the CRLB of range estimate is discussed in [32]. In contrast, in this article we jointly minimize both CRLBs of range and velocity estimates to design and optimize the joint waveform. Additionally, we consider standard-compliance aspects of practical mobile communication systems where the base station (BS) is utilized simultaneously for radar purposes while transmitting the downlink data modulated signal. Hence, the BS simultaneously acts as a joint radar transceiver (TRX) and communication TX with shared waveform. This is enabled by the assumed time-division duplexing (TDD) principle of the network [1] together with the full-duplex capability of the BS [33], allowing to measure and process the reflections from targets being illuminated by the TX waveform.

The main application framework in our work is 5G New Radio (NR) networks and their long-term evolution for enhanced JCAS support. Hence, stemming from the 5G NR standard [1], orthogonal frequency-division multiplexing (OFDM) is assumed as the baseline TX waveform, likely to be important also in 6G systems. In general, much research has already been done using the same OFDM waveform for sensing purposes, see, e.g., [34], [35]. Compared to other possible JCAS waveforms, e.g., linear frequency-modulated chirp [8] and cyclic prefixed single carrier [36], OFDM is of particular importance in mobile radio networks due to its natural support for multiple-input multiple-output (MIMO) processing and the resilience to frequency-selective fading through computationally efficient channel equalization methods. It is also helpful in sensing since it decouples the range and velocity estimation [8], while providing computationally efficient processing prospects. However, it has also selected drawbacks, e.g., high side-lobes in the range/velocity profiles, sensitivity to carrier-frequency offset, and high peak-to-average power ratio (PAPR) − something that we address along this work as part of the optimization framework.

In this work, we assume that the OFDM TX frame is not fully loaded, meaning that there are empty subcarriers that form the physical basis for the waveform optimization. Specifically, the empty subcarriers are filled using optimized frequency-domain samples to allow for improved sensing performance. Therefore, assuming that the total transmit power is constrained, some power of the communication subcarriers is effectively reallocated to these *radar subcarriers*, that basically controls the two subsystems' performance trade-off (fairness). Further, the amount of power reallocated can be decided by the BS according to the link budget. Specifically, the frequency-domain samples at the radar subcarriers are chosen by solving an optimization problem, such that they improve the accuracy of the delay and velocity estimation.

We note that the radar subcarriers are transparent to the communication RX, that can simply discard them in the frequency domain data detection, and hence the approach does not influence the communication RX design.

It is also shortly noted that the assumed availability of empty subcarriers within the 5G NR physical downlink shared channel (PDSCH) depends on instantaneous network load and scheduling decisions. Interestingly, however, most of the mobile applications correspond to bursty data, and thus one can argue that the PDSCH resources are commonly not fully utilized. Additionally, other physical signal structures such as the downlink synchronization signal block (SSB) burst is standardized such that there are good amount of empty subcarriers [1] within the applicable OFDM symbols.

The scope and technical contributions of this article can be finally summarized as follows:

- Adapting CRLB expressions for range and velocity estimates found in existing literature, the solution to the joint optimization of the two CRLBs is derived analytically for an OFDM JCAS system to find the optimal radar subcarrier allocation.
- A computationally efficient algorithm is presented to find the solution to the joint optimization which provides the optimal trade-off between the delay and Doppler CRLBs.
- It is shown that the radar subcarriers' phases do not affect the joint optimization, hence allowing for further optimization of the TX waveform for PAPR minimization.
- The derived solutions to the optimization problems are numerically evaluated and validated through simulations in the timely 5G NR network context.
- We analyze the trade-off between the two subsystems and show that there is an optimum power allocation which allows both to function with sufficient performance.
- Finally, 5G NR waveforms with and without optimized radar subcarriers are used for RF measurements at 28 GHz band to sense and map an outdoor environment, showcasing the improvement of the range side-lobes in the radar image.

The rest of the paper is organized as follows. Section II describes the considered JCAS system model, together with the signal expressions for both subsystems. Section III outlines the general optimization problem, and the solution is derived analytically. A computationally feasible algorithm is also discussed for calculating the solution efficiently. Section IV then applies the proposed solutions in 5G NR system context, while providing a large collection of numerical results and their analysis. Section V concludes the main ideas of our research work. Finally, selected CRLB derivations and proofs are provided in Appendices A and B.

II. SYSTEM MODEL

The considered JCAS system is shown in Fig. 1. The radar TRX is also a communication TX, which can feature multiple antenna arrays for TX and RX purposes, especially in case 5G and beyond networks operating at the mm-wave bands. The same OFDM waveform is utilized for both communication and sensing. The TX signal $x(t)$ is reflected from the targets
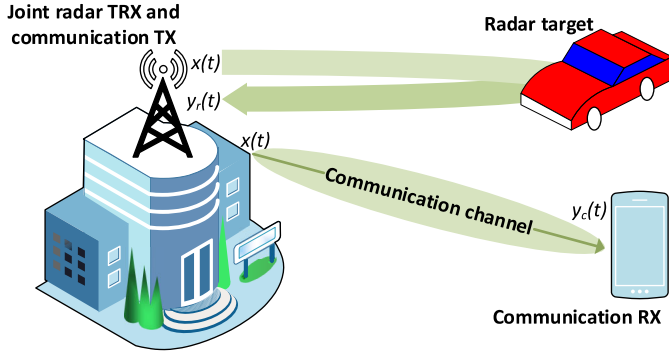
Fig. 1. The considered JCAS system model with the radar TRX and the communication TX, adopting the joint waveform.

in the environment and received back at the BS as $y_r(t)$, and is used for detecting the targets. For this, the TX operates in a full-duplex manner [33]. The received signal at the communication RX is denoted by $y_c(t)$.

The number of OFDM symbols for the whole waveform is denoted by M, with N denoting the number of active subcarriers per each symbol. The number of communication and radar subcarriers in the whole waveform are given by N_c and N_r, respectively, with $N_c + N_r = NM$. Additionally, the active communication subcarriers are divided into two classes—data and control—with their total number of subcarriers being N_{data} and N_{ctrl}, respectively, with $N_{data} + N_{ctrl} = N_c$. The time–frequency indices of the control subcarriers are fixed, while those of data and radar subcarriers are uniformly distributed.

We note that both types of subcarriers are used for radar processing at the radar RX. So, even without any dedicated radar subcarriers in the waveform, targets can still be detected with only the communication subcarriers. This will, however, reduce the potential to improve the sensing performance with JCAS waveform optimization, as shown in Section IV. Additionally, the symbols on communication subcarriers are assumed to be fixed, whereas those on radar subcarriers can be modified.

The TX downlink signal is then given by

$$x(t) = \sum_{m \in \mathcal{M}} \frac{p(t - t_m)}{N} \left(\sum_{n \in \mathcal{R}_m} X_{r,n,m} e^{j2\pi f_n(t - t_m)} \right.$$
$$\left. + \sum_{n \in \mathcal{C}_m} X_{c,n,m} e^{j2\pi f_n(t - t_m)} \right), \quad (1)$$

where the two separate inner summations correspond to the radar and communication subcarriers, respectively, while the outer summation is over the OFDM symbols. The n and m indices correspond to the subcarrier and OFDM symbol index, respectively, with $n \in [0, \ldots, N - 1]$ and $m \in [0, \ldots, M - 1]$.

The variables $p(t)$, $X_{r,n,m}$, $X_{c,n,m}$, f_n and t_m denote the pulse-shaping function, the TX symbol on a radar and communication subcarrier, frequencies of the subcarriers and the starting time instants of the OFDM symbols, respectively. Moreover, $\mathcal{R}_m$ and $\mathcal{C}_m$ are the radar and communication subcarrier indices for the mth symbol, with $\mathcal{R}_m \cup \mathcal{C}_m = \mathcal{N}$, and $\mathcal{N} = \{n | n \in [0, \ldots, N - 1]\}$. The set of OFDM symbols

is given by $\mathcal{M}$, with $\mathcal{M} = \{m | m \in [0, \ldots, M - 1]\}$. The total bandwidth of the signal is $f_{N-1} - f_0$ and the total signal duration is $t_{M-1} + \Delta t_{M-1} - t_0$, where Δt_{M-1} is the duration of last OFDM symbol. The frequencies and time instants are given by $f_n \in \{f_0, \ldots, f_{N-1}\}$ and $t_m \in \{t_0, \ldots, t_{M-1}\}$.

The instantaneous power for the radar and communication subcarriers over the whole waveform are

$$P_r = \sum_{m \in \mathcal{M}} \sum_{n \in \mathcal{R}_m} P_{n,m}, \quad P_c = \sum_{m \in \mathcal{M}} \sum_{n \in \mathcal{C}_m} P_{n,m}, \quad (2)$$

where $P_{n,m} = |X_{n,m}|^2$ represents the power of either subcarrier. Additionally, $P_t = P_r + P_c$ denotes the total TX power.

A. Radar Subsystem

The received signal at the radar RX is given by

$$y_r(t) = \sum_{k=1}^{K_r} A_{r,k} x(t - \tau_{r,k}) e^{j2\pi f_{r,D,k} t} + v_r(t), \quad (3)$$

where K_r, $A_{r,k}$, $\tau_{r,k}$ and $f_{r,D,k}$ are the number of point targets in the environment, two-way attenuation constant between the radar TRX and a particular target (from the radar equation), delay to the target, and Doppler shift of the target, respectively. The additive white Gaussian noise (AWGN) at the radar RX $v_r(t)$ is normally distributed with zero mean and σ_r^2 variance. The reflections from the kth target will be received at the radar RX with a signal-to-noise ratio (SNR) of

$$\text{SNR}_{r,k} = \frac{P_t |A_{r,k}|^2}{\sigma_r^2}. \quad (4)$$

Substituting (1) to (3) and performing the discrete Fourier transform (DFT) yields the relation between the TX and RX frequency-domain symbols $X_{n,m}$ and $Y_{r,n,m}$, respectively, as

$$Y_{r,n,m} = \sum_{k=1}^{K_r} A_{r,k} X_{n,m} e^{-j2\pi f_n \tau_{r,k}} e^{j2\pi f_{r,D,k} t_m} + V_{r,n,m}, \quad (5)$$

where the frequency-domain noise sample is denoted by $V_{r,n,m}$. This can be simplified for a single target as

$$Y_{r,n,m} = \underbrace{X_{n,m} e^{-j2\pi f_n \tau} e^{j2\pi t_m f_D}}_{S_{n,m}} + V_{r,n,m}, \quad (6)$$

showing that the delay and Doppler shift cause RX symbol's phase to differ from that of the TX symbol. Furthermore, the attenuation constant is normalized to unity while noise variance is scaled accordingly, but we do not introduce new symbols for $Y_{r,n,m}$ and $V_{r,n,m}$ in order to keep notation simple.

B. Delay and Doppler-Shift Estimation

Re-writing (6) in matrix form yields

$$\mathbf{Y} = \mathbf{DXB} + \mathbf{V}, \quad (7)$$

where $\mathbf{Y}$ is the RX symbol matrix with $(\mathbf{Y})_{n,m} = Y_{r,n,m}$, $\mathbf{X}$ is the TX symbol matrix with $(\mathbf{X})_{n,m} = X_{n,m}$ and $\mathbf{V}$ is the noise matrix with $(\mathbf{V})_{n,m} = V_{r,n,m}$, all of the same size $N \times M$. The diagonal matrix $\mathbf{D}$ is of size $N \times N$ with $(\mathbf{D})_{n,n} = D_{n,n} = e^{-j2\pi f_n \tau}$. Similar diagonal matrix $\mathbf{B}$ is such that $(\mathbf{B})_{m,m} = B_{m,m} = e^{j2\pi t_m f_D}$, of size $M \times M$.

The delay and Doppler shift of the target are then estimated using maximum likelihood estimation (MLE), given by

$$\boldsymbol{\theta} = [\tau, f_{\mathrm{D}}]^T, \tag{8}$$

where $\boldsymbol{\theta}$ is the set of parameters. For this, vectorizing (7) yields

$$\mathbf{y} = \mathbf{s} + \mathbf{v}, \tag{9}$$

where $\mathbf{y} = \mathrm{vec}(\mathbf{Y})$, $\mathbf{s} = \mathrm{vec}(\mathbf{DXB})$ and $\mathbf{v} = \mathrm{vec}(\mathbf{v})$ are all of the size $NM \times 1$, and $\mathrm{vec}(\cdot)$ is the vector operation. Vector $\mathbf{y}$ is assumed to be normally distributed with mean $\boldsymbol{\mu}$ and covariance $\boldsymbol{\Sigma}$, and

$$\boldsymbol{\mu} = \mathbb{E}\{\mathbf{y} - \mathbf{s}\} = \mathbf{0}, \tag{10}$$

$$\boldsymbol{\Sigma} = \mathbb{E}\{(\mathbf{y} - \mathbf{s})(\mathbf{y} - \mathbf{s})^H\} = \sigma_{\mathrm{r}}^2 \mathbf{I}, \tag{11}$$

where $\mathbf{0}$, $\mathbb{E}\{\cdot\}$ and $\mathbf{I}$ denote the zero vector, the expectation operation and the identity matrix, respectively.

The likelihood function of $\mathbf{y}$ can then be written as

$$\mathcal{P}_{\mathbf{y}}(\mathbf{y};\boldsymbol{\theta}) = \frac{1}{|\boldsymbol{\Sigma}|\pi^{NM}} \exp\left(-(\mathbf{y}-\mathbf{s})^H\boldsymbol{\Sigma}^{-1}(\mathbf{y}-\mathbf{s})\right)$$
$$= \frac{1}{\sigma_{\mathrm{r}}^2\pi^{NM}} \exp\left(-\frac{(\mathbf{y}-\mathbf{s})^H(\mathbf{y}-\mathbf{s})}{\sigma_{\mathrm{r}}^2}\right). \tag{12}$$

Taking the logarithm of (12) yields the log-likelihood function

$$\log\mathcal{P}_{\mathbf{y}}(\mathbf{y};\boldsymbol{\theta}) = -\log\left(\sigma_{\mathrm{r}}^2\pi^{NM}\right) - \frac{(\mathbf{y}-\mathbf{s})^H(\mathbf{y}-\mathbf{s})}{\sigma_{\mathrm{r}}^2}. \tag{13}$$

Removing terms that do not depend on the parameters results in the simplified log-likelihood function as

$$\log\mathcal{P}_{\mathbf{y}}'(\mathbf{y};\boldsymbol{\theta}) = \Re\left(\mathbf{y}^H\mathbf{s}\right). \tag{14}$$

The estimated delay and Doppler shift, given by $\hat{\tau}$ and $\hat{f}_{\mathrm{D}}$, respectively, are found by maximizing (14) as

$$\max_{\boldsymbol{\theta}} \log\mathcal{P}_{\mathbf{y}}'(\mathbf{y};\boldsymbol{\theta}). \tag{15}$$

Consequently, $\hat{\boldsymbol{\theta}} = [\hat{\tau}, \hat{f}_{\mathrm{D}}]^T$ is the vector containing those two estimated parameters.

When the frequencies and time instants are uniformly spaced as $f_n = n\Delta f$ and $t_m = \frac{m}{\Delta f}$, where Δf denotes the frequency spacing, a grid-based method can be used to estimate the parameters. In this case, the simplified log-likelihood function in (14) can be re-written as

$$\log\mathcal{P}_{\mathbf{Y}}'(\mathbf{Y};\boldsymbol{\theta}) = \Re \sum_{m\in\mathcal{M}}\sum_{n\in\mathcal{N}} \tilde{Y}_{\mathrm{r},n,m}X_{n,m}e^{-j2\pi n\Delta f\tau}e^{\frac{j2\pi m f_{\mathrm{D}}}{\Delta f}}, \tag{16}$$

where $\tilde{Y}_{\mathrm{r},n,m}$ denotes the conjugate of $Y_{\mathrm{r},n,m}$. Then, quantizing the delay and Doppler parameters as

$$\tau_{n'} = \frac{n'}{N\Delta f}, \quad n' \in \mathcal{N}, \tag{17}$$

$$f_{\mathrm{D}m'} = \frac{m'\Delta f}{M}, \quad m' \in \mathcal{M}, \tag{18}$$

and substituting to (16) yields

$$\log\mathcal{P}_{\mathbf{Y}}'(n',m') = \Re\left[\overbrace{\sum_{m\in\mathcal{M}}\left(\underbrace{\sum_{n\in\mathcal{N}}Y_{\mathrm{r},n,m}'e^{\frac{-j2\pi nn'}{N}}}_{\text{element }n'\text{ in }N\text{-length DFT}}\right)e^{\frac{j2\pi mm'}{M}}}^{\text{element }m'\text{ in }M\text{-length IDFT}}\right], \tag{19}$$

where $Y_{\mathrm{r},n,m}' = \tilde{Y}_{\mathrm{r},n,m}X_{n,m}$. It is then observed that the inner and outer sums correspond to the DFT and inverse DFT (IDFT), respectively. As such, $n_{\max}'$ and $m_{\max}'$ are found as those values that maximize (19) as

$$\max_{n',m'} \log\mathcal{P}_{\mathbf{Y}}'(n',m'). \tag{20}$$

These are substituted back in (17) and (18) to yield the quantized delay and Doppler variables as

$$\hat{\boldsymbol{\theta}} = \left[\frac{n_{\max}'}{N\Delta f}, \frac{m_{\max}'\Delta f}{M}\right]^T. \tag{21}$$

C. Communication Subsystem

The RX signal at the communication RX is given by

$$y_{\mathrm{c}}(t) = h_{\mathrm{c}}(t) * x(t) + v_{\mathrm{c}}(t), \tag{22}$$

where $*$, $h_{\mathrm{c}}(t)$ and $v_{\mathrm{c}}(t)$ denote the convolution, impulse response of the communication channel and the AWGN noise at the communication RX with variance σ_{c}^2, respectively, and

$$h_{\mathrm{c}}(t) = \sum_{k=1}^{K_{\mathrm{c}}} A_{\mathrm{c},k}\delta(t - \tau_{\mathrm{c},k})e^{j2\pi f_{\mathrm{c,D},k}t}. \tag{23}$$

Here, K_{c} and $A_{\mathrm{c},k}$ are the number of scatterers in the environment and the corresponding attenuation constant for the path between each scatterer and communication RX, $\tau_{\mathrm{c},k}$ and $f_{\mathrm{c,D},k}$ are the delay and Doppler shift of each scatterer, and $\delta(t)$ is the Dirac-delta function, respectively. In frequency domain, this can be written per each communication subcarrier as

$$H_{\mathrm{c},n,m} = \sum_{k=1}^{K_{\mathrm{c}}} A_{\mathrm{c},k}e^{-j2\pi f_n\tau_{\mathrm{c},k}}e^{j2\pi f_{\mathrm{c,D},k}t_m}, \tag{24}$$

where $H_{\mathrm{c},n,m}$ is assumed to remain constant for the duration of each OFDM symbol.

The RX symbols at the communication RX can then be written as

$$Y_{\mathrm{c},n,m} = H_{\mathrm{c},n,m}X_{\mathrm{c},n,m} + V_{\mathrm{c},n,m}, \tag{25}$$

where $Y_{\mathrm{c},n,m}$ and $V_{\mathrm{c},n,m}$ are the RX communication symbol and the frequency-domain noise sample, respectively. The capacity of the communication subcarriers is then given as

$$\beta_{\mathrm{c}} = \Delta f \sum_{m\in\mathcal{M}}\sum_{n\in\mathcal{C}_m} \log_2\left(1 + \frac{|H_{\mathrm{c},n,m}|^2\,\mathbb{E}\{|X_{\mathrm{c},n,m}|^2\}}{\sigma_{\mathrm{c}}^2}\right). \tag{26}$$

TABLE I

OPTIMIZATION PARAMETERS

Parameter	Definition
ϕ	Maximum allowable CRLB($\hat{f}_D$)
$P_{\max}$	Maximum power for a radar subcarrier
N_{act}	Number of activated radar subcarriers
P_{Δ}	Residual power allocated to one activated radar subcarrier
$\mathcal{R}_{m,\text{act}}$	Set of subcarrier indices of the activated radar subcarriers in the mth OFDM symbol
SNR_r	SNR at the radar RX
MS_f	Mean square bandwidth
MS_t	Mean square time
α	Communication loading ($\alpha = \frac{N_{\text{data}}}{MN} \cdot 100\%$)
ΔPSD	Power spectral density difference between a radar and a communication subcarrier

III. OPTIMIZATION OF RADAR SUBCARRIERS

This section discusses the methodology by which the radar subcarriers are filled with optimized frequency-domain samples to improve the performance of the JCAS system. The optimization is performed in two stages: first for the radar subcarriers' amplitudes (or powers) and then for their phases.

A. Power Optimization for CRLB Minimization

For the sensing subsystem, the error variances of the estimated parameters in (21) need to be minimized in the ideal case, but for this, the explicit expressions of them cannot be found. Instead, the lower bounds for these error variances can be calculated easily, and are given by their CRLBs as

$$\text{var}\{\hat{\tau}\} \geq \text{CRLB}(\hat{\tau}), \quad \text{var}\{\hat{f}_D\} \geq \text{CRLB}(\hat{f}_D), \qquad (27)$$

where $\text{var}\{\cdot\}$ is the variance, $\text{CRLB}(\hat{\tau})$ and $\text{CRLB}(\hat{f}_D)$ denote the CRLB of the delay and Doppler estimate, respectively.

The CRLBs can be minimized, presuming that they also minimize the corresponding practical error variances. Later in the numerical results, we illustrate that such improvements are possible. For this, the radar subcarriers within the OFDM waveform are optimized such that they jointly minimize the delay and Doppler CRLBs. For the signal model in (6), these are derived in Appendix A, and given by (46)–(47b), indicating that they only depend on the amplitudes of the subcarriers and not their phases. Table I defines some important parameters necessary for the rest of the paper, in the order they appear in the text.

Optimization problem 1 (Joint Optimization): *The joint minimization of the delay and Doppler CRLBs aims at finding*

$$\min_{P_{n,m}, \mathcal{R}_m} \text{CRLB}(\hat{\tau}) \qquad (28a)$$

$$\textit{subject to } \text{CRLB}(\hat{f}_D) \leq \phi, \qquad (28b)$$

$$P_r \leq P_t - P_c, \qquad (28c)$$

$$0 \leq P_{n,m} \leq P_{\max}, \quad n \in \mathcal{R}_m, \forall m. \qquad (28d)$$

Thus, $\text{CRLB}(\hat{\tau})$ is minimized when $\text{CRLB}(\hat{f}_D)$ is constrained to be below ϕ, where the power allocated to a radar subcarrier is limited by $P_{\max}$. The total radar power is based on the difference between the TX power and communication power. Here, we consider that P_t of the BS is known, as well

as P_c. As such, P_r can be found readily, and the optimization intends to find the optimal powers $P_{n,m}$ for the individual radar subcarriers. Although the optimization minimizes the CRLBs of sensing, the performance of the communication subsystem can be kept at a satisfactory level by tuning P_c, which essentially controls the fairness between the two.

To solve this joint optimization problem, due to the very large search space of the subcarrier indices, optimal radar subcarrier indices receiving some power according to (28d) cannot be easily found. As such, a two-step process is applied for solving the optimization problem. Firstly, it is assumed that the optimal radar subcarrier indices are known. In that case, the solution is given by the following theorem.

Theorem 1: *In solving Optimization problem 1, there is an optimal set of radar subcarrier indices of cardinality N_{act}, out of which $N_{\text{act}} - 1$ radar subcarriers are allocated a power of $P_{\max}$, while an additional radar subcarrier with indices $\{K, L\}$ is allocated remainder power P_{Δ}. The delay estimate's CRLB at this point is given by*

$$\text{CRLB}(\hat{\tau}) = \phi \frac{\text{NUM}_c + P_{\max} \sum_{m \in \mathcal{M}} \sum_{n \in \mathcal{R}_{m,\text{act}}} \bar{t}_m^2 + \bar{t}_L^2 P_{\Delta}}{\text{DEN}_c + P_{\max} \sum_{m \in \mathcal{M}} \sum_{n \in \mathcal{R}_{m,\text{act}}} \bar{f}_n^2 + \bar{f}_K^2 P_{\Delta}}.$$

$$(29)$$

Here

$$\bar{f}_n = f_n - \frac{1}{N} \sum_{n \in \mathcal{N}} f_n, \quad \bar{t}_m = t_m - \frac{1}{M} \sum_{m \in \mathcal{M}} t_m, \qquad (30)$$

$$\text{NUM}_c = \sum_{m \in \mathcal{M}} \sum_{n \in \mathcal{C}_m} \bar{t}_m^2 P_{n,m}, \quad \text{DEN}_c = \sum_{m \in \mathcal{M}} \sum_{n \in \mathcal{C}_m} \bar{f}_n^2 P_{n,m},$$

$$(31)$$

$$N_{\text{act}} = \left\lceil \frac{P_t - P_c}{P_{\max}} \right\rceil, \qquad (32)$$

$$P_{\Delta} = P_t - P_c - P_{\max}(N_{\text{act}} - 1), \qquad (33)$$

where $\lceil . \rceil$ is the ceiling operation, and N_{act} is the number of activated radar subcarriers needed to satisfy the total radar power constraint. Due to the ceiling operation in (32), one radar subcarrier will receive a lesser power than $P_{\max}$, which is given by P_{Δ}. The set of activated radar subcarriers for the mth OFDM symbol is denoted by $\mathcal{R}_{m,\text{act}}$.

Proof: See Appendix B. $\qquad \square$

The next step in solving the joint optimization is to find the set of N_{act} activated radar subcarriers out of all the possible radar subcarriers. Since the possible combinations for the activated radar subcarriers are given by $\binom{N_r}{N_{\text{act}}}$, the search space is still huge. To reduce this, optimal radar subcarrier indices for the separate optimizations of $\text{CRLB}(\hat{\tau})$ and $\text{CRLB}(\hat{f}_D)$ are utilized to derive the optimal indices for the joint optimization. These optimization approaches are described next.

Optimization problem 2 (Separate Minimization):
(a) $\min_{P_{n,m}, \mathcal{R}_m} \text{CRLB}(\hat{\tau})$ *subject to* $P_r \leq P_t - P_c$, *and* $0 \leq P_{n,m} \leq P_{\max}, n \in \mathcal{R}_m, \forall m$,
(b) $\min_{P_{n,m}, \mathcal{R}_m} \text{CRLB}(\hat{f}_D)$ *subject to* $P_r \leq P_t - P_c$, *and* $0 \leq P_{n,m} \leq P_{\max}, n \in \mathcal{R}_m, \forall m$.

The optimal radar subcarrier indices for the two separate CRLB optimizations are then given by the following theorem.

Theorem 2: *The activated radar subcarrier indices for separate minimization of* $\mathrm{CRLB}(\hat{\tau})$ *and* $\mathrm{CRLB}(\hat{f}_{\mathrm{D}})$ *are respectively given by the edge-most radar subcarriers in frequency domain and edge-most OFDM symbols in time domain.*

Proof: When only one parameter in (8) needs to be estimated, Fisher information matrix will also have one element, given by (43) for $i = j = 1$. For the two estimates, these are given separately by (45a) and (45c), and the CRLBs are then

$$\mathrm{CRLB}(\hat{\tau})_{\mathrm{sep}} = \frac{1}{8\pi^2(\mathrm{SNR}_{\mathrm{r}})}$$

$$\cdot \frac{1}{\underbrace{\left(\mathrm{DEN}_{\mathrm{c}} + P_{\max}\sum_{m\in\mathcal{M}}\sum_{n\in\mathcal{R}_{m,\mathrm{act}}}\bar{f}_n^2 + \bar{f}_K^2 P_\Delta\right)}_{\mathrm{MS}_f}} \quad (34)$$

and

$$\mathrm{CRLB}(\hat{f}_{\mathrm{D}})_{\mathrm{sep}} = \frac{1}{8\pi^2(\mathrm{SNR}_{\mathrm{r}})}$$

$$\cdot \frac{1}{\underbrace{\left(\mathrm{NUM}_{\mathrm{c}} + P_{\max}\sum_{m\in\mathcal{M}}\sum_{n\in\mathcal{R}_{m,\mathrm{act}}}\bar{t}_m^2 + \bar{t}_L^2 P_\Delta\right)}_{\mathrm{MS}_t}}. \quad (35)$$

Here, $\mathrm{CRLB}(\hat{\tau})_{\mathrm{sep}}$ and $\mathrm{CRLB}(\hat{f}_{\mathrm{D}})_{\mathrm{sep}}$ are the minimum CRLBs when optimal radar subcarrier indices are used, and to find these, separate optimizations are performed as in Optimization problem 2.

From (34), to minimize $\mathrm{CRLB}(\hat{\tau})$, MS_f should be maximized. Hence, the edge-most $N_{\mathrm{act}} - 1$ radar subcarriers (maximum $\bar{f}_n^2$) are allocated $P_{\max}$, while the $N_{\mathrm{act}}^{\mathrm{th}}$ edge-most radar subcarrier is allocated P_Δ.

From (35), to minimize $\mathrm{CRLB}(\hat{f}_{\mathrm{D}})$, MS_t should be maximized. Hence, all radar subcarriers of the edge-most OFDM symbols (maximum $\bar{t}_m^2$) are allocated $P_{\max}$, while also for some radar subcarriers in the least edge-most OFDM symbol, depending on N_{act}. In that OFDM symbol, a single radar subcarrier is allocated P_Δ. $\square$

Due to the joint estimation, both the CRLBs are degraded w.r.t. the separate estimations, as observed from (47a) and (47b). To find the optimal radar subcarrier indices for the joint optimization, those for the separate delay optimization are then used as a starting point to reduce the complexity of the search space. A computationally efficient algorithm for this task is provided by the following theorem.

Theorem 3: *The optimal radar subcarrier indices for the joint optimization can be efficiently calculated by the Algorithm 1.*

Proof: The two CRLBs are inversely related as in (48). Hence

$$\min \mathrm{CRLB}(\hat{\tau}) \implies \max \mathrm{MS}_f, \quad (36)$$

$$\min \mathrm{CRLB}(\hat{f}_{\mathrm{D}}) \implies \max \mathrm{MS}_t. \quad (37)$$

The minimum $\mathrm{CRLB}(\hat{\tau})$ is given by (34), and it represents the case when MS_f is the maximum. This is the starting point of the algorithm. Let the frequency-domain symbols on N_{move} ($\leq N_{\mathrm{act}}$) activated radar subcarriers with indices

---

Algorithm 1 Joint Optimization Algorithm

1: Set $i = 0$
2: Initialize $\mathcal{R}_{\mathrm{act},i}$ to be the edge-most radar subcarriers
3: Set $\mathcal{R}_{\mathrm{act,new},i} = \varnothing$
4: **while** $i \leq N_{\mathrm{act}}$ **do**
5:     Compute $\mathrm{CRLB}(\hat{\tau})_i$ and $\mathrm{CRLB}(\hat{f}_{\mathrm{D}})_i$
6:     Select the activated radar subcarrier having the minimum $\bar{f}_n$, with indices $\{n_{\min}, m_{\min}\}$
7:     Select the unactivated radar subcarrier having the maximum $\bar{f}_n$ on the maximum $\bar{t}_m$ time instant, with indices $\{n_{\max}, m_{\max}\}$
8:     Set $X_{\mathrm{r},n_{\max},m_{\max}} = X_{\mathrm{r},n_{\min},m_{\min}}$
9:     Set $X_{\mathrm{r},n_{\min},m_{\min}} = 0$
10:    $\mathcal{R}_{\mathrm{act},i+1} = \mathcal{R}_{\mathrm{act},i} \setminus \{n_{\min}, m_{\min}\}$
11:    $\mathcal{R}_{\mathrm{act,new},i+1} = \mathcal{R}_{\mathrm{act,new},i} \cup \{n_{\max}, m_{\max}\}$
12:    $i \leftarrow i + 1$

$\{n'_a, m'_a\}$, $a \in [1, N_{\mathrm{move}}]$ be moved to unactivated radar subcarriers with indices $\{n_a, m_a\}$. The maximum MS_f is then

$$\mathrm{MS}_f = \mathrm{DEN}_{\mathrm{c}} + P_{\max}\sum_{m\in\mathcal{M}}\sum_{n\in\mathcal{R}_{m,\mathrm{act}}}\bar{f}_n^2 + \bar{f}_K^2 P_\Delta$$

$$+ P_{\max}\sum_{a=2}^{N_{\mathrm{move}}}\left(\bar{f}_{n_a}^2 - \bar{f}_{n'_a}^2\right) + P_\Delta(\bar{f}_{n_1}^2 - \bar{f}_{n'_1}^2). \quad (38)$$

Similarly from (35), the MS_t at this point is

$$\mathrm{MS}_t = \mathrm{NUM}_{\mathrm{c}} + P_{\max}\sum_{m\in\mathcal{M}}\sum_{n\in\mathcal{R}_{m,\mathrm{act}}}\bar{t}_m^2 + \bar{t}_L^2 P_\Delta$$

$$+ P_{\max}\sum_{a=2}^{N_{\mathrm{move}}}\left(\bar{t}_{m_a}^2 - \bar{t}_{m'_a}^2\right) + P_\Delta(\bar{t}_{m_1}^2 - \bar{t}_{m'_1}^2). \quad (39)$$

For least degradation of MS_f, the indices n'_a are chosen such that they have the least frequencies $\bar{f}_{n'_a}$ out of all the activated radar subcarriers, while the indices n_a are the next highest frequencies $\bar{f}_{n_a}$, out of all the unactivated radar subcarriers, ensuring that $\left(\bar{f}_{n_a}^2 - \bar{f}_{n'_a}^2\right)$ is degraded the least.

Once the subcarrier indices for the activated radar subcarriers are found, the next step is to choose the OFDM symbols for them. Following a similar logic, from (39) it can be deduced that the indices m'_a should have the least time instants $\bar{t}_{m'_a}$ out of all the activated radar subcarriers, while m_a should have the next highest time instants $\bar{t}_{m_a}$, for the remaining unactivated radar subcarriers. This ascertains that $\left(\bar{t}_{m_a}^2 - \bar{t}_{m'_a}^2\right)$ is maximized as much as possible. This is done until all N_{act} radar subcarriers are moved. In the end, this would generate the waveform with the highest MS_t, viz. the waveform when only Doppler estimation is performed.

For the same number of activated radar subcarriers moved N_{move}, better CRLBs cannot be found than the ones provided by the algorithm since for any other combination of radar subcarrier and OFDM symbol indices, either $\left(\bar{f}_{n_a}^2 - \bar{f}_{n'_a}^2\right)$ or $\left(\bar{t}_{m_a}^2 - \bar{t}_{m'_a}^2\right)$ will be less than the one provided by Algorithm 1, which ensures that the two CRLBs reside on the Pareto curve. This completes the proof. $\square$

The i variable in the algorithm denotes the number of active radar subcarriers moved from MS_f to MS_t maximization. Thus, each $\text{CRLB}(\hat{\tau})_i$ and $\text{CRLB}(\hat{f}_D)_i$ correspond to the trade-off between the CRLBs of the two estimates and $\text{CRLB}(\hat{\tau})_0$ and $\text{CRLB}(\hat{f}_D)_{N_{\text{act}}}$ correspond to the CRLB values when the waveform is only optimized separately for either optimization. Once the indices of the activated radar subcarriers are found (contingent on the indices of the communication subcarriers), depending on i, their amplitudes are given readily as $\sqrt{P_{\max}}$ (or P_Δ). As such, the computational complexity is low for the amplitude optimization of the activated radar subcarriers.

B. Phase Optimization for PAPR Minimization

Since the CRLBs depend only on the amplitudes, the phases can be optimized separately to minimize PAPR that is notoriously high for default OFDM waveforms [37]. Hence, the phases of activated radar subcarriers are optimized to reduce the PAPR in our work [30], [38]. To reduce the complexity, phase optimization is done for each OFDM symbol to reduce that particular symbol's PAPR, which allows to reduce the PAPR of the whole waveform.

The PAPR of the mth OFDM symbol is

$$\text{PAPR}_{x_m[a]} = 10\log_{10}\frac{\max\{|x_m[a]|^2\}}{\mathbb{E}\{|x_m[a]|^2\}}, \tag{40}$$

where $x_m[a]$ is the sampled sequence of the mth OFDM symbol's time-domain waveform, based on $x(t)$ in (1). Here, $a \in [0, N_{\text{IDFT}} - 1]$ and N_{IDFT} is the IDFT size for one OFDM symbol, and $\max\{\cdot\}$ is the maximum operation. The phase optimization can then be denoted as below.

Optimization problem 3 (Phase optimization of activated radar subcarriers): *We aim to find* $\min_{\boldsymbol{\zeta}_m} \text{PAPR}_{x_m[a]}$, *where* $\boldsymbol{\zeta}_m$ *is the set of phases for the activated radar subcarriers in the* m^{th} *OFDM symbol, while* $\boldsymbol{\zeta}_{\text{opt},m}$ *denotes the corresponding optimum phases.*

To solve Optimization problem 3, selective mapping (SLM) is used in this article [39]. Thus, U sets of random phases are chosen for the activated radar subcarriers of each OFDM symbol. For the mth OFDM symbol, these are given as $\mathbf{Z}_m = [\boldsymbol{\zeta}_{0,m}, \ldots, \boldsymbol{\zeta}_{U-1,m}]$, $u \in [0, U-1]$, with $\mathbb{C}\{\boldsymbol{\zeta}_{u,m}\} = \mathbb{C}\{\mathcal{R}_{m,\text{act}}\}$, where $\mathbb{C}\{\cdot\}$ is the cardinality.

This operation thus produces U possible waveforms for each OFDM symbol, and these can be given based on (1) as

$$x_m^u(t) = \frac{p(t - t_m)}{N}\left(\sum_{n \in \mathcal{C}_m} X_{\text{c},n,m}e^{j2\pi f_n(t-t_m)}\right.$$
$$\left. + P_{\max}\sum_{n \in \mathcal{R}_{m,\text{act}}} e^{j2\pi\zeta_{u,n,m}}e^{j2\pi f_n(t-t_m)}\right), \tag{41}$$

where $\zeta_{u,n,m} = (\boldsymbol{\zeta}_{u,m})_n$, and $x_m^u(t)$ is the uth time-domain waveform of the mth OFDM symbol. Since the U sets of phases are random, the PAPR of each waveform is different, and one set of phases will produce the minimum PAPR. These are found by solving Optimization problem 3. This is repeated for all the OFDM symbols to minimize the PAPR of the whole TX waveform. This PAPR minimization scheme is summarized in Algorithm 2.

Algorithm 2 Phase Optimization Algorithm

1: Set $m = 0, u = 0$
2: **while** $m \leq M - 1$ **do**
3:     **while** $u \leq U - 1$ **do**
4:         Set $\boldsymbol{\zeta}_{u,m}$ as uniformly distributed random numbers
5:         between $[0, 1]$
6:         For $n \in \mathcal{R}_{m,\text{act}}$, set $X_{\text{r},n,m} = P_{\max}e^{j2\pi\zeta_{u,n,m}}$
7:         Compute the PAPR of the OFDM symbol (40)
8:         $u \leftarrow u + 1$
    Set $\boldsymbol{\zeta}_{\text{opt},m}$ using Optimization problem 3
9:     For $n \in \mathcal{R}_{m,\text{act}}$, set $X_{\text{r},n,m} = P_{\max}e^{j2\pi(\zeta_{\text{opt},m})_n}$
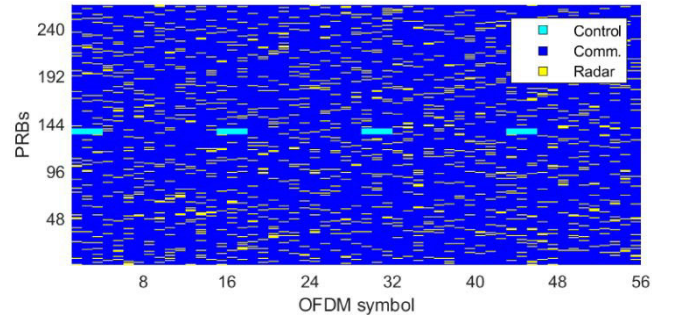10: $m \leftarrow m + 1$

Fig. 2. Resource grid showing the distribution of different PRBs of the considered 5G NR waveform for $M = 56$ and $\alpha = 90\%$.

For Algorithm 2, the search space is massive and an exhaustive search is infeasible to be performed. Hence, the solution obtained is suboptimal in comparison to the global optimum. Additionally, this cannot be performed in a real-time system, while finding computationally more efficient solutions to facilitate real-time processing is an important future research topic. However, in this work, we demonstrate the general prospects of also optimizing the phases of the activated radar subcarriers for PAPR minimization. Further, any other method which optimizes the phases of the subcarriers can be readily applied for PAPR minimization, instead of the SLM approach used herein, e.g., a modified version of the method adopted in [40].

IV. NUMERICAL RESULTS

A 5G NR waveform is used for the simulations with parameters: $M = 560$, total bandwidth of 400 MHz, $\Delta f = 120$ kHz and centered around $f_c = 28$ GHz. For this bandwidth, the number of physical resource blocks (PRBs) is 264 with $N = 3168$ subcarriers [41]. The total duration of the frame is 0.5 ms and the TX power is used at 30 dBm.

The resource grid in frequency domain is depicted in Fig. 2, for a communication loading α of 90%, with $\alpha = \frac{N_{\text{data}}}{MN} \cdot 100\%$. It shows the distribution of different PRBs. The control PRBs recur for every slot (14 OFDM symbols) and span over three OFDM symbols, with six PRBs. Within each communication PRB, there exist two pilot subcarriers. The communication subcarriers constitute quadrature phase-shift keying symbols, while the pilots are binary phase-shift keying symbols. Each OFDM symbol has a fixed number of radar subcarriers.
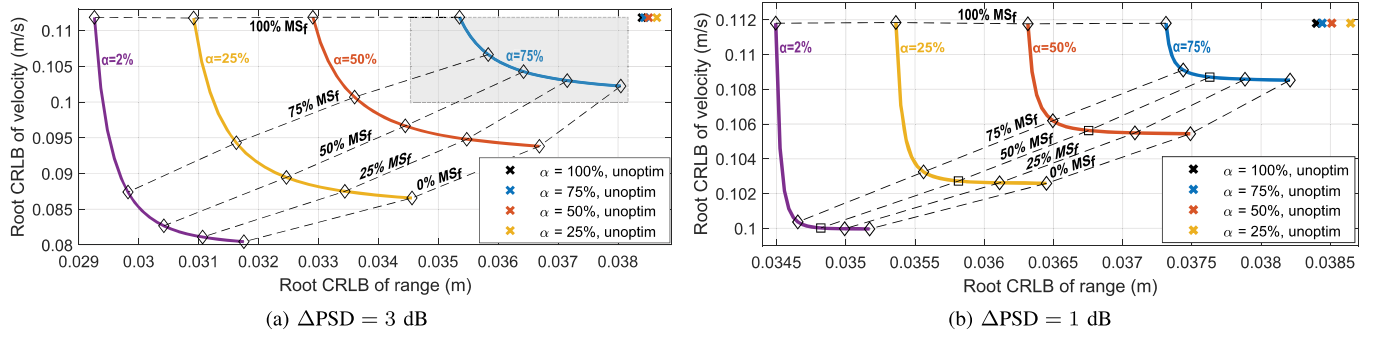
(a) ΔPSD = 3 dB

(b) ΔPSD = 1 dB

Fig. 3. Trade-off between range and velocity root CRLBs for different α and MS$_f$ %, for (a) ΔPSD = 3 dB and (b) 1 dB, when activated radar subcarriers are moved. The grey rectangle in (a) depicts the area corresponding to (b). When α = 2% and unoptimized, that corresponds to the point (0.0438, 0.1119).
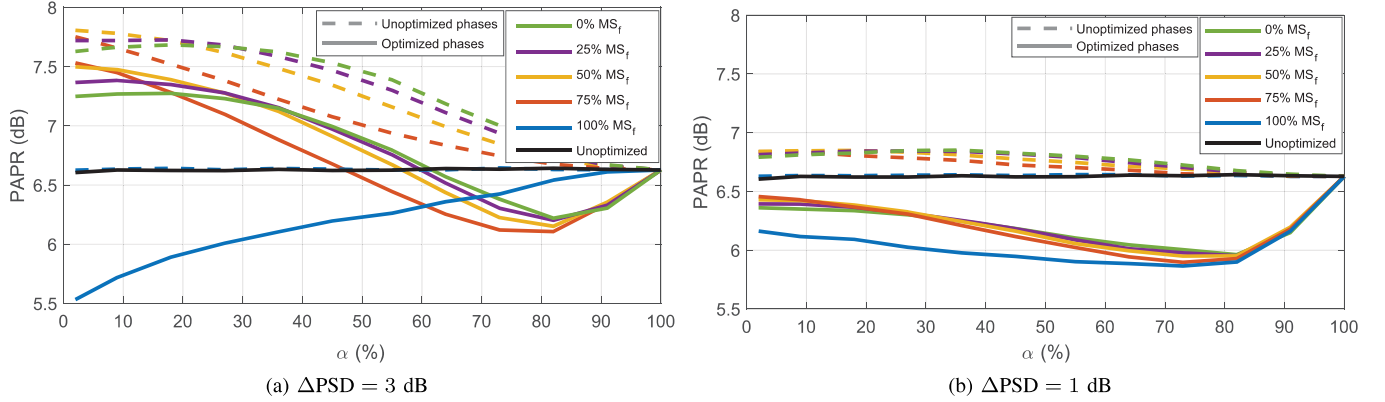

(a) ΔPSD = 3 dB

(b) ΔPSD = 1 dB

Fig. 4. The effect of optimizing phases of the activated radar subcarriers on the PAPR of waveforms, for different α, and (a) ΔPSD = 3 dB and (b) 1 dB.

A. Simulation Results

Figure 3 shows the results for the joint CRLB optimization. The delay and Doppler values are converted to range and velocity, with the use of $\hat{d} = \frac{c\hat{\tau}}{2}$ and $\hat{v} = \frac{c\hat{f}_D}{2f_c}$, where $\hat{d}$, $\hat{v}$ and c are the range estimate, velocity estimate, and speed of light, respectively. The power spectral density (PSD) difference (ΔPSD) between a radar and communication subcarrier is maintained at two values, 3 dB and 1 dB, and these cases are denoted by Figs. 3(a) and 3(b), respectively.

For the optimized waveform, when α decreases, both CRLBs also decrease. This is because with decreased α, number of radar subcarriers increases, and it gives more degrees of freedom for the optimization. Comparing between the two figures, reduced CRLBs are observed for the higher ΔPSD. Increasing this value increases the power allocated to a radar subcarrier ($P_{\max}$), and from (32), this will reduce the number of active radar subcarriers. This allows maximizing either the MS$_f$ or MS$_t$ as required. Both figures also show the CRLBs of the unoptimized waveform, where the radar subcarriers are empty, and the communication subcarriers use all the available power. Therefore, reallocating some power from the communication subcarriers to the radar subcarriers allows to minimize the CRLBs in comparison with the case when the total power is allocated to the communication subcarriers.

Since the starting point of Algorithm 1 is the optimized waveform with maximum MS$_f$, radar power is allocated

to those radar subcarriers at the edges of the spectrum. To improve MS$_t$, some active radar subcarriers at the edges of the spectrum can be moved to the edge OFDM symbols, which in turn decreases MS$_f$. Thus, when MS$_f$ % decreases, the CRLB of range increases, while that of velocity decreases, which depicts the inherent trade-off between the two CRLBs. Here, MS$_f$ % denotes $100\% - \frac{i}{N_{act}} \cdot 100\%$ in Algorithm 1.

The effect of optimizing the radar subcarriers' phases on the PAPR is shown in Figs. 4(a) and 4(b), for ΔPSD = 3 dB and 1 dB, and $U = 50$. Here and in the subsequent figures, the default 5G waveform without any radar subcarriers is denoted as *unoptimized* (black curve). Instead of using pure random phases as in Algorithm 2, the chosen random phases are further iterated using the `fminunc` function of the optimization toolbox of MATLAB. This was done to lower the required U than that is needed from pure randomization, but which also depicts sufficient PAPR improvement. Then, the phases that give the minimum PAPR are chosen as the optimum phases.

The *unoptimized phases* cases denote the waveforms where the locations and amplitudes of activated radar subcarriers are optimized to minimize the CRLBs, but their phases are not, being simply uniformly distributed within $[0, 2\pi]$. In these waveforms, when MS$_f$ % decreases, the number of activated radar subcarriers in the edge OFDM symbols increases, while in the center OFDM symbols, they will be decreased. Consequently, these waveforms will have more power allocated
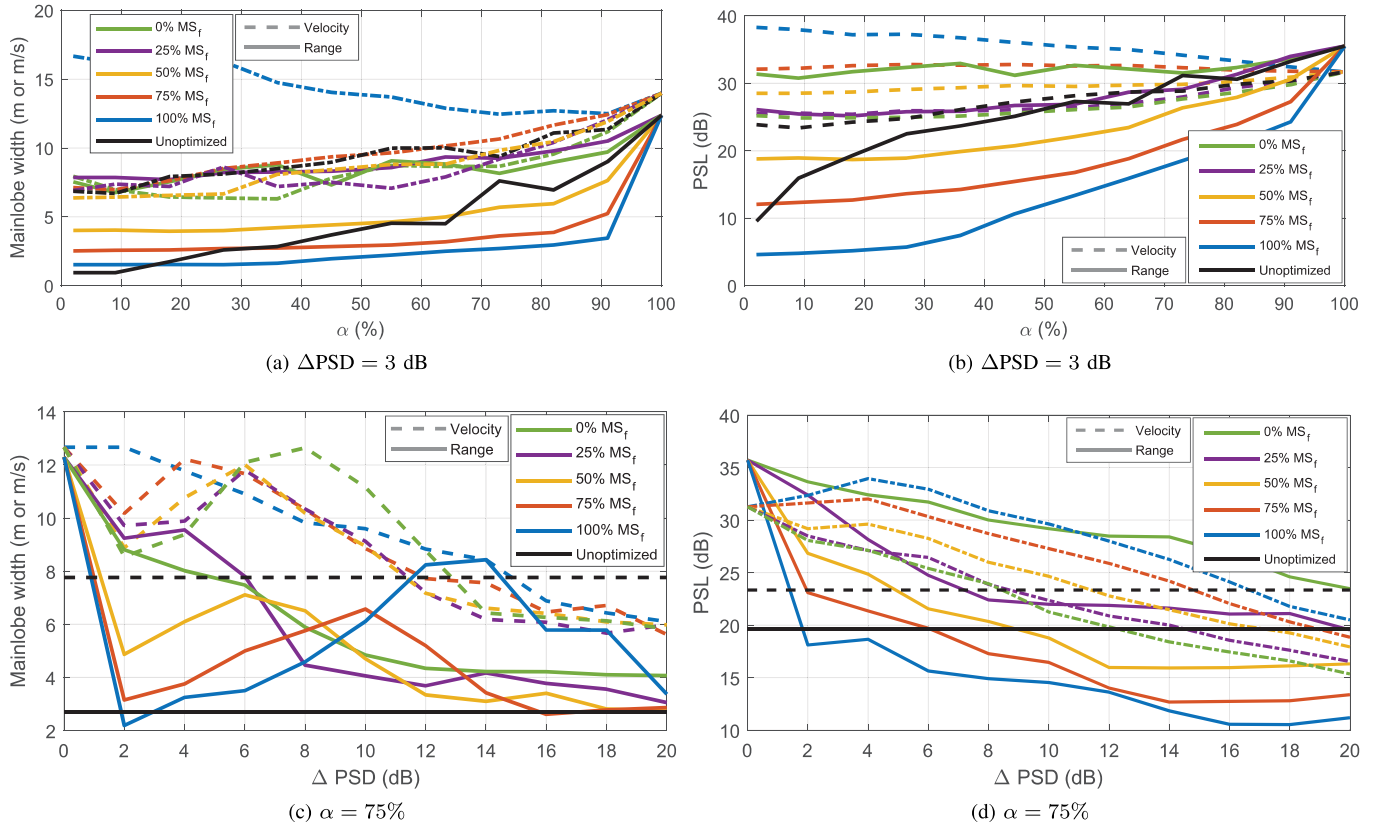
Fig. 5. Comparison between the main-lobe widths and PSLs, for fixed ΔPSD = 3 dB shown in (a) and (b), and for fixed $\alpha = 75\%$, shown in (c) and (d).

to the edges of the time-domain signal than for the center. Although the average power of the time-domain signal remains the same, this results in the peak power of the edge OFDM symbols to increase. Thus, these waveforms will then have higher peak power than that of the default 5G waveform, whereas the average power is the same for both. This is the reason for the PAPR to increase in the phase unoptimized cases compared to the default 5G waveform. The same analogy can be applied as the reason for the PAPR to increase when MS_f % decreases in both phase unoptimized and optimized cases.

Comparing between the Figs. 4(a) and 4(b), it can be observed that when ΔPSD increases, the PAPR increases. This is because when $P_{\max}$ increases, the number of activated radar subcarriers in (32) decreases, and hence the peak power of the time-domain signal increases even more. Further, the PAPR decreases with the increase of α, due to the reduction of the activated radar subcarriers in the edge OFDM symbols. However, phase optimization is observed to reduce the PAPR, indicating the feasibility of numerically optimizing the phases of the activated radar subcarriers.

To evaluate the improved performance in a practical scenario, simulations are performed by placing a point target with varying velocity at different ranges. Then, the optimized joint waveform is used as the TX waveform, and the reflected RX signal is used for target detection. Next, MLE is performed to estimate the range and relative velocity of the target. The main-lobe width and PSL of the target in range and velocity profiles are also then calculated. This is performed for many iterations to obtain the average performance.
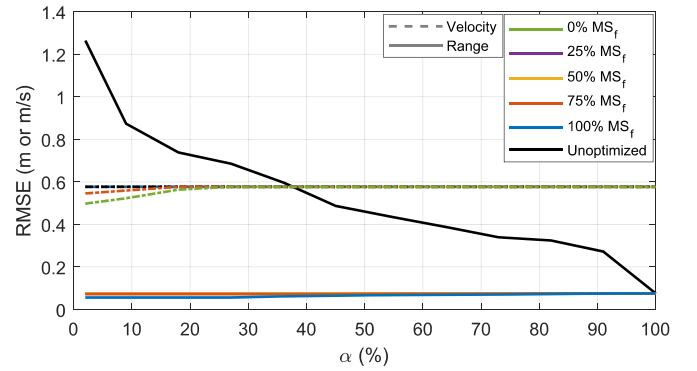
Fig. 6. The RMSEs of range and velocity for $SNR_r = -10$ dB and ΔPSD = 3 dB, for unoptimized and optimized waveforms.

Figure 5(a) depicts the main-lobe widths of the peak corresponding to the detected target, in both range and velocity, for ΔPSD = 3 dB, which are calculated as the null-to-null distance of the main-lobe peak. The range profile's main-lobe width decreases when either α decreases or MS_f % increases, i.e., when more radar subcarriers are available for MS_f maximization, the target can be made narrower in the range domain. Additionally, the main-lobe width of the optimized waveform can be lowered compared to that of the unoptimized waveform, depending on α and MS_f %. Similarly for the velocity, having more radar subcarriers for MS_t maximization (lower MS_f %), improves its main-lobe width, while marginally better main-lobe width can be obtained than that of
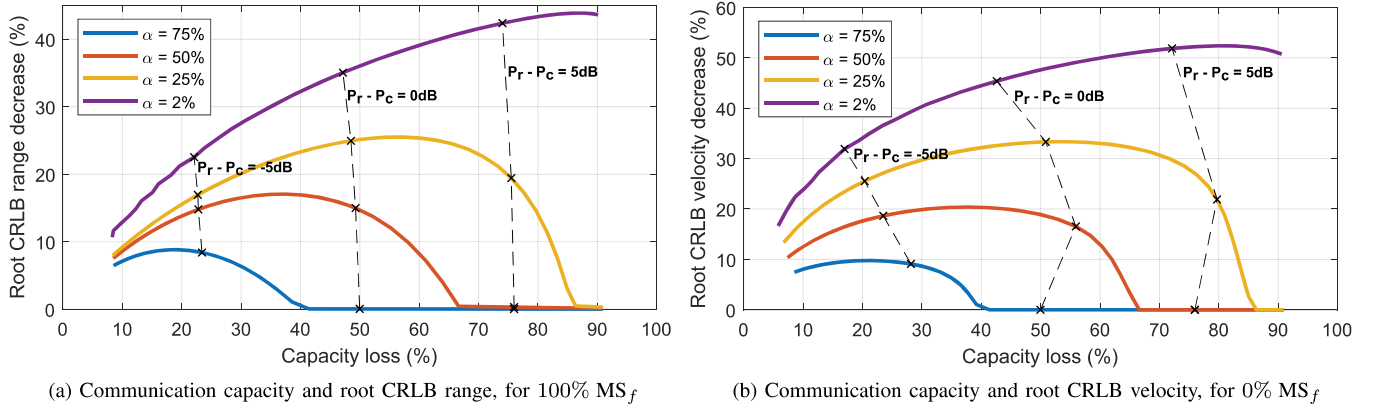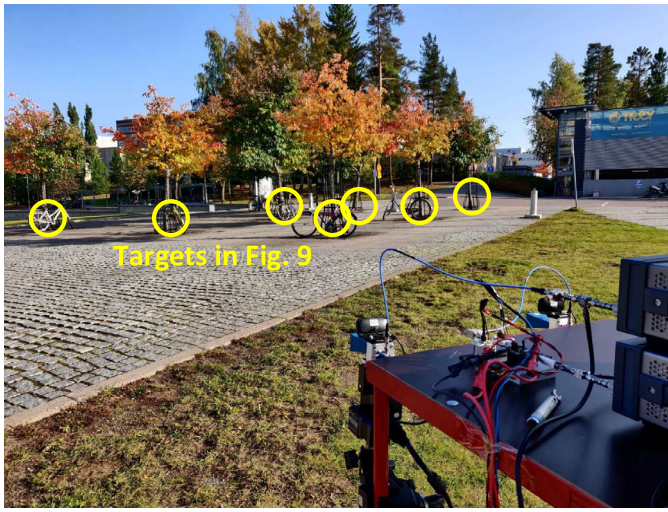
(a) Communication capacity and root CRLB range, for 100% MS_f (b) Communication capacity and root CRLB velocity, for 0% MS_f

Fig. 7. Trade-off between communication capacity and two CRLBs for different α and $\Delta\mathrm{PSD} = 3$ dB, when $P_\mathrm{r} - P_\mathrm{c}$ is varied between -10 dB and 10 dB.

(a) Mapped outdoor environment (b) Equipment used in the measurement setup

Fig. 8. The outdoor sensing and mapping scenario indicating the targets in the environment, and the hardware measurement setup, which emulates the joint radar TRX at 27.7 GHz.

the corresponding unoptimized waveform. So, the target can be made narrower in range or velocity domains by allocating radar subcarriers for either MS_f or MS_t maximization.

Figure 5(b) illustrates the PSLs for both range and velocity, for $\Delta\mathrm{PSD} = 3$ dB. The PSL is calculated as the difference between the main-lobe peak and the next peak within 40 samples, and a higher PSL is thus suitable for target detection. The range profile's PSL decreases when either α decreases (increase of radar power) or MS_f % increases (more radar power for MS_f maximization). When either of these happens, most of the radar power is pushed to the edges of the spectrum, increasing the ambiguity in range domain. For the velocity profile, its PSL decreases when MS_f % decreases. Hence, this maximizes MS_t by pushing more power towards the edge OFDM symbols, thereby increasing the ambiguity in velocity profile. To summarize, allocating radar power to either the edges of frequency or time increases the ambiguity in the corresponding range and velocity profiles. However, by varying MS_f % for a given α, either profile's PSL can be improved by properly allocating the active radar subcarriers, outperforming the corresponding unoptimized waveform.

Next, the variation of main-lobe width of both profiles is analyzed for different $\Delta\mathrm{PSD}$ values, when α is fixed at 75%, with the results depicted in Fig. 5(c). The main-lobe widths in the figure are calculated as null-to-null distance while averaging over different point targets and TX frequency-domain symbol realizations. This results in somewhat wild variations, however, a general observation is that for both profiles, when $\Delta\mathrm{PSD}$ passes some threshold value for a given MS_f %, the main-lobe width decreases, and for certain combinations, they can be made lower than that of the unoptimized waveform.

Figure 5(d) depicts the variation of PSLs of both profiles with $\Delta\mathrm{PSD}$, for a fixed $\alpha = 75\%$. An increase of $\Delta\mathrm{PSD}$ is observed to generally decrease the PSLs of both profiles. Doing that increases P_max and from (32), the number of active radar subcarriers is decreased. Since the radar power is fixed due to fixed α, all that power is distributed among a lesser number of active radar subcarriers. Hence, more power is pushed to the edges of either the frequency spectrum or the time-domain waveform, increasing MS_f or MS_t, respectively. Following a similar analogy as for Fig. 5(b), the corresponding
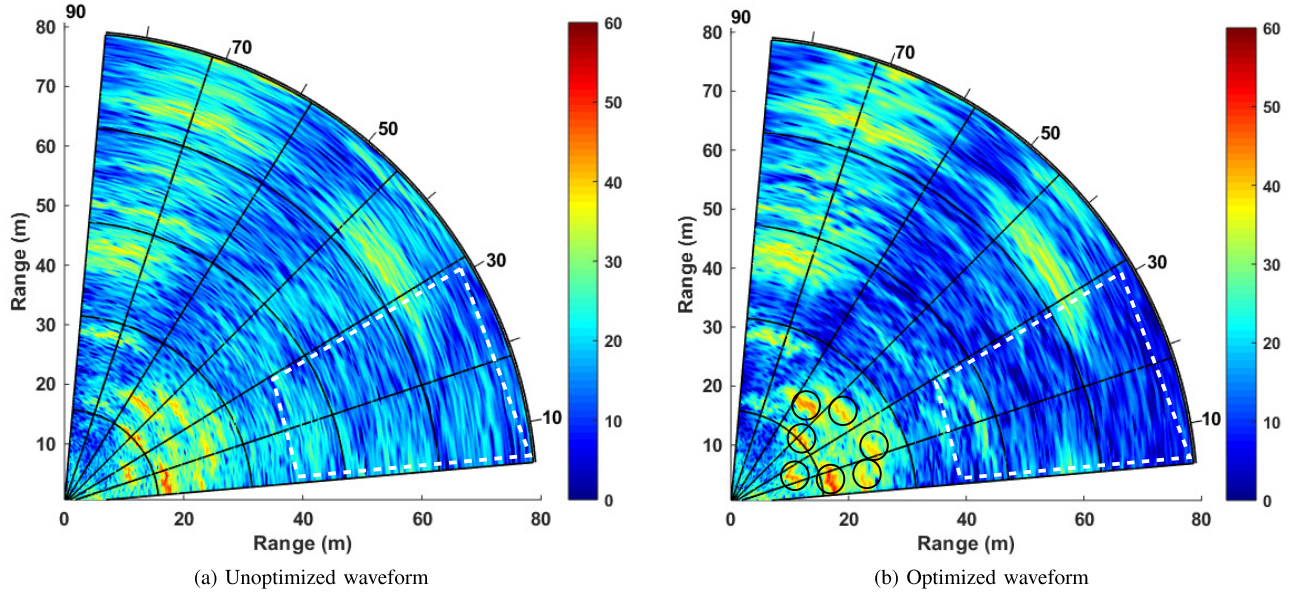
Fig. 9. The outdoor environment mapped with the unoptimized and the optimized standard compliant 5G NR waveforms at 27.7 GHz, for $\alpha = 25\%$ and ΔPSD = 3 dB. Waveform bandwidth is 400 MHz.

PSLs of the profiles decrease accordingly. By suitably choosing ΔPSD for a given MS$_f$ %, however, allows to increase the PSL behavior beyond that of the unoptimized waveform.

The root mean square errors (RMSEs) of both range and velocity estimates are next calculated, and Fig. 6 shows these results for SNR$_r = -10$ dB. For both estimates, optimized waveforms have lower RMSEs than those of the corresponding unoptimized waveforms. Moreover, the improvement is clearly visible for the range estimate. Therefore, optimizing the waveform based on the theoretical CRLBs also enables to achieve performance improvement in a practical scenario.

To evaluate communication subsystem's performance, a multipath channel is simulated with free-space path loss of 121.4 dB, and RX noise power of -87.1 dBm. The communication capacity of the communication subcarriers is then calculated based on (26). Since some power is taken away from the communication subcarriers to fill the radar subcarriers, there will be a trade-off between each subsystem's performance with the power allocation $P_r - P_c$. Figures 7(a) and 7(b) depict this in terms of the communication capacity and the two CRLBs, when $P_r - P_c$ is varied. Further, the percentages of CRLB decrease/capacity loss denote the improvement/degradation w.r.t. the unoptimized cases.

Both figures show that the CRLB improvement reaches a maximum, decreasing there onward. When $P_r - P_c$ increases, more power is allocated for the radar subcarriers. Depending on $P_{\max}$, there is a maximum number of active radar subcarriers in the waveform, and once all of them are allocated $P_{\max}$, there will be a residual power of $P_t - P_c - P_{\max}(N_{\text{act}} - 1) - P_\Delta$ that is reallocated to the communication subcarriers. As such, this will reduce the CRLB improvement.

The optimum power allocation $P_r - P_c$ for CRLB improvement would thus be at the maximum point of each curve. Increasing the power allocation beyond that would be detrimental for both subsystems. Moreover, this power allocation is less for higher α values. In that case, less number of radar subcarriers exist, and less radar power is required. Therefore, these two figures depict the trade-off between the two subsystems, and depending on α, power allocation can also be varied for optimum performance.

B. Measurement Results at 28 GHz Band

To observe and illustrate the performance in a practical measurement-based scenario, the unoptimized and optimized waveforms are next used to sense and map a real-world outdoor environment. This section discusses the related measurement setup and the scenario, while also illustrating the results.

1) Measurement Campaign and the Scenario: Figure 8(a) depicts the measurement scenario, with static targets highlighted (bicycles near some metallic structures). A vector signal transceiver (VST) of model PXIe-5840 is used for TX and RX processing at an intermediate frequency of 3.2 GHz. Two mixers of model N5183B-MXG, operating at 24.5 GHz are used at both ends of the VST to up/down-convert the signals to/from the mm-wave frequency of 27.7 GHz. Standard-compliant 5G NR waveform with 400 MHz channel bandwidth is utilized, without and with the optimized radar subcarriers. As the TX and RX antennas, two horn antennas of model PE9851A-20 are used to emulate the joint radar TRX, with a 3-dB beamwidth of $17°$ and a gain of 20 dBi. Having these directional beams emulate phased arrays, and allow to compensate for the high attenuation evident in the mm-wave frequencies. These antennas are then mechanically steered between $5°$ and $85°$ directions with a step size of $2°$. A trolley is used to mount the two antennas and carry all

the equipment. Two power amplifiers are also used at the TX chain. This setup is shown in Fig. 8(b).

2) Sensing Results: Since only static targets are sensed, the waveform with 100% of activated radar subcarriers for MS_f is used as the optimized TX signal, with $\Delta\mathrm{PSD}$ of 3 dB. Further, $M = 20$ OFDM symbols are used, but the other parameters are the same as used in the simulations. For each angle, range estimation is performed for the 20 OFDM symbols, and they are coherently combined to obtain a single range profile. These are then used to generate the map of the outdoor environment.

Figure 9(a) shows these mapping results for the unoptimized waveform, with $\alpha = 25\%$, while Fig. 9(b) shows the corresponding results when the waveform is optimized. The targets in Fig. 8(a) are also circled in Fig. 9(b) for better understanding and visualization of the environment. Comparing between the two figures (e.g., highlighted area for 40–80m and 0–30°), it is clearly observed that the optimized waveform enables to considerably minimize range side-lobes in the radar image, indicating that allocating power for the radar subcarriers has allowed clearly identifying the detected targets. Additionally, the overall clutter level is clearly reduced. Therefore, though the optimization is based on minimizing the theoretical CRLB of the range estimate, it shows promising results in a practical scenario as well. More comprehensive measurement results and assessment are available in our related work in [20].

V. Conclusion

This article addressed the OFDM waveform optimization for 5G–6G JCAS systems. Empty subcarriers within the waveform are filled with optimized frequency-domain samples to improve the radar subsystem's performance, by reallocating a portion of the communication subcarriers' power. The results indicate that the CRLBs and RMSEs of range and velocity, as well as the transmit waveform PAPR can be efficiently controlled and minimized through the described optimization approaches. Further, the optimization is shown to narrow the main-lobe widths of the range and velocity profiles, at the cost of decreasing their PSLs. However, by properly selecting the optimization parameters, improved performance is observed when compared with the corresponding unoptimized waveform. Additionally, the trade-off between the subsystems indicates that the power allocation can be chosen intelligently for optimal performance of both subsystems. Finally, over-the-air RF measurements were performed at 28 GHz, with both optimized and unoptimized 5G NR waveforms, for an outdoor environment sensing mapping scenario to demonstrate the range side-lobe improvement due to the optimization.

Appendix A
CRLB Expressions for the OFDM Signal Model

Here, we derive the expressions for the delay and Doppler CRLBs, using the Fisher information matrix, for the OFDM signal model.

When the parameter estimation is considered to be unbiased, $\int(\hat{\boldsymbol{\theta}} - \boldsymbol{\theta})\mathcal{P}_\mathbf{y}(\mathbf{y};\boldsymbol{\theta})dy = \mathbf{0}$, where $\mathcal{P}_\mathbf{y}(\mathbf{y};\boldsymbol{\theta})$ is centered around the zero vector. Differentiating w.r.t. $\boldsymbol{\theta}$, it can be restated

as $\mathbb{E}\{(\hat{\boldsymbol{\theta}} - \boldsymbol{\theta})\frac{\partial \log \mathcal{P}_\mathbf{y}(\mathbf{y};\boldsymbol{\theta})}{\partial \boldsymbol{\theta}}^T\} = \mathbf{I}$. Pre/post-multiplying this by $\mathbf{w}^T$ and $\mathcal{I}^{-1}(\boldsymbol{\theta})\mathbf{w}$ respectively, where $\mathbf{w}$ is an arbitrary vector and $\mathcal{I}(\boldsymbol{\theta})$ is the Fisher information matrix, and using the Cauchy–Schwarz inequality yields $(\mathbf{w}^T\mathcal{I}^{-1}(\boldsymbol{\theta})\mathbf{w})^2 \leq \mathbf{w}^T\mathrm{cov}(\hat{\boldsymbol{\theta}})\mathbf{w} \cdot \mathbf{w}^T\mathcal{I}^{-1}(\boldsymbol{\theta})\mathcal{I}(\boldsymbol{\theta})\mathcal{I}^{-1}(\boldsymbol{\theta})\mathbf{w}$. Simplifying it results in the matrix $\mathrm{cov}(\hat{\boldsymbol{\theta}}) - \mathcal{I}^{-1}(\boldsymbol{\theta})$ being positive semi-definite, where $\mathrm{cov}(\hat{\boldsymbol{\theta}}) = \mathbb{E}\{(\hat{\boldsymbol{\theta}} - \boldsymbol{\theta})(\hat{\boldsymbol{\theta}} - \boldsymbol{\theta})^T\}$ denotes the covariance matrix of the zero-mean estimates.

Additionally, each element of $\mathcal{I}(\boldsymbol{\theta})$ is given by $\mathcal{I}(\boldsymbol{\theta})_{i,j} = \mathbb{E}\left(\frac{\partial \log \mathcal{P}_\mathbf{y}(\mathbf{y};\boldsymbol{\theta})}{\partial \theta_i}\frac{\partial \log \mathcal{P}_\mathbf{y}(\mathbf{y};\boldsymbol{\theta})}{\partial \theta_j}\right)$, where i and j are the row and column numbers of the matrix. Then, CRLBs of delay and Doppler estimates are given by the diagonal elements of $\mathcal{I}^{-1}(\boldsymbol{\theta})$ as [42]

$$\mathrm{CRLB}(\hat{\tau}) = \frac{\mathcal{I}(\boldsymbol{\theta})_{2,2}}{\det\{\mathcal{I}(\boldsymbol{\theta})\}}, \quad \mathrm{CRLB}(\hat{f}_\mathrm{D}) = \frac{\mathcal{I}(\boldsymbol{\theta})_{1,1}}{\det\{\mathcal{I}(\boldsymbol{\theta})\}}, \quad (42)$$

where $\det\{\cdot\}$ represents the determinant. Using the definition of the second derivative and some simplifying analysis steps, each element of $\mathcal{I}(\boldsymbol{\theta})$ can be restated as

$$\mathcal{I}(\boldsymbol{\theta})_{i,j} = -\mathbb{E}\left\{\frac{\partial^2 \log \mathcal{P}_\mathbf{y}(\mathbf{y};\boldsymbol{\theta})}{\partial \theta_i \partial \theta_j}\right\}. \quad (43)$$

Substituting $\mathcal{P}_\mathbf{y}(\mathbf{y};\boldsymbol{\theta})$ from (13) and using (10), (43) then becomes $\mathcal{I}(\boldsymbol{\theta})_{i,j} = \left(\frac{2}{\sigma_\mathrm{r}^2}\right)\Re\left(\frac{\partial \mathbf{s}^H}{\partial \theta_i}\frac{\partial \mathbf{s}}{\partial \theta_j}\right)$. After performing the two partial differentiations, this can next be written in the form of

$$\mathcal{I}(\boldsymbol{\theta})_{i,j} = \frac{2}{\sigma_\mathrm{r}^2}\Re\left(\mathbf{s}^H \mathbf{D}_{\boldsymbol{\theta}_i}^H \mathbf{D}_{\boldsymbol{\theta}_j}\mathbf{s}\right). \quad (44)$$

Here, $\mathbf{D}_{\theta_1} = (-j2\pi)\mathrm{diag}(\mathbf{d}_\tau)$, in which $\mathbf{d}_\tau$ is of size $NM \times 1$, where the first N elements are $[\bar{f}_0, \bar{f}_{N-1}]$, and being repeated for M times. Similarly, $\mathbf{D}_{\theta_2} = (j2\pi)\mathrm{diag}(\mathbf{d}_{f_\mathrm{D}})$, in which $\mathbf{d}_{f_\mathrm{D}}$ is of size $NM \times 1$ where sets of M elements are the same, with the starting and ending indices being $\bar{t}_0$ and $\bar{t}_{M-1}$, respectively. Mean-shifted frequency and time variables are used since $\mathcal{P}_\mathbf{y}(\mathbf{y};\boldsymbol{\theta})$ is centered around zero. Elements of the Fisher information matrix are then

$$\mathcal{I}(\boldsymbol{\theta})_{1,1} = \frac{8\pi^2}{\sigma_\mathrm{r}^2}\sum_{m\in\mathcal{M}}\sum_{n\in\mathcal{N}}\bar{f}_n^2|S_{n,m}|^2$$
$$= 8\pi^2(\mathrm{SNR}_\mathrm{r})\sum_{m\in\mathcal{M}}\sum_{n\in\mathcal{N}}\bar{f}_n^2 P_{n,m}$$
$$= 8\pi^2(\mathrm{SNR}_\mathrm{r})(\mathrm{MS}_f), \quad (45\mathrm{a})$$
$$\mathcal{I}(\boldsymbol{\theta})_{1,2} = \mathcal{I}(\boldsymbol{\theta})_{2,1} = -8\pi^2(\mathrm{SNR}_\mathrm{r})\sum_{m\in\mathcal{M}}\sum_{n\in\mathcal{N}}\bar{t}_m\bar{f}_n P_{n,m}$$
$$= -8\pi^2(\mathrm{SNR}_\mathrm{r})(\mathrm{MS}_{f,t}), \quad (45\mathrm{b})$$
$$\mathcal{I}(\boldsymbol{\theta})_{2,2} = 8\pi^2(\mathrm{SNR}_\mathrm{r})\sum_{m\in\mathcal{M}}\sum_{n\in\mathcal{N}}\bar{t}_m^2 P_{n,m}$$
$$= 8\pi^2(\mathrm{SNR}_\mathrm{r})(\mathrm{MS}_t), \quad (45\mathrm{c})$$

where $\frac{|S_{n,m}|^2}{P_\mathrm{t}} = P_{n,m}$, and $\mathrm{MS}_{f,t}$ is the mean square bandwidth–time. Using (42), the two CRLBs are given as

$$\mathrm{CRLB}(\hat{\tau}) = \frac{1}{8\pi^2(\mathrm{SNR}_\mathrm{r})f(\mathbf{P})},$$
$$\mathrm{CRLB}(\hat{f}_\mathrm{D}) = \frac{1}{8\pi^2(\mathrm{SNR}_\mathrm{r})g(\mathbf{P})}, \quad (46)$$

where

$$f(\mathbf{P}) = (\mathrm{MS}_f) - \frac{(\mathrm{MS}_{f,t})^2}{(\mathrm{MS}_t)}$$

$$= \sum_{m \in \mathcal{M}} \sum_{n \in \mathcal{N}} \bar{f}_n^2 P_{n,m} - \frac{\left(\sum_{m \in \mathcal{M}} \sum_{n \in \mathcal{N}} \bar{t}_m \bar{f}_n P_{n,m}\right)^2}{\sum_{m \in \mathcal{M}} \sum_{n \in \mathcal{N}} \bar{t}_m^2 P_{n,m}},$$
(47a)

$$g(\mathbf{P}) = (\mathrm{MS}_t) - \frac{(\mathrm{MS}_{f,t})^2}{(\mathrm{MS}_f)},$$
(47b)

where the CRLBs are in a similar format as those in [43].

APPENDIX B
PROOF OF THEOREM 1

Here, the solution to Optimization problem 1 is derived. Substituting for $\mathrm{MS}_{f,t}$ from (47a) to (47b) gives $\frac{g(\mathbf{P})}{f(\mathbf{P})} = \frac{\mathrm{MS}_t}{\mathrm{MS}_f}$. Using this relation in (46) then results in

$$\frac{\mathrm{CRLB}(\hat{\tau})}{\mathrm{CRLB}(\hat{f}_{\mathrm{D}})} = \frac{\mathrm{MS}_t}{\mathrm{MS}_f}.$$
(48)

Since the right-hand side of this equation denotes an inverse relation, it can be deduced that the two CRLBs also have an inverse relationship. Hence, for the minimum value of $\mathrm{CRLB}(\hat{\tau})$ in Optimization problem 1, the value of $\mathrm{CRLB}(\hat{f}_{\mathrm{D}})$ should be maximized. This means that the inequality constraint in (28b) simplifies into an equality constraint.

Differentiating $\mathrm{CRLB}(\hat{\tau})$ in (46) w.r.t. the power of a general radar subcarrier with indices $\{k, l\}$ results in

$$\frac{\partial \mathrm{CRLB}(\hat{\tau})}{\partial P_{k,l}} = \left(\frac{-1}{8\pi^2(\mathrm{SNR_r})}\right)$$
$$\cdot \left(\frac{\bar{f}_k - \frac{\bar{t}_l \sum_{m \in \mathcal{M}} \sum_{n \in \mathcal{N}} \bar{t}_m \bar{f}_n P_{n,m}}{\sum_{m \in \mathcal{M}} \sum_{n \in \mathcal{N}} \bar{t}_m^2 P_{n,m}}}{f(\mathbf{P})}\right)^2 \le 0. \quad (49)$$

We next address the condition for which $\frac{\partial \mathrm{CRLB}(\hat{\tau})}{\partial P_{k,l}} = 0$. Specifically, this happens when

$$\frac{\bar{f}_k}{\bar{t}_l} = \frac{\sum_{m \in \mathcal{M}} \sum_{n \in \mathcal{N}} \bar{t}_m \bar{f}_n P_{n,m}}{\sum_{m \in \mathcal{M}} \sum_{n \in \mathcal{N}} \bar{t}_m^2 P_{n,m}} = \frac{\mathrm{MS}_{f,t}}{\mathrm{MS}_t},$$
(50)

where (45b) and (45c) are used to arrive at $\frac{\mathrm{MS}_{f,t}}{\mathrm{MS}_t}$. This ratio is fixed for a given waveform and does not necessarily become exactly equal to $\frac{\bar{f}_k}{\bar{t}_l}$. Even at the extremely unlikely case where it does, it happens only for one $\{k, l\}$ pair, and not for all radar subcarriers. Hence, this means that $\frac{\partial \mathrm{CRLB}(\hat{\tau})}{\partial P_{k,l}} < 0$, and therefore $\mathrm{CRLB}(\hat{\tau})$ always decreases when a radar subcarrier's power increases. Hence, the minimum is found when the power constraint in (28c) is satisfied with equality: $P_\mathrm{r} = P_\mathrm{t} - P_\mathrm{c}$. Thus, inequality constraints (28b) and (28c) simplify into equality constraints.

Based on (48), the relation between the two CRLBs can be written also using (45a) and (45c) as

$$\mathrm{CRLB}(\hat{\tau}) = \left(\mathrm{CRLB}(\hat{f}_{\mathrm{D}})\right) \frac{\sum_{m \in \mathcal{M}} \sum_{n \in \mathcal{N}} \bar{t}_m^2 P_{n,m}}{\sum_{m \in \mathcal{M}} \sum_{n \in \mathcal{N}} \bar{f}_n^2 P_{n,m}}$$
$$= \left(\mathrm{CRLB}(\hat{f}_{\mathrm{D}})\right) \eta(\mathbf{P}).$$
(51)

The derivatives of $\mathrm{CRLB}(\hat{f}_{\mathrm{D}})$ and $\eta(\mathbf{P})$ will be necessary for solving the optimization problem. They are given below by using (46) and (51) respectively as

$$\frac{\partial \mathrm{CRLB}(\hat{f}_{\mathrm{D}})}{\partial P_{k,l}} = \left(\frac{-1}{8\pi^2(\mathrm{SNR_r})}\right)$$
$$\cdot \left(\frac{\bar{t}_l - \frac{\bar{f}_k \sum_{m \in \mathcal{M}} \sum_{n \in \mathcal{N}} \bar{t}_m \bar{f}_n P_{n,m}}{\sum_{m \in \mathcal{M}} \sum_{n \in \mathcal{N}} \bar{f}_n^2 P_{n,m}}}{g(\mathbf{P})}\right)^2 < 0,$$
(52)

$$\frac{\partial \eta(\mathbf{P})}{\partial P_{k,l}} = \frac{\bar{t}_l^2}{\sum_{m \in \mathcal{M}} \sum_{n \in \mathcal{N}} \bar{f}_n^2 P_{n,m}}$$
$$- \frac{\bar{f}_k^2 \sum_{m \in \mathcal{M}} \sum_{n \in \mathcal{N}} \bar{t}_m^2 P_{n,m}}{\left(\sum_{m \in \mathcal{M}} \sum_{n \in \mathcal{N}} \bar{f}_n^2 P_{n,m}\right)^2}.$$
(53)

To solve the optimization problem in (28a)–(28d), the Lagrangian function is used [44], and can be denoted as

$$Q(\mathbf{P}, \zeta, \boldsymbol{\beta}, \boldsymbol{\gamma}, \delta)$$
$$= \left(\mathrm{CRLB}(\hat{f}_{\mathrm{D}})\right) \eta(\mathbf{P})$$
$$+ \zeta \left(P_\mathrm{t} - P_\mathrm{c} - \sum_{l \in \mathcal{M}} \sum_{k \in \mathcal{R}_l} P_{k,l}\right)$$
$$+ \sum_{l \in \mathcal{M}} \sum_{k \in \mathcal{R}_l} \beta_{k,l}(P_{\max} - P_{k,l}) - \sum_{l \in \mathcal{M}} \sum_{k \in \mathcal{R}_l} \gamma_{k,l} P_{k,l}$$
$$+ \delta \left(\phi - \mathrm{CRLB}(\hat{f}_{\mathrm{D}})\right),$$
(54)

where the objective function $\mathrm{CRLB}(\hat{\tau})$ is replaced by $\left(\mathrm{CRLB}(\hat{f}_{\mathrm{D}})\right) \eta(\mathbf{P})$ using (51). Here, $\zeta, \boldsymbol{\beta}, \boldsymbol{\gamma}$ and δ are the Karush–Kuhn–Tucker (KKT) multiplier corresponding to the total radar power constraint, matrices of KKT multipliers corresponding to the upper and lower bounds of power for the individual radar subcarriers and the KKT multiplier corresponding to the CRLB of the Doppler estimate, respectively. To have an optimal solution, the KKT conditions should be satisfied, which are given as

$$\frac{\partial Q(\mathbf{P}, \zeta, \boldsymbol{\beta}, \boldsymbol{\gamma}, \delta)}{\partial P_{k,l}} = \left(\mathrm{CRLB}(\hat{f}_{\mathrm{D}})\right) \frac{\partial \eta(\mathbf{P})}{\partial P_{k,l}} + (\eta(\mathbf{P}) - \delta)$$
$$\times \frac{\partial \mathrm{CRLB}(\hat{f}_{\mathrm{D}})}{\partial P_{k,l}} - \zeta - \beta_{k,l} - \gamma_{k,l} = 0,$$
(55)

$$\beta_{k,l}(P_{\max} - P_{k,l}) = 0,$$
(56)

$$\gamma_{k,l} P_{k,l} = 0,$$
(57)

$$\beta_{k,l} \ge 0,$$
(58)

$$\gamma_{k,l} \ge 0,$$
(59)

$$\sum_{l \in \mathcal{M}} \sum_{k \in \mathcal{R}_l} P_{k,l} = P_\mathrm{t} - P_\mathrm{c},$$
(60)

$$\mathrm{CRLB}(\hat{f}_{\mathrm{D}}) = \phi,$$
(61)

$$P_{k,l} \le P_{\max},$$
(62)

$$P_{k,l} \ge 0.$$
(63)

Defining two sets for the cases when the radar subcarriers are activated and not activated, respectively, as

$$\mathbf{Z}_\beta = \{\{k,l\}|\beta_{k,l} \neq 0\}, \tag{64}$$

$$\mathbf{Z}_\gamma = \{\{k,l\}|\gamma_{k,l} \neq 0\}, \tag{65}$$

where from (56), $\mathbf{Z}_\beta$ is the set of radar subcarriers for which $P_{k,l} = P_{\max}$ (activated), while from (57), $\mathbf{Z}_\gamma$ is the set of radar subcarriers for which $P_{k,l} = 0$ (unactivated). Further, $\mathbf{Z}_\beta \cap \mathbf{Z}_\gamma = \varnothing$.

$N_{act} \geq N_r$: In this case, all radar subcarriers are activated and receive $P_{\max}$. If $N_{act}P_{\max} > P_t - P_c$, the residual power is reallocated to the communication subcarriers. Some special cases can also arise, such as when $N_{act} - 1 = N_r$, the total radar power is exactly divided among all the radar subcarriers, while when $N_{act} = N_r$, all but one subcarrier receive $P_{\max}$ power, while the remaining power is given to the last. These are uninteresting cases, and much attention is given to the cases when the number of activated radar subcarriers is less when compared with the total radar subcarriers.

$N_{act} < N_r$: The expression in (55) needs to be satisfied for all the k and l values. It is clear that when $\mathbf{Z}_\beta = \varnothing$ and $\mathbf{Z}_\gamma = \varnothing$, it cannot be satisfied for all the radar subcarriers. Thus, at least one $\{k,l\}$ dependent β or γ parameter (either the radar subcarrier should receive $P_{\max}$ or zero power) should exist. Evaluating KKT conditions for all these possible cases of $\beta_{k,l}$ and $\gamma_{k,l}$,

$\mathbf{Z}_\beta = \varnothing, \mathbb{C}\{\mathbf{Z}_\gamma\} = N_r$: All radar subcarriers are empty and the radar power constraint is not satisfied.

$\mathbb{C}\{\mathbf{Z}_\beta\} = z, \mathbb{C}\{\mathbf{Z}_\gamma\} = N_r - z, z \in [1, N_{act} - 1]$: z radar subcarriers are active with $P_{k,l} = P_{\max}$ power. Since $\sum_{l \in \mathcal{M}} \sum_{k \in \mathcal{R}_l} P_{k,l} < P_t - P_c$, power constraint is not satisfied.

$\mathbb{C}\{\mathbf{Z}_\beta\} = N_{act}, \mathbb{C}\{\mathbf{Z}_\gamma\} = N_r - N_{act}$: The power requirement is met exactly (no fractional part due to the division in (32)), and much attention is given to the next, which represents a practical situation.

$\mathbb{C}\{\mathbf{Z}_\beta\} = N_{act} - 1, \mathbb{C}\{\mathbf{Z}_\gamma\} = N_r - N_{act}$: Here $N_{act} - 1$ radar subcarriers receive the maximum power, while an additional radar subcarrier receives a power of $P_{K,L} = P_\Delta$. This denotes the feasible solution to this optimization problem and the function value at this point is given by (29).

REFERENCES

[1] H. Holma, A. Toskala, and T. Nakamura, *5G Technology: 3GPP New Radio*. Hoboken, NJ, USA: Wiley, 2019.

[2] F. Liu, C. Masouros, A. P. Petropulu, H. Griffiths, and L. Hanzo, "Joint radar and communication design: Applications, state-of-the-art, and the road ahead," *IEEE Trans. Commun.*, vol. 68, no. 6, pp. 3834–3862, Jun. 2020.

[3] J. H. Reed *et al.*, "On the co-existence of TD-LTE and radar over 3.5 GHz band: An experimental study," *IEEE Wireless Commun. Lett.*, vol. 5, no. 4, pp. 368–371, Aug. 2016.

[4] M. Ghorbanzadeh, E. Visotsky, P. Moorut, W. Yang, and C. Clancy, "Radar inband and out-of-band interference into LTE macro and small cell uplinks in the 3.5 GHz band," in *Proc. IEEE Wireless Commun. Netw. Conf. (WCNC)*, Mar. 2015, pp. 1829–1834.

[5] B. D. Cordill, S. A. Seguin, and L. Cohen, "Electromagnetic interference to radar receivers due to in-band OFDM communications systems," in *Proc. IEEE Int. Symp. Electromagn. Compat.*, Aug. 2013, pp. 72–75.

[6] F. Hessar and S. Roy, "Spectrum sharing between a surveillance radar and secondary Wi-Fi networks," *IEEE Trans. Aerosp. Electron. Syst.*, vol. 52, no. 3, pp. 1434–1448, Jun. 2016.

[7] Q. Zhao and A. Swami, "A survey of dynamic spectrum access: Signal processing and networking perspectives," in *Proc. IEEE Int. Conf. Acoust., Speech Signal Process. (ICASSP)*, vol. 4, Apr. 2007, pp. 1349–1352.

[8] B. Paul, A. R. Chiriyath, and D. W. Bliss, "Survey of RF communications and sensing convergence research," *IEEE Access*, vol. 5, pp. 252–270, 2017.

[9] C. De Lima *et al.*, "Convergent communication, sensing and localization in 6G systems: An overview of technologies, opportunities and challenges," *IEEE Access*, vol. 9, pp. 26902–26925, Jan. 2021.

[10] D. Ma, N. Shlezinger, T. Huang, Y. Liu, and Y. C. Eldar, "Joint radar-communication strategies for autonomous vehicles: Combining two key automotive technologies," *IEEE Signal Process. Mag.*, vol. 37, no. 4, pp. 85–97, Jul. 2020.

[11] F. Liu and C. Masouros, "A tutorial on joint radar and communication transmission for vehicular networks—Part I: Background and fundamentals," *IEEE Commun. Lett.*, vol. 25, no. 2, pp. 322–326, Feb. 2021.

[12] F. Liu and C. Masouros, "A tutorial on joint radar and communication transmission for vehicular networks—Part II: State of the art and challenges ahead," *IEEE Commun. Lett.*, vol. 25, no. 2, pp. 327–331, Feb. 2021.

[13] F. Liu and C. Masouros, "A tutorial on joint radar and communication transmission for vehicular networks—Part III: Predictive beamforming without state models," *IEEE Commun. Lett.*, vol. 25, no. 2, pp. 332–336, Feb. 2021.

[14] J. Andrew Zhang *et al.*, "Enabling joint communication and radar sensing in mobile networks–a survey," 2020, *arXiv:2006.07559*. [Online]. Available: http://arxiv.org/abs/2006.07559

[15] A. R. Chiriyath, B. Paul, and D. W. Bliss, "Radar-communications convergence: Coexistence, cooperation, and co-design," *IEEE Trans. Cognit. Commun. Netw.*, vol. 3, no. 1, pp. 1–12, Mar. 2017.

[16] C. B. Barneto *et al.*, "High-accuracy radio sensing in 5G new radio networks: Prospects and self-interference challenge," in *Proc. 53rd Asilomar Conf. Signals, Syst., Comput.*, Nov. 2019, pp. 1159–1163.

[17] M. L. Rahman, J. A. Zhang, X. Huang, Y. J. Guo, and R. W. Heath, "Framework for a perceptive mobile network using joint communication and radar sensing," *IEEE Trans. Aerosp. Electron. Syst.*, vol. 56, no. 3, pp. 1926–1941, Jun. 2020.

[18] P. Kumari, J. Choi, N. Gonzalez-Prelcic, and R. W. Heath, "IEEE 802.11Ad-based radar: An approach to joint vehicular communication-radar system," *IEEE Trans. Veh. Technol.*, vol. 67, no. 4, pp. 3012–3027, Apr. 2018.

[19] H. Wymeersch, G. Seco-Granados, G. Destino, D. Dardari, and F. Tufvesson, "5G mmWave positioning for vehicular networks," *IEEE Wireless Commun.*, vol. 24, no. 6, pp. 80–86, Dec. 2017.

[20] S. D. Liyanaarachchi, C. B. Barneto, T. Riihonen, and M. Valkama, "Experimenting joint vehicular communications and sensing with optimized 5G NR waveform," in *Proc. IEEE 93rd Veh. Technol. Conf. (VTC-Spring)*, Apr. 2021, pp. 1–5.

[21] C. B. Barneto, T. Riihonen, M. Turunen, M. Koivisto, J. Talvitie, and M. Valkama, "Radio-based sensing and indoor mapping with millimeter-wave 5G NR signals," in *Proc. Int. Conf. Localization GNSS (ICL-GNSS)*, Jun. 2020, pp. 1–5.

[22] A. R. Chiriyath, B. Paul, G. M. Jacyna, and D. W. Bliss, "Inner bounds on performance of radar and communications co-existence," *IEEE Trans. Signal Process.*, vol. 64, no. 2, pp. 464–474, Jan. 2016.

[23] P. Kumari, S. A. Vorobyov, and R. W. Heath, "Adaptive virtual waveform design for millimeter-wave joint communication–radar," *IEEE Trans. Signal Process.*, vol. 68, pp. 715–730, 2020.

[24] K. V. Mishra, M. R. Bhavani Shankar, V. Koivunen, B. Ottersten, and S. A. Vorobyov, "Toward millimeter-wave joint radar communications: A signal processing perspective," *IEEE Signal Process. Mag.*, vol. 36, no. 5, pp. 100–114, Sep. 2019.

[25] A. Aubry, A. De Maio, Y. Huang, M. Piezzo, and A. Farina, "A new radar waveform design algorithm with improved feasibility for spectral coexistence," *IEEE Trans. Aerosp. Electron. Syst.*, vol. 51, no. 2, pp. 1029–1038, Apr. 2015.

[26] M. Bica, K.-W. Huang, U. Mitra, and V. Koivunen, "Opportunistic radar waveform design in joint radar and cellular communication systems," in *Proc. IEEE Global Commun. Conf. (GLOBECOM)*, Dec. 2014, pp. 1–7.

[27] M. Bica, K.-W. Huang, V. Koivunen, and U. Mitra, "Mutual information based radar waveform design for joint radar and cellular communication systems," in *Proc. IEEE Int. Conf. Acoust., Speech Signal Process. (ICASSP)*, Mar. 2016, pp. 3671–3675.

[28] T. Guo and R. Qiu, "OFDM waveform design compromising spectral nulling, side-lobe suppression and range resolution," in *Proc. IEEE Radar Conf.*, May 2014, pp. 1424–1429.

[29] C. B. Barneto, S. D. Liyanaarachchi, T. Riihonen, L. Anttila, and M. Valkama, "Multibeam design for joint communication and sensing in 5G new radio networks," in *Proc. IEEE Int. Conf. Commun. (ICC)*, Jun. 2020, pp. 1–6.

[30] C. B. Barneto, S. D. Liyanaarachchi, T. Riihonen, M. Heino, L. Anttila, and M. Valkama, "Beamforming and waveform optimization for OFDM-based joint communications and sensing at mm-waves," in *Proc. 54th Asilomar Conf. Signals, Syst., Comput.*, Nov. 2020, pp. 1–6.

[31] S. D. Liyanaarachchi, C. B. Barneto, T. Riihonen, and M. Valkama, "Joint OFDM waveform design for communications and sensing convergence," in *Proc. ICC - IEEE Int. Conf. Commun. (ICC)*, Jun. 2020, pp. 1–6.

[32] M. Bica and V. Koivunen, "Radar waveform optimization for target parameter estimation in cooperative radar-communications systems," *IEEE Trans. Aerosp. Electron. Syst.*, vol. 55, no. 5, pp. 2314–2326, Oct. 2019.

[33] C. Baquero Barneto *et al.*, "Full-duplex OFDM radar with LTE and 5G NR waveforms: Challenges, solutions, and measurements," *IEEE Trans. Microw. Theory Techn.*, vol. 67, no. 10, pp. 4042–4054, Oct. 2019.

[34] C. Sturm and W. Wiesbeck, "Waveform design and signal processing aspects for fusion of wireless communications and radar sensing," *Proc. IEEE*, vol. 99, no. 7, pp. 1236–1259, Jul. 2011.

[35] C. Sturm, T. Zwick, and W. Wiesbeck, "An OFDM system concept for joint radar and communications operations," in *Proc. IEEE 69th Veh. Technol. Conf. (VTC Spring)*, Apr. 2009.

[36] Y. Zeng, Y. Ma, and S. Sun, "Joint radar-communication with cyclic prefixed single carrier waveforms," *IEEE Trans. Veh. Technol.*, vol. 69, no. 4, pp. 4069–4079, Apr. 2020.

[37] Y. Rahmatallah and S. Mohan, "Peak-to-average power ratio reduction in OFDM systems: A survey and taxonomy," *IEEE Commun. Surveys Tuts.*, vol. 15, no. 4, pp. 1567–1592, Mar. 2013.

[38] C. B. Barneto, S. D. Liyanaarachchi, M. Heino, T. Riihonen, and M. Valkama, "Full duplex radio/radar technology: The enabler for advanced joint communication and sensing," *IEEE Wireless Commun.*, vol. 28, no. 1, pp. 82–88, Feb. 2021.

[39] T. Jiang and Y. Wu, "An overview: Peak-to-average power ratio reduction techniques for OFDM signals," *IEEE Trans. Broadcast.*, vol. 54, no. 2, pp. 257–268, Jun. 2008.

[40] T. Huang and T. Zhao, "Low PMEPR OFDM radar waveform design using the iterative least squares algorithm," *IEEE Signal Process. Lett.*, vol. 22, no. 11, pp. 1975–1979, Nov. 2015.

[41] *NR; Base Station (BS) Radio Transmission and Reception*, 3GPP document TS 38.104 v15.10.0, Tech. Spec. Group Radio Access Network, Rel. 15, Jul. 2020.

[42] S. M. Kay, *Fundamentals of Statistical Signal Processing: Estimation Theory*. Upper Saddle River, NJ, USA: Prentice-Hall, 1997.

[43] T. Zhao and T. Huang, "Cramer-Rao lower bounds for the joint delay-Doppler estimation of an extended target," *IEEE Trans. Signal Process.*, vol. 64, no. 6, pp. 1562–1573, Mar. 2016.

[44] S. Boyd and L. Vandenberghe, *Convex Optimization*. Cambridge, U.K.: Cambridge Univ. Press, 2004.

Sahan Damith Liyanaarachchi (Graduate Student Member, IEEE) received the B.Sc. degree (Hons.) from the University of Peradeniya, Sri Lanka, in 2016, and the M.Sc. degree (Hons.) from Tampere University, Finland, in 2019, where he is currently pursuing the Ph.D. degree with the Unit of Electrical Engineering. His research interests include waveform optimization for joint communication and sensing systems, with current research interest includes the evolution of beyond 5G systems.

Taneli Riihonen (Member, IEEE) received the D.Sc. degree (Hons.) in electrical engineering from Aalto University, Helsinki, Finland, in 2014. He is currently a tenure-track Assistant Professor with the Faculty of Information Technology and Communication Sciences, Tampere University, Finland. His research interests include physical-layer OFDM(A), multiantenna, multihop, and full-duplex wireless techniques with current research interest includes the evolution of beyond 5G systems.

Carlos Baquero Barneto (Graduate Student Member, IEEE) received the B.Sc. and M.Sc. degrees in telecommunication engineering from the Universidad Politécnica de Madrid, Spain, in 2017 and 2018, respectively. He is currently pursuing the Ph.D. degree with the Unit of Electrical Engineering, Tampere University, Finland. His research interests include joint communication and sensing systems' design, with particular emphasis on 5G and beyond mobile radio networks.

Mikko Valkama (Senior Member, IEEE) received the M.Sc. and D.Sc. degrees (both with Hons.) from the Tampere University of Technology in 2000 and 2001, respectively. He is currently a Full Professor and the Head of the Unit of Electrical Engineering, Tampere University. His research interests include radio communications, radio localization, and radio-based sensing, with particular emphasis on 5G and beyond mobile radio networks.

Publication 2

Joint OFDM Waveform Design for Communications and Sensing Convergence

S. D. Liyanaarachchi, C. Baquero Barneto, T. Riihonen and M. Valkama

Joint OFDM Waveform Design for Communications and Sensing Convergence

Sahan Damith Liyanaarachchi, Carlos Baquero Barneto, Taneli Riihonen, and Mikko Valkama

Electrical Engineering, Faculty of Information Technology and Communication Sciences, Tampere University, Finland

email: sahan.liyanaarachchi@tuni.fi

Abstract—This paper discusses waveform design for a joint radar and communication system, where the radar transceiver and the communication transmitter are considered to be the same full-duplex base station. The downlink orthogonal frequency-division multiplexing (OFDM) waveform of the communication system is used also for sensing. Thus, unused subcarriers within the OFDM symbols are exploited for radar purposes and filled up with optimized complex-valued data, so as to minimize the lower bounds of the variances of the delay and Doppler estimates of radar target parameters, while maintaining an acceptable level of performance for the communication system. The results indicate that significant improvements can be made for the radar system, but in compensation, the power allocated for the communication subcarriers needs to be reduced. Thus, a trade-off between the converged systems allows both to operate together with reduced performance degradation.

Fig. 1. Joint radar and downlink communication system.

I. Introduction

Conventional radar and communication systems operate separately at predefined frequencies so that one does not interfere the other. The ever-increasing demand for mobile communication devices has resulted them being ubiquitous, and to keep up with this demand, spectrum authorities have extended the bands of operational frequencies of these, thereby overlapping on the frequency bands of legacy radar systems, resulting in mutual interference to both systems. Instead of the two systems' separated operation, a joint system thus needs to be devised to mitigate the interference to both systems and allow satisfactory performance, and different solutions have surfaced to address this [1]. Radio-frequency convergence is the most novel category of solutions that encompasses methods where both systems jointly use the available scarce spectrum [2], [3], is also the focus of this paper.

In a joint system with co-located transmitter (TX) antennas for radar and communication systems, a joint waveform is used for both, and it can be differentiated on time, frequency, code and space domains, by having them orthogonal to each other [4]. However, to address the spectrum scarcity evident in the present world, modern systems utilize the same frequency allocation. Thus, in principle, the performance of each system is dependent on the proportion of bandwidth allocated for it, and the improved performance of one happens at the cost of reduced performance of the other [5].

Most often, a joint waveform is generated through an optimization algorithm, while considering the performance of both radar and the communication systems. The function to be optimized is taken as some metric of performance of either
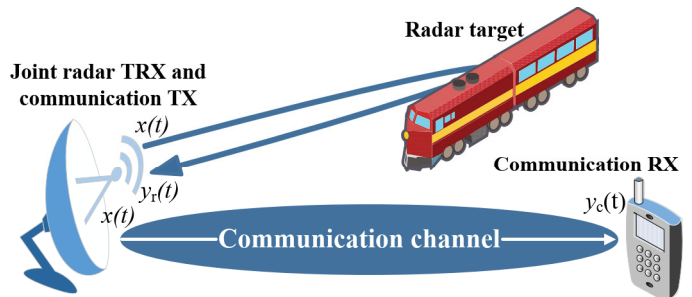
system, while the performance of the other is often set as a constraint. In the perspective of the radar system, performance can be improved by maximizing the signal-to-interference-plus-noise ratio at the radar receiver (RX). The interference on the communication system by the radar system can be controlled by imposing a constraint to reduce the energy in the interfering bands of frequencies [6]. More constraints can also be applied to achieve a better radar waveform, with some properties being the range resolution, modulus of the signal, and integrated and peak side-lobe levels of the autocorrelation function [7]. Another waveform optimization method could be to maximize the detection probability of the radar system while constraining the probability of false alarm. The performance of the communication system can be controlled by imposing a constraint on its capacity [8].

Some researchers have also proposed to maximize the mutual information at the radar RX [9]. A communication system can be used passively here so that the reflected signals from it are also used for target detection. Thus, mutual information about the targets from both radar and communication systems is maximized to generate the waveform [10], [11]. Others have generated the waveform based on target delay estimation, where the Cramer–Rao lower bound (CRLB) of the delay parameter is optimized [12], [13].

This paper concerns the generation of a joint orthogonal frequency-division multiplexing (OFDM) waveform for a converged radar and communication system, as illustrated in Fig. 1. Unlike earlier research on the topic, this paper considers the ability of the base stations of modern OFDM systems to perform also sensing. There often exist unused subcarriers that are not utilized by the communication system, and these can be filled with optimized complex-valued data to improve the

performance of the radar system, based on the minimization of the CRLBs of error variances of the delay and Doppler estimates of the targets, while ascertaining the performance of the communication system is retained at a satisfactory level. The power allocated to the filled *radar subcarriers* and communication subcarriers is set to maintain uniform spectral density, due to which the improved performance of one will come at the expense of the other.

II. SYSTEM MODEL

Figure 1 depicts the considered joint system architecture. The radar transceiver (TRX) and the communication TX are considered to be the same device, e.g., a base station. Thus, it also receives in full-duplex manner the reflected echoes to perform sensing. The transmit signal $x(t)$ is an OFDM waveform with M symbols and each with N subcarriers. The received signals at the radar RX and the communication RX are denoted by $y_r(t)$ and $y_c(t)$, respectively.
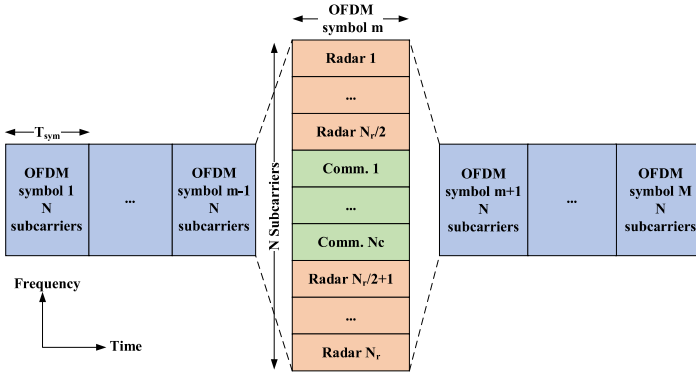
Fig. 2. Structure of the transmitted joint OFDM waveform.

The locations of the radar subcarriers are assumed to be symmetrically placed at the two edges of OFDM spectrum while the communication subcarriers are at the center, as denoted in Fig. 2. Here, N_c and N_r are the number of communication and radar subcarriers in an OFDM symbol, respectively, and $N_c + N_r = N$. The transmitted complex symbols on a radar and a communication subcarrier are denoted by $X_{r,n,m}$ and $X_{c,n,m}$, where the n and m correspond to subcarrier and OFDM symbol indices, respectively.

The radar system performs detection with the help of both radar and communication subcarriers, at the radar RX. For the radar subcarriers, each symbol's amplitude and phase can be freely controlled, whereas for the communication subcarriers, such freedom is not evident. For them, the amplitudes are herein scaled according to the power allocated, prior to optimization, and they are not modified by the optimization.

The joint transmit signal can be written as

$$x(t) = \frac{1}{N} \sum_{m=0}^{M-1} p(t - mT_{\text{sym}}) \Bigg(\sum_{n \in \mathcal{R}} X_{r,n,m} e^{j2\pi n \Delta f(t - mT_{\text{sym}})} + \sum_{n \in \mathcal{C}} X_{c,n,m} e^{j2\pi n \Delta f(t - mT_{\text{sym}})} \Bigg), \quad (1)$$

where $\Delta f, p(t), T_{\text{sym}}, \mathcal{C}$ and $\mathcal{R}$ denote the frequency spacing between subcarriers, the pulse shape, the time duration of an OFDM symbol and sets for communication and radar subcarriers in each OFDM symbol with $\mathcal{C} = \{n | n \in [\frac{-N_c}{2}, \frac{N_c}{2} - 1]\}$ and $\mathcal{R} = \{n | n \in [\frac{-N}{2}, \frac{-N}{2} + \frac{N_r}{2} - 1] \cup [\frac{N}{2} - \frac{N_r}{2}, \frac{N}{2} - 1]\}$. The power of the radar and communication sub-waveforms over M symbols can then be written as

$$P_r = \frac{1}{MN} \sum_{m=0}^{M-1} \sum_{n \in \mathcal{R}} |X_{r,n,m}|^2, \quad (2a)$$

$$P_c = \frac{1}{MN} \sum_{m=0}^{M-1} \sum_{n \in \mathcal{C}} |X_{c,n,m}|^2. \quad (2b)$$

A. Radar System

The received radar signal at the radar RX can be written as

$$y_r(t) = \sum_{k=1}^{K_r} A_{r,k} x(t - \tau_{r,k}) e^{j2\pi f_{r,D,k} t} + v_r(t), \quad (3)$$

which is the sum of multiple copies of attenuated and delayed versions of $x(t)$. Further, the phases are also varying due to the Doppler shifts, which correspond to the relative speed between the radar TRX and targets. Here, K_r and $A_{r,k}$ are the total number of point targets and the two-way attenuation constant for the path between the radar TRX and the kth target, while $\tau_{r,k}$ and $f_{r,D,k}$ are the two-way delay and Doppler shift of the target, respectively, that the radar tries to estimate. The noise $v_r(t)$ is assumed to be additive, white, and Gaussian. The signal-to-noise ratio (SNR) at the radar RX due to the kth target is

$$\text{SNR}_{r,k} = \frac{|A_{r,k}|^2 P_r}{\sigma_r^2}, \quad (4)$$

where σ_r^2 is the variance of the noise samples.

Substituting (1) to (3) and performing the discrete Fourier transform (DFT) yields after simplification the relation between the frequency-domain TX and RX symbols as

$$Y_{r,n,m} = \sum_{k=1}^{K_r} A_{r,k} X_{n,m} e^{-j2\pi n \Delta f \tau_{r,k}} e^{j2\pi f_{r,D,k} mT_{\text{sym}}} + V_{r,n,m}, \quad (5)$$

where $X_{n,m}, Y_{r,n,m}$ and $V_{r,n,m}$ are the transmitted frequency-domain symbol, received frequency-domain symbol at the radar RX, and the frequency-domain noise sample, all on the nth subcarrier and the mth OFDM symbol, respectively.

It is observed from (5) that the received noisy frequency-domain symbol has been attenuated and the phase of it has changed from that of the transmitted symbol, due to the delay and Doppler shift of each target. The received frequency-domain symbols can be represented in matrix notation for the case of a single target, assuming the attenuation constant is known, as

$$\mathbf{Y} = \mathbf{DXB} + \mathbf{V}, \quad (6)$$

where $\mathbf{Y}$ is the received symbol matrix of size $N \times M$ with $(\mathbf{Y})_{n,m} = Y_{r,n,m}$, $\mathbf{D} = \text{diag}(\mathbf{d})$ is a diagonal matrix of size $N \times N$ where each element is given by $\mathbf{d}_n = e^{-j2\pi n \Delta f \tau}$,

and $n \in \{\frac{-N}{2}, ..., \frac{N}{2} - 1\}$. The transmitted symbol matrix $\mathbf{X}$ is of size $N \times M$ with $(\mathbf{X})_{n,m} = X_{n,m}$, $\mathbf{B} = \mathrm{diag}(\mathbf{B})$ is a diagonal matrix of size $M \times M$ where each element is given by $\mathbf{b}_m = e^{j2\pi m f_{\mathrm{D}} T_{\mathrm{sym}}}$, and $m \in \{0, ..., M - 1\}$. The noise matrix $\mathbf{V}$ is of size $N \times M$ with $(\mathbf{V})_{n,m} = V_{n,m}$.

B. Maximum Likelihood Estimation

The radar system uses the received frequency-domain symbols to estimate the delays and Doppler shifts to the different targets. A maximum likelihood estimator (MLE) is used for this. The parameter vector that needs to be estimated is

$$\boldsymbol{\theta} = [\tau, f_{\mathrm{D}}]^T. \tag{7}$$

Since the noise samples are assumed to be independently and identically Gaussian distributed, the simplified log-likelihood function for (6) can be written based on [14] as

$$\mathcal{L}(\mathbf{Y}; \boldsymbol{\theta}) = \Re \left[\sum_{m=0}^{M-1} \left(\sum_{n=0}^{N-1} Z_{n,m} e^{-j2\pi n \Delta f \tau} \right) e^{j2\pi m f_{\mathrm{D}} T_{\mathrm{sym}}} \right], \tag{8}$$

where $Z_{n,m} = Y_{n,m}^* X_{n,m}$. It is seen that the inner and outer sums have close similarity to the definitions of DFT and inverse DFT (IDFT). Therefore, the MLE is found with the help of these by quantizing the delay and Doppler parameters as

$$\tau' = \frac{n'}{N\Delta f}, \ n' = 0, ..., N - 1, \tag{9}$$

$$f_{\mathrm{D}}' = \frac{m'}{M T_{\mathrm{sym}}}, \ m' = 0, ..., M - 1. \tag{10}$$

Substituting these in (8) results in

$$\mathcal{L}(n', m') = \Re \left[\sum_{m=0}^{M-1} \overbrace{\left(\underbrace{\sum_{n=0}^{N-1} Z_{n,m} e^{\frac{-j2\pi n n'}{N}}}_{\text{element n' in } N\text{-length DFT}} \right) e^{\frac{j2\pi m m'}{M}}}^{\text{element m' in } M\text{-length IDFT}} \right]. \tag{11}$$

To find the parameters which correspond to the MLE, the values of m' and n' are found as those that maximize the log-likelihood function and denoted as

$$(n_{\max}, m_{\max}) = \arg\max \mathcal{L}(n', m'). \tag{12}$$

Finally, these are substituted in (9) and (10) to estimate the parameter value set

$$\hat{\boldsymbol{\theta}} = [\hat{\tau}, \hat{f}_{\mathrm{D}}]^T = \left[\frac{n_{\max}}{N\Delta f}, \frac{m_{\max}}{M T_{\mathrm{sym}}} \right]^T. \tag{13}$$

C. Communication System

The impulse response of the communication channel is

$$h_{\mathrm{c}}(t) = \sum_{k=1}^{K_{\mathrm{c}}} A_{\mathrm{c},k} \delta(t - \tau_{\mathrm{c},k}) e^{j2\pi f_{\mathrm{c,D},k} t}, \tag{14}$$

where $K_{\mathrm{c}}, A_{\mathrm{c},k}, f_{\mathrm{c,D},k}$ and $\tau_{\mathrm{c},k}$ are the total number of scatterers in the communication channel, attenuation constant for the path between the communication TX and RX, Doppler

shift and delay of each scatterer, respectively. The received frequency-domain symbols at the communication RX can be written based on (5) as

$$Y_{\mathrm{c},n,m} = \sum_{k=1}^{K_{\mathrm{c}}} A_{\mathrm{c},k} X_{\mathrm{c},n,m} e^{-j2\pi n \Delta f \tau_{\mathrm{c},k}} e^{j2\pi f_{\mathrm{c,D},k} m T_{\mathrm{sym}}} + V_{\mathrm{c},n,m}, \tag{15}$$

where $Y_{\mathrm{c},n,m}$ and $V_{\mathrm{c},n,m}$ are received frequency-domain communication symbols and the noise samples, respectively. The SNR of a communication subcarrier can then be denoted as

$$\mathrm{SNR}_{\mathrm{c},n,m} = \frac{\mathbb{E}\{|X_{\mathrm{c},n,m}|^2\}|H_{\mathrm{c},n,m}|^2}{\sigma_{\mathrm{c}}^2}, \tag{16}$$

where $\mathbb{E}$ and σ_{c}^2 denote the expectation operation and the variance of noise at the communication RX, respectively, and

$$H_{\mathrm{c},n,m} = \sum_{k=1}^{K_{\mathrm{c}}} A_{\mathrm{c},k} e^{-j2\pi n \Delta f \tau_{\mathrm{c},k}} e^{j2\pi f_{\mathrm{c,D},k} m T_{\mathrm{sym}}} \tag{17}$$

is the frequency-domain per-subcarrier representation of the impulse response given in (14). Since the communication RX is assumed to have knowledge about the locations of the radar subcarriers in different OFDM symbols, as is the case with conventional OFDM processing, it can easily discard those, without any extra burden.

III. Optimization of Radar Subcarriers

In estimating the parameters according to (11)–(13), they usually deviate from the actual values. It is essential that the variances of these errors be minimized to improve the accuracy of the parameter estimation process. These variances are bounded from below by the CRLBs as [15]

$$\mathbf{var}(\hat{\tau}) \geq \mathrm{CRLB}(\hat{\tau}), \tag{18a}$$

$$\mathbf{var}(\hat{f}_{\mathrm{D}}) \geq \mathrm{CRLB}(\hat{f}_{\mathrm{D}}). \tag{18b}$$

For the signal model in (6), these are given in the Appendix by (27a) and (27b).

The waveform optimization which minimizes the CRLBs of the delay and Doppler estimates can then be denoted as

$$\arg\min_{\mathbf{X}_{\mathrm{r}}} \mathrm{CRLB}(\hat{\tau}) \text{ or } \arg\min_{\mathbf{X}_{\mathrm{r}}} \mathrm{CRLB}(\hat{f}_{\mathrm{D}}) \tag{19a}$$

subject to the constraints

$$P_{\mathrm{r}} = \left(\frac{N_{\mathrm{r}}}{N} \right) P_{\mathrm{total}}, \tag{19b}$$

$$\mathrm{PAPR}_{x(t)} \leq \mathrm{PAPR}_{\max}, \tag{19c}$$

where $\mathbf{X}_{\mathrm{r}}, P_{\mathrm{total}}, \mathrm{PAPR}_{x(t)}$ and $\mathrm{PAPR}_{\max}$ denote the matrix of optimized complex-valued data for the radar subcarriers, total TX power, peak-to-average power ratio (PAPR) of the joint waveform and the maximum PAPR tolerable by the TX, respectively. The power between radar and communication subcarriers is dependent on their subcarrier ratio within an OFDM symbol. The first constraint therefore ensures that the radar subcarriers would have a proportion of the total transmit power while the second constraint limits the PAPR of the generated OFDM waveform. In what follows, this optimization problem is numerically solved through the constrained optimization function *fmincon* in MATLAB.

IV. Numerical Results

The parameters used for the waveform optimization are $P_{\text{total}} = 39\text{dBm}$, $\text{PAPR}_{\max} = 8\text{dB}$, $M = 64, N = 128, \Delta f = 120\text{kHz}$ and carrier frequency $f_c = 28\text{GHz}$. Figure 3 depicts the effect of optimization on the root CRLBs for distance and velocity estimates, after converting the delay and Doppler estimates as $\hat{d} = \frac{c\hat{\tau}}{2}$ and $\hat{v} = \frac{c\hat{f}_D}{2f_c}$, with c being the speed of light. It can be observed that waveform optimization allows reduced root CRLBs when compared with the respective unoptimized waveforms. In the unoptimized cases, the radar subcarriers are assumed to be empty, mimicking the unused subcarriers. The worst errors under optimization for both cases are when all are communication subcarriers. However, the availability of increased number of radar subcarriers allows to further minimize the errors of the radar system. From (19b), it is however evident that the increase of the number of radar subcarriers will imply reduced power for the communication subcarriers.

The waveform optimizations based on the minimization of delay and Doppler estimates' CRLBs are considered as separate optimizations that output two different waveforms, and Fig. 3 also denotes how one waveform optimization affects the other. Due to one waveform optimization, the error of the other estimate also increases with N_c. However, this is higher than in the case when that particular parameter is the objective for waveform optimization. Thus, the optimization of one impacts in an inverse way on the other, as is the case usually for contrasting optimizations.

Figure 4 shows the PAPR of the waveform for the two optimizations, with and without the PAPR constraint applied. In optimizing the waveform to minimize the CRLB of the distance estimate, it is observed that the PAPR is high when only radar subcarriers exist, and the inclusion of communication subcarriers is seen to decrease the PAPR of the waveform. However, these PAPR values are still considered to be high for the communication system. For the other waveform optimization, though a higher PAPR is not observed w.r.t. the distance case, it is still undesirable for a practical TX. For both of these, it is observed that the addition of the PAPR constraint allows to control the PAPR of the waveform to the required level of 8dB. One point to note is that when all the subcarriers are used for communication, the optimization does not have any degrees of freedom and, thus, the PAPR of the waveform cannot be controlled.

To evaluate the effect on the communication system, a multipath channel is simulated with a free space path loss of 116dB, a noise power of -96dBm at the communication RX, root mean square delay spread of 0.63ns and a ratio of -13dB between the direct and average multipath components. Each communication symbol $X_{c,n,m}$ uses quadrature phase-shift keying in this paper. For different channel realizations, the average SNR of the communication subcarriers at the communication RX is calculated and Fig. 5 depicts the variation of the empirical cumulative distribution functions (CDF) for different number of communication subcarriers in each OFDM
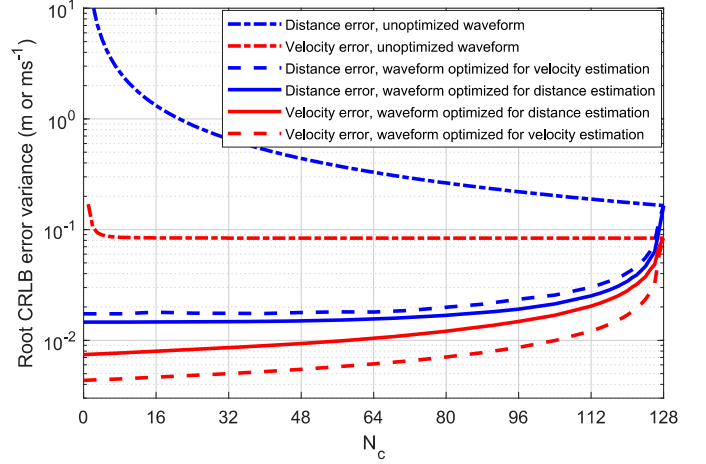
Fig. 3. Root CRLB error variances of the distance and velocity estimates, for optimized and unoptimized waveforms, with $\text{PAPR}_{\max} = 8\text{dB}$.
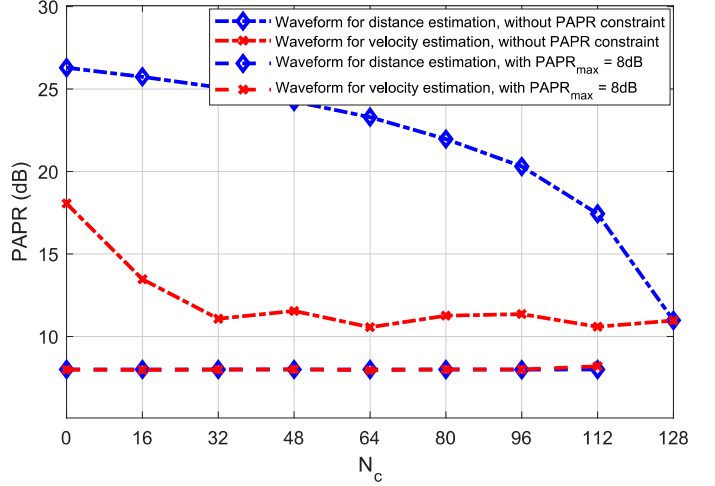

Fig. 4. The effect of constraining the PAPR of the optimized waveforms for distance and velocity estimations, with $\text{PAPR}_{\max} = 8\text{dB}$.
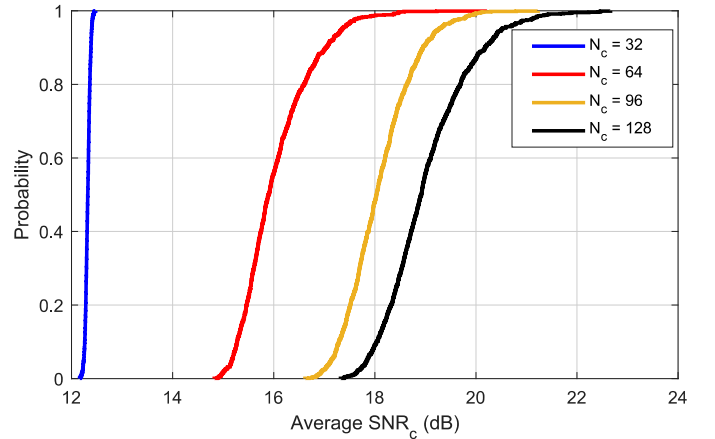

Fig. 5. Empirical CDFs of the average SNR of the communication subcarriers at the communication RX for different number of communication subcarriers, with $P_{\text{total}} = 39\text{dBm}$, noise power of -96dBm, and free space path loss of 116dB.

(a) Distance estimate, unoptimized waveform

(b) Velocity estimate, unoptimized waveform

(c) Distance estimate, optimized waveform
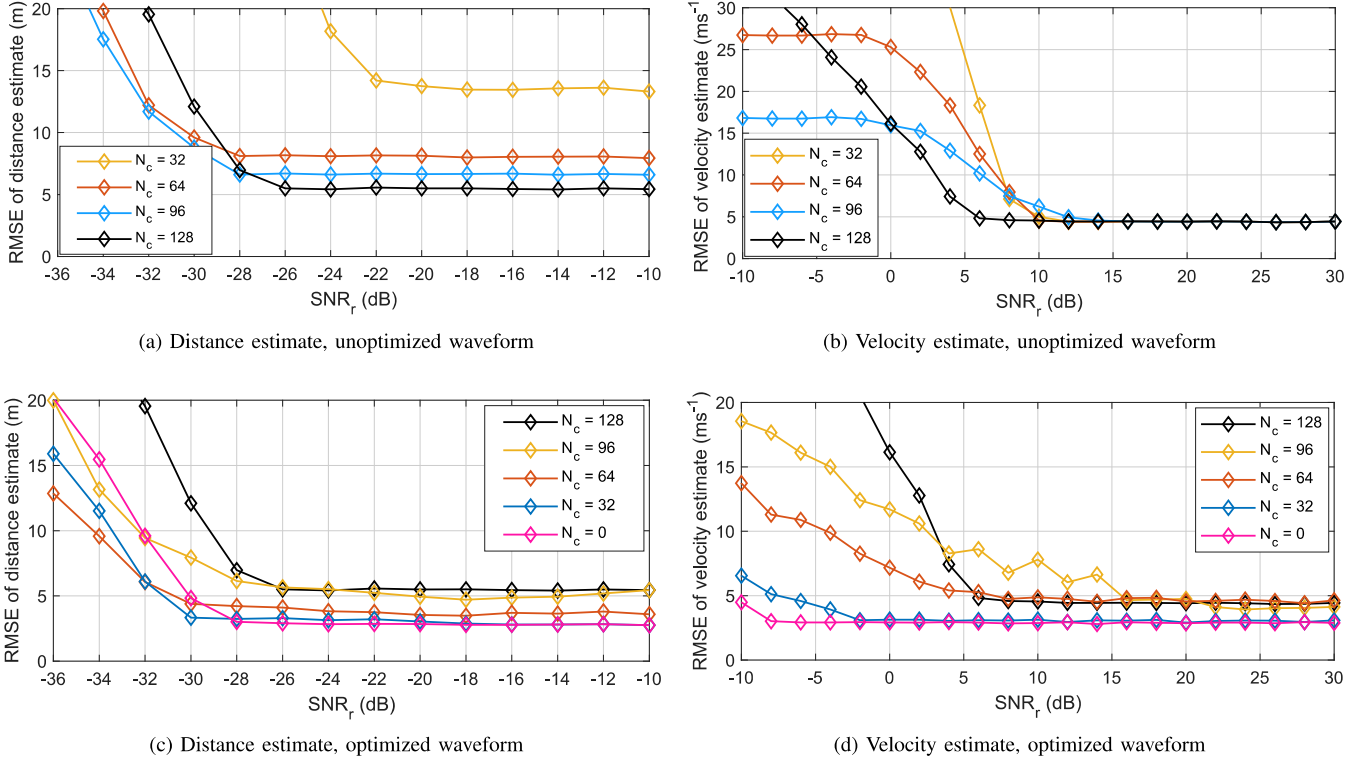

(d) Velocity estimate, optimized waveform

Fig. 6. The RMSE of distance and velocity estimates for the unoptimized and optimized cases, for different number of communication subcarriers.

symbol, where the rest is considered to be filled by the radar subcarriers. Due to this, a part of the total transmit power is allocated for the radar subcarriers, which in turn reduces the power allocated for the communication subcarriers, thus reducing the SNR of the communication subcarriers at the RX. This effect can be observed from the figure in which decreasing the number of communication subcarriers is seen to decrease the average SNR of these subcarriers. This loss of average SNR due to the addition of radar subcarriers is proportional to the ratio of how loaded the OFDM waveform is w.r.t. the communication subcarriers, on average.

Finally, to evaluate the performance of the optimized waveforms for distance and velocity estimation, MLE is performed for a practical scenario. For a range of SNR values at the radar RX, a target with some velocity is placed at some distance, with them being uniformly distributed with standard deviations of the target location and velocity as $\Delta r = \frac{c}{2N\Delta f}$ [m] and $\Delta v = \frac{c}{2Mf_cT_{\text{sym}}}$ [ms^{-1}]. For each SNR, root mean square error (RMSE) is calculated.

Figure 6 depicts the error performance for unoptimized and optimized waveforms. Figures 6(a) and 6(b) show the effect of the addition of the communication subcarriers for the distance and velocity estimates, for the unoptimized cases, where the rest is considered to be unused. For the distance estimate, increase in the number of communication subcarriers decreases the error, where different error floors are reached, with higher the number of communication subcarriers, lower

the error floor. For the velocity estimate, the same error floor is reached. Figures 6(c) and 6(d) show the effect of optimization through the addition of the radar subcarriers, by decreasing the number of communication subcarriers. For the distance estimate, increase of the number of radar subcarriers allows for reduced errors, while similar performance is observed for the velocity estimate.

V. Conclusion

This paper discussed OFDM waveform design for joint communications and sensing. Unused subcarriers within the radio frames of modern cellular systems employing OFDM are exploited to improve the performance of the radar system, while keeping the performance of the communication system at an acceptable level. The unused subcarriers are filled with optimized complex-valued data through the minimization of the theoretical lower bounds of the parameters of interest of the radar system, namely the delay and Doppler estimates. The results showcase that these bounds can be lowered by waveform optimization at the cost of reducing the power allocated for the communication subcarriers. Thus, the performance improvement of one system is subject to a trade-off with the performance of the other. However, this allows both to work together with reduced performance degradation. Further, the optimized waveforms were shown to offer good performance in actual maximum likelihood estimation. In future work, we extend this to 5G New Radio waveforms and analyze its effects.

Converting the matrix notation in (6) to a vectorized form yields

$$\mathbf{y} = \mathbf{s} + \mathbf{v}, \tag{20}$$

where $\mathbf{y} = \text{vec}(\mathbf{Y})$, $\mathbf{s} = \text{vec}(\mathbf{DXB})$ and $\mathbf{v} = \text{vec}(\mathbf{V})$ are all of the size $NM \times 1$. The mean vector and covariance matrix of $\mathbf{y}$ can be denoted as

$$\mathbf{m_y} = \mathbf{s}, \tag{21}$$

$$\boldsymbol{\Sigma} = \mathbb{E}(\mathbf{ss}^H) + \sigma^2\mathbf{I} = \mathbf{ss}^H + \sigma^2\mathbf{I}, \tag{22}$$

where $\mathbf{I}$ is an identity matrix of size $NM \times NM$. For a given parameter set, the minimum variance of an estimator is given by the CRLB. For the signal model given by (20), CRLBs for the estimators are calculated from [15]

$$I(\boldsymbol{\theta})_{i,j} = 2\Re\left[\frac{\partial\mathbf{s}^H}{\partial\theta_i}\boldsymbol{\Sigma}^{-1}\frac{\partial\mathbf{s}}{\partial\theta_j}\right], \tag{23}$$

where $I(\boldsymbol{\theta})_{i,j}$ denotes each element of the Fisher information matrix while $i = 1, 2$ and $j = 1, 2$ with $\theta_1 = \tau$ and $\theta_2 = f_{\mathrm{D}}$, similar to (7). Depending on the variable with respect to which the vector $\mathbf{s}$ is differentiated, this can be simplified after substituting for $\boldsymbol{\Sigma}$ from (22) as

$$I(\boldsymbol{\theta})_{i,j} = 2\Re\left[\mathbf{s}^H\mathbf{D}_i(\mathbf{ss}^H + \sigma^2\mathbf{I})^{-1}\mathbf{D}_j\mathbf{s}\right]. \tag{24}$$

If the differentiating variable is τ, $\mathbf{D}_i = \mathbf{D}_\tau = \text{diag}(\mathbf{d}_\tau)$, in which $\mathbf{d}_\tau$ is a vector of size $NM \times 1$ where the first N elements are $(-N/2, ..., N/2-1)$ and these N elements being repeated for M times. Similarly, if the differentiating variable is f_{D}, $\mathbf{D}_j = \mathbf{D}_{f_{\mathrm{D}}} = \text{diag}(\mathbf{d}_{f_{\mathrm{D}}})$, in which $\mathbf{d}_{f_{\mathrm{D}}}$ is a vector of size $NM \times 1$ where sets of N elements are the same, with the starting and ending indices being zero and $M-1$, respectively. Each element of the Fisher matrix, which is now of size 2×2, is derived using (24) as

$$I(\boldsymbol{\theta})_{1,1} = 2\Re\left[(2\pi\Delta f)^2\mathbf{s}^H\mathbf{D}_\tau(\mathbf{ss}^H + \sigma^2\mathbf{I})^{-1}\mathbf{D}_\tau\mathbf{s}\right], \tag{25a}$$

$$I(\boldsymbol{\theta})_{1,2} = 2\Re\left[(-4\pi^2\Delta f T_{\text{sym}})\mathbf{s}^H\mathbf{D}_\tau(\mathbf{ss}^H + \sigma^2\mathbf{I})^{-1}\mathbf{D}_{f_{\mathrm{D}}}\mathbf{s}\right], \tag{25b}$$

$$I(\boldsymbol{\theta})_{2,1} = 2\Re\left[(-4\pi^2\Delta f T_{\text{sym}})\mathbf{s}^H\mathbf{D}_{f_{\mathrm{D}}}(\mathbf{ss}^H + \sigma^2\mathbf{I})^{-1}\mathbf{D}_\tau\mathbf{s}\right], \tag{25c}$$

$$I(\boldsymbol{\theta})_{2,2} = 2\Re\left[(2\pi T_{\text{sym}})^2\mathbf{s}^H\mathbf{D}_{f_{\mathrm{D}}}(\mathbf{ss}^H + \sigma^2\mathbf{I})^{-1}\mathbf{D}_{f_{\mathrm{D}}}\mathbf{s}\right]. \tag{25d}$$

Therefore, the Fisher matrix and its inverse are given by

$$I(\boldsymbol{\theta}) = \begin{bmatrix} I(\boldsymbol{\theta})_{1,1} & I(\boldsymbol{\theta})_{1,2} \\ I(\boldsymbol{\theta})_{2,1} & I(\boldsymbol{\theta})_{2,2} \end{bmatrix}, \tag{26a}$$

$$I^{-1}(\boldsymbol{\theta}) = \frac{\begin{bmatrix} I(\boldsymbol{\theta})_{2,2} & -I(\boldsymbol{\theta})_{1,2} \\ -I(\boldsymbol{\theta})_{2,1} & I(\boldsymbol{\theta})_{1,1} \end{bmatrix}}{\det I(\boldsymbol{\theta})}. \tag{26b}$$

Finally, the CRLBs for the two estimators are given by the diagonal elements of the inverse Fisher matrix, where the first diagonal element corresponds to CRLB of the delay estimate

while the second corresponds to that of the Doppler estimate. Thus, these are given as

$$\text{CRLB}(\hat{\tau}) = \frac{I(\boldsymbol{\theta})_{2,2}}{\det I(\boldsymbol{\theta})}, \tag{27a}$$

$$\text{CRLB}(\hat{f}_{\mathrm{D}}) = \frac{I(\boldsymbol{\theta})_{1,1}}{\det I(\boldsymbol{\theta})}. \tag{27b}$$

REFERENCES

[1] Y. Han, E. Ekici, H. Kremo, and O. Altintas, "Spectrum sharing methods for the coexistence of multiple RF systems: A survey," *Ad Hoc Networks*, vol. 53, Sep. 2016.

[2] B. Paul, A. R. Chiriyath, and D. W. Bliss, "Survey of RF communications and sensing convergence research," *IEEE Access*, vol. 5, pp. 252–270, 2017.

[3] C. Baquero Barneto, T. Riihonen, M. Turunen, L. Anttila, M. Fleischer, K. Stadius, J. Ryynänen, and M. Valkama, "Full-duplex OFDM radar with LTE and 5G NR waveforms: Challenges, solutions, and measurements," *IEEE Transactions on Microwave Theory and Techniques*, vol. 67, no. 10, pp. 4042–4054, Oct. 2019.

[4] Y. Liu, G. Liao, Z. Yang, and J. Xu, "Design of integrated radar and communication system based on MIMO-OFDM waveform," *Journal of Systems Engineering and Electronics*, vol. 28, no. 4, pp. 669–680, Aug. 2017.

[5] H. Safavi-Naeini, S. Roy, and S. Ashrafi, "Spectrum sharing of radar and Wi-Fi networks: The sensing/throughput tradeoff," *IEEE Transactions on Cognitive Communications and Networking*, vol. 1, no. 4, pp. 372–382, Dec. 2015.

[6] A. Aubry, A. D. Maio, Y. Huang, M. Piezzo, and A. Farina, "A new radar waveform design algorithm with improved feasibility for spectral coexistence," *IEEE Transactions on Aerospace and Electronic Systems*, vol. 51, no. 2, pp. 1029–1038, Apr. 2015.

[7] T. Guo and R. Qiu, "OFDM waveform design compromising spectral nulling, side-lobe suppression and range resolution," in *Proc. IEEE Radar Conference*, May 2014, pp. 1424–1429.

[8] M. Bica, K. Huang, U. Mitra, and V. Koivunen, "Opportunistic radar waveform design in joint radar and cellular communication systems," in *Proc. IEEE Global Communications Conference*, Dec. 2015, pp. 1–7.

[9] M. R. Bell, "Information theory and radar waveform design," *IEEE Transactions on Information Theory*, vol. 39, no. 5, pp. 1578–1597, Sep. 1993.

[10] M. Bica, K. Huang, V. Koivunen, and U. Mitra, "Mutual information based radar waveform design for joint radar and cellular communication systems," in *Proc. IEEE International Conference on Acoustics, Speech and Signal Processing*, Mar. 2016, pp. 3671–3675.

[11] K.-W. Huang, M. Bica, U. Mitra, and V. Koivunen, "Radar waveform design in spectrum sharing environment: Coexistence and cognition," in *Proc. IEEE Radar Conference*, May 2015, pp. 1698–1703.

[12] M. Bica and V. Koivunen, "Delay estimation method for coexisting radar and wireless communication systems," in *Proc. IEEE Radar Conference*, May 2017, pp. 1557–1561.

[13] ——, "Radar waveform optimization for target parameter estimation in cooperative radar-communications systems," *IEEE Transactions on Aerospace and Electronic Systems*, vol. 55, no. 5, pp. 2314–2326, Oct. 2019.

[14] M. Braun, C. Sturm, and F. K. Jondral, "Maximum likelihood speed and distance estimation for OFDM radar," in *Proc. IEEE Radar Conference*, May 2010, pp. 256–261.

[15] S. Kay, *Fundamentals of Statistical Signal Processing: Detection theory*. PTR Prentice-Hall, 1993.

Publication 3

Experimenting Joint Vehicular Communications and Sensing with Optimized 5G NR Waveform

S. D. Liyanaarachchi, C. Baquero Barneto, T. Riihonen and M. Valkama

Experimenting Joint Vehicular Communications and Sensing with Optimized 5G NR Waveform

Sahan Damith Liyanaarachchi, Carlos Baquero Barneto, Taneli Riihonen, and Mikko Valkama

Electrical Engineering, Faculty of Information Technology and Communication Sciences, Tampere University, Finland

email: sahan.liyanaarachchi@tuni.fi

Abstract—This article contributes to the experimentation of joint vehicular communications and radio-based sensing using a fifth-generation (5G) New Radio (NR) waveform. Firstly, simulations are carried out to observe the effect of using default (communication-purpose) 5G NR waveforms for sensing, and they indicate high side-lobes in the range profile due to the existence of unused communication subcarriers within the frames of the 5G NR waveform. These can be filled with optimized frequency-domain symbols to minimize the side-lobes. As the main result, these observations are validated through over-the-air measurements with practical 5G NR waveforms, operating at the mm-wave frequency of 27.7 GHz. For this, an outdoor environment is mapped with both the default 5G NR waveform and the optimized waveform, and the latter showcases considerable improvement in the mapping image due to side-lobe suppression.

I. Introduction

Developing joint communications and sensing (JCAS) for vehicular systems with the fifth-generation (5G) New Radio (NR) waveforms is important especially for two reasons [1]. Firstly, such vehicular systems are ubiquitous, requiring wireless connectivity between nearby vehicles, pedestrians, and roadside infrastructure. These communications need high capacity and low latency links to allow for efficient decision-making [2], and 5G networks have facilitated this requirement. Secondly, apart from communications, such systems also require a sensing platform to detect and estimate the different distances to the road users, to prevent possible collisions [3].

In JCAS vehicular scenarios, the sensing transceiver (TRX) and the communications transmitter (TX) are the same device. Moreover, the TRX must continuously process the reflections from the same TX communications signal to detect the road users, and a joint waveform is thus used for both communications and sensing [4]. For this to be viable, the TRX has to operate in a full-duplex manner, mitigating the self-interference due to the strong TX signal leakage. Using the fourth-generation Long-Term Evolution system for this purpose is discussed in [5], showing the feasibility of incorporating sensing in such modern communications systems.

The sensing performance of using 5G NR waveforms can be quantified through the conventional detection and estimation metrics. These are the accuracy of the range or the velocity estimate [6], peak side-lobe level of the range profile and the spatial waveform [7], the signal-to-interference-plus-noise ratio at the sensing receiver (RX) [8], and the probability of detection or false alarm [9].
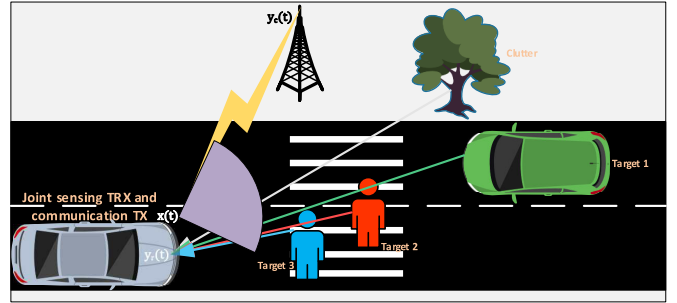

Fig. 1. General overview of the considered joint vehicular communications and sensing scenario.

The default 5G NR waveforms usually have unused communication subcarriers, depending on the number of users served by the network. These are observed in the physical downlink shared channels and in the synchronization signal block burst [10]. The sensing performance of directly using these 5G NR waveforms with null subcarriers needs to be investigated. To further improve this performance, they can also be populated with optimized frequency-domain symbols.

In this paper, we experiment with vehicular JCAS using 5G NR waveforms. First, the null subcarriers of the waveform are filled with optimized frequency-domain symbols, ensuring that some proportion of TX power is allocated to these filled *radar* subcarriers. Additionally, we also minimize the peak-to-average power ratio (PAPR) of the waveform. Then, simulations are performed to analyze the range profile's side-lobes of the default and the optimized 5G NR waveforms. These indicate that the side-lobes can be minimized considerably through the use of radar subcarriers. Especially, over-the-air radio-frequency (RF) measurements are carried out at the mm-wave frequency of 27.7 GHz to validate the feasibility of using the 5G NR waveforms in vehicular scenarios.

II. System Model

The considered vehicular scenario is shown in Fig. 1. The vehicle at left carries the sensing TRX that is also the communications TX. A 5G waveform is used as the TX signal $x(t)$. This is reflected from the targets in the environment, e.g., pedestrians, vehicles, obstacles and sources of clutter, and received back at the sensing TRX as $y_r(t)$. The reflected echoes are processed at the TRX in a full-duplex manner. Moreover, the same TX communications signal is used to communicate with a roadside base station, where the RX signal is $y_c(t)$.

A. 5G NR Waveform

The TX communications signal consists of M orthogonal frequency-division multiplexing (OFDM) symbols, each with N_{PRB} physical resource blocks (PRBs). The total number of subcarriers in one OFDM symbol is denoted by N. Communication and radar PRBs are randomly distributed throughout the whole waveform, with N_{r} and N_{c} denoting the total radar and communication subcarriers, and $N_{\text{r}} + N_{\text{c}} = NM$.

The time-domain TX signal is given by

$$x(t) = \sum_{m=0}^{M-1} p(t - t_m) \left(\sum_{n \in \mathcal{C}_m} X_{\text{c},n,m} e^{j2\pi n \Delta f(t - t_m)} + \sum_{n \in \mathcal{R}_m} X_{\text{r},n,m} e^{j2\pi n \Delta f(t - t_m)} \right),$$
(1)

where $m, n, p(t), t_m, \Delta f, X_{\text{c},n,m}$ and $X_{\text{r},n,m}$ denote the OFDM symbol index, subcarrier index, pulse shaping function, starting time instant of the mth OFDM symbol, subcarrier spacing, frequency-domain symbol on a communication and radar subcarrier, respectively, with $m \in [0, M-1]$ and $n \in [0, N-1]$. The set of subcarrier indices corresponding to communications and radar are denoted by $\mathcal{C}$ and $\mathcal{R}$, with cardinalities N_{c} and N_{r}, respectively, and $\mathcal{C}_m$ and $\mathcal{R}_m$ denote the corresponding indices in the mth OFDM symbol.

B. Processing for the Sensing System

The TX signal is reflected from the targets and received back at the JCAS vehicle as $y_{\text{r}}(t)$, as illustrated in Fig. 1. Without the Doppler effect, this signal can be written as

$$y_{\text{r}}(t) = \sum_{k=1}^{K_{\text{r}}} A_{\text{r},k} x(t - \tau_{\text{r},k}) + v_{\text{r}}(t),$$
(2)

where $K_{\text{r}}, A_{\text{r},k}, \tau_{\text{r},k}$ and v_{r} are the total number of targets in the vicinity of the sensing TRX, the effective attenuation constant for the kth target, the two-way delay between the kth target and the sensing TRX, and the noise at the sensing RX, respectively. Here, the noise is assumed to be additive, white and Gaussian, i.e., normally distributed with zero mean.

Upon substituting (1) to (2) and converting the time-domain expression to frequency domain with the use of discrete Fourier transform (DFT) results in the relation between a TX and RX frequency-domain symbol as

$$Y_{n,m} = \sum_{k=1}^{K_{\text{r}}} A_{\text{r},k} X_{n,m} e^{-j2\pi n \Delta f \tau_{\text{r},k}} + V_{n,m},$$
(3)

where $Y_{n,m}$, $X_{n,m}$, and $V_{n,m}$ denote the frequency-domain symbol on each subcarrier for reception, transmission, and noise, respectively. Both radar and communication subcarriers are used for sensing purposes at the JCAS RX and no distinction is made between the two. Further, to cancel the interference from the radar reflections at the communications RX, additional techniques, e.g., transmit precoding, will be necessary to implement.

For brevity, the relation between a TX and RX frequency-domain symbol due to a single target can be represented as

$$Y_{n,m} = A X_{n,m} e^{-j2\pi n \Delta f \tau} + V_{n,m}.$$
(4)

It is then observed that the delay to the target induces a phase-shift between the TX and RX frequency-domain symbols, which can be used to estimate it. Representing the relation in a matrix format yields

$$\mathbf{Y} = \mathbf{D}\mathbf{X} + \mathbf{V},$$
(5)

where $\mathbf{Y}, \mathbf{X}$ and $\mathbf{V}$ are of the same size $N \times M$, and $(\mathbf{Y})_{n,m} = Y_{n,m}$, $(\mathbf{X})_{n,m} = X_{n,m}$ and $(\mathbf{V})_{n,m} = V_{n,m}$. The matrix $\mathbf{D}$ is a diagonal matrix of size $N \times N$, with $(\mathbf{D})_{n,n} = D_{n,n} = A e^{-j2\pi n \Delta f \tau}$ representing each element of the diagonal.

C. Calculation of Range Profile

The frequency-domain TX and RX symbols can be used for estimating the delay to the target through maximum likelihood estimation. The simplified log-likelihood function for the signal model in (5) can be represented based on [6] as

$$\mathcal{L}(\tau) = \Re \left(\sum_{m=0}^{M-1} \sum_{n=0}^{N-1} Z_{n,m} e^{-j2\pi n \Delta f \tau} \right),$$
(6)

where $Z_{n,m} = Y_{n,m}^* X_{n,m}$ and $\Re(\cdot)$ denotes the real operation. Quantizing the delay as $\tau_{n'} = \frac{n'}{N\Delta f}$, with $n' = 0, \ldots, N-1$, the range profile is then given by

$$Q(n') = \frac{1}{M} \left| \mathcal{L}\left(\frac{n'}{N\Delta f} \right) \right|^2,$$
(7)

where $|\cdot|$ denotes the absolute value, and it is calculated with the help of the DFT [6].

III. WAVEFORM OPTIMIZATION

The goal of our waveform optimization is to find the frequency-domain symbols for the radar subcarriers such that the Cramer–Rao lower bound (CRLB) of the distance estimate is minimized. In the expression for the CRLB, it is observed that it only depends on the amplitudes of the subcarriers. So, two separate optimizations can be performed, firstly for the amplitudes and then for the phases of radar subcarriers.

The amplitude optimization can be written as

$$\min_{\mathbf{A}_{\text{r}}} \text{CRLB}(\hat{d})$$
(8a)

subject to the constraints

$$P_{\text{r}} = P_{\text{t}} - P_{\text{c}},$$
(8b)

$$0 \leq A_{n,m} \leq A_{\max}, m \in \mathcal{M}_{\text{r}} \text{ and } n \in \mathcal{R}_m,$$
(8c)

where $\mathbf{A}_{\text{r}}, \text{CRLB}(\hat{d}), P_{\text{t}}, P_{\text{r}}$ and P_{c} denote the set of amplitudes of the radar subcarriers, the CRLB of the distance estimate, total available TX power, total power allocated for the radar and communication subcarriers, respectively. Further, $A_{n,m}, A_{\max}$ and $\mathcal{M}_{\text{r}}$ represent the amplitude of an individual radar subcarrier, maximum amplitude for a radar subcarrier and the set of OFDM symbol indices having the radar subcarriers, respectively. The first constraint (8b) decides the total power

allocated for the radar subcarriers and this is proportional to the ratio $\frac{N_r}{NM}$. The second constraint (8c) limits the maximum amplitude of a radar subcarrier.

In the analytical solution (that is omitted herein for brevity), the available power will be allocated mostly to the edges of the spectrum. So, the radar subcarriers at the edges would be activated with the amplitude $A_{\max}$, while the ones at the center remain empty. The phases of the radar subcarriers are then optimized further to minimize the PAPR of the waveform, as illustrated in our related work in [11].

IV. Measurement Campaign And Simulation Setup

A measurement campaign is conducted in an outdoor environment within the Tampere University premises to emulate a scenario with vehicles. Firstly, this environment is simulated in MATLAB as closely as possible to the outdoor environment, to observe the effects of optimizing the waveform. Then, the viability of the optimization is investigated through experimental over-the-air RF measurements. The parameters of the 5G NR waveform used for the simulations and experimental measurements are: $P_t = 30$ dBm, $M = 20$, $N_{\mathrm{PRB}} = 264$, $N = 3168$ and $\Delta f = 120$ kHz.

Figure 2(a) depicts the measurement setup. Two horn antennas of model PE9851A-20 are arranged on a trolley and they emulate the TX and RX antennas of the vehicle's TRX. To map the environment, these are mechanically rotated from $5°$ to $85°$, with a step size of $2°$. Each horn antenna has 3-dB beamwidth of $17°$ and a 20 dBi gain. The TX and RX signals are processed through a vector signal transceiver (VST) of model PXIe-5840. Both the TX and RX signals are at an intermediate frequency of 3.2 GHz before up/down-converted to/from the mm-wave frequency of 27.7 GHz through two mixers of model N5183B-MXG, that are operating at 24.5 GHz. The self-interference due to the required full-duplex operation is canceled similar to [5], [12].

The considered outdoor vehicular scenario is shown in Fig. 2(b), where the landmarks A, B, C, and D depict a building, walls of a building and a grassy surface, several buildings, and metal cylinder-like structures with bicycles, respectively. These are highlighted for a better comparison of the measurement results, which depict the sensed environment in the outdoor mapping. For each angle of the antennas, the range profile is calculated and they are combined for all the antenna angles to construct a map of the environment. In these measurements, we only consider mapping static targets.

For the simulations, a uniform linear array of 16 antenna elements is used as the TX and RX antennas. For the TX, this generates a main beam at some preferred angle. The RX is also tuned for the same angle, and the corresponding range profile is calculated. Then the main beam is swept between $0°$ to $90°$ to generate a map of the environment.

V. Range Profiles And The Mapping Results

To observe the effect of optimizing the waveform, the range profiles are analyzed first. For each angle, the range profile per each OFDM symbol is calculated and they are then coherently
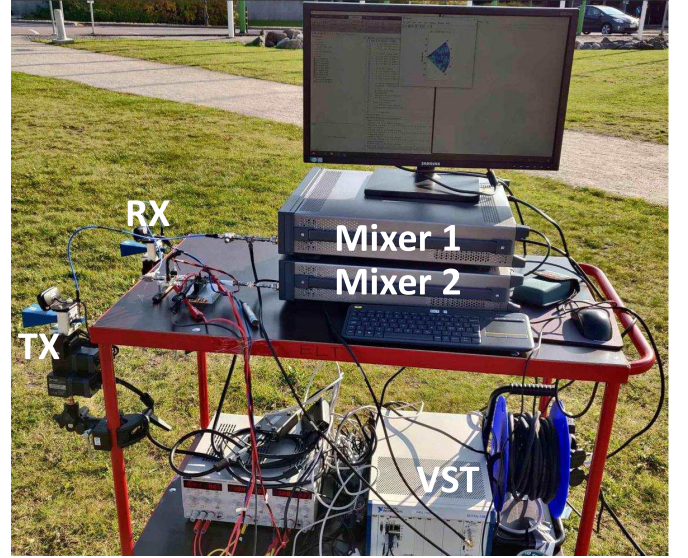
(a) The measurement setup used to map the outdoor environment

(b) Outdoor mapping scenario with the important landmarks highlighted

Fig. 2. The measurement campaign conducted within the university premises.

combined to obtain the final range profile, in accordance with (7). In the unoptimized waveform, the TX power is allocated fully to the communication subcarriers. In the optimized waveform, the power is split between the communication and radar subcarriers, according to the communication loading. Hence, the communication subcarriers have less power compared to the unoptimized waveform. Additionally, the trade-off between radar and communication subcarriers due to this power allocation is analyzed in [6]. Here in these results, the power spectral density difference between a radar and communication subcarrier is maintained at 1 dB.

The range profiles are shown in Fig. 3, for an angle of $20°$, so that the reflections from only one landmark (D) are received strongly while those from the others are weak. Figure 3(a) depicts the range profiles for the simulation results at a communication loading of 25% for both unoptimized and optimized waveforms, with normalized RX power for better comparison. Both have peaks around the distances corresponding to the landmark D. However, for other distances, the optimized waveform has lesser side-lobes when compared with the unoptimized waveform. Figure 3(b) depicts the range profiles for the experimental measurements. Similar observations can be made here too, indicating the side-lobe suppression.

The range profiles of each direction are then combined in a polar plot to formulate a map, which are shown in Fig. 4, for both the simulation and experimental measurement results.

(a) Simulation range profiles
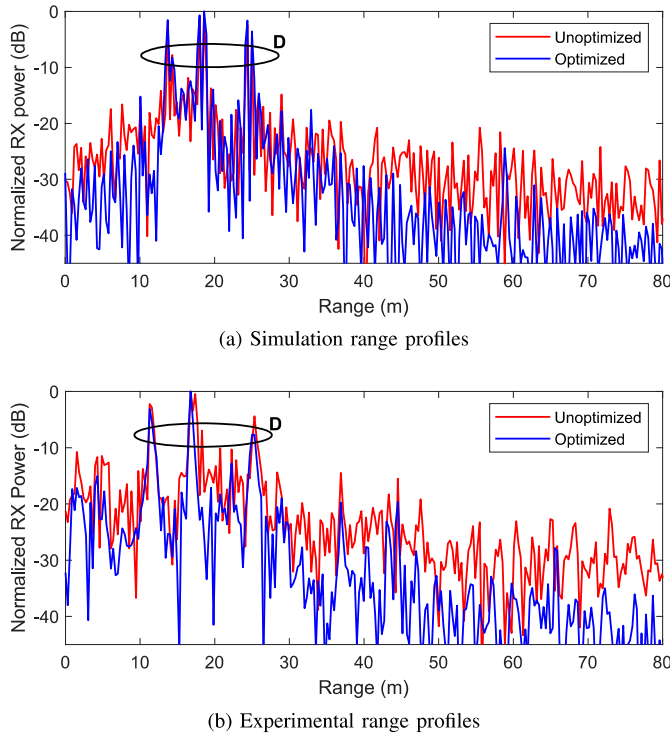

(b) Experimental range profiles

Fig. 3. The range profiles for the unoptimized and optimized waveforms for both simulation and experimental measurements, at 20° and a communication loading of 25%.

Figures 4(a)–4(f) are with the unoptimized waveform whereas Figs. 4(g)–4(l) are with the optimized waveform. Moreover, each column is with different communication loading of 25%, 50% and 75%, respectively. Figure 4(l) also depicts the sensed landmarks highlighted in the Fig. 2(b) for comparison.

For the unoptimized waveform, as the communication loading increases from 25% to 75%, the side-lobes also improve, as shown in the Figs. 4(a)–4(c) and 4(d)–4(f). The sensed targets are better observed for a higher communication loading. The reason for this behavior is due to the existence of null subcarriers. As the communication loading increases, the number of null subcarriers decreases, and this causes the side-lobe performance to also improve.

For the same communication loading, better side-lobes are observed for the optimized waveform when compared with the unoptimized waveform, due to the addition of radar subcarriers. This improvement in the side-lobes is visible in comparing Figs. 4(b) and 4(h), and Figs. 4(e) and 4(k), where the communication loading is 50%. As the communication loading decreases further, the side-lobe suppression improves. Comparing Figs. 4(a) and 4(g), and Figs. 4(d) and 4(j), for a communication loading of 25%, showcases this behavior.

Therefore, it can be concluded from the simulation results and the experimental RF measurements that the optimized waveform performs better than the unoptimized one in improving the side-lobes of the corresponding range profiles, and consequently those of the mapping image. Further improvement of the side-lobe suppression between the two waveforms is observed as the communication loading decreases.

VI. Conclusion

This article considers the experimentation of 5G NR waveform for joint vehicular communications and sensing. The simulation results indicate that adopting the default 5G waveform also for sensing causes high side-lobes in the range profile, due to the existence of unused communication subcarriers. To improve the side-lobe performance, these are then filled with optimized frequency-domain symbols. It is then observed that the optimized waveform allows for better side-lobe performance than the unoptimized waveform, while simultaneously minimizing the PAPR of the waveform. This idea is validated through over-the-air RF measurements for a 5G NR waveform operating at an mm-wave frequency of 27.7 GHz.
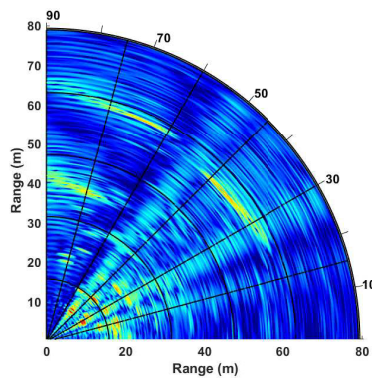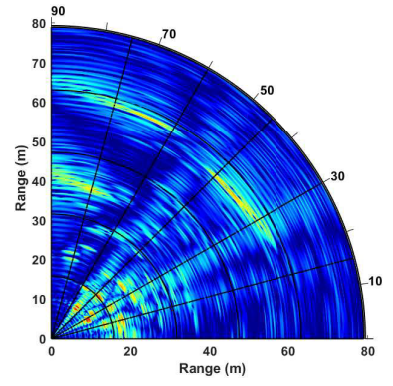
References

[1] F. Liu, C. Masouros, A. P. Petropulu, H. Griffiths, and L. Hanzo, "Joint radar and communication design: Applications, state-of-the-art, and the road ahead," *IEEE Transactions on Communications*, vol. 68, no. 6, pp. 3834–3862, Jun. 2020.

[2] S. Chen, J. Hu, Y. Shi, and L. Zhao, "LTE-V: A TD-LTE-based V2X solution for future vehicular network," *IEEE Internet of Things Journal*, vol. 3, no. 6, pp. 997–1005, Dec. 2016.

[3] P. Kumari, J. Choi, N. González-Prelcic, and R. W. Heath, "IEEE 802.11ad-based radar: An approach to joint vehicular communication-radar system," *IEEE Transactions on Vehicular Technology*, vol. 67, no. 4, pp. 3012–3027, Apr. 2018.

[4] C. Sturm and W. Wiesbeck, "Waveform design and signal processing aspects for fusion of wireless communications and radar sensing," *Proceedings of the IEEE*, vol. 99, no. 7, pp. 1236–1259, Jul. 2011.

[5] C. Baquero Barneto, T. Riihonen, M. Turunen, L. Anttila, M. Fleischer, K. Stadius, J. Ryynänen, and M. Valkama, "Full-duplex OFDM radar with LTE and 5G NR waveforms: Challenges, solutions, and measurements," *IEEE Transactions on Microwave Theory and Techniques*, vol. 67, no. 10, pp. 4042–4054, Oct. 2019.

[6] S. D. Liyanaarachchi, C. Baquero Barneto, T. Riihonen, and M. Valkama, "Joint OFDM waveform design for communications and sensing convergence," in *Proc. IEEE International Conference on Communications*, Jun. 2020.

[7] C. Baquero Barneto, S. D. Liyanaarachchi, T. Riihonen, L. Anttila, and M. Valkama, "Multibeam design for joint communication and sensing in 5G New Radio networks," in *Proc. IEEE International Conference on Communications*, Jun. 2020.

[8] A. Aubry, A. D. Maio, Y. Huang, M. Piezzo, and A. Farina, "A new radar waveform design algorithm with improved feasibility for spectral coexistence," *IEEE Transactions on Aerospace and Electronic Systems*, vol. 51, no. 2, pp. 1029–1038, Apr. 2015.

[9] A. R. Chiriyath, B. Paul, and D. W. Bliss, "Simultaneous radar detection and communications performance with clutter mitigation," in *Proc. IEEE Radar Conference*, May 2017, pp. 279–284.

[10] E. Dahlman, S. Parkvall, and J. Skold, *5G NR: The Next Generation Wireless Access Technology*. Academic Press, Inc., 2018.

[11] C. B. Barneto, S. D. Liyanaarachchi, M. Heino, T. Riihonen, and M. Valkama, "Full duplex radio/radar technology: The enabler for advanced joint communication and sensing," *IEEE Wireless Communications*, vol. 28, no. 1, pp. 82–88, Feb. 2021.

[12] C. Baquero Barneto, M. Turunen, S. D. Liyanaarachchi, L. Anttila, A. Brihuega, T. Riihonen, and M. Valkama, "High-accuracy radio sensing in 5G New Radio networks: Prospects and self-interference challenge," in *Proc. Asilomar Conference on Signals, Systems, and Computers*, Nov. 2019, pp. 1159–1163.
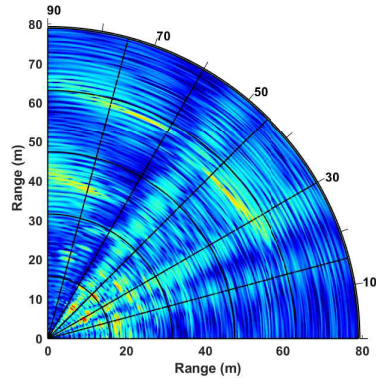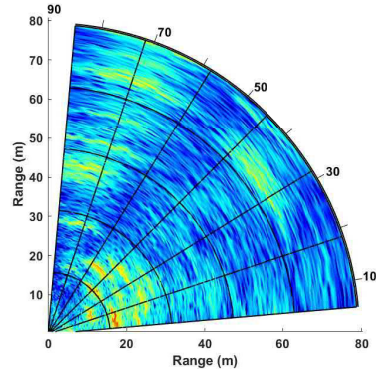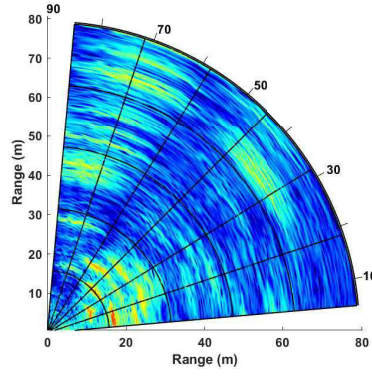
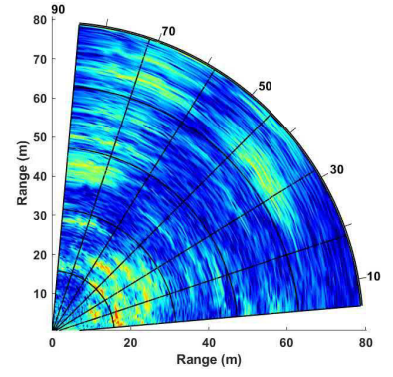(a) Simulation, 25%, unoptimized   (b) Simulation, 50%, unoptimized   (c) Simulation, 75%, unoptimized
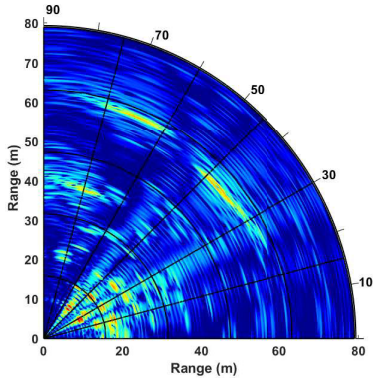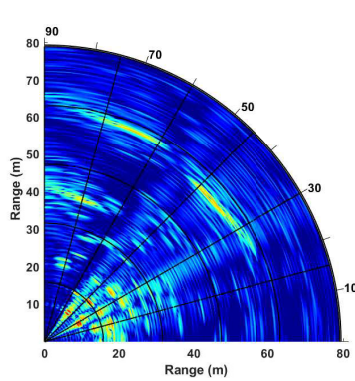
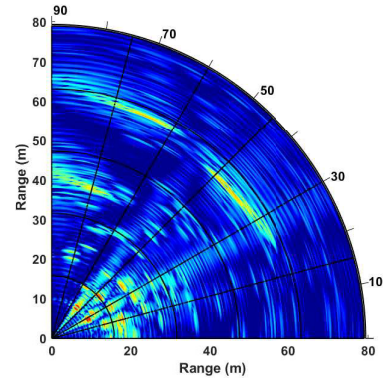(d) Experimental, 25%, unoptimized   (e) Experimental, 50%, unoptimized   (f) Experimental, 75%, unoptimized
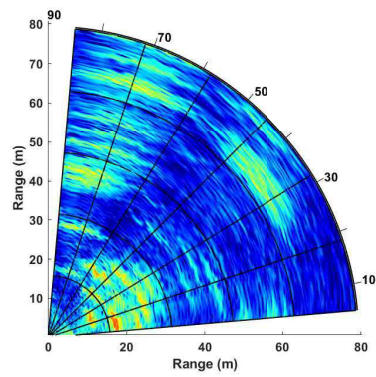
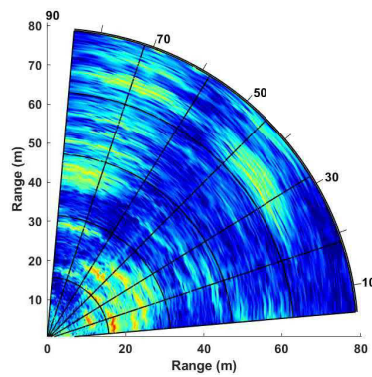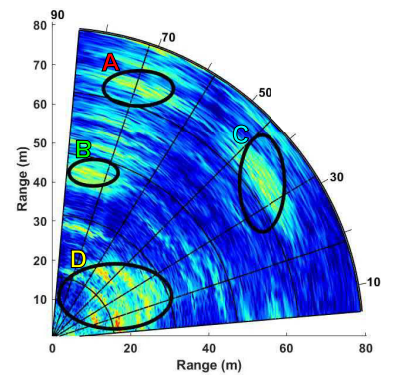(g) Simulation, 25%, optimized   (h) Simulation, 50%, optimized   (i) Simulation, 75%, optimized

(j) Experimental, 25%, optimized   (k) Experimental, 50%, optimized   (l) Experimental, 75%, optimized

Fig. 4. The simulation and experimental mapping results for the unoptimized and optimized waveforms with communication loading of 25%, 50% and 75%.

Publication 4

Joint MIMO Communications and Sensing with Hybrid Beamforming Architecture and OFDM Waveform Optimization

S. D. Liyanaarachchi, T. Riihonen, C. Baquero Barneto and M. Valkama

Publication 5

Joint Multi-User Communication and MIMO Radar Through Full-Duplex Hybrid Beamforming

S. D. Liyanaarachchi, C. Baquero Barneto, T. Riihonen, M. Heino and M. Valkama

Joint Multi-User Communication and MIMO Radar Through Full-Duplex Hybrid Beamforming

Sahan Damith Liyanaarachchi, Carlos Baquero Barneto, Taneli Riihonen, Mikko Heino, and Mikko Valkama

Electrical Engineering, Faculty of Information Technology and Communication Sciences, Tampere University, Finland

email: sahan.liyanaarachchi@tuni.fi

Abstract—**Performing joint communication and sensing in multiple-input multiple-output (MIMO) systems is important for efficiently utilizing the crowded spectrum, through providing high capacity links to the communication users, while simultaneously facilitating improved sensing capabilities. Towards this, we optimize the transmit beamforming to provide concurrent multiple beams for communication and sensing, while effectively mitigating the cross-interference between different communication users. Moreover, the receive beamforming is optimized to observe reflections from the radar targets, while also canceling the self-interference due to the required full-duplex operation. We demonstrate that MIMO processing can separate the communication users and radar targets in the angular domain. Additionally, the super-resolution provided by angle estimation allows differentiating between radar targets having the same range, but with minuscule angular separation.**

I. Introduction

Communication and sensing systems are converging towards operating at the same frequency bands, inferring radio frequency (RF) spectrum congestion and mutual interference. To overcome this challenge, a new trend referred to as the RF convergence proposes to design joint communication and sensing (JCAS) systems that efficiently manage the spectral resources [1]. The (re)use of same hardware components for both purposes has accelerated the design of these even further.

At the same time, multiple-input multiple-output (MIMO) is an increasingly important technology for both communication and sensing functionalities at mm-waves (30–300 GHz), enabling new interesting applications [2]–[4]. For communications, it can provide high capacity links to the users through spatial multiplexing. Further, MIMO processing can be used at the sensing receiver (RX) to facilitate, e.g., super-resolution direction of arrival (DoA) estimation [5].

In this work, we propose a multi-user (MU) MIMO system for JCAS operation, where the MIMO transmitter (TX) provides multiple beams for communications, while a separate additional beam concurrently senses the environment. This idea is explored in [6] for a phased array system, whereas in this article, we extend this to a true MIMO system context. This functionality is facilitated by optimizing the effective TX beam pattern, which is the combination of the baseband (BB) and RF beamforming weights, similar to [3], [7]. Additionally,
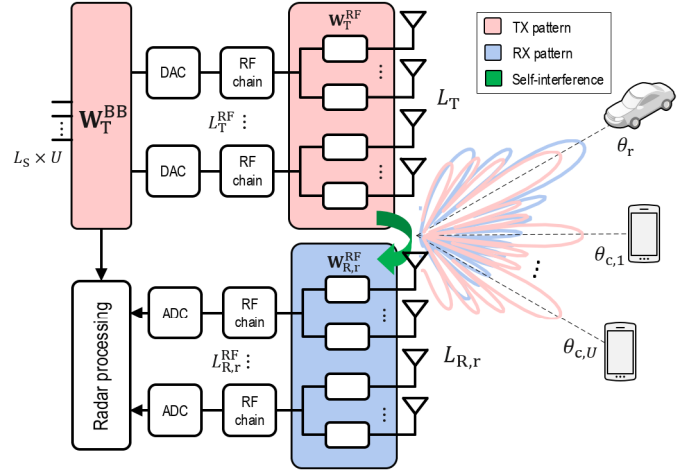
Fig. 1. Considered JCAS multi-user MIMO system.

the inter-user interference between different communication users is also minimized.

Moreover, we have illustrated in [8] that the key enabler for future JCAS systems is the simultaneous transmit-and-receive operation, and the major challenge for implementing it is the self-interference (SI) due to the TX signal leakage to the RX. As such, the RX RF beamforming weights are optimized to minimize the SI, while providing a single beam in the sensing direction to receive the reflections from the radar targets.

We also illustrate that multiple signal classification (MU-SIC) algorithm [9] can be used for DoA estimation, by utilizing properly the RX spatial signal. Specifically, we demonstrate that it can be applied for a hybrid MIMO system [10], and show how to differentiate between the different targets in the angular domain, allowing to separate multiple targets with the same range within the sensing beam. Throughout the work, we utilize orthogonal frequency-division multiplexing (OFDM) as the JCAS waveform.

II. System Model

As depicted in Fig. 1, we assume a hybrid MU-MIMO-OFDM system with U communication users. The considered JCAS system simultaneously operates as a communication TX and radar transceiver, providing communication and radar beams at $\theta_{c,u}$ and θ_r, respectively, with $u \in [1, U]$. We consider a JCAS TX with L_T TX antennas and L_T^{RF} RF chains, while the

corresponding numbers of the RX antennas and RF chains are given by $L_{R,r}$ and $L_{R,r}^{RF}$, respectively. We also assume uniform linear arrays (ULAs) as TX and RX antenna systems, with half-wavelength separation. The OFDM waveform contains M OFDM symbols, each having N active subcarriers. The frequency-domain symbols for the uth communication user's L_S parallel streams at the nth subcarrier and the mth OFDM symbol are given by $\mathbf{x}_{u,n,m}$, of size $L_S \times 1$.

Applying both RF and BB precoding, the TX frequency-domain symbols at the antenna elements for all the users are

$$\tilde{\mathbf{x}}_{n,m} = \mathbf{W}_T^{RF} \sum_{u=1}^{U} \mathbf{W}_{T,u}^{BB} \mathbf{x}_{u,n,m}, \tag{1}$$

where $\tilde{\mathbf{x}}_{n,m}$ is of size $L_T \times 1$. The TX RF precoder $\mathbf{W}_T^{RF}$ of size $L_T \times L_T^{RF}$ is common for all users. The BB precoder of the uth user is $\mathbf{W}_{T,u}^{BB}$, which is of size $L_T^{RF} \times L_S$. Denoting

$$\mathbf{W}_T^{BB} = \left[\mathbf{W}_{T,1}^{BB}, \mathbf{W}_{T,2}^{BB}, \ldots, \mathbf{W}_{T,U}^{BB} \right], \tag{2}$$

$$\mathbf{x}_{n,m} = \left[\mathbf{x}_{1,n,m}^T, \mathbf{x}_{2,n,m}^T, \ldots, \mathbf{x}_{U,n,m}^T \right]^T, \tag{3}$$

where the BB precoder matrix of all the users $\mathbf{W}_T^{BB}$ is of size $L_T^{RF} \times (L_S \cdot U)$ and $\mathbf{x}_{n,m}$ is the vector containing all the users' streams, of size $(L_S \cdot U) \times 1$, (1) can be rewritten as

$$\tilde{\mathbf{x}}_{n,m} = \mathbf{W}_T^{RF} \mathbf{W}_T^{BB} \mathbf{x}_{n,m}. \tag{4}$$

A. MIMO Radar RX Signals

The RX frequency-domain symbols at the radar RX's elements due to K_t point target reflections can be written as

$$\tilde{\mathbf{y}}_{r,n,m} = \sum_{k=1}^{K_t} b_{t,k} e^{-j2\pi f_n \tau_{t,k}} \mathbf{a}_R(\theta_{t,k}) \mathbf{a}_T^H(\theta_{t,k}) \tilde{\mathbf{x}}_{n,m}$$
$$+ \mathbf{H}_{SI,n} \tilde{\mathbf{x}}_{n,m} + \tilde{\mathbf{v}}_{r,n,m}, \tag{5}$$

where $b_{t,k}$ and $\tau_{t,k}$ model the attenuation factor and relative delay of the kth target reflection, while $\tilde{\mathbf{v}}_{r,n,m}$ is the noise vector of size $L_{R,r} \times 1$. The BB frequency of the nth subcarrier is given by f_n. The TX and RX steering vectors are represented by $\mathbf{a}_T(\theta_{t,k})$ and $\mathbf{a}_R(\theta_{t,k})$, which are of sizes $L_T \times 1$ and $L_{R,r} \times 1$, respectively, while $\theta_{t,k}$ denotes either the angle of departure or arrival due to the kth target that are equal in the considered monostatic setup – assuming for simplicity relatively far away targets and small TX-RX array separation. For an ideal ULA with L antennas and half-wavelength separation, the steering vector is given by [10]

$$\mathbf{a}(\theta) = \left[1, e^{j\pi \sin(\theta)}, \ldots, e^{j\pi(L-1)\sin(\theta)} \right]^T. \tag{6}$$

Representing (5) in matrix notation yields

$$\tilde{\mathbf{y}}_{r,n,m} = \mathbf{A}_R(\theta) \mathbf{H}_{r,n} \mathbf{A}_T^H(\theta) \tilde{\mathbf{x}}_{n,m} + \mathbf{H}_{SI,n} \tilde{\mathbf{x}}_{n,m} + \tilde{\mathbf{v}}_{r,n,m}, \tag{7}$$

where $\mathbf{A}_T(\theta) = [\mathbf{a}_T(\theta_{t,1}), \ldots, \mathbf{a}_T(\theta_{t,K_t})]$ and $\mathbf{A}_R(\theta) = [\mathbf{a}_R(\theta_{t,1}), \ldots, \mathbf{a}_R(\theta_{t,K_t})]$ are the TX and RX steering matrices for all the targets, of sizes $L_T \times K_t$ and $L_{R,r} \times K_t$, respectively. The DoAs of all the targets are denoted by $\theta = [\theta_{t,1}, \ldots, \theta_{t,K_t}]^T$. The radar channel matrix $\mathbf{H}_{r,n}$ is

diagonal with size $K_t \times K_t$, and its kth diagonal element is given by $(\mathbf{H}_{r,n})_{k,k} = b_{t,k} e^{-j2\pi f_n \tau_{t,k}}$.

In the above modeling, the SI matrix of size $L_{R,r} \times L_T$ is given by $\mathbf{H}_{SI,n}$, and it represents the channel between the TX and RX antenna elements, i.e., direct coupling due to full-duplex operation. After RF combining at the radar RX, the BB RX frequency-domain symbol vector of size $L_{R,r}^{RF} \times 1$ reads

$$\mathbf{y}_{r,n,m} = (\mathbf{W}_{R,r}^{RF})^H \tilde{\mathbf{y}}_{r,n,m}, \tag{8}$$

where $\mathbf{W}_{R,r}^{RF}$ is the RF combiner of size $L_{R,r} \times L_{R,r}^{RF}$.

B. Estimation of Sensing Parameters

The RX frequency-domain symbols are given combining (4), (7) and (8) as

$$\mathbf{y}_{r,n,m} \simeq \underbrace{(\mathbf{W}_{R,r}^{RF})^H \mathbf{A}_R(\theta) \mathbf{H}_{r,n} \mathbf{A}_T^H(\theta) \mathbf{W}_T^{RF} \mathbf{W}_T^{BB}}_{\mathbf{A}_n(\theta)} \mathbf{x}_{n,m} + \mathbf{v}_{r,n,m},$$
$$\tag{9}$$

where $\mathbf{v}_{r,n,m}$ represents the noise vector. In this subsection, the effect of SI on the RX symbols is assumed to be negligible due to the SI cancellation method described in Section III-B, and thus neglected in the radar processing. Additionally, the matrix $\mathbf{A}_n(\theta)$ of size $L_{R,r}^{RF} \times (L_S \cdot U)$ denotes the effective radar channel between the TX streams and the RX symbols.

Based on these RX symbols, the K_t targets' delays and DoAs that need to be estimated are given by

$$\boldsymbol{\alpha} = [\underbrace{\tau_{t,1}, \ldots, \tau_{t,K_t}}_{\boldsymbol{\tau}}, \underbrace{\theta_{t,1}, \ldots, \theta_{t,K_t}}_{\boldsymbol{\theta}}]^T. \tag{10}$$

The RX symbols in (9) are separately used for range-profile estimation [11], and DoA estimation using MUSIC [9].

1) Range-Profile Estimation: For the lth RX RF chain and l_S^{th} TX stream, with $l \in [1, L_{R,r}^{RF}]$ and $l_S \in [1, L_S \cdot U]$, the relation between the TX and RX frequency-domain symbols can be written based on (9) as

$$y_{r,n,m,l} = \sum_{l_S=1}^{L_S \cdot U} a_{n,l,l_S} x_{n,m,l_S} + v_{r,n,m,l}, \tag{11}$$

where x_{n,m,l_S}, $y_{r,n,m,l}$, a_{n,l,l_S}, and $v_{r,n,m,l}$ denote a TX stream's frequency-domain symbol, a RX frequency-domain symbol, a complex coefficient to denote the effective channel, and the noise sample, respectively, with $(\mathbf{x}_{n,m})_{l_S} = x_{n,m,l_S}$, $(\mathbf{y}_{r,n,m})_l = y_{r,n,m,l}$, $(\mathbf{A}_n(\theta))_{l,l_S} = a_{n,l,l_S}$, and $(\mathbf{v}_{r,n,m})_l = v_{r,n,m,l}$. Next, element-wise multiplication is performed to calculate z_{n,m,l,l_S} as

$$z_{n,m,l,l_S} = y_{r,n,m,l} x_{n,m,l_S}^*, \tag{12}$$

where $(\cdot)^*$ denotes complex conjugation.

The range profile is then given as

$$d_{l,l_S}(n') = \frac{1}{M} \left| \sum_{m=0}^{M-1} \left(\sum_{n=0}^{N-1} z_{n,m,l,l_S} e^{\frac{j2\pi n n'}{N}} \right) \right|^2, \tag{13}$$

where calculating the inner sum is performed through the inverse discrete Fourier transform (IDFT) [11]. Here, each target's estimated delay is quantized using $\tau_{t,k,n'} = \frac{n'}{N \Delta f}$, where Δf is the subcarrier spacing.

2) DoA Estimation: This is performed through the MUSIC algorithm by utilizing the RX time-domain spatial sample vectors. Below, we also derive DoA estimation using RX frequency-domain symbols. As such, the relation between the two is shown first, needed for later derivations. This can be obtained by stacking the symbols for different subcarriers in (9) to a matrix and applying IDFT operation as

$$\mathbf{Y}_{r,m} = [\mathbf{y}_{r,0,m}, \ldots, \mathbf{y}_{r,N-1,m}]\mathbf{Q}$$
$$= [\mathbf{A}_0(\boldsymbol{\theta})\mathbf{x}_{0,m}, \ldots, \mathbf{A}_{N-1}(\boldsymbol{\theta})\mathbf{x}_{N-1,m}]\mathbf{Q} + \mathbf{V}_{r,m}, \quad (14)$$

where the matrices $\mathbf{Y}_{r,m}$ and $\mathbf{V}_{r,m}$ are of the same size $L_{R,r}^{RF} \times N$, and they denote the RX time-domain samples and noise samples, respectively. The $N \times N$ IDFT matrix is represented by $\mathbf{Q} = [\mathbf{q}_0, \ldots, \mathbf{q}_{N-1}]$, where each element is given by $(\mathbf{Q})_{n,i} = (\mathbf{q}_i)_n = e^{\frac{j2\pi ni}{N}}$, with $n, i \in [0, N-1]$.

The vector of time-domain samples for the ith sampling instant is given by

$$(\mathbf{Y}_{r,m})_i = [\mathbf{A}_0(\boldsymbol{\theta})\mathbf{x}_{0,m}, \ldots, \mathbf{A}_{N-1}(\boldsymbol{\theta})\mathbf{x}_{N-1,m}]\mathbf{q}_i + (\mathbf{V}_{r,m})_i, \quad (15)$$

where $(\mathbf{V}_{r,m})_i$ is the corresponding noise vector. The covariance matrix of these samples, $\mathbf{R}_{\mathbf{Y},m,i}$, is then written as

$$\mathbf{R}_{\mathbf{Y},m,i} = \mathbb{E}\{[\mathbf{A}_0(\boldsymbol{\theta})\mathbf{x}_{0,m}, \ldots, \mathbf{A}_{N-1}(\boldsymbol{\theta})\mathbf{x}_{N-1,m}]\mathbf{q}_i\mathbf{q}_i^H$$
$$\cdot [\mathbf{A}_0(\boldsymbol{\theta})\mathbf{x}_{0,m}, \ldots, \mathbf{A}_{N-1}(\boldsymbol{\theta})\mathbf{x}_{N-1,m}]^H\} + \sigma_r^2\mathbf{I}$$
$$= \mathbb{E}\left\{\left(\sum_{n=0}^{N-1} q_{i,n}\mathbf{A}_n(\boldsymbol{\theta})\mathbf{x}_{n,m}\right)\left(\sum_{n=0}^{N-1} q_{i,n}^*\mathbf{x}_{n,m}^H\mathbf{A}_n^H(\boldsymbol{\theta})\right)\right\} + \sigma_r^2\mathbf{I}$$
$$= \sum_{n=0}^{N-1} \mathbf{A}_n(\boldsymbol{\theta})\mathbb{E}\{\mathbf{x}_{n,m}\mathbf{x}_{n,m}^H\}\mathbf{A}_n^H(\boldsymbol{\theta}) + \sigma_r^2\mathbf{I}, \quad (16)$$

where $\mathbb{E}\{\cdot\}$, σ_r^2 and $\mathbf{I}$ denote the expectation operation, noise variance and the identity matrix, respectively. Additionally, $q_{i,n}q_{i,n}^* = 1$, while the expectation between the frequency-domain symbols on different subcarriers becomes zero as they are assumed mutually uncorrelated.

As observed in (16), the covariance matrix of the time-domain samples is the same for all sampling instants. Moreover, assuming $\mathbb{E}\{\mathbf{x}_{n,m}\mathbf{x}_{n,m}^H\} = \sigma_x^2\mathbf{I}$, $\mathbf{R}_{\mathbf{Y},m,i}$ can be represented as $\mathbf{R}_{\mathbf{Y}}$. Utilizing (9), $\mathbf{R}_{\mathbf{Y}}$ in (16) can be written as $\mathbf{R}_{\mathbf{Y}} = \sum_{n=0}^{N-1} \mathbb{E}\{\mathbf{y}_{r,n,m}(\mathbf{y}_{r,n,m})^H\}$, and thus it can be denoted as the sum of covariance matrices of the individual subcarriers. Then, substituting from (9) results in

$$\mathbf{R}_{\mathbf{Y}} = (\mathbf{W}_{R,r}^{RF})^H\mathbf{A}_R(\boldsymbol{\theta})\mathbf{R}_s\left((\mathbf{W}_{R,r}^{RF})^H\mathbf{A}_R(\boldsymbol{\theta})\right)^H + \sigma_r^2\mathbf{I}, \quad (17)$$

where

$$\mathbf{R}_s = \sigma_x^2 \sum_{n=0}^{N-1} \mathbf{H}_{r,n}\mathbf{A}_T^H(\boldsymbol{\theta})\mathbf{W}_T^{RF}\mathbf{W}_T^{BB}(\mathbf{H}_{r,n}\mathbf{A}_T^H(\boldsymbol{\theta})\mathbf{W}_T^{RF}\mathbf{W}_T^{BB})^H. \quad (18)$$

The signal part of $\mathbf{R}_{\mathbf{Y}}$ in (17) will have K_t positive eigenvalues and $(L_{R,r}^{RF} - K_t)$ zero eigenvalues. Expressing each of the eigenvectors of the zero eigenvalues (null eigenvectors) as $\boldsymbol{\gamma}_l$, $l \in [1, L_{R,r}^{RF} - K_t]$, it should satisfy

$$(\mathbf{W}_{R,r}^{RF})^H\mathbf{A}_R(\boldsymbol{\theta})\mathbf{R}_s\left((\mathbf{W}_{R,r}^{RF})^H\mathbf{A}_R(\boldsymbol{\theta})\right)^H\boldsymbol{\gamma}_l = \mathbf{0}, \quad (19)$$

where $\mathbf{0}$ is the zero vector. This can be simplified to obtain $\left((\mathbf{W}_{R,r}^{RF})^H\mathbf{A}_R(\boldsymbol{\theta})\right)^H\boldsymbol{\gamma}_l = \mathbf{0}$. Thus, the steering vectors at the RX RF chains, given by $(\mathbf{W}_{R,r}^{RF})^H\mathbf{a}_R(\theta_{t,k})$, with $k \in [1, K_t]$, are orthogonal to the null subspace.

From (17), it is seen that the eigenvectors of $\mathbf{R}_{\mathbf{Y}}$ are the same as those of the signal part of $\mathbf{R}_{\mathbf{Y}}$, but with increased eigenvalues due to the noise addition. Therefore to find the DoAs, eigendecomposition of $\mathbf{R}_{\mathbf{Y}}$ is performed first to find the eigenvectors corresponding to the lowest $L_{R,r}^{RF} - K_t$ eigenvalues, which are then the same as $\boldsymbol{\gamma}_l$. Then, using the orthogonality condition, the MUSIC pseudo-spectrum is written as [9]

$$P(\theta) = \frac{1}{\tilde{\mathbf{a}}^H(\theta)\boldsymbol{\Gamma}\boldsymbol{\Gamma}^H\tilde{\mathbf{a}}(\theta)}, \quad (20)$$

where $\boldsymbol{\Gamma} = [\boldsymbol{\gamma}_1, \ldots, \boldsymbol{\gamma}_{L_{R,r}^{RF}-K_t}]$, $\theta = [-90°, 90°]$ and $\tilde{\mathbf{a}}(\theta) = (\mathbf{W}_{R,r}^{RF})^H\mathbf{a}_R(\theta)$ denotes the effective steering vector at the RX RF chains. The K_t highest peaks of the pseudo-spectrum will then correspond to the DoAs. To calculate $\mathbf{R}_{\mathbf{Y}}$, the sample average is used as an approximation, and is given by

$$\mathbf{R}_{\mathbf{Y}} \approx \frac{1}{MN} \sum_{m=0}^{M-1} \sum_{n=0}^{N-1} \mathbf{y}_{r,n,m}(\mathbf{y}_{r,n,m})^H. \quad (21)$$

III. JCAS MIMO Beamforming Design

In this section, we discuss how the TX BB and RF, and RX RF beamforming weights are optimized, while also canceling the SI due to full-duplex operation.

A. Proposed TX Beamforming

The TX beamforming needs to provide different effective beams for each communication user while an additional beam is used for sensing. In this work, we consider that the streams are used for both communication and sensing functionalities, however, dedicated streams could also be utilized for radar [7]. For simplicity, in this part we assume that each user has a single stream ($L_S = 1$). Considering the presented hybrid architecture, the BB and RF weights are jointly optimized to provide multiple (viz. U) communication links while reducing the inter-user interference. In this case, we assume full control of the amplitudes and phases of these TX weights.

Based on (1)–(5), the proposed TX beamforming design maximizes the TX radar power in the radar direction θ_r, described as

$$P_{T,r} = \mathbb{E}\{|\mathbf{a}_T^H(\theta_r)\mathbf{W}_T^{RF}\mathbf{W}_T^{BB}\mathbf{x}_{n,m}|^2\} \quad (22)$$
$$= \sum_{u=1}^{U} |\mathbf{a}_T^H(\theta_r)\mathbf{W}_T^{RF}\mathbf{w}_{T,u}^{BB}|^2 P_{u,n,m} = \sum_{u=1}^{U} G_{T,u}(\theta_r)P_{u,n,m},$$

where $\mathbf{w}_{T,u}^{BB}$ and $P_{u,n,m} = \mathbb{E}\{|x_{u,n,m}|^2\}$ refer to the TX BB weights and the TX power of the uth user's stream.

The TX BB weights of each user are optimized such that they minimize the inter-user interference, which can be perfectly canceled if $\mathbf{a}_T^H(\theta_{c,u'})\mathbf{W}_T^{RF}\mathbf{w}_{T,u}^{BB} = 0$, where $u' \neq u$. To simultaneously isolate the rest of the users U', the TX BB weights of the uth user need to satisfy

$$\underbrace{[\mathbf{a}_T^H(\theta_{c,1})\mathbf{W}_T^{RF}, \ldots, \mathbf{a}_T^H(\theta_{c,U'})\mathbf{W}_T^{RF}]}_{=\mathbf{X}_u}\mathbf{w}_{T,u}^{BB} = \mathbf{0}. \quad (23)$$

Based on Moore–Penrose pseudoinverse's definition, a null-space projection (NSP) method can be implemented to suppress the inter-user interference [6]. Thus, the TX BB weights need to fulfill the condition

$$\mathbf{W}_{\text{T}}^{\text{BB}} = [\mathbf{N}_1 \hat{\mathbf{w}}_{\text{T},1}^{\text{BB}}, \ldots, \mathbf{N}_U \hat{\mathbf{w}}_{\text{T},U}^{\text{BB}}], \tag{24}$$

where $\mathbf{N}_u = (\mathbf{I} - \mathbf{X}_u^+ \mathbf{X}_u)$ denotes the NSP matrix for the uth user and $(\cdot)^+$ is the pseudo-inverse. The auxiliary TX BB weights $\hat{\mathbf{W}}_{\text{T}}^{\text{BB}} = [\hat{\mathbf{w}}_{\text{T},1}^{\text{BB}}, \ldots, \hat{\mathbf{w}}_{\text{T},U}^{\text{BB}}]$, with $\hat{\mathbf{w}}_{\text{T},u}^{\text{BB}}$ being any arbitrary vector of size $L_{\text{T}}^{\text{RF}} \times 1$, will be optimized to achieve the desired TX patterns.

The objective for optimization is to maximize the TX radar power (22) by jointly optimizing the RF and BB weights, $\mathbf{W}_{\text{T}}^{\text{RF}}$ and $\hat{\mathbf{W}}_{\text{T}}^{\text{BB}}$, and is written as

$$\max_{\hat{\mathbf{w}}_{\text{T}}^{\text{BB}}, \mathbf{W}_{\text{T}}^{\text{RF}}} \sum_{u=1}^{U} G_{\text{T},u}(\theta_{\text{r}}) \tag{25a}$$

$$\text{s.t.} \left\| \mathbf{W}_{\text{T}}^{\text{RF}} \mathbf{w}_{\text{T},u}^{\text{BB}} \right\| = 1, \forall u \tag{25b}$$

$$|\mathbf{a}_{\text{T}}^H (\theta_{\text{c},u}) \mathbf{W}_{\text{T}}^{\text{RF}} \mathbf{w}_{\text{T},u}^{\text{BB}}|^2 \geq \mu_u, \forall u \tag{25c}$$

$$\mathbf{W}_{\text{T}}^{\text{BB}} = [\mathbf{N}_1 \hat{\mathbf{w}}_{\text{T},1}^{\text{BB}}, \ldots, \mathbf{N}_U \hat{\mathbf{w}}_{\text{T},U}^{\text{BB}}], \tag{25d}$$

where the effective TX weights of each user are normalized with (25b) to constrain the TX power. The required TX gain for each user μ_u is imposed by the communication system with (25c). In addition, the NSP constraint (25d) reduces the inter-user interference according to (24).

To obtain numerical results, in the next section, we solve the above constrained beamforming optimization using the optimization toolbox of MATLAB.

B. RX Beamforming

In the RX side, a single beam is required to sense the radar direction, while SI is to be effectively suppressed as illustrated in Fig. 1. In this case, we optimize the RX RF weights at the different RF chains separately. The effective SI channel between each TX stream and RX RF chain is given by

$$\hat{\mathbf{H}}_{\text{SI},n} = (\mathbf{W}_{\text{R},\text{r}}^{\text{RF}})^H \mathbf{H}_{\text{SI},n} \mathbf{W}_{\text{T}}^{\text{RF}} \mathbf{W}_{\text{T}}^{\text{BB}}, \tag{26}$$

where $\{\hat{\mathbf{H}}_{\text{SI},n}\}_{l_{\text{R}}^{\text{RF}},u}$ with $u \in [1,U]$ and $l_{\text{R},\text{r}}^{\text{RF}} \in [1, L_{\text{R}}^{\text{RF}}]$. Similar to (24), an NSP method is implemented to cancel the frequency-dependent SI in (26). As mm-wave JCAS systems are most likely having large bandwidths in order to provide high data rates and highly accurate radar measurements, we consider an NSP method which implements $\mathcal{N}_{\text{freq}}$ frequency nulls in the operating band. Therefore, the RX RF weights $\mathbf{w}_{\text{R},\text{r},l_{\text{R}}^{\text{RF}}}$ for the l_{R}^{RF}th subarray need to satisfy

$$(\mathbf{w}_{\text{R},\text{r},l_{\text{R}}^{\text{RF}}}^{\text{RF}})^H \underbrace{\left[\mathbf{H}_{\text{SI},1} \mathbf{W}_{\text{T}}^{\text{RF}} \mathbf{W}_{\text{T}}^{\text{BB}}, \ldots, \mathbf{H}_{\text{SI},\mathcal{N}_{\text{freq}}} \mathbf{W}_{\text{T}}^{\text{RF}} \mathbf{W}_{\text{T}}^{\text{BB}} \right]}_{=\mathbf{X}_{l_{\text{R}}^{\text{RF}}}} = \mathbf{0}^T, \tag{27}$$

where $\mathbf{W}_{\text{R},\text{r}}^{\text{RF}} = [\mathbf{w}_{\text{R},\text{r},1}^{\text{RF}}, \ldots, \mathbf{w}_{\text{R},\text{r},L_{\text{R}}^{\text{RF}}}^{\text{RF}}]$. Similar to [6], the RF RX weights of each subarray are optimized to maximize the RX gain at the radar direction $G_{\text{R}}(\theta_{\text{r}}) = |(\mathbf{w}_{\text{R},\text{r},l_{\text{R}}^{\text{RF}}}^{\text{RF}})^H \mathbf{a}_{\text{R}}(\theta_{\text{r}})|^2$,

while effectively suppressing the SI at the desired frequencies. Then, the final weights are described as [6]

$$\mathbf{w}_{\text{R},\text{r},l_{\text{R}}^{\text{RF}}}^{\text{RF}} = \frac{(\mathbf{I} - \mathbf{X}_{l_{\text{R}}^{\text{RF}}} \mathbf{X}_{l_{\text{R}}^{\text{RF}}}^+) \mathbf{a}_{\text{R}}(\theta_{\text{r}})}{\left\| (\mathbf{I} - \mathbf{X}_{l_{\text{R}}^{\text{RF}}} \mathbf{X}_{l_{\text{R}}^{\text{RF}}}^+) \mathbf{a}_{\text{R}}(\theta_{\text{r}}) \right\|}. \tag{28}$$

IV. NUMERICAL RESULTS

Numerical evaluations are next carried out to demonstrate the performance of the proposed MIMO JCAS system, by considering a hybrid architecture. In the following results, realistic linear patch antenna arrays simulated with CST Studio Suite are used. In addition, the simulated arrays incorporate the mutual coupling effects that model the SI in a band with center frequency of $f_{\text{c}} = 28$ GHz and bandwidth of 500 MHz.

Figure 2 shows illustrative examples of the proposed MU-MIMO JCAS beamforming with two communication links at $-30°$ and $40°$, while an additional beam at $10°$ is used for sensing. As it can be observed in Fig. 2(a), streams from different UEs experience different effective TX patterns depending on their TX BB weights. Moreover, all the streams are transmitted towards the radar direction. The effective pattern of each user minimizes the inter-user interference by imposing nulls in the other user's directions. On the RX side, a separate design of the RF weights of each subarray is implemented to maximize the radar gain as shown in Fig. 2(b). In addition, these weights are optimized to efficiently suppress the wideband SI signal by implementing multiple frequency nulls as illustrated in Fig. 2(c).

Next, RX MIMO processing is applied for estimating the range and angle profiles using similar simulation parameters as in Fig. 2 considering $L_{\text{R},\text{r}}^{\text{RF}} = 8$ (i.e., eight RX RF chains). Separate point targets are placed at each communication direction ($-30°$ and $40°$), while two more are placed at the radar direction, with a $2°$ angular separation ($10°$ and $12°$). Additionally, the communication users are at different ranges, but the radar targets have almost the same range. A standard-compliant 5G OFDM waveform is then used at the MIMO TX with the following parameters: one OFDM symbol, $N = 3168$ and $\Delta f = 120$ kHz. Then, the RX spatial signal is used for range and DoA estimation as described in Section II-B.

Figure 3(a) depicts a range profile corresponding to the targets. Although there are four separate targets, the range profile depicts only three, where the two radar targets are shown as one. This is because the bandwidth of the waveform is not high enough to differentiate between the two radar targets that are very closely situated in range. To observe if the targets can be differentiated in angular domain, the MUSIC pseudo-spectrum is calculated according to (20) for finding the angle profile of the targets. Figure 3(b) depicts that four separate directions can be estimated in the angle profile. Due to the super-resolution DoA estimation, it can additionally be observed that there exist two radar targets. It should be stated here that the DoAs are still not associated with the ranges directly though since the range and angle profiles are estimated separately.
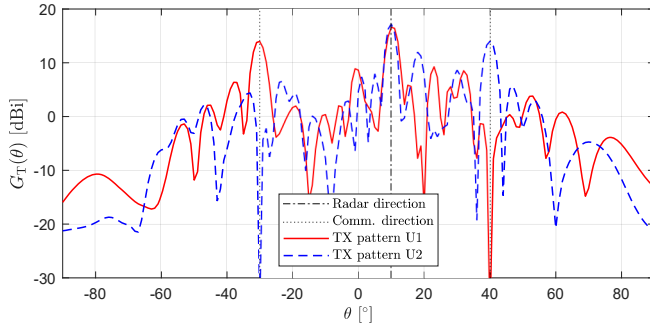
(a) Effective TX pattern for each stream
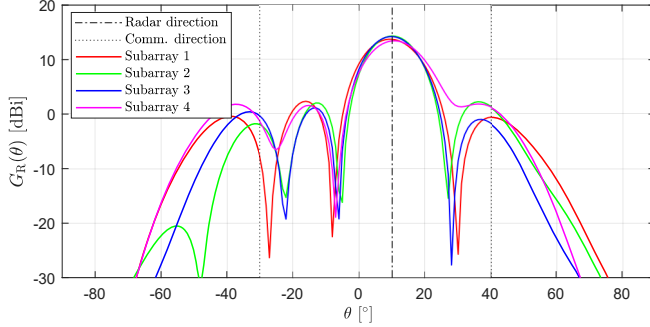

(b) Subarrays' RX patterns
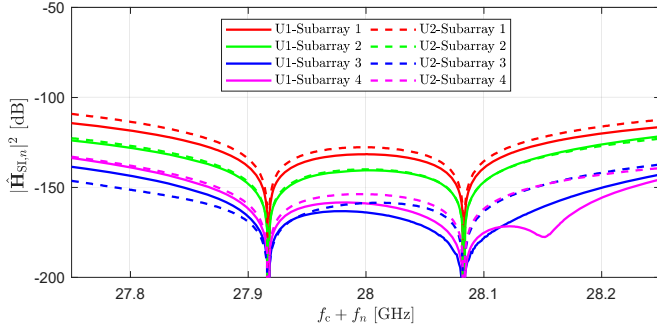
(c) SI frequency response

Fig. 2. Illustration of JCAS MIMO performance with a radar beam at $\theta_r = 10°$ and two communication users (U1 and U2) located at $\theta_{c,1} = -30°$ and $\theta_{c,2} = 40°$, respectively. The rest of simulation parameters are $U = 2$, $L_S = 1$, $L_T = 32$, $L_{R,r} = 32$, $L_T^{RF} = 8$, $L_{R,r}^{RF} = 4$, and $\mathcal{N}_{freq} = 2$.

V. CONCLUSION

In this article, we addressed the beamforming optimization and other related signal processing aspects in a hybrid MIMO JCAS system context. The TX BB and RF beamforming weights were optimized to provide multiple simultaneous beams for communication and sensing while suppressing the inter-user interference between different users. The RX RF beamforming was optimized to receive reflections from the sensing direction while minimizing the SI due to full-duplex operation. Additionally, the RX spatial signal was used to estimate the range and angle profiles corresponding to the targets. The results indicate that TX and RX beampatterns can be optimized for improved performance of the JCAS system. Moreover, the DoA estimation allows to separate multiple targets with the same range within the sensing beam.
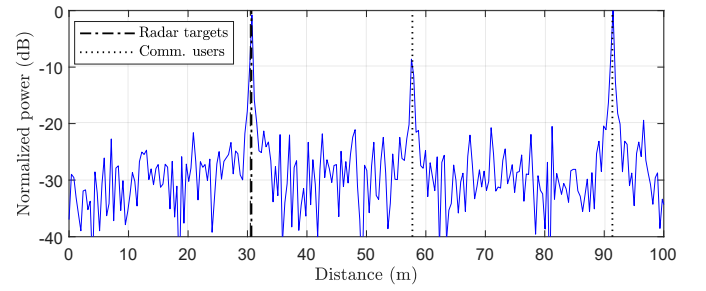
(a) Range profile
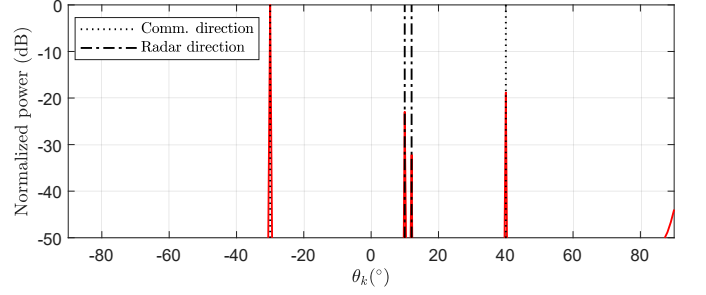
(b) Angle profile

Fig. 3. The estimated range and angle profiles for the simulated scenario with angles $\theta_{c,1} = -30°$, $\theta_{c,2} = 40°$, $\theta_{t,1} = 10°$, $\theta_{t,2} = 12°$, and ranges $d_{c,1} = 57.74\text{m}$, $d_{c,2} = 91.38\text{m}$, $d_{t,1} = 30.46\text{m}$, $d_{t,2} = 30.67\text{m}$.

REFERENCES

[1] F. Liu, C. Masouros, A. P. Petropulu, H. Griffiths, and L. Hanzo, "Joint radar and communication design: Applications, state-of-the-art, and the road ahead," *IEEE Trans. Commun.*, vol. 68, no. 6, pp. 3834–3862, Feb. 2020.

[2] S. A. Busari, K. M. S. Huq, S. Mumtaz, L. Dai, and J. Rodriguez, "Millimeter-wave massive MIMO communication for future wireless systems: A survey," *IEEE Commun. Surveys Tuts.*, vol. 20, no. 2, pp. 836–869, Dec. 2017.

[3] F. Liu, C. Masouros, A. Li, H. Sun, and L. Hanzo, "MU-MIMO communications with MIMO radar: From co-existence to joint transmission," *IEEE Trans. Wireless Commun.*, vol. 17, no. 4, pp. 2755–2770, Apr. 2018.

[4] S. Biswas, K. Singh, O. Taghizadeh, and T. Ratnarajah, "Design and analysis of FD MIMO cellular systems in coexistence with MIMO radar," *IEEE Trans. Wireless Commun.*, vol. 19, no. 7, pp. 4727–4743, Jul. 2020.

[5] Y. L. Sit, C. Sturm, J. Baier, and T. Zwick, "Direction of arrival estimation using the MUSIC algorithm for a MIMO OFDM radar," in *Proc. IEEE Radar Conf.*, May 2012, pp. 226–229.

[6] C. Baquero Barneto *et al.*, "Beamforming and waveform optimization for OFDM-based joint communications and sensing at mm-waves," in *Proc. Asilomar Conf. on Signals, Syst., Comput.*, Nov. 2020.

[7] X. Liu, T. Huang, N. Shlezinger, Y. Liu, J. Zhou, and Y. C. Eldar, "Joint transmit beamforming for multiuser MIMO communications and MIMO radar," *IEEE Trans. Signal Process.*, vol. 68, pp. 3929–3944, Jun. 2020.

[8] C. Baquero Barneto, S. D. Liyanaarachchi, M. Heino, T. Riihonen, and M. Valkama, "Full-duplex radio/radar technology: The enabler for advanced joint communication and sensing," *IEEE Wireless Commun.*, Feb. 2021.

[9] R. Schmidt, "Multiple emitter location and signal parameter estimation," *IEEE Trans. Antennas Propag*, vol. 34, no. 3, pp. 276–280, Mar. 1986.

[10] R. W. Heath, N. González-Prelcic, S. Rangan, W. Roh, and A. M. Sayeed, "An overview of signal processing techniques for millimeter wave MIMO systems," *IEEE J. Sel. Topics Signal Process.*, vol. 10, no. 3, pp. 436–453, Apr. 2016.

[11] S. D. Liyanaarachchi, C. B. Barneto, T. Riihonen, and M. Valkama, "Joint OFDM waveform design for communications and sensing convergence," in *Proc. IEEE Int. Conf. on Commun.*, Jun. 2020.

Publication 6

Range–Angle Processing for Target Detection in Joint MIMO-OFDM
Communications and Sensing

S. D. Liyanaarachchi, C. Baquero Barneto, T. Riihonen, M. Heino and M. Valkama

Range–Angle Processing for Target Detection in Joint MIMO-OFDM Communications and Sensing

Sahan Damith Liyanaarachchi, Carlos Baquero Barneto, Taneli Riihonen, Mikko Heino, and Mikko Valkama
Electrical Engineering, Faculty of Information Technology and Communication Sciences, Tampere University, Finland
Email: {sahan.liyanaarachchi, carlos.baquerobarneto, taneli.riihonen, mikko.heino, mikko.valkama}@tuni.fi

Abstract—Utilizing multiple-input multiple-output (MIMO) communication systems to jointly perform sensing will be a key ingredient in future mobile networks. To accommodate this, here we propose a signal processing approach for target detection in hybrid MIMO orthogonal frequency-division multiplexing communication systems. We utilize multiple transmit beams for communication users, while an additional beam is used simultaneously to sense the environment. Then, the reflections from the targets due to the transmitted streams are utilized at the MIMO receiver to obtain the range–angle map corresponding to the environment. Simulations depict that targets can be detected reliably using this approach. Moreover, it showcases that MIMO processing allows differentiating between very close targets in the angular domain, demonstrating the achievable super-resolution.

Index Terms—Joint communication and sensing, MIMO, MU-SIC, OFDM, radar.

Fig. 1. The considered MIMO-OFDM JCAS system.

I. INTRODUCTION

The separate operation of communication and sensing systems has caused spectrum scarcity and mutual interference. Joint communication and sensing (JCAS) systems have emerged as a solution for these challenges where they are designed for efficient resource allocation [1], and many applications have benefited from the joint functioning, e.g., automotive radar, cellular networks, and indoor mapping [2].

Mobile communication systems are moving to operate around mm-wave frequencies to provide increased data rates to the users. However, due to the high attenuation evident in these frequencies, multiple-input multiple-output (MIMO) technology is necessary, which provides high gains through spatial multiplexing and directional beams [3].

Sensing systems can also benefit due to the MIMO operation since they provide more degrees of freedom in radar processing, improving the target detection [4]. Typically in these MIMO radars, the receive (RX) antennas are spaced at a half-wavelength distance, while the transmit (TX) antennas have a much farther separation. Additionally, the signals from different TX antennas are made orthogonal, which allow super-resolution in direction of arrival (DoA) estimation [5]. Thus, the design of MIMO JCAS systems has received increased interest due to these advantages for both communication and sensing functionalities [6].

In this work, we consider performing JCAS in the perspective of a MIMO communication system. Unlike in MIMO radars, the additional constraints on the antenna separation and the orthogonality between the TX antennas' signals cannot be practically implemented in such a system. Therefore, the contribution of this paper is on performing JCAS by also considering these limitations. We adopt a MIMO system with hybrid analog-digital architecture [7], where both the TX and RX antennas are spaced at half-wavelength. Orthogonal frequency-division multiplexing (OFDM) is used as the TX waveform, and the signals are not necessarily orthogonal between different TX antennas. Multiple beams are employed to cater to different users, while a sensing beam is used concurrently to sense the environment. Additionally, the cross-interference between the users is also suppressed.

We then demonstrate a signal processing approach to obtain the range profiles, which are utilized to obtain the angle profiles using multiple signal classification (MUSIC) algorithm [8], thereby constructing the range–angle map of the considered environment. The numerical results indicate that the targets can be reliably observed even if they are spaced very close in the angular domain, indicating that super-resolution can be achieved with the related range–angle processing.

II. SYSTEM MODEL

A MIMO-OFDM system is used in this work, as illustrated in Fig. 1, using a hybrid analog-digital architecture. The JCAS system works as a communication TX as well as a radar transceiver. At the TX side, multiple communication links are maintained, while an additional beam is used to sense the environment. The number of antenna elements and radio-frequency (RF) chains (equivalent to the number of subarrays) are given by L_T and L_T^{RF}, and L_R and L_R^{RF}, for the TX and RX sides, respectively. As the TX waveform, OFDM is utilized, with M symbols, each with N active subcarriers.

Each communication user is assumed to have S streams, and the TX frequency-domain symbols of the uth user at n^{th} subcarrier and m^{th} OFDM symbol are given by $\mathbf{x}_{u,n,m}$, which is of size $S \times 1$, with $n \in [1, N]$, $m \in [1, M]$, and $u \in [1, U]$, where U is the number of communication users. The baseband (BB) weights for the uth user are given by $\mathbf{W}_{\text{T},u}^{\text{BB}}$, which is a matrix of size $L_{\text{T}}^{\text{RF}} \times S$. The TX RF weights are common to all users and are given by the matrix $\mathbf{W}_{\text{T}}^{\text{RF}}$, which is of size $L_{\text{T}} \times L_{\text{T}}^{\text{RF}}$. Then, the frequency-domain symbols at the TX antenna elements are given by

$$\tilde{\mathbf{x}}_{n,m} = \mathbf{W}_{\text{T}}^{\text{RF}} \sum_{u=1}^{U} \mathbf{W}_{\text{T},u}^{\text{BB}} \mathbf{x}_{u,n,m} = \mathbf{W}_{\text{T}}^{\text{RF}} \mathbf{W}_{\text{T}}^{\text{BB}} \mathbf{x}_{n,m}, \quad (1)$$

where $\tilde{\mathbf{x}}_{n,m}$ is of size $L_{\text{T}} \times 1$, and

$$\mathbf{W}_{\text{T}}^{\text{BB}} = \left[\mathbf{W}_{\text{T},1}^{\text{BB}}, \mathbf{W}_{\text{T},2}^{\text{BB}}, \dots, \mathbf{W}_{\text{T},U}^{\text{BB}} \right], \quad (2)$$

$$\mathbf{x}_{n,m} = \left[\mathbf{x}_{1,n,m}^T, \mathbf{x}_{2,n,m}^T, \dots, \mathbf{x}_{U,n,m}^T \right]^T, \quad (3)$$

which are respectively of sizes $L_{\text{T}}^{\text{RF}} \times (S \cdot U)$ and $(S \cdot U) \times 1$.

A. TX and RX Beamforming

At the TX side, multiple beams are provided for the U communication users at angles denoted by $\theta_{\text{c},u}$, while a sensing beam is used additionally at θ_{r}. We assume that the angles $\theta_{\text{c},u}$ are known by the MIMO transceiver, whereas θ_{r} could be any arbitrary angle. Having a separate sensing beam allows to detect any target at θ_{r}, but since it is not known beforehand, θ_{r} is chosen arbitrarily. Further, the inter-user interference between the communication users is minimized by imposing nulls in the TX beam pattern at other users' directions. To achieve all these requirements, BB and RF beamforming weights are optimized similar to [9]. At the RX side, any type of RF beamforming weights can be used, i.e., either directional or omnidirectional beam patterns. However, here they are designed to maximize the gain at the angle corresponding to the sensing beam θ_{r}, providing a directional beam pattern.

B. MIMO Radar

Assuming there are K_{t} point targets, the TX signal is reflected from these and received back at the radar RX as

$$\tilde{\mathbf{y}}_{n,m} = \sum_{k=1}^{K_{\text{t}}} b_k e^{-j2\pi n \Delta f \tau_k} \mathbf{a}_{\text{R}}(\theta_k) \mathbf{a}_{\text{T}}^H(\theta_k) \tilde{\mathbf{x}}_{n,m} + \tilde{\mathbf{v}}_{n,m}, \quad (4)$$

where $\tilde{\mathbf{y}}_{n,m}$ and $\tilde{\mathbf{v}}_{n,m}$ are the RX frequency-domain symbol vector and the noise sample vector, respectively, of sizes $L_{\text{R}} \times 1$. The variables b_k and τ_k denote the attenuation constant and two-way delay of the kth target, while $\mathbf{a}_{\text{R}}(\theta_k)$ and $\mathbf{a}_{\text{T}}(\theta_k)$ are the RX and TX steering vectors corresponding to the same target. The subcarrier spacing is denoted by Δf. Additionally, angles of departure and arrival, expressed by θ_k, are considered to be the same, assuming far targets and the TX and RX arrays being closely situated. For a uniform linear array with half-wavelength separation between the L antenna elements, the steering vector for a general angle θ is given by

$$\mathbf{a}(\theta) = \left[1, e^{j\pi \sin(\theta)}, \dots, e^{j\pi(L-1)\sin(\theta)} \right]^T. \quad (5)$$

Converting (4) into a matrix notation yields

$$\tilde{\mathbf{y}}_{n,m} = \mathbf{A}_{\text{R}}(\boldsymbol{\theta}) \mathbf{H}_{\text{rad},n} \mathbf{A}_{\text{T}}^H(\boldsymbol{\theta}) \tilde{\mathbf{x}}_{n,m} + \tilde{\mathbf{v}}_{n,m}, \quad (6)$$

where $\mathbf{A}_{\text{R}}(\boldsymbol{\theta}) = [\mathbf{a}_{\text{R}}(\theta_1), \dots, \mathbf{a}_{\text{R}}(\theta_{K_{\text{t}}})]$ is of size $L_{\text{R}} \times K_{\text{t}}$ and $\mathbf{A}_{\text{T}}(\boldsymbol{\theta}) = [\mathbf{a}_{\text{T}}(\theta_1), \dots, \mathbf{a}_{\text{T}}(\theta_{K_{\text{t}}})]$ is of size $L_{\text{T}} \times K_{\text{t}}$, and they contain the steering vectors for all the targets. Additionally, $\boldsymbol{\theta} = [\theta_1, \dots, \theta_{K_{\text{t}}}]^T$ is the vector of all targets' directions. The diagonal matrix $\mathbf{H}_{\text{rad},n}$ is of size $K_{\text{t}} \times K_{\text{t}}$, and it represents the radar channel where $(\mathbf{H}_{\text{rad},n})_{k,k} = b_k e^{-j2\pi n \Delta f \tau_k}$. Then, the RX BB frequency-domain symbols are given by

$$\begin{aligned} \mathbf{y}_{n,m} &= (\mathbf{W}_{\text{R}}^{\text{RF}})^H \tilde{\mathbf{y}}_{n,m} \\ &= \underbrace{(\mathbf{W}_{\text{R}}^{\text{RF}})^H \mathbf{A}_{\text{R}}(\boldsymbol{\theta}) \mathbf{H}_{\text{rad},n} \mathbf{A}_{\text{T}}^H(\boldsymbol{\theta}) \mathbf{W}_{\text{T}}^{\text{RF}} \mathbf{W}_{\text{T}}^{\text{BB}}}_{\mathbf{H}_n} \mathbf{x}_{n,m} + \mathbf{v}_{n,m}, \end{aligned}$$

$$(7)$$

where the RX RF combiner $\mathbf{W}_{\text{R}}^{\text{RF}}$ is of size $L_{\text{R}} \times L_{\text{R}}^{\text{RF}}$ and $\mathbf{y}_{n,m}$ is a vector of size $L_{\text{R}}^{\text{RF}} \times 1$. The effective channel between the TX streams and the RX BB symbols is given by $\mathbf{H}_n$, which is of size $L_{\text{R}}^{\text{RF}} \times (S \cdot U)$.

Assuming $\mathbf{H}_n$ to be a time-invariant channel for different OFDM symbols, (7) can alternatively be written by stacking for different OFDM symbols as

$$\underbrace{\begin{bmatrix} \mathbf{y}_{n,1} \\ \mathbf{y}_{n,2} \\ \vdots \\ \mathbf{y}_{n,M} \end{bmatrix}}_{\mathbf{y}_n} = \underbrace{\begin{bmatrix} x_{n,1,1}\mathbf{I} & \dots & x_{n,1,S\cdot U}\mathbf{I} \\ x_{n,2,1}\mathbf{I} & \dots & x_{n,2,S\cdot U}\mathbf{I} \\ \vdots & \vdots & \vdots \\ x_{n,M,1}\mathbf{I} & \dots & x_{n,M,S\cdot U}\mathbf{I} \end{bmatrix}}_{\mathbf{X}_n} \underbrace{\begin{bmatrix} \mathbf{h}_{n,1} \\ \mathbf{h}_{n,2} \\ \vdots \\ \mathbf{h}_{n,S\cdot U} \end{bmatrix}}_{\mathbf{h}_n} + \mathbf{v}_n,$$

$$(8)$$

where $x_{n,m,s} = (\mathbf{x}_{n,m})_s$ for $s \in [1, S \cdot U]$ denotes the sth element of $\mathbf{x}_{n,m}$ and $\mathbf{h}_{n,s} = (\mathbf{H}_n)_s$ denotes the sth column of $\mathbf{H}_n$. Here, $\mathbf{I}$ is the $L_{\text{R}}^{\text{RF}} \times L_{\text{R}}^{\text{RF}}$ identity matrix, and $\mathbf{y}_n$, $\mathbf{X}_n$, $\mathbf{h}_n$ and $\mathbf{v}_n$ are of dimensions $(L_{\text{R}}^{\text{RF}} \cdot M) \times 1$, $(L_{\text{R}}^{\text{RF}} \cdot M) \times (S \cdot U \cdot L_{\text{R}}^{\text{RF}})$, $(S \cdot U \cdot L_{\text{R}}^{\text{RF}}) \times 1$, and $(L_{\text{R}}^{\text{RF}} \cdot M) \times 1$, respectively.

III. RANGE–ANGLE PROCESSING

This section showcases the procedure adopted in obtaining the range–angle map corresponding to the targets. In this paper, we build upon the work done in [9], where range and angle profiles were calculated separately from the RX BB symbols. Due to this reason, ranges and angles of the targets were not associated with each other. However in this work, the calculated range profiles are subsequently used to calculate the angle profiles. Hence, the targets' ranges can be associated with the corresponding angles. This is the main difference compared to [9], while here we also extensively discuss the processing involved.

The objective of radar processing is to estimate targets' delays and angles, which can be done by estimating $\mathbf{h}_n$ as

$$\hat{\mathbf{h}}_n = \begin{bmatrix} \hat{\mathbf{h}}_{n,1} \\ \hat{\mathbf{h}}_{n,2} \\ \vdots \\ \hat{\mathbf{h}}_{n,S\cdot U} \end{bmatrix} = \mathbf{X}_n^\dagger \mathbf{y}_n = \mathbf{h}_n + \bar{\mathbf{h}}_n, \quad (9)$$

where $\hat{\mathbf{h}}_n$ is the estimate for $\mathbf{h}_n$, $\bar{\mathbf{h}}_n$ is the estimation error vector and $(\cdot)^\dagger$ is the pseudo-inverse operation. When sufficient number of OFDM symbols is used, $\mathbf{X}_n$ can be assumed to have full rank, i.e., it is quite unlikely that different OFDM symbols carry the same stream of frequency-domain symbols. In this case, the matrix $\mathbf{X}_n^H \mathbf{X}_n$ will also be of full rank. Hence, the inverse of that matrix, i.e., $(\mathbf{X}_n^H \mathbf{X}_n)^{-1}$, exists, and therefore the pseudo-inverse is given by $\mathbf{X}_n^\dagger = (\mathbf{X}_n^H \mathbf{X}_n)^{-1} \mathbf{X}_n^H$.

A. Calculation of the Range Profiles

For the sth TX stream, L_R^RF different values can be calculated for the ith range bin by applying the inverse discrete Fourier transform (IDFT) to $\hat{\mathbf{h}}_{n,s}$, similar to the scalar case in [10] as

$$\mathbf{d}_{i,s} = \sum_{n=1}^{N} q_{i,n} \hat{\mathbf{h}}_{n,s} = \left[\hat{\mathbf{h}}_{1,s}, \ldots, \hat{\mathbf{h}}_{N,s} \right] \mathbf{q}_i, \qquad (10)$$

where $i \in [1, N]$ and $\mathbf{q}_i$ is the IDFT vector of size $N \times 1$, and each element of it is given by $(\mathbf{q}_i)_n = q_{i,n} = e^{\frac{j 2\pi n i}{N}}$, while $\mathbf{d}_{i,s}$ is a vector of size $L_\text{R}^\text{RF} \times 1$. Although $\mathbf{d}_{i,s}$ depends on $\boldsymbol{\theta}$, it is not shown explicitly for simplicity of notation. The delay of each target is discretized as $\tau_i = \frac{i}{N \Delta f}$.

Since there are L_R^RF different range bin values for the sth stream, they can be combined at the radar RX to yield a single value. The angle-dependent complex coefficient of the RX beam pattern at a particular direction θ, including also the BB weights at the RX is given as

$$g_\text{R}(\theta) = (\mathbf{w}_\text{R}^\text{BB}(\theta))^H (\mathbf{W}_\text{R}^\text{RF})^H \mathbf{a}_\text{R}(\theta), \qquad (11)$$

where $\mathbf{w}_\text{R}^\text{BB}(\theta)$ is of size $L_\text{R}^\text{RF} \times 1$. Then, the RX BB weights that maximize $g_\text{R}(\theta)$ under the constraint $\|\mathbf{w}_\text{R}^\text{BB}(\theta)\| = 1$ (unit norm), are given by the solution for the spatial matched-filter (MF) as

$$\mathbf{w}_\text{R}^\text{BB}(\theta) = \frac{(\mathbf{W}_\text{R}^\text{RF})^H \mathbf{a}_\text{R}(\theta)}{\|(\mathbf{W}_\text{R}^\text{RF})^H \mathbf{a}_\text{R}(\theta)\|}. \qquad (12)$$

Then, the single value for the ith range bin and for the sth TX stream is given by $(\mathbf{w}_\text{R}^\text{BB}(\theta))^H \mathbf{d}_{i,s}$, and performing this for all the streams, they can be stacked into a vector as

$$\mathbf{d}_i = [(\mathbf{w}_\text{R}^\text{BB}(\theta))^H \mathbf{d}_{i,1}, \ldots, (\mathbf{w}_\text{R}^\text{BB}(\theta))^H \mathbf{d}_{i,S \cdot U}]^T, \qquad (13)$$

where $\mathbf{d}_i$ is of size $(S \cdot U) \times 1$.

B. Calculation of the Angle Profiles

For calculating the angle profiles, the covariance matrix of the range bin values across different RF chains is needed. Hence, this will be first calculated based on (10). Adopting (9), $\hat{\mathbf{h}}_{n,s} = \mathbf{h}_{n,s} + \bar{\mathbf{h}}_{n,s}$, where $\bar{\mathbf{h}}_{n,s}$ is the corresponding estimation error vector, the covariance matrix of the ith range bin is then given by

$$\mathbf{R}_{\mathbf{d},i,s} = \mathbb{E}\{\mathbf{d}_{i,s} \mathbf{d}_{i,s}^H\}$$
$$= \mathbb{E}\left\{ \left(\sum_{n_1=1}^{N} q_{i,n_1} \hat{\mathbf{h}}_{n_1,s} \right) \left(\sum_{n_2=1}^{N} q_{i,n_2}^* \hat{\mathbf{h}}_{n_2,s}^H \right) \right\}$$
$$= \sum_{n_1=1}^{N} \sum_{n_2=1}^{N} q_{i,n_1} q_{i,n_2}^* \mathbf{h}_{n_1,s} \mathbf{h}_{n_2,s}^H + \sigma^2 \mathbf{I}. \qquad (14)$$

Here, the expectation operation is denoted by $\mathbb{E}\{\cdot\}$ and the covariance matrix of the estimation error is given by $\sigma^2 \mathbf{I} = \sum_{n_1=1}^{N} \sum_{n_2=1}^{N} q_{i,n_1} q_{i,n_2}^* \mathbb{E}\{\bar{\mathbf{h}}_{n_1,s} \bar{\mathbf{h}}_{n_2,s}^H\}$. Since $\mathbf{h}_{n,s}$ corresponds to $(\mathbf{H}_n)_s = (\mathbf{W}_\text{R}^\text{RF})^H \mathbf{A}_\text{R}(\boldsymbol{\theta}) \mathbf{H}_{\text{rad},n} \mathbf{A}_\text{T}^H(\boldsymbol{\theta}) \mathbf{W}_\text{T}^\text{RF}(\mathbf{W}_\text{T}^\text{BB})_s$, (14) can be rewritten as

$$\mathbf{R}_{\mathbf{d},i,s} = \mathbf{A}_\text{RF}(\boldsymbol{\theta}) \mathbf{R}_{\text{res},i,s} \mathbf{A}_\text{RF}^H(\boldsymbol{\theta}) + \sigma^2 \mathbf{I}, \qquad (15)$$

where $\mathbf{A}_\text{RF}(\boldsymbol{\theta}) = (\mathbf{W}_\text{R}^\text{RF})^H \mathbf{A}_\text{R}(\boldsymbol{\theta})$ is of size $L_\text{R}^\text{RF} \times K_\text{t}$ and

$$\mathbf{R}_{\text{res},i,s} = \sum_{n_1=1}^{N} \sum_{n_2=1}^{N} q_{i,n_1} q_{i,n_2}^* (\mathbf{H}_{\text{rad},n_1} \mathbf{A}_\text{T}^H(\boldsymbol{\theta}) \mathbf{W}_\text{T}^\text{RF}(\mathbf{W}_\text{T}^\text{BB})_s)$$
$$\cdot (\mathbf{H}_{\text{rad},n_2} \mathbf{A}_\text{T}^H(\boldsymbol{\theta}) \mathbf{W}_\text{T}^\text{RF}(\mathbf{W}_\text{T}^\text{BB})_s)^H \qquad (16)$$

is the covariance matrix due to the residual terms apart from $\mathbf{A}_\text{RF}(\boldsymbol{\theta})$ in $(\mathbf{H}_n)_s$. In practice, an approximation is used for the covariance matrix in (14), given by $\mathbf{R}_{\mathbf{d},i,s} \approx \mathbf{d}_{i,s} \mathbf{d}_{i,s}^H$.

The first term on the right-side in (15) will have $(L_\text{R}^\text{RF} - K_\text{t})$ zero eigenvalues, where each corresponding eigenvector is represented by $\boldsymbol{\gamma}_p$, of size $L_\text{R}^\text{RF} \times 1$, with $p \in [1, L_\text{R}^\text{RF} - K_\text{t}]$. Each of them should obey $\mathbf{A}_\text{RF}(\boldsymbol{\theta}) \mathbf{R}_{\text{res},i,s} \mathbf{A}_\text{RF}^H(\boldsymbol{\theta}) \boldsymbol{\gamma}_p = \mathbf{0}$, where the zero vector is denoted by $\mathbf{0}$. After some simplification, the solution can be given as $\mathbf{A}_\text{RF}^H(\boldsymbol{\theta}) \boldsymbol{\gamma}_p = \mathbf{A}_\text{R}^H(\boldsymbol{\theta}) \mathbf{W}_\text{R}^\text{RF} \boldsymbol{\gamma}_p = \mathbf{0}$. Then, it can be shown that the eigenvectors of $\mathbf{R}_{\mathbf{d},i,s}$ corresponding to the $(L_\text{R}^\text{RF} - K_\text{t})$ lowest eigenvalues are the same as $\boldsymbol{\gamma}_p$. Hence, to find the angle profile, eigendecomposition of $\mathbf{R}_{\mathbf{d},i,s}$ is first performed to find $\boldsymbol{\gamma}_p$ to write the MUSIC pseudo-spectrum of the ith range bin and s^{th} stream as [9]

$$P(\theta)_{i,s} = \frac{1}{\tilde{\mathbf{a}}^H(\theta) \boldsymbol{\Gamma}_{i,s} \boldsymbol{\Gamma}_{i,s}^H \tilde{\mathbf{a}}(\theta)}, \qquad (17)$$

where $\boldsymbol{\Gamma}_{i,s} = [\boldsymbol{\gamma}_{i,s,1}, \ldots, \boldsymbol{\gamma}_{i,s,L_\text{R}^\text{RF} - K_\text{t}}]$ is the matrix containing eigenvectors corresponding to the zero eigenvalues, $\theta \in [-90°, 90°]$, and $\tilde{\mathbf{a}}(\theta) = (\mathbf{W}_\text{R}^\text{RF})^H \mathbf{a}_\text{R}(\theta)$. This is performed for all the range bins to obtain the range–angle map corresponding to each TX stream.

The complexity of range–angle processing depends mainly on three operations: the pseudo-inverse in (9), the IDFT in (10), and the eigendecomposition of $\mathbf{R}_{\mathbf{d},i,s}$ in (14), respectively. The computational complexity of all these operations depends on the dimensions of the corresponding matrices, i.e., M, N, S, U, and L_R^RF. Generally, N is the highest value out of these, and thus a higher value for it increases the computational complexity, while simultaneously improving range resolution, indicating its trade-off.

C. Combination of Range and Angle Profiles

As observed from (17), $S \cdot U$ TX streams will produce that many different angle profiles for the ith range bin, and hence different range–angle maps. This is due to $\mathbf{W}_\text{T}^\text{BB}$ having disparate weights for the TX streams. However, in the perspective of radar processing, a single range–angle map is required, which can be performed through maximum-ratio combining. For the sth TX stream, the angle-dependent complex coefficient of the beam pattern is given as

$$g_{\text{T},s}(\theta) = \mathbf{a}_T^H(\theta) \mathbf{W}_\text{T}^\text{RF}(\mathbf{W}_\text{T}^\text{BB})_s, \qquad (18)$$

and thus the combined MUSIC pseudo-spectrum can be written for the ith range bin as

$$P(\theta)_i = \sum_{s=1}^{S \cdot U} |g_{\text{T},s}(\theta)|^2 P(\theta)_{i,s}$$

$$= \sum_{s=1}^{S \cdot U} \frac{|g_{\text{T},s}(\theta)|^2}{\tilde{\mathbf{a}}^H(\theta)\boldsymbol{\Gamma}_{i,s}\boldsymbol{\Gamma}_{i,s}^H\tilde{\mathbf{a}}(\theta)}. \quad (19)$$

Finally, a similar approach could be applied to $\mathbf{d}_i$ in (13) to obtain a single range bin value as

$$d_{\text{comb},i} = \sum_{s=1}^{S \cdot U} g_{\text{T},s}^*(\theta_{\text{r}})(\mathbf{d}_i)_s, \quad (20)$$

where $g_{\text{T},s}^*(\theta_{\text{r}})$ is used to coherently combine the different range bin values computed for different TX streams.

IV. NUMERICAL RESULTS

In this section, the proposed range–angle processing is simulated for the considered MIMO hybrid architecture. The parameters used for the simulations are $L_{\text{T}} = L_{\text{R}} = 32$, $L_{\text{T}}^{\text{RF}} = L_{\text{R}}^{\text{RF}} = 8$, $U = 2$, $S = 1$, $M = 10$, $N = 3168$, $\Delta f = 120$ kHz, and a signal-to-noise ratio of 30 dB at the radar RX. It should be noted that the processing still works for $S > 1$, but for simplicity we consider $S = 1$. Additionally, the TX and RX antenna arrays are simulated with CST Studio Suite to observe the performance with realistic antennas.

Three beams are used in the TX at angles $\theta_{\text{r}} = 10°$, $\theta_{\text{c},1} = -40°$ and $\theta_{\text{c},2} = 30°$, where only the first user's stream is transmitted at $\theta_{\text{c},1}$, while the second user's stream is only transmitted at $\theta_{\text{c},2}$. However, both streams are transmitted to θ_{r}. Additionally, for the first user's TX beam pattern, a null is imposed at $\theta_{\text{c},2}$, while for the second user's beam pattern, that null is at $\theta_{\text{c},1}$, to cancel the inter-user interference between the two users. All these requirements are performed by optimizing $\mathbf{W}_{\text{T}}^{\text{BB}}$ and $\mathbf{W}_{\text{T}}^{\text{RF}}$, similar to [9]. Then at the RX side, a single beam is used at θ_{r}, obtained by optimizing $\mathbf{W}_{\text{R}}^{\text{RF}}$. Six point targets with a radar cross section of $50\ m^2$ are placed as depicted in Fig. 2(a). Targets that have almost the same angle are grouped together as depicted in the figure. Here, $\theta_{\text{oth}} \approx 19°$, and it denotes the angle where there is some clutter, separate from the communication users and the sensing target.

Figure 2(b) depicts the range profiles for the considered scenario, where a single range profile is obtained per each TX stream using (11)–(13). For the first user's stream transmitted at $\theta_{\text{c},1}$, the target at $\theta_{\text{c},2}$ is not observed, while those at $\theta_{\text{c},1}$ are not observed with the second user's TX stream at $\theta_{\text{c},2}$. This is because the TX beam pattern corresponding to one user has a null at the other user's direction to mitigate the inter-user interference [9]. Then, the radar target at θ_{r} is observed by the two TX streams since they both are transmitted at that angle. Although there are two targets at θ_{oth}, only a single target is observed by both TX streams since the range resolution is not high enough to differentiate between them. The figure also shows the single range profile obtained by combining the range profiles corresponding to the two TX streams using (20).
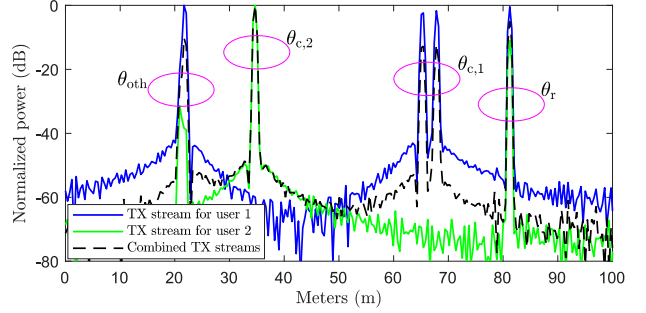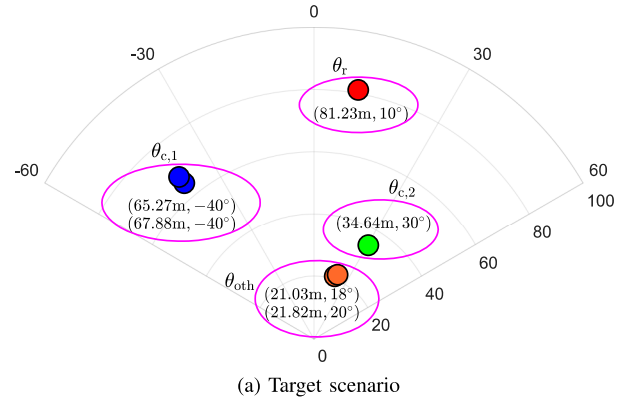
(a) Target scenario

(b) The range profiles obtained for the different TX streams

Fig. 2. The considered target scenario and the corresponding range profiles obtained for the different TX streams.

Then, Figs. 3(a)–(c) show the 3D range–angle maps using a MF approach, whereas Figs. 3(d)–(f) are with the MUSIC approach. In both approaches, the three figures are with the first TX stream, second stream, and both streams combined, respectively. In the MF approach, the L_{R}^{RF} different range profiles for the sth TX stream are combined for a particular angle θ using (11)–(13). Performing this for $\theta \in [-90°, 90°]$, the corresponding range–angle map is found, and the single range–angle map can be obtained using (19).

Figures 3(a)–(b) show that although the targets' ranges can be clearly distinguished, there are ambiguities in the angles. This is because of the grating lobes in the effective pattern of each subarray (combination of RF and BB), due to the distance between them being more than a half-wavelength separation. Figure 3(c) then depicts the combined range–angle map for all the targets. Despite of the ambiguities, the combination has reduced the noise level of the range–angle map.

In the MUSIC approach, combination of different range profiles are done similarly with (11)–(13), but only for the sensing direction θ_{r}, while range–angle maps are combined with (19). The ambiguities in the angles are quite weak with this approach, as illustrated in Figs. 3(d)–(e). Moreover, the target(s) at the second/first user's direction is(/are) not observed by the first/second TX stream, as in Fig. 2(b), while the target at θ_{r} is observed by both. Then, combining the two streams allows to cancel the ambiguities well, distinguishing between all the targets, as shown in Fig. 3(f).

The two closely situated targets at θ_{oth} can now be observed, which are not seen in Fig. 2(b), indicating the super-resolution

(a) TX stream 1, MF   (b) TX stream 2, MF   (c) TX streams combined, MF

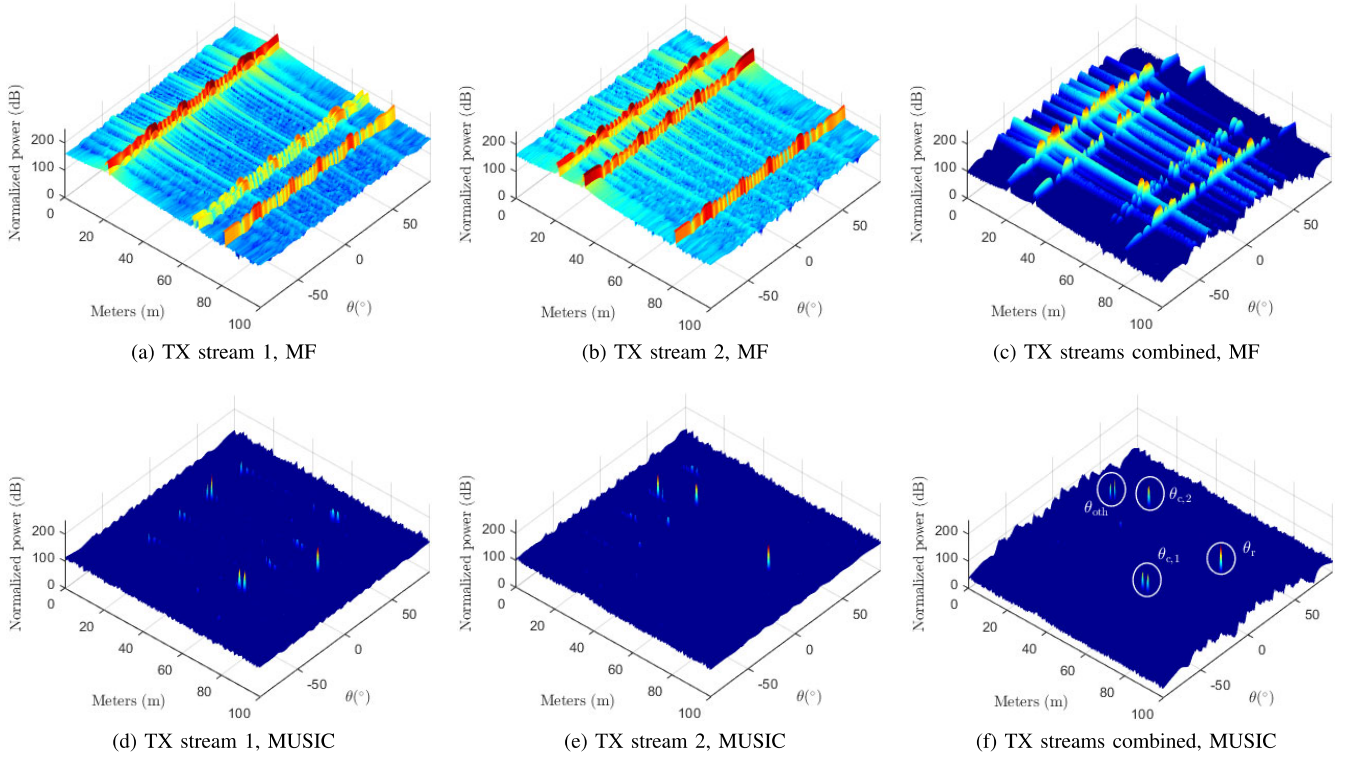(d) TX stream 1, MUSIC   (e) TX stream 2, MUSIC   (f) TX streams combined, MUSIC

Fig. 3. The range–angle maps corresponding to the considered scenario, using the MF and MUSIC approaches, where (f) also shows the targets in Fig. 2(a).

provided in the angular domain. Comparing the range–angle map in Fig. 3(f) with the one obtained in [5], it can be observed that the proposed processing scheme works quite well similar to that of a MIMO radar. Additionally, although a single RX beam is used at the sensing direction, the range–angle map also shows targets from other directions. This provides more information for the communication system which can use that to better cater to its users. Once the range–angle map is obtained, any detection scheme can be applied afterwards.

V. Conclusion

The sensing signal processing involved with obtaining the range–angle map is discussed here for a hybrid MIMO JCAS system employing OFDM. At the TX side, multiple beams are used to cater to different communication users, while an additional beam is used to sense the environment. Then, at the MIMO RX, different users' TX streams are used to obtain the range profiles corresponding to the targets in the environment, and they are subsequently utilized to derive the angle profiles using the MUSIC algorithm. The simulations indicate that it performs better than the spatial MF, while even targets situated very close in the angular domain can be reliably observed owing to the super-resolution of the MIMO processing.

Acknowledgment

References

[1] B. Paul, A. R. Chiriyath, and D. W. Bliss, "Survey of RF communications and sensing convergence research," *IEEE Access*, vol. 5, pp. 252–270, 2017.

[2] C. Baquero Barneto, S. D. Liyanaarachchi, M. Heino, T. Riihonen, and M. Valkama, "Full-duplex radio/radar technology: The enabler for advanced joint communication and sensing," *IEEE Wireless Communications*, Feb. 2021.

[3] S. A. Busari, K. M. S. Huq, S. Mumtaz, L. Dai, and J. Rodriguez, "Millimeter-wave massive MIMO communication for future wireless systems: A survey," *IEEE Communications Surveys Tutorials*, vol. 20, no. 2, pp. 836–869, Dec. 2017.

[4] L. Xu, J. Li, and P. Stoica, "Target detection and parameter estimation for MIMO radar systems," *IEEE Transactions on Aerospace and Electronic Systems*, vol. 44, no. 3, pp. 927–939, Oct. 2008.

[5] Y. L. Sit, C. Sturm, J. Baier, and T. Zwick, "Direction of arrival estimation using the MUSIC algorithm for a MIMO OFDM radar," in *Proc. IEEE Radar Conference*, May 2012, pp. 226–229.

[6] F. Liu, C. Masouros, A. Li, H. Sun, and L. Hanzo, "MU-MIMO communications with MIMO radar: From co-existence to joint transmission," *IEEE Trans. Wireless Commun.*, vol. 17, no. 4, pp. 2755–2770, Apr. 2018.

[7] X. Gao, L. Dai, S. Han, C. I, and R. W. Heath, "Energy-efficient hybrid analog and digital precoding for mmwave MIMO systems with large antenna arrays," *IEEE Journal on Selected Areas in Communications*, vol. 34, no. 4, pp. 998–1009, Apr. 2016.

[8] X. Zhang, L. Xu, L. Xu, and D. Xu, "Direction of departure (DOD) and direction of arrival (DOA) estimation in MIMO radar with reduced-dimension MUSIC," *IEEE Communications Letters*, vol. 14, no. 12, pp. 1161–1163, Nov. 2010.

[9] S. D. Liyanaarachchi, C. Baquero Barneto, T. Riihonen, M. Heino, and M. Valkama, "Joint multi-user communication and MIMO radar through full-duplex hybrid beamforming," in *Proc. IEEE International Online Symposium on Joint Communications & Sensing*, Feb. 2021.

[10] S. D. Liyanaarachchi, C. Baquero Barneto, T. Riihonen, and M. Valkama, "Joint OFDM waveform design for communications and sensing convergence," in *Proc. IEEE Int. Conf. on Commun.*, Jun. 2020.

Publication 7

MIMO Ambiguity Function Enhancement for Integrated OFDM
Communications and Sensing

S. D. Liyanaarachchi and T. Riihonen

Proc. IEEE Sensor Array and Multichannel Signal Processing Workshop (SAM), (2022)
DOI: 10.1109/SAM53842.2022.9827782

MIMO Ambiguity Function Enhancement for Integrated OFDM Communications and Sensing

Sahan Damith Liyanaarachchi and Taneli Riihonen

Electrical Engineering, Faculty of Information Technology and Communication Sciences, Tampere University, Finland

Email: sahan.liyanaarachchi@tuni.fi

Abstract—**Utilizing a multiple-input multiple-output (MIMO) communication transceiver to perform sensing is critical in future mobile communication systems. To improve sensing performance, the MIMO ambiguity function (AF) of such a system should ideally have a thumbtack shape, which improves target detection while minimizing the ambiguities observed in delay, Doppler, and angle profiles. Hence, this article analyzes the MIMO AF of orthogonal frequency-division multiplexing (OFDM) waveforms. We illustrate that using the MIMO transmitter for conventional single-stream OFDM communication results in high ambiguities in the MIMO AF's angle profile. As a solution, we propose to reduce the ambiguities by incorporating independent radar streams together with the communication stream. Numerical results depict that this method significantly reduces the integrated side-lobe level of the angle profile. Further, the power allocation between the two types of streams can be controlled to obtain an optimal trade-off between communication and sensing.**

I. INTRODUCTION

A unique requirement in modern and future communication systems, e.g., beyond fifth-generation (5G) and sixth-generation (6G) networks, is the ability to perform joint communication and sensing (JCAS) [1]–[3]. Multiple-input multiple-output (MIMO) antenna arrays in communication systems have further supplemented the advancement of JCAS systems due to their advantages for both communication and sensing [4]–[6], e.g., increased spectral efficiency [7], spatial multiplexing [8], improved detection probability and super-resolution in angle estimation [9].

Typically in these JCAS systems, a joint transmit (TX) waveform is utilized for sharing the same spectral resources, such that it provides an optimal trade-off between the two functionalities [10]. There are many candidate waveforms in the literature for the joint waveform, e.g., frequency-modulated continuous wave, single-carrier, and orthogonal frequency-division multiplexing (OFDM) waveforms [11]. The suitability of the waveform for sensing purposes depends mainly on its MIMO ambiguity function (AF), which illustrates how a target echo is observed at the receiver (RX) in comparison to the side-lobes in delay, Doppler, and angle profiles [12], [13].

Since OFDM waveforms are primarily used in communications, they outperform the other candidate waveforms by facilitating high capacity for the users. Furthermore, the two-dimensional delay–Doppler AF of OFDM waveforms has

inherently the desirable thumbtack shape, i.e., a peak corresponding to the target echo with reduced side-lobes, due to its noise-like resemblance [14]. However, OFDM waveforms' ambiguities in the angle profile are a less-discussed topic. Since future communication systems will inevitably feature MIMO antenna arrays, it is necessary to also evaluate the ambiguities in the angle profile of the MIMO AF in addition to the typical two-dimensional AF.

Hence, we analyze the MIMO AF of OFDM waveforms in this work. We illustrate that using a MIMO TX array to beamform (BF) at a specific user's direction with a communication stream results in high ambiguities in the angle profile. As a solution, we propose including separate independent spatial radar streams and communication stream, sharing the total TX power between the two sets of streams. Moreover, radar streams are considered to have their own TX precoding, separate from the communication stream. The interference at the communication user due to the inclusion of radar streams is canceled by suitably designing the radar TX precoding. The results indicate that ambiguities in the angle profile can be significantly reduced through this approach.

II. SYSTEM MODEL

We consider a fully-digital architecture for the MIMO TX and RX, having L_T and L_R antennas, respectively. We assume there is a communication RX at a line-of-sight direction of θ_c. Using the MIMO TX for conventional communication, TX time-domain signal at the antenna elements is given by

$$\tilde{\mathbf{x}}(t) = \mathbf{w}_{T,c}^{BB} x_c(t), \tag{1}$$

where $\mathbf{w}_{T,c}^{BB}$ is the communication BF vector of size $L_T \times 1$, $x_c(t)$ is the time-domain signal of the communication stream which we consider here to be an OFDM waveform with N active subcarriers and M OFDM symbols, while $\tilde{\mathbf{x}}(t)$ is of size $L_T \times 1$ correspondingly. Additionally, the stream's power is given by $P_t = \mathbb{E}\{|x_c(t)|^2\}$, where $\mathbb{E}\{\cdot\}$ denotes expectation.

Assuming the TX signal reflects off a point target and returns back at the MIMO RX, received signal at the l_R^{th} RX antenna after down-conversion to baseband can be denoted as

$$y_{l_R}(t, \mathbf{\Phi}_1) = b \sum_{l_T=1}^{L_T} \tilde{x}_{l_T}\left(t - \tau_{l_T, l_R}(\mathbf{p}_1)\right)$$
$$\cdot e^{-j2\pi \tau_{l_T, l_R}(\mathbf{p}_1) f_c} e^{j2\pi f_{l_T, l_R}(\mathbf{p}_1) t} + n_{l_R}(t), \tag{2}$$

where $\mathbf{p}_1$, $\tau_{l_{\mathrm{T}},l_{\mathrm{R}}}(\mathbf{p}_1)$, $f_{l_{\mathrm{T}},l_{\mathrm{R}}}(\mathbf{p}_1)$, b, and $n_{l_{\mathrm{R}}}(t)$ denote the two-dimensional coordinates of the point target, two-way delay and Doppler-shift due to the target, attenuation constant, and noise signal, respectively, while the target parameters are given by $\boldsymbol{\Phi}_1 = [\tau_{l_{\mathrm{T}},l_{\mathrm{R}}}(\mathbf{p}_1), f_{l_{\mathrm{T}},l_{\mathrm{R}}}(\mathbf{p}_1)]$. In addition, $\tilde{x}_{l_{\mathrm{T}}}(t)$ denotes the time-domain signal at the $l_{\mathrm{T}}^{\mathrm{th}}$ TX antenna.

Next, a bank of filters is used to match $y_{l_{\mathrm{R}}}(t, \boldsymbol{\Phi}_1)$ to the different TX signals $\tilde{x}_i(t)$ with a different set of target parameters $\boldsymbol{\Phi}_2 = [\tau_{i,l_{\mathrm{R}}}(\mathbf{p}_2), f_{i,l_{\mathrm{R}}}(\mathbf{p}_2)]$ with $i \in [1, L_{\mathrm{T}}]$, and can be written as

$$\bar{y}_{l_{\mathrm{R}}}(\boldsymbol{\Phi}_1, \boldsymbol{\Phi}_2) = b \sum_{l_{\mathrm{T}}=1}^{L_{\mathrm{T}}} \left(\int \tilde{x}_{l_{\mathrm{T}}}\big(t - \tau_{l_{\mathrm{T}},l_{\mathrm{R}}}(\mathbf{p}_1)\big) \tilde{x}_i^*\big(t - \tau_{i,l_{\mathrm{R}}}(\mathbf{p}_2)\big) \right.$$
$$\left. \cdot e^{j2\pi\left(f_{l_{\mathrm{T}},l_{\mathrm{R}}}(\mathbf{p}_1) - f_{i,l_{\mathrm{R}}}(\mathbf{p}_2)\right)t} dt \right)$$
$$\cdot e^{-j2\pi\tau_{l_{\mathrm{T}},l_{\mathrm{R}}}(\mathbf{p}_1)f_{\mathrm{c}}} e^{j2\pi\tau_{i,l_{\mathrm{R}}}(\mathbf{p}_2)f_{\mathrm{c}}} + \bar{n}_{l_{\mathrm{R}}}$$
$$= b \sum_{l_{\mathrm{T}}=1}^{L_{\mathrm{T}}} \mathbf{R}_{l_{\mathrm{T}},i}(\boldsymbol{\Phi}_1, \boldsymbol{\Phi}_2, l_{\mathrm{R}})$$
$$\cdot e^{-j2\pi\tau_{l_{\mathrm{T}},l_{\mathrm{R}}}(\mathbf{p}_1)f_{\mathrm{c}}} e^{j2\pi\tau_{i,l_{\mathrm{R}}}(\mathbf{p}_2)f_{\mathrm{c}}} + \bar{n}_{l_{\mathrm{R}}}, \tag{3}$$

where $\mathbf{R}(\boldsymbol{\Phi}_1, \boldsymbol{\Phi}_2, l_{\mathrm{R}})$ is the covariance matrix of size $L_{\mathrm{T}} \times L_{\mathrm{T}}$ corresponding to the integration terms and $(\cdot)^*$ denotes the conjugate operation.

Moreover, the RX signal at the communication user with a single antenna can be written using (1) as

$$\tilde{y}_{\mathrm{c}}(t) = \mathbf{h}_{\mathrm{c}}^H(t) \mathbf{w}_{\mathrm{T,c}}^{\mathrm{BB}} x_{\mathrm{c}}(t) + \tilde{n}_{\mathrm{c}}(t), \tag{4}$$

where $\mathbf{h}_{\mathrm{c}}(t)$ is the $L_{\mathrm{T}} \times 1$ channel vector and $\tilde{n}_{\mathrm{c}}(t)$ is the noise signal. Due to the line-of-sight conditions, $\mathbf{h}_{\mathrm{c}}(t) = \sqrt{g}\mathbf{a}_{\mathrm{T}}(\theta_{\mathrm{c}})$, where $\mathbf{a}_{\mathrm{T}}(\theta_{\mathrm{c}})$ is the TX steering vector corresponding to θ_{c}, while $\sqrt{g}$ corresponds to the free-space path loss value. In this case, $\mathbf{w}_{\mathrm{T,c}}^{\mathrm{BB}} = \frac{\mathbf{a}_{\mathrm{T}}^*(\theta_{\mathrm{c}})}{\sqrt{L_{\mathrm{T}}}}$, i.e., the spatial matched filter (MF) response, produces a single beam at θ_{c}, and it is referred to as the *single-beam case* in this paper.

III. MIMO AMBIGUITY FUNCTION

The general MIMO AF is defined based on (3) as [12]

$$\mathcal{X}(\boldsymbol{\Phi}_1, \boldsymbol{\Phi}_2) = \left| \sum_{l_{\mathrm{T}}=1}^{L_{\mathrm{T}}} \mathbf{R}_{l_{\mathrm{T}},i}(\boldsymbol{\Phi}_1, \boldsymbol{\Phi}_2, l_{\mathrm{R}}) \right.$$
$$\left. \cdot e^{-j2\pi\tau_{l_{\mathrm{T}},l_{\mathrm{R}}}(\mathbf{p}_1)f_{\mathrm{c}}} e^{j2\pi\tau_{i,l_{\mathrm{R}}}(\mathbf{p}_2)f_{\mathrm{c}}} \right|^2. \tag{5}$$

This MIMO AF can be further simplified based on some assumptions, which we consider in this article are: TX and RX antennas of the MIMO transceiver are situated close to each other, targets are in the far-field of the MIMO array, and waveforms are narrowband. In this case, the simplified MIMO AF is given by [13]

$$\mathcal{X}(\Delta\tau, \Delta f_{\mathrm{D}}, \theta_1, \theta_2) = \left| \mathbf{a}_{\mathrm{T}}^H(\theta_1)\mathbf{R}(\Delta\tau, \Delta f_{\mathrm{D}})\mathbf{a}_{\mathrm{T}}(\theta_2) \right|^2$$
$$\cdot \left| \mathbf{a}_{\mathrm{R}}^H(\theta_1)\mathbf{a}_{\mathrm{R}}(\theta_2) \right|^2, \tag{6}$$

where $\mathbf{R}(\Delta\tau, \Delta f_{\mathrm{D}}) = \int \tilde{x}_{l_{\mathrm{T}}}(t)\tilde{x}_i^*(t - \Delta\tau)e^{j2\pi\Delta f_{\mathrm{D}}t}dt$ with $\Delta\tau$ and Δf_{D} being the difference in delay and Doppler-shift

between two targets. In addition, $\mathbf{a}_{\mathrm{T}}(\theta)$ and $\mathbf{a}_{\mathrm{R}}(\theta)$ correspond to the TX and RX steering vectors for a given angle θ. Moreover, θ_1 denotes the actual direction of the target, while θ_2 corresponds to the direction of the target as observed from the MIMO RX.

A. Ambiguity Problem in Angle Profile

Although OFDM waveforms generally have an ideal thumb-tack shape in the two-dimensional delay–Doppler AF, they can have ambiguities in the angle profile, depending on the time-domain signals at the MIMO TX antenna elements. To analyze this problem, we define two different slices of the four-dimensional MIMO AF in (6) as the RX angle profile (along θ_2) and delay profile (along $\Delta\tau$). These are given by

$$\mathbf{h}_{\theta_2} = \mathcal{X}(0, 0, \theta, \theta_2), \tag{7}$$
$$\mathbf{h}_{\Delta\tau} = \mathcal{X}(\Delta\tau, 0, \theta, \theta), \tag{8}$$

where θ represents the actual angle of the target. To quantify the level of ambiguity visible in either profile, we use the metric integrated side-lobe level (ISL), which is defined separately for the two profiles as the ratio between the energy of the side-lobes to that of the main-lobe, and given by

$$\mathrm{ISL}_{\mathrm{angle}} = \frac{\int_{-\frac{\pi}{2}}^{-\theta_{\mathrm{main}}} \mathbf{h}_{\theta_2}(\theta')d\theta' + \int_{\theta_{\mathrm{main}}}^{\frac{\pi}{2}} \mathbf{h}_{\theta_2}(\theta')d\theta'}{\int_{-\theta_{\mathrm{main}}}^{\theta_{\mathrm{main}}} \mathbf{h}_{\theta_2}(\theta')d\theta'}, \tag{9}$$

$$\mathrm{ISL}_{\mathrm{delay}} = \frac{\int_{-\tau_{\mathrm{min}}}^{-\tau_{\mathrm{main}}} \mathbf{h}_{\Delta\tau}(\tau)d\tau + \int_{\tau_{\mathrm{main}}}^{\tau_{\mathrm{max}}} \mathbf{h}_{\Delta\tau}(\tau)d\tau}{\int_{-\tau_{\mathrm{main}}}^{\tau_{\mathrm{main}}} \mathbf{h}_{\Delta\tau}(\tau)d\tau}. \tag{10}$$

Here, $2\theta_{\mathrm{main}}$ and $2\tau_{\mathrm{main}}$ are the null-to-null main-lobe lengths of the angle and delay profiles, while τ_{min} and τ_{max} are the minimum and maximum delays considered in the delay profile, respectively. Thus, any low value for ISL indicates that the corresponding profile has more minor ambiguities.

When conventional communication is performed at the MIMO TX for a stream that is beamformed at θ_{c} as in (1), many ambiguities appear in the angle profile, as illustrated later in Section IV. The communication stream can also be split at another direction θ_{r}, apart from θ_{c}, which helps for sensing since the MIMO RX then receives some reflections also from this other direction. This is referred to as the *two-beams case*, and here the BF vector can be given by $\mathbf{w}_{\mathrm{T,c}}^{\mathrm{BB}} = \frac{\mathbf{a}_{\mathrm{T}}^*(\theta_{\mathrm{c}})+\mathbf{a}_{\mathrm{T}}^*(\theta_{\mathrm{r}})}{\|\mathbf{a}_{\mathrm{T}}(\theta_{\mathrm{c}})+\mathbf{a}_{\mathrm{T}}(\theta_{\mathrm{r}})\|}$, where $\|\cdot\|$ is the norm operation. However, the ambiguity problem still persists even in this case, and a solution to this is discussed in the following section.

B. Radar Streams and Beamforming Design

The main idea here is that now separate radar streams are transmitted to the environment apart from just the communication stream, where each radar stream also consists of N active subcarriers and M OFDM symbols. The vector of TX streams can then be written as

$$\mathbf{x}(t) = [x_{\mathrm{c}}(t), \overbrace{x_{\mathrm{r},1}(t), \ldots, x_{\mathrm{r},S_{\mathrm{r}}}(t)}^{\mathbf{x}_{\mathrm{r}}^T(t)}]^T, \tag{11}$$

where S_r is the number of radar streams with total streams $S = S_r + 1$. Here, $x_{r,s}(t)$ for $s \in [1, S_r]$ denotes a separate time-domain radar stream, while $\mathbf{x}(t)$ is of size $S \times 1$. Now, total TX power is shared between the communication stream and radar streams as $P_t = P_c + P_r$, where $P_c = \mathbb{E}\{|x_c(t)|^2\}$ and $P_r = \mathbb{E}\{\sum_{s=1}^{S_r} |x_{r,s}(t)|^2\}$. Then, the time-domain signals at the antenna elements are given by modifying (1) as

$$\tilde{\mathbf{x}}(t) = \mathbf{W}_T^{BB}\mathbf{x}(t) = \left[\mathbf{w}_{T,c}^{BB}, \mathbf{W}_{T,r}^{BB}\right] \left[x_c(t), \mathbf{x}_r^T(t)\right]^T, \quad (12)$$

where $\mathbf{W}_{T,r}^{BB}$ and $\mathbf{W}_T^{BB}$ are the radar BF matrix and the total BF matrix, of sizes $L_T \times S_r$, and $L_T \times S$, respectively. Moreover, the TX power at a general direction θ by considering all streams is given as

$$P(\theta) = \mathbb{E}\left\{|\mathbf{a}_T^H(\theta)\mathbf{W}_T^{BB}\mathbf{x}(t)|^2\right\}. \quad (13)$$

The inclusion of radar streams in (12) also modifies (4), i.e., the RX signal at the communication user, as

$$\tilde{y}_c(t) = \sqrt{g}\mathbf{a}_T^H(\theta_c)\mathbf{w}_{T,c}^{BB}x_c(t) + \sqrt{g}\mathbf{a}_T^H(\theta_c)\mathbf{W}_{T,r}^{BB}\mathbf{x}_r(t) + \tilde{n}_c(t), \quad (14)$$

where the first term represents the RX signal due to the communication stream, while the second term denotes the interference by the radar streams. Hence, the performance of the communication system depends on the chosen $\mathbf{W}_{T,r}^{BB}$ matrix too. It could either be based on a codebook, or optimized separately. Therefore, the choice of $\mathbf{W}_{T,r}^{BB}$ would cause a trade-off between the interference cancellation at the communication user and the suitability of the BF for radar purposes.

IV. Numerical Results

The parameters considered in the simulations are the following: $M = 10$, $N = 256$, $P_t = 30$ dBm, $L_T = 8$, $L_R = 8$, $\theta_c = -30°$, and $\theta_r = 10°$. The power allocated to each radar stream is given by $\frac{P_r}{S_r}$, where $1 \leq S_r \leq L_T$. Uniform linear arrays are considered for both the TX and RX antennas, with half-wavelength antenna element separation, and therefore the steering vector for either TX or RX array is given as

$$\mathbf{a}(\theta) = \left[1, e^{j\pi \sin(\theta)}, \ldots, e^{j\pi(L-1)\sin(\theta)}\right]^T, \quad (15)$$

where L is the number of antenna elements. We consider that $\Delta f_D = 0$, for simplicity. The frequency-domain symbols of radar streams are complex Gaussian with zero mean and unit variance. The $\mathbf{W}_{T,r}^{BB}$ matrix is designed based on null-space projection to cancel the interference in (14) as [15]

$$\mathbf{W}_{T,r}^{BB} = \left(\mathbf{I} - \frac{1}{L_T}\mathbf{a}_T(\theta_c)\mathbf{a}_T^H(\theta_c)\right)\hat{\mathbf{W}}_{T,r}^{BB}, \quad (16)$$

where $\hat{\mathbf{W}}_{T,r}^{BB}$ is chosen as a random orthonormal matrix so that instantaneous beampatterns of different radar streams illuminate different directions, while $(\cdot)^\dagger$ denotes the pseudo-inverse operation. Hence, this ascertains that each radar stream's beampattern has a null at θ_c direction.

Figure 1(a) first depicts the gain of the TX beampattern in (13) for different S_r values, averaged over many random radar beampatterns. For the single-beam case, $S_r = 0$ corresponds to
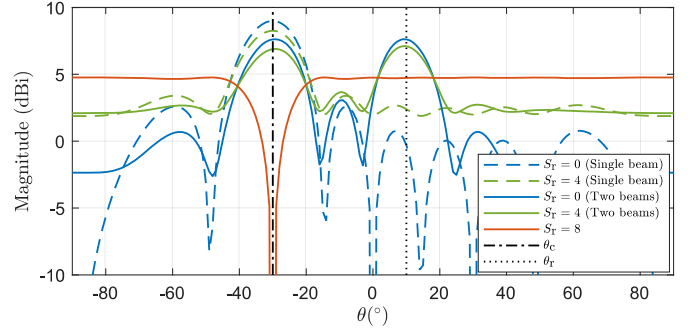
(a)
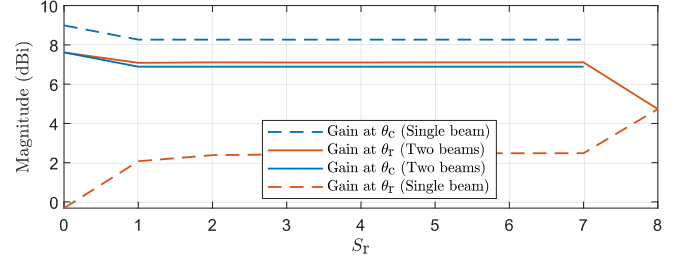
(b)

Fig. 1. The TX BF design where (a) illustrates the gain of TX beampattern and (b) depicts the gain at θ_c and θ_r, both for different S_r values.
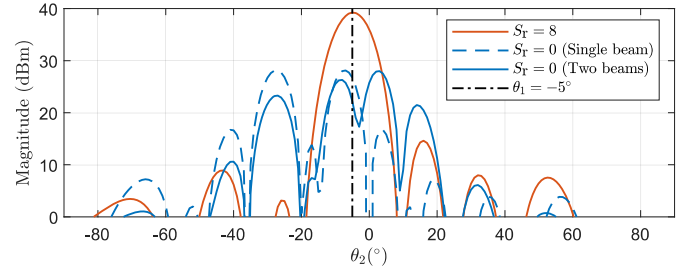

Fig. 2. Angle profile of MIMO AF corresponding to $\theta_1 = -5°$.

the case when only the communication stream is transmitted at θ_c. Then, when $S_r = 4$, the gain at θ_c is decreased due to the inclusion of random radar beampatterns. A similar observation is made for the two-beams case, for both θ_c and θ_r directions. When $S_r = 8$, all radar beampatterns have a null at θ_c, so the gain at that angle is quite low. However, when $S_r = 4$, the gain at θ_c is not low due to the communication beampattern.

Next, the gains at θ_c and θ_r directions are illustrated in Fig. 1(b) for the two different BF cases. Additionally, the figure denotes the gains averaged over many random radar beampatterns. In both BF cases, the highest gain for θ_c is when $S_r = 0$, while having $S_r = 1$ is observed to decrease the gain from that value, but it remains constant after that. When $S_r = 8$, there is a deep null at θ_c, so the gain at θ_c is not illustrated. For θ_r, the highest gain is when $S_r = 0$ for the two-beams case. Then, as S_r is increased, the gain first decreases and remains constant, whereas the lowest gain happens when $S_r = 8$. However, the opposite behavior is observed in the single-beam case.

To illustrate the ambiguity problem discussed in Section III-A, Fig. 2 depicts the angle profile for $\theta_1 = -5°$, i.e., the angle profile observed at the MIMO RX when there is a target at $-5°$. When $S_r = 0$, it can be observed that for both BF cases, the observed peak is not precisely at $-5°$, while there are a considerable amount of side-lobes that increase the ambiguities. In contrast, when $S_r = 8$, the peak corresponds to the actual target direction, while the side-lobes are also considerably lower, thus improving target detection.

To observe the effect of proposed MIMO AF enhancement, we analyze the ISL of angle and delay profiles for different power allocation values, i.e., $P_c - P_r$ in decibel scale, as well as for different S_r values, in Fig. 3. Firstly, Fig. 3(a) depicts ISL$_{\text{angle}}$ for possible target directions. For example, ISL value at $\theta_1 = -5°$ for $S_r = 8$ is calculated based on Fig. 2, i.e., when there is a target at $-5°$, ambiguity of angle profile across θ_2 is used to calculate the corresponding ISL value. This is performed for all θ_1 values to obtain Fig. 3(a).

This figure depicts that when $S_r = 0$, the ISL in the angle profile is quite high. For either single/two-beam(s) case, the minimum ISL is observed around θ_c/θ_c and θ_r, respectively. However, increasing the number of independent radar streams decreases the ISL values for almost all angles. It is also noticeable that when $\theta_1 = \theta_c$, the ISL of $S_r = 8$ is very high. This is because θ_c has a deep null, as illustrated in Fig. 1(a). However, if $S_r < 8$, that means the communication stream is transmitted at θ_c, and therefore the MIMO RX receives some reflections from that direction, which is why those curves do not have a high ISL value at θ_c. Then, Fig. 3(b) depicts that ISL$_{\text{angle}}$ can be controlled by changing the power allocated to the communication and sensing streams. It can be observed that by increasing P_r (or decreasing P_c), the ISL of the angle profile can be improved for the waveform with a specific number of radar streams.

The ISL of delay profile is next depicted in Fig. 3(c). First, it depicts that by changing either P_c or P_r, the ISL in the delay profile can be controlled, although the change in ISL is quite minor compared with the angle profile. Secondly, the embedded plot illustrates the variation of ISL$_{\text{delay}}$ when $P_c - P_r = 4$ dB and $\theta_1 = \theta_2 = -15°$, and it shows that increasing S_r slightly increases the ISL, that is contrasting to the ISL performance in the angle profile depicted in Fig. 3(a). However, this also shows that the ambiguities in the delay profile are quite low in OFDM waveforms since the ISL values are already good.

Therefore, the ISL of the angle profile of MIMO AF can be improved by including independent radar streams. The addition of such radar streams slightly increases the ISL in the delay profile. However, the loss is negligible compared to the gains in the angle profile. Further, since the radar streams consist of random frequency-domain symbols, while their precoding matrix $\mathbf{W}_{\text{T,r}}^{\text{BB}}$ can be calculated readily as in (16), the proposed MIMO AF enhancement is of very low complexity for practical implementation. If necessary, MIMO AF can be further improved by optimizing radar streams and the $\mathbf{W}_{\text{T,r}}^{\text{BB}}$ matrix, which will be an interesting future topic.
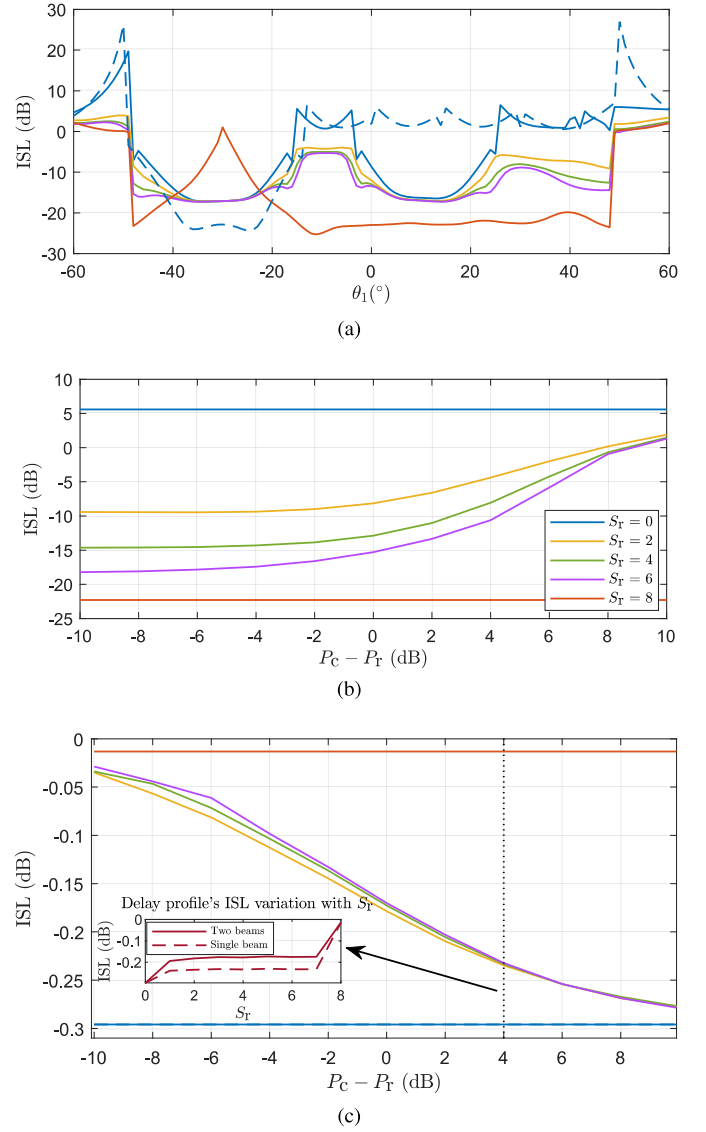

Fig. 3. The ISL variation of angle and delay profiles of the MIMO AF, where (a) depicts ISL$_{\text{angle}}$ for $P_c - P_r = 4$ dB, with the dashed curve corresponding to $S_r = 0$ with a single beam, while all others are with two beams, (b) depicts ISL$_{\text{angle}}$ of $\theta_1 = -15°$ for different $P_c - P_r$ values, and (c) depicts ISL$_{\text{range}}$ at $\theta_1 = \theta_2 = -15°$ for different $P_c - P_r$ values.

V. CONCLUSION

This article analyzed the ambiguities observed in the MIMO AF of an OFDM JCAS system. Employing an OFDM communication stream to perform sensing increases ambiguities in the angle profile, although OFDM waveforms generally have a thumbtack shape in two-dimensional delay–Doppler AF. Employing independent spatial radar streams on top of the communication stream, where the TX power is shared between the two sets of streams, is shown to significantly decrease the ISL, by even more than 25 dB for some angles. The interference from radar streams at the communication user is also canceled by designing their BF matrix. Moreover, by altering the power allocation between the two types of streams, the level of ambiguities can be controlled, allowing an optimal trade-off between communications and sensing.

REFERENCES

[1] D. K. Pin Tan, J. He, Y. Li, A. Bayesteh, Y. Chen, P. Zhu, and W. Tong, "Integrated sensing and communication in 6G: Motivations, use cases, requirements, challenges and future directions," in *Proc. IEEE International Online Symposium on Joint Communications & Sensing (JC&S)*, Feb. 2021.

[2] F. Liu, C. Masouros, A. P. Petropulu, H. Griffiths, and L. Hanzo, "Joint radar and communication design: Applications, state-of-the-art, and the road ahead," *IEEE Transactions on Communications*, vol. 68, no. 6, pp. 3834–3862, Feb. 2020.

[3] B. Paul, A. R. Chiriyath, and D. W. Bliss, "Survey of RF communications and sensing convergence research," *IEEE Access*, vol. 5, pp. 252–270, 2017.

[4] X. Liu, T. Huang, N. Shlezinger, Y. Liu, J. Zhou, and Y. C. Eldar, "Joint transmit beamforming for multiuser MIMO communications and MIMO radar," *IEEE Transactions on Signal Processing*, vol. 68, pp. 3929–3944, Jun. 2020.

[5] R. S. Prasobh Sankar, B. Deepak, and S. P. Chepuri, "Joint communication and radar sensing with reconfigurable intelligent surfaces," in *Proc. IEEE 22nd International Workshop on Signal Processing Advances in Wireless Communications (SPAWC)*, Sep. 2021, pp. 471–475.

[6] S. Buzzi, C. D'Andrea, and M. Lops, "Using massive MIMO arrays for joint communication and sensing," in *Proc. Asilomar Conference on Signals, Systems, and Computers*, Nov. 2019.

[7] O. E. Ayach, S. Rajagopal, S. Abu-Surra, Z. Pi, and R. W. Heath, "Spatially sparse precoding in millimeter wave MIMO systems," *IEEE Transactions on Wireless Communications*, vol. 13, no. 3, pp. 1499–1513, Jan. 2014.

[8] S. Sun, T. S. Rappaport, R. W. Heath, A. Nix, and S. Rangan, "MIMO for millimeter-wave wireless communications: Beamforming, spatial multiplexing, or both?" *IEEE Communications Magazine*, vol. 52, no. 12, pp. 110–121, Dec. 2014.

[9] S. D. Liyanaarachchi, C. Baquero Barneto, T. Riihonen, M. Heino, and M. Valkama, "Range–angle processing for target detection in joint MIMO-OFDM communications and sensing," in *Proc. IEEE 22nd International Workshop on Signal Processing Advances in Wireless Communications (SPAWC)*, Sep. 2021, pp. 486–490.

[10] S. D. Liyanaarachchi, T. Riihonen, C. Baquero Barneto, and M. Valkama, "Optimized waveforms for 5G–6G communication with sensing: Theory, simulations and experiments," *IEEE Transactions on Wireless Communications*, vol. 20, no. 12, pp. 8301–8315, Dec. 2021.

[11] T. Wild, V. Braun, and H. Viswanathan, "Joint design of communication and sensing for beyond 5G and 6G systems," *IEEE Access*, vol. 9, pp. 30 845–30 857, Feb. 2021.

[12] G. San Antonio, D. R. Fuhrmann, and F. C. Robey, "MIMO radar ambiguity functions," *IEEE Journal of Selected Topics in Signal Processing*, vol. 1, no. 1, pp. 167–177, Jun. 2007.

[13] Y. Li, S. A. Vorobyov, and V. Koivunen, "Generalized ambiguity function for the MIMO radar with correlated waveforms," in *Proc. IEEE International Conference on Acoustics, Speech and Signal Processing (ICASSP)*, May 2014, pp. 5302–5306.

[14] N. Levanon, "Multifrequency radar signals," in *Proc. IEEE International Radar Conference*, May 2000, pp. 683–688.

[15] S. D. Liyanaarachchi, C. Baquero Barneto, T. Riihonen, M. Heino, and M. Valkama, "Joint multi-user communication and MIMO radar through full-duplex hybrid beamforming," in *Proc. IEEE International Online Symposium on Joint Communications & Sensing (JC&S)*, Feb. 2021.